Exploration of M Oy-Al O -SiO systems through their dynamics and their structure, from the melted medium to the low temperature

Ilse Maria Ermini

UNIVERSITÉ D'ORLÉANS

ÉCOLE DOCTORALE

Énergie - Matériaux - Sciences de la Terre et de l'Univers

Conditions Extrêmes et Matériaux : Haute Température et Irradiation

CEMHTI UPR 3079 CNRS

THÈSE présentée par :

Ilse Maria ERMINI

soutenue le : **15 Décembre 2023**

pour obtenir le grade de : **Docteur de l'Université d'Orléans**

Discipline/ Spécialité : Sciences physiques

Exploration of M_xO_y-Al_2O_3-SiO_2 systems through their dynamics and their structure, from the melted medium to the low temperature

THÈSE dirigée par :

FAYON Franck	Directeur de recherche, CNRS Orléans

RAPPORTEURS :

DE LIGNY Dominique	Professeur, Friedrich-Alexander-Universität
ISPAS Simona	Maître de conférences HDR Université de Montpellier

---

JURY :

FAYON Franck	Directeur de recherche, CNRS Orléans
DE LIGNY Dominique	**Président du jury,** Professeur Friedrich-Alexander-Universität
ISPAS Simona	Maître de conférences HDR Université de Montpellier
GROSS Christoph	Expert, SCHOTT
LÓPEZ Gabriel Alejandro	Maître de conférences, Universidad del País Vasco
TARDIVAT Caroline	Expert, Saint-Gobain
DE SOUSA MENESES Domingos	Professeur, Université d'Orléans
GONZÁLEZ DE ARRIETA Iñigo	Professeur associé, Universidad del País Vasco

UNIVERSITÉ D'ORLÉANS

ÉCOLE DOCTORALE

Énergie - Matériaux - Sciences de la Terre et de l'Univers

Conditions Extrêmes et Matériaux : Haute Température et Irradiation

CEMHTI UPR 3079 CNRS

THÈSE présentée par :

Ilse Maria ERMINI

soutenue le : **15 Décembre 2023**

pour obtenir le grade de : **Docteur de l'Université d'Orléans**

Discipline/ Spécialité : Sciences physiques

Exploration des systèmes M_xO_y-Al_2O_3-SiO_2 à travers leur dynamique et leur structure, depuis le milieu fondu jusqu'à basse température

THÈSE dirigée par :

FAYON Franck	Directeur de recherche, CNRS Orléans

RAPPORTEURS :

DE LIGNY Dominique	Professeur Friedrich-Alexander-Universität
ISPAS Simona	Maître de conférences HDR, Université de Montpellier

---

JURY :

FAYON Franck	Directeur de Recherche, CNRS Orléans
DE LIGNY Dominique	**Président du jury**, Professeur Friedrich-Alexander-Universität
ISPAS Simona	Maître de conférences HDR, Université de Montpellier
GROSS Christoph	Expert, SCHOTT
LÓPEZ Gabriel Alejandro	Maître de conférences, Universidad del País Vasco
TARDIVAT Caroline	Expert, Saint-Gobain
DE SOUSA MENESES Domingos	Professeur, Université d'Orléans
GONZÁLEZ DE ARRIETA Iñigo	Professeur associé, Universidad del País Vasco

Acknowledgements

I am very happy to be able to express my gratitude to the many people who have been an important part of my life during these 3 years or more.

I am very grateful for all the help and support I received in CEMHTI and in my personal life and all the good memories that I had and that I will treasure forever.

I thank all the jury members for their insights and their interest in this work.

A special thanks goes to DE SOUSA MENESES Domingos and FAYON Franck for their help and supervision, CANIZARES Aurelien for the Raman measurements, RIDOUARD Amandine for glass synthesis, DUNCAN Euan and VALOIS Renaud for the aerodynamic levitation and HACHEM Clement for the XRD measurements.

I also would like to express my gratitude to all of my friends and family for staying by my side even during difficult times.

Ilse Maria Ermini

Orléans, France, Dicember 2023

Contents

1

Introduction

"It is nonsense to conceive of nature as a static fact, even for an instant devoid of duration. There is no nature apart from transition, and there is no transition apart from temporal duration. This is why an instant of time, conceived as a primary simple fact, is nonsense" - A.N. Whitehead, Modes of Thought (1938)

Contents

1.1 Time, causality and process

Scientific research is strongly correlated and motivated by civilization development and the curious nature of humanity. The conscious nature of human beings leads inevitably to the research of answers and explanations to questions regading nature and natural phenomena.

From a physics' point of view, the link between space and time has long been established by the special theory of relativity,[1] leading to the replacement of the three-dimensional Euclidean space with the four-dimensional Minkowski space[2] that includes time as the forth dimension.

This discovery, coupled with the development of quantum mechanics, soon caused a paradigm shift[3] first in the scientific community and later in the general public. This concept is a fundamental one in philosophy of science: a discipline that overlaps with metaphysics, ontology and epistemology with the objective of an exploration of the relationship between science and truth.

Science is mainly conducted within a paradigm, a logically consistent set of rules that are known, whereas when scientific revolutions occur, the paradigm "shifts" and a new framework is used for latter research. The choice of a paradigm completely changes the aims and the interpretations of science. Whether this choice is made or not depends on rational as well as social justifications.

This argument illustrates the strong link existing between metaphysics and physics, as well as their mutual influence. This is due to the fact that the metaphysical interpretation of nature and its laws affects the scientific practice and viceversa.

The example of the speculative philosopher Alfred North Whitehead is perhaps one of the best to describe this phenomenon. Whitehead was educated as a mathematician, yet his most famous works mainly regard metaphysics and ontology, from a philosophy of science point of view.

In his book "Process and Reality",[4] considered the cornerstone of process metaphysics,[5] he describes two kinds of existence of an entity. Actual entities refer to to those that really exist in nature as spatiotemporally extented processes and events. The world, in his view, is a multiplicity of actual entities and their correlations. Abstract entities are abstracted from or derived from actual entities: a principle that can give a particular form to an actual entity.[6]

In this case, actual existence is seen as a process of becoming, strongly linked to the concept of time as each actual entity inherently possess its respective

dimension of time. The principle of causality is well respected since each actual entity is causally consequential on those which precedes it in time and has as its causal consequences those which follow.

We can easily observe that this metaphysical approach to nature is perfectly coherent with the viewpoint of Einstein's theory of special relativity and with Minkowski's spacetime geometry. Whitehead's work has been influential among scientists including physical chemist Ilya Prigogine, biologist Conrad Hal Waddington, and geneticists Charles Birch and Sewall Wright, illustrating yet again the mutual influence of science and philosophy.

The quotation chosen as the opening for this work fits perfectly with its content, as the dynamic aspect and its link to time is fundamental to it. The aim is to develop a real-time apparatus to be able to observe phase transition from molten state and investigate the microstructural changes that occur therein. In order to reach this goal, it is important to consider carefully another key factor: time.

1.2 Real-time definition, timescales of natural phenomena

The main feature of this study is the ability to perform real-time dynamic measurements. Yet, it is extremely difficult to define what "real-time" stands for and whether it is an instant or a time interval.

The concept of the light cone (illustrated in figure 1.1) in the Minkowski space illustrates clearly that casuality links events and through this principle it is possible to distinguish past and future events. In this example, the present is denoted by the single event occurring at an instant of time t_0, illustrated as a point. The hypersurface of the present contains all the other events at t_0 that are uncorrelated to this event.

In this framework, we can see that real-time coincides with the present and more specifically with t_0. From a mathematical and logical point of view, this definition is theoretically the best possible but from an human point of view this concept is unattanaible and even useless for application.

The shortest theoretically measurable time interval is the Planck time[7] corresponding approximately to 5.39 x 10^{-44} s.

All physical processes occur at longer timescales, from 10^{-27} (mean lifetime of W and Z bosons) to 10^{-6} s (lifetime of a muon).

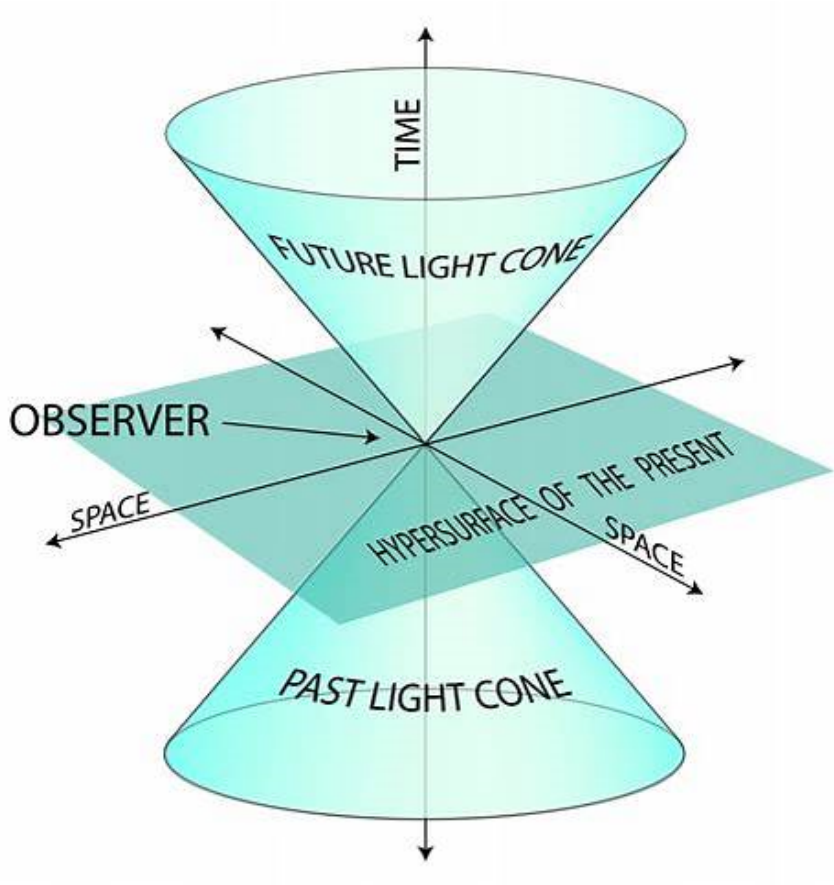

Figure 1.1: Light cone representing the path that a flash of light from a single event would take through spacetime. Future and past events are correlated through causality.

However, these times include also how fast the technology is able to operate such as short laser pulses (10^{-18} s) and the speed of execution of one machine cycle (10^{-6} s).

Units greater than 10^{-3} s start to involve human life and our perception of it: this is the time needed for a neuron to fire an impulse and, if we multiply it by 10, we obtain the average time of human reflex response. Human life expectancy is in the order of 10^9 s.

Longer timescales involve lifetimes of biological species (10^{12} s), half-life of long lasting isotopes (for example for ^{235}U it is 22 x 10^{15} s), geological time scales (an eon is 31.6 x10^{15} s) and approximate lifetime of main-sequence stars (315 x10^{15} s).

All times beyond this scale are theoretical since they surpass the lifetime of the universe and they regard lifetimes of red dwarves, half-lives of very long lasting radioactive isotopes such as bismuth-209 and tellurium-128 and approximate lifespans of black holes (6x 10^{73} s).[8]

All of the described natural and physical phenomena have their own timescale and their classification as fast or slow phenomena lies entirely on human perspective since we are the observers. We can easily consider that all the phenomena occurring at timescales shorter than our perception (10^{-3} s) are fast, and viceversa.

Nonetheless, it is still important to reflect on how to properly describe real-time from a more human and practical point of view. First of all, we need to take into account the limitations imposed by technology, restricting it to up to 10^{-6}. Lastly, the description of real-time has to be linked to how we perceive the present moment. It has been found that human perception of the present moment is inherently linked to perceptual information[9] that can be stored for up to 10^{-3} . After this time, the information has been stored and so it belongs to the past. This also means that time is not experienced directly.

In conclusion, there seems to be a huge discrepancy between the scientific nature and existence of time and our experience of it. This metaphysical question will not be discussed any further, as it is out of the scope of this work.

The next chapters present the outline and motivation of the study, the state of art and finally some results and discussion.

2

Solidification pathway control and fast acquisition techniques for material engineering and design

Contents

2.1 Time-resolved in-situ high temperature studies

The quest for high speed data acquisition is still ongoing due to the necessity of instrumentation improvement to be able to observe fast occurring phenomena. This is because the appearance and the study of transient states, metastable or out of equilibrium phases is still an open question in science, forcing scientists to find new and fast ways to probe materials. Large scale industrial production is also affected since fast phenomena also occur at high temperature during melt solidification processes.

Indeed, the mechanical and physical properties of a material are highly dependent on the parameters involved in its production through cooling from liquid state, even when its chemical composition stays unaltered.

Through the complete knowledge and control of the temperature and cooling rate of a material, it is possible to modify its microstructure, resulting in different macroscopical properties in the solid state.[10–12]

In other words, the selection of a solidification pathway can allow the creation of materials that possess advantageous properties to be used for a particular application. Some examples are glass-ceramics,[13] bioactive glasses[14,15] and transparent ceramics[16,17] along many others. This strategical approach to material design combined with the knowledge obtained through high temperature studies, phase formation and microstructural properties will contribute to both the improvement of well-known applicable materials and the development of new materials with enhanced properties.

In order to observe materials in extreme conditions it is necessary to develop instrumental setups that are able to perform these measurements with different techniques. The importance of a multitechnical approach to material science can be easily explained by the fact that the information extracted differs depending on the technique employed. Material characterization techniques, such as light scattering or diffraction techniques, are thus complementary to each other to be able to reach a wider understanding of the microstructural properties.

This chapter will present the main problems concerning industrial production of materials through solidification from liquid and the main research topics involved in this discussion. It also illustrates the main techniques used to probe materials and the instrumental advances in terms of acquisition speed. The focus will be set on high temperature studies and the observation of the cooling phenomenon.

2.2 Advances in industrial production

One of the main reasons motivating scientific reseach on materials is the possibility to apply the acquired knowledge for technological advance. Industrial production of many materials is mainly performed from molten state, a state in which matter has the ability to flow and acquire the form of its container (for example glass, polymers...).

In order to obtain a solid, the liquid has to be cooled down, a process which is still not widely studied. The formation of exotic non-equilibrium microstructures through solidification pathway control and selection has been observed, even though the relationship between the involved parameters and the final microstructure has not yet been clarified.[18]

The importance of acquiring information about this phenomenon lies in the quality and characteristics that the formed solid state has to possess and in the possibility of stabilizing exotic phases leading to new applications. Great progress in this field has been made even though further research is still necessary to overcome recurring problems found during and after production.

The open areas of research can be summarized as follows:[19]

- Kinetics of solidification
- Prediction of phase diagrams
- Prediction of the effect of impurities
- Design of fluid dynamics
- Process control
- Polymorph screening
- Stabilization of non-stable phases
- Product design

Solving these problems would lead to a better development and an optimization of new materials and products that can match the industries' specific demands. These new products will be more functional with fullfilling additional requirements like increased purity and stability, lower costs and improved sustainability.

Progress can be obtained through a multidisciplinary approach which includes characterization at a molecular level of the structure with the goal of improving

its properties, then with product design and lastly through the use of an efficient process control.

Some of these aspects have to be discussed in further depth since they will be crucial to understand the practical aim of this work.

- **Prediction of phase diagrams**
  The understanding of phase diagrams is very important for product design since these charts (an example is illustrated in figure 2.1) show the conditions in which thermodynamically distinct phases exist and cohexist in equilibrium conditions. They are based on the knowledge of the thermodynamic properties of the material, acquired through experimental data. In the case of well-known mono-component materials, the informations on its changes through pressure and temperature changes have been studied in details.

  However, real materials are complex and this complexity shows itself in experimental studies as well.[20,21] This complexity is caused by the multicomponent nature of materials and the possibility of forming different microstructures while still keeping the same composition. Moreover, the extreme temperature conditions can cause evaporation of some of these compounds in the material, thus modifying the final composition.

  For this reason, computation, modeling and simulation techniques are used to simulate the phase diagrams of complex multicomponent systems.[20,21]

  Nonetheless, this approach is only possible if supported by reliable and consistent one-component data to be able to have databases to model the system to perform the simulation. Yet again, this problem arises from the difficulties encountered with high temperature and high pressure experimental work, as these extreme conditions are complicated to reproduce.

- **Prediction of effects of impurities**
  As illustrated in figure 2.2, the network is not homogeneously formed if impurities or defects are present, and this can be reflected in terms of the physical properties. Still, addition of impurities can be beneficial to the network since their presence in the network strongly affect its properties such as its nucleation, crystal growth and morphology as well as crystal stability.[22,23]

  Additives such as metal ions can also have an impact and since both can perturbate the metastable zone width and the crystal growth rate, it is important to obtain the knowledge necessary to prevent the formation of unwanted morphologies. This is due to the fact that a modification

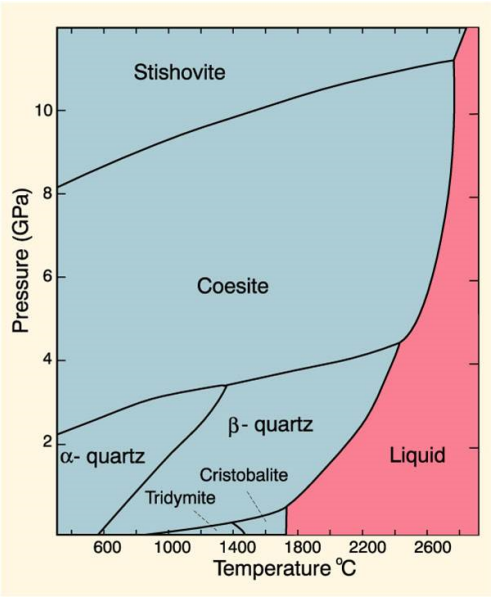

Figure 2.1: Scheme of the phase diagram of SiO_2. The various phases are obtained through different temperature or pressure conditions. Solid phases (in light blue) are distinguished by their different crystallography.

of these parameters can highly affect product quality after industrial processing.[24]

The prevention of the formation of different morphologies is usually done by additives inserted in the material in an empirical approach, due to the fact that the mechanisms of formation of diffent networks are still not well known. The role of additives is also important for stabilization of metastable polymorphs.[25–27]

- **Presence and stabilization of polymorphs**
  A polymorph is a different arrangement or conformation of molecules within the same chemical composition.[29] Differences in structures give rise to differences in the physical and macroscopical properties of the solid. This is another reason why the occurrence of an unwanted polymorph should be taken into consideration when it comes to design and control.[30,31]

  In order to do this, a deep understanding of the kinetics and thermodynamics of the polymorphic system is required[32] as well as the conditions of their formation and transformation. In this case, molecular modelings are not yet advanced enough to be helpful, leaving room for direct observation.

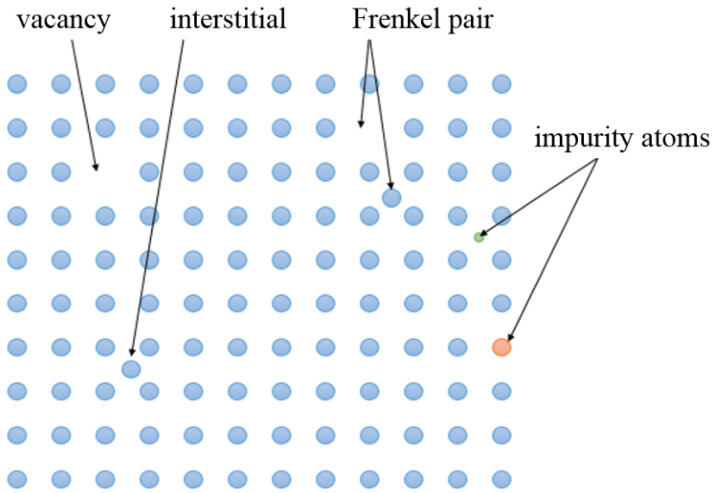

Figure 2.2: Schematic representation of defects and impurities.[28] Their presence in the structure of the material might be beneficial or, on the contrary, might lower the optical or mechanical properties.

New methods are necessary to discover different phases, especially through a real-time (and in-situ) monitoring of the phenomenon. In-situ techniques could shed light on the intrinsically dynamic nature of this transformation and the instability of some polymorphs (metastable phases) by acquiring kinetic data to identify and quantify the formation of polymorphs in real time.

The possibility of stabilizing metastable polymorphs is very important for the discovery of new materials that could possess interesting properties. Less stable polymorphs could then be crystallized from melt or from an amorphous state (for example: quenched glasses or sol-gel routes) but, up to now, these methods may still be difficult to control such that the formation of various polymorphs would be avoided.[33,34]

Isolation of a polymorph can also be a very challenging task. The limited success of these methods is due to the non-consideration of kinetic factors that play a dominant role, as they are not completely known yet.

2.2.1 Material design through solidification pathway control

The importance of cooling process' control for the production and design of solid products with desired properties is very high and it can be achieved only

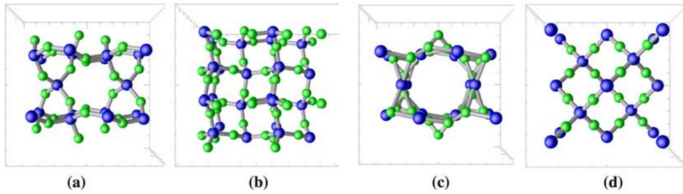

Figure 2.3: Schematic representation of polymorphism in SiO_2. The blue spheres represent Si atoms and the green ones O atoms. The polymorphs illustrated are: a) α-quartz, b) α-cristobalite, c) β-quartz and d) β-cristobalite.[35]

through extensive knowledge of the entire solidification process.[19]

It has already been observed that fast cooling of molten materials can allow stabilization of metastable phases in the solid.[36,37] The stabilization process is obtained by suppressing the growth and nucleation of the stable phase. This process can be performed when the cooling rate used during solidification is very high.[38]

The formation of different new unexplained microstructures, mainly through the use of fast solidification techniques such as additive manufacturing and melt spinning, raised questions on the physical mechanisms that can allow the creation of homogeneous microstructures in the sample.

It has been shown that the techniques listed before, even though they present similar cooling rates, created microscopical differences, leading to the hypothesis that the main difference should reside in the solidification pathway taken by the liquid at the time of cooling.[18]

During fast solidification, microstructures develop due to interfacial velocity, temperature and concentration at the solid-liquid interface.[39] Interface dynamics is complicated due to the kinetics involved in the process and the solid morphology is determined both by the temperature gradient in the molten state and the velocities at the interface.[40]

Due to the complexity of this problem from an experimental point of view, most of the research has been conducted through numerical calculations. Nonetheless, the negligence of thermal history, temperature gradients and possible inhomogeneities in the sample prove the importance of performing also experimental observations of the solidification process.

Additional experimental work is still needed to shed light on the aforementioned mechanisms and a variety of techniques which aim to characterize the material have to be employed.

2.3 In situ techniques for material characterization

There are various techniques that can be used to probe materials and their kinetics. It is important to consider the intrinsic features of these techniques which exhibit different characteristic timescales depending on their type of interaction with matter, as well as their absolute sensitivity, detection limits and relaxation speeds. Figure 2.4 provides a scheme to compare the techniques. In this work, we will use FT-IR spectroscopy to observe the solidification of materials from molten state. This type of spectroscopy is used to probe vibrations, that have a timescale of $10^{-15} - 10^{-12}$ s,[41] yet in this framework, we would like to employ it to observe motions in the liquid and the mechanisms of bond creation and breaking. These phenomena are slower compared to vibrations, so the technique is able to obtain the information required. The experimental setting will be presented in Chapter 3 and a theoretical presentation of the technique is illustrated in Chapter 4.

Due to the complementarity to other techniques, this section will present other mainly used techniques that have been employed to study this phenomenon and the type of information that can be obtained.

- **X-ray and neutron diffraction**
  Diffraction techniques are mainly used to probe the structure of materials at the atomic scale. Their principle lies on an elastic scattering process such that scattered particles, recollected by the detector, have the same energy but a modified direction depending on the position of the atoms in the sample. If we consider a crystal, X-rays will be diffracted in accordance to Bragg's law. The constructive interference peaks are thus associated with the crystalline lattice spacings.

  The information on liquid and glass structure is obtained by the measurement of the structure factor S, used then to calculate the real space pair distribution function g which corresponds to the probability $g(r)$ of finding two atoms at a given distance r.

  As the radial distribution function is retrieved, it is possible to integrate it to obtain the average number of neighboring atoms in a coordination shell. In other words, diffraction techniques provide information about interatomic distances and the number of neighboring atoms at a specific distance.[43]

  Nonetheless, the information retrieved is more complex when dealing with multicomponent systems as the calculation of g is complicated by

the overlap of many pulses for large distances. In those cases, diffraction techniques are employed to observe the first sharp diffraction peak, especially in glasses and liquids. In order to simplify the problem, anomalous diffraction is used to select the K-edge (innermost electron shell) of only one element.

The sensitivity of X-ray increases with atomic number, while the scattering power of neutron varies. These techniques have an energy resolution of 10^{-7} of the incident light[44] and, as seen in figure 2.4, a timescale of ns to ps.

X-ray diffraction has already been used to study the solidification process of melts.[45] Hennet et al. describe the methodology they used to obtain time resolved spectra by combining the technique with aerodynamic levitation.[46]

The structural evolution of the sample has been analyzed by acquiring S values and computing the corresponding g every 100 ms after the start of the cooling. Nonetheless, the major problem encountered by using this technique is the detection system that limits the structural information that can be obtained by the measurement.

In order to develop the technique further, it is necessary to have a detector that enables a wider q range, with q being the scattering vector which defines the direction of scattering, $q = 4\pi sin\theta/\lambda$ with θ being the scattering angle and λ the wavelength.[47]

This is because the $g(r)$ values are obtained by the Fourier transform of the structure factors $S(q)$ and a low q value leads to poor resolution in the r-space, a requirement necessary to resolve all the peaks present. The features observed at high-q mainly relate to local structural ordering since each peak of g corresponds to an interatomic distance.

Diffraction techniques require the use of an high-flux source such as syncrotron radiation to perform high speed measurements.

- **Nuclear Magnetic Resonance (NMR)**
  Nuclear Magnetic Resonance (NMR) spectroscopy can be used to probe the chemical environment of atoms. Its principle relies on the interaction between the nuclear magnetic moment of a specific nucleus and a strong external magnetic field known as the Zeeman Effect.[48] In order to observe an NMR signal, the nucleus under study should have a non-zero nuclear spin such that it can interact with the static magnetic field. For nuclei with an even number of neutrons and protons, the resulting spin quantum number is zero and are therefore unobservable in NMR (e.g. ^{12}C). Other

isotopes are NMR active with intrinsic sensitivity depending on their respective natural abundance (e.g. 1.1% for ^{13}C).

The nuclear magnetic moments interact with the external field and undergo precession at their Larmor frequency (which is proportional to the gyromagnetic ratio of the nucleus and the external field). This gives rise to a net nuclear magnetization along the applied static magnetic field. This nuclear spin magnetization can be manipulated by applying a radiofrequency (RF) field at the Larmor frequency (thereby satisfying the resonance condition) to get the NMR signal.

NMR spectroscopy is a quantitative technique. As mentioned above, each isotope has its own Larmor frequency making the technique isotope selective.

The nuclear spins also interact with local magnetic fields which depend on the local environment and this modifies the total magnetic field causing different frequencies. The most relevant interactions are the chemical shift interaction which is due to the shielding effect of the electron cloud around the nucleus, the dipolar nuclear spin couplings between neighboring isotopes (proportional to the inverse cube of the interatomic distances) and the quadrupolar coupling for isotopes wich nuclear spin $> 1/2$. The chemical shift interaction is the key factor used to probe the structure of a material since different peaks in an NMR spectrum are caused by a different degree of nuclear shielding. These new frequencies are compared to a standard one and their difference will be expressed as a chemical shift.[49,50]

In the solid state, these magnetic interactions are anisotropic and depend on the orientation with respect to the external field. For polycristalline or amorphous samples, this gives rise to a large broadening of the NMR spectra. This anisotropic broadening can be removed (or partially cancelled) by using the Magic Angle Spinning technique to obtain high-resolution NMR spectra exhibiting narrow peaks associated to the different chemical environments of the studied material.[51–53] In the liquid state, the anisotropic interactions are averaged out by the brownian motions (motional narrowing) such that the remaining effects are only the isotropic chemical shift and the weaker isotropic indirect spin-spin couplings.

The timescale of the NMR technique is qualified as relatively slow with respect to X-Ray scattering or IR spectroscopy, for example. It ranges from 10^{-8} to 10^{-10} s (hundred MHz frequency range) when performing spin relaxation measurements and can be extended from 10^{-5} down to 10^{-1} s (100 kHz - 10 Hz range) by probing the residual anisotropic interactions or by using two-dimensional chemical exchange NMR spectroscopy.[54,55]

Structural and dynamical information in high temperature liquids and in-situ studies of free-cooling from the melt have been conducted with NMR.[56] In those cases, the observed nuclei must be of high NMR sensitivity. This approach is therefore limited to the observation of isotopes with a high natural abundance and a relatively high Larmor frequency, like ^{27}Al (n.a. 100%, Larmor frequency of 78.2 MHz in a magnetic field of 7.0 T). In the high temperature liquid, motional narrowing occurs at a very fast timescale such that the isotropic chemical shift information is averaged and a single NMR peak is oberved at the average frequency of the different environments. Time-resolved NMR data is obtained every 25 ms from the start of the free-cooling phenomenon. In order to obtain temperature determination during the experiment, a pyrometer is used and it is automatically triggered as soon as the acquisition starts. In this case, the following of the evolution of the average chemical shift is obtained as a function of temperature, allowing a characterization of the variation of ^{27}Al local structures during the solidification process of alumina.

- **Raman spectroscopy**
  Raman spectroscopy is a technique used to obtain information on the vibrational modes present in a system. The main process on which the technique is based on is the inelastic scattering of light.[43]

  As the sample is irradiated, most of the incident photons undergo an elastic scattering yet a fraction of them interact and exchange vibrational energy with the system.

  The inelastic scattering (Raman scattering) produces photons having lower ("Stokes") or higher ("Anti-Stokes") wavenumbers by comparison to those of the laser beam that correspond to the creation or destruction of a quantum of vibrational energy of the system.

  Since the allowed quanta of vibrational energy depends on the material (Raman active phonons, molecular vibrations...), the technique can provide the spectral signature of a given material. This means that the position of the Raman lines or bands are characteristic of the composition and their intensities are correlated to the concentration of chemical species.

  It usually covers a wavenumber range from 5 to 5000 cm^{-1} (in frequency: 100 GHz-200 THz). The probed range is between 10^{-4} and 10^{-2} nm^{-1} so it does not allow the observation of the geometric details of motions at the molecular level. A disadvantage of the technique is that high fluorescence signals under laser excitation can lead to a weaker accuracy of the measurement.[44]

Time-resolved Raman spectroscopy has been used to study ultrafast structural changes in femtoseconds[57] and to observe crystallization.[58]

- **Molecular dynamics simulations**
  Classic Molecular Dynamics (MD) simulations are used to get insight on a material through the generation of a phase space trajectory by integrating the classical equations of motion for an N-particle system.[59]

  A good model representing the atomic forces acting on the particles in the system is mandatory to obtain reliable results. For this reason, experimental work results are used to obtain parameters necessary to obtain the expression of the potential that can simulate the intermolecular forces.

  In order to start the simulation, the initial positions of each particle can be generated randomly or computed from a crystallographic structure. The initial velocities are then randomly attributed from a Maxwellian distribution centered on the desired temperature. Boundary conditions are then set to create the main simulation box surrounded by infinite replicas of itself, but the atoms considered will be those of the main cell. This is due to the fact that an atom can be replaced by an image particle if it exits the main cell.

  In the case of disordered systems, it is important to consider that the boxes created will induce an artificial periodicity which is not observable in reality. This problem is solved by creating a box large enough to discard this effect.

  The utility of MD simulations is to understand the microscopic origins of a physical property from an atomistic model. More importantly, MD simulations can be used to predict behaviours at conditions which can not be accessed experimentally. For this reason, they are usually performed in the case of extreme temperature liquids,[60–62] to model complex systems[63] and also to study solidification processes.[64]

  MD simulations are always under constant progress, now allowing modelling of larger systems with increased number of atoms in the box[65] or using extended timescales[66] during the simulation or by using an improved description of chemical bonds and interactions (ab-initio).[67,68]

Technique	Timescale (s)	Structural information
IR	10^{-12}-10^{-15}	Bond vibrations
XRD	10^{-12}-10^{-13}	Interatomic distances, number of neighboring atoms
NMR	10^{-8}-10^{-10}, 10^{-5}-10^{-1}	Local environment of atoms
Raman	10^{-11}-10^{-15}	Molecular vibrations
MD	10^{-8}-10^{-12}	Behaviour predictions

Table 2.1: General features of the main in-situ techniques used in material science and at extreme temperatures.

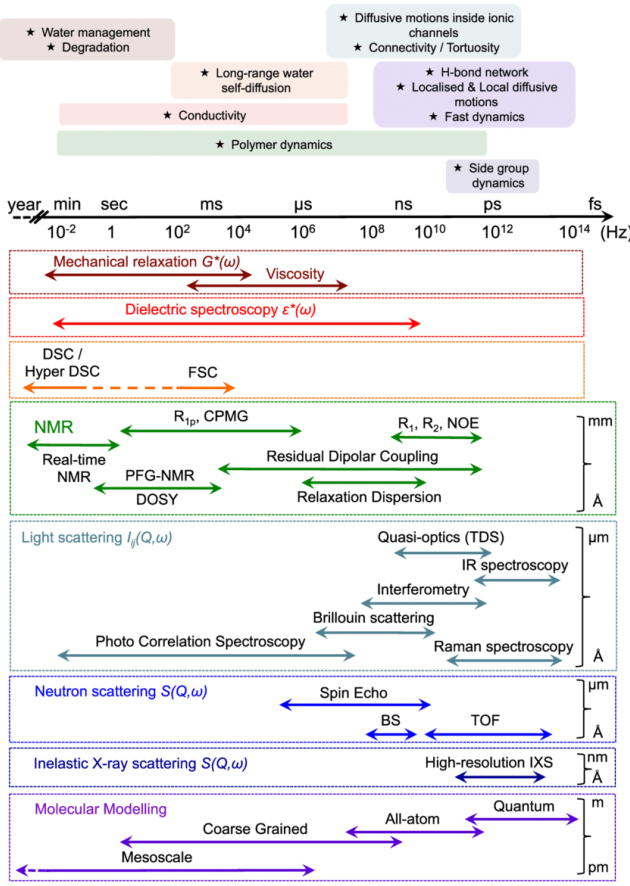

Figure 2.4: Comparative illustration of the frequency (time) and length scale ranges accessible with different probing techniques.[42] In this study, we are mainly concerned with motions in the liquid and the characterization of disordered structures, so the main techniques capable of providing these kind of structural information are presented in the text.

3

Real time FT-IR observation of materials during their cooling from molten state

Contents

3.1 From static to dynamic measurements

Equilibrium is "a state in which opposing forces or influences are balanced": since the third law of motion, this concept is a fundamental one when it comes to science. Matter transforms and reorganizes itself to create new structures when modified by an external agent, all of it to reach the minimum energy, as stated by the second law of thermodynamics.

As matter has reached an equilibrium given by the external conditions it had been set in, its properties do not change. This situation is the most common one allowing scientific experiments to be performed: in order to quantify a property of matter, it should be given enough time to stabilize the said property to get precise measurements.

However, some phenomena could seem very fast, at least from an human point of view on how we perceive time. From a very basic perspective, matter is modifying itself starting from an equilibrium condition, passes through a state of non equilibrium when an external agent is modified and finally reaches a new equilibrium at the end. Regardless of what happens during the transformation, the most common approach to measure a property is to quantify it in the two states of equilibrium. Yet, this approach leaves behind a very important question: how that particular property has changed during the phenomenon and whether it involves transient states between the two equilibrium configurations. In order to understand the conditions which determine whether a property is transformed in a way or another, a follow up of the disequilibrium region has to be made to allow a deeper understanding.

The kinetic information which can be extracted from the phenomena could then be used to design materials which can be produced by controlling the understood phenomenon and being able to reproduce it at will. To be able to do so, instrumentation must be upgraded to reach higher acquisition speeds and spectral quality: two requisites which are generally in contrast with each other due to the limitations imposed by electronics.

This chapter will illustrate the specifics used to upgrade the instrumentation to perform infrared time-resolved emissivity to be able to follow the real time cooling from molten state, starting from the theoretical principles and concluding with more technical aspects.

3.2 Original setup

The original experimental setup[69] will be presented to explain the improvements which were implemented to allow out-of-equilibrium measurements.

A blackbody reference (PYROX PY8) and a heating apparatus based on a CO_2 laser system (Coherent E400) are placed on a turntable (Aerotech ALAR-150) inside a purged enclosure. The design of the system ensures a constant and local heating of the sample even during motion of the turnable. The large diameter (12 mm at $1/e^2$) of the laser beam and the setting at 1 mm of the measurement aperture are enough to guarantee temperature homogeneity inside the spot during flux acquisition. The turntable makes possible the positioning of the sample and the reference at the focus points of the single path optical system which recollects the fluxes. A picture and a graphical scheme of the layout are presented in figure 3.1 and 3.2.

The temperature of the sample is inferred from the Christiansen point, a physical property of ceramics, mostly found in the opaque region for the materials we will be interested in, and can be computed through a comparison with a blackbody since at this particular wavelength the material behaves as a perfect emitter. The samples used are solid pellets of compressed powders, heated above the melting point to form a pool of liquid on the top part. These self-containing samples will avoid any possibility of chemical contamination with a container. The flux will be acquired in only few 10 μm below surface level, thus the temperature gradient is minimized.

The spectral range obtainable with the setting depends on the detector used. In this case, we employ a bolometer for the Far Infrared (FIR) and a DLaTGS for the Mid Infrared (MIR) measurements. The bolometer is cooled with liquid He whilst the DLaTGS operates at room temperature.

Vibrational motions are mainly encountered in the range 100-2000 cm^{-1} so the use of two detectors is necessary. A spectral merge is possible in the regions 350-500 cm^{-1} since both detectors cover this range of wavenumbers. In this way, a complete spectrum of vibrational motions will be obtained.

The setting presented can be employed to perform static measurements at different temperatures, controlled by the laser's settings. These measurements are usually performed with a resolution of 4 cm^{-1}, a mirror speed of 5 kHz and 64 spectra are acquired during 1 minute. An example measurement is illustrated in figure 3.3.

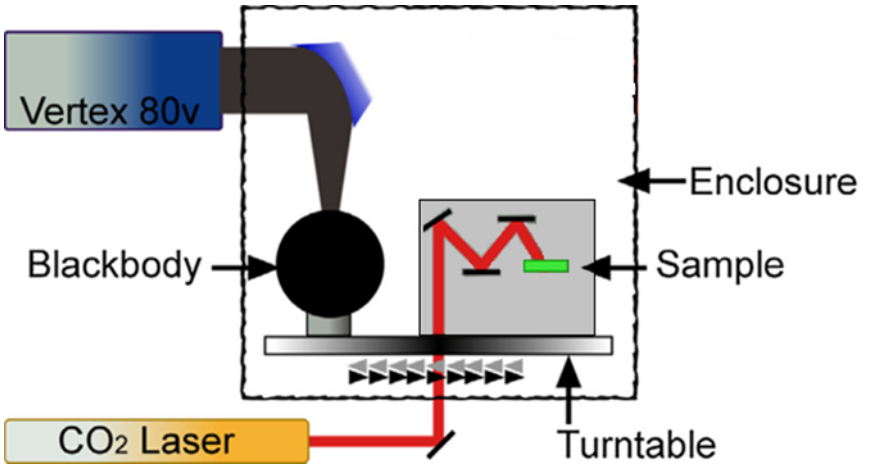

Figure 3.1: Graphical scheme of the layout. Laser heating is performed with a CO_2 laser to reach the molten state by heating the top part of the sample, the blackbody furnace is included as a temperature reference and the turntable allows the alignment of the optical paths for optimal flux retrieval.

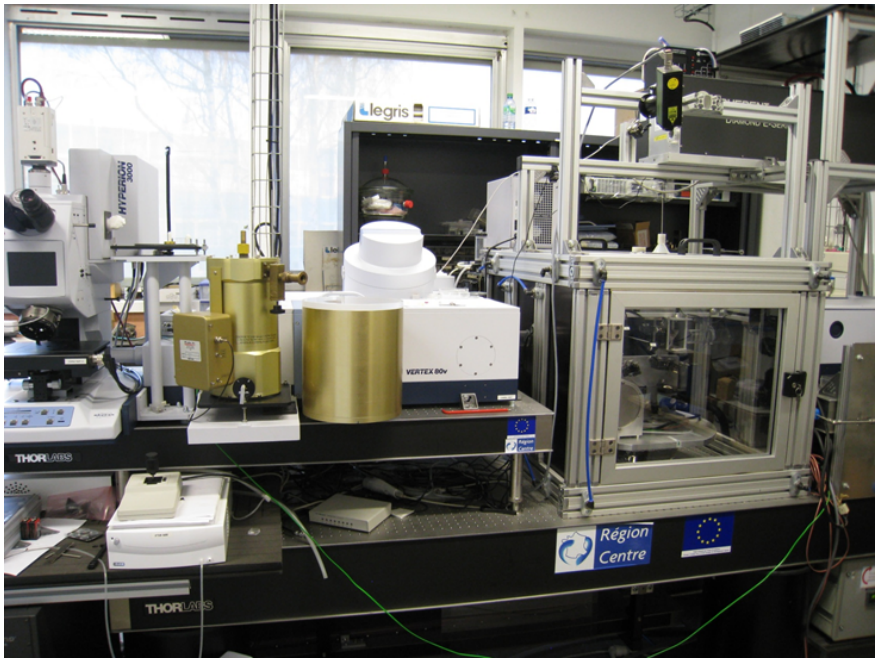

Figure 3.2: A photo of the layout at CEMHTI. The main setting is shown at the right. Additional instruments such as the Bolometer and the Hyperion 3000 Microscope are also included.

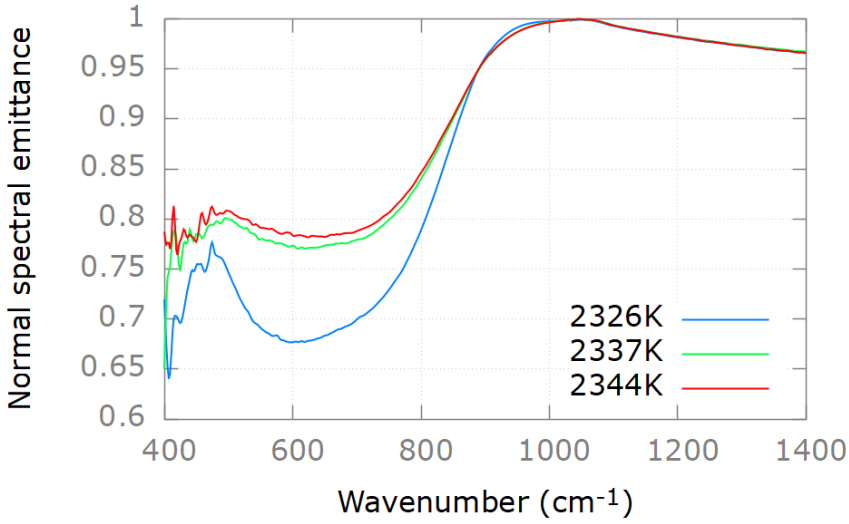

Figure 3.3: Normal spectral emittance of Al_2O_3 acquired with DLaTGS in static conditions at temperatures of 2326 K (blue), 2337 K (green) and 2344 K (red). The lowest temperature spectrum is in the solid region, the others in the liquid. The time needed to perform these measurements is around 10 minutes to achieve temperature homogeneity and stabilization and to acquire 64 scans (to be averaged) at a resolution of 4 cm^{-1}.

A new feature had to be implemented in order to reduce the measurement time and reach the real-time domain.

3.3 Time-resolved emissivity

As mentioned before, the study on the materials will be conducted during the cooling phenomenon starting from the liquid phase. The implementation of a Rapid Scan feature in the spectrometer was necessary to reach real-time data acquisition. This update consists in an increase of the speed of the moving mirror set inside the interferometer, reaching a maximum of 320 kHz. In this case, the maximum theorical acquisition would be 104 scan/s.[70]

In order to understand in detail the implications of the update and the problems arising from kinetic measurements, it is important to consider all the parts involved in the setup both from a theoretical and a practical point of view.

This discussion will start by describing the most affected part of the setup: the spectrometer.

3.3.1 FT-IR spectrometers

Infrared spectrometry is based on a main component called an interferometer and the mathematical method of the Fourier transform.

The interferometers used are very similar to the Michelson interferometer, shown in figure 3.4. A source (S) of monocromatic radiation entering the interferometer will encounter a beamsplitter (B) where it gets split into two components, one reflected (1) and one transmitted (2). The reflected beam will be then reflected by the movable mirror (M_1), pass through the beamsplitter again and get collected finally by the detector (D). The transmitted beam will encounter a fixed mirror (M_2) and be reflected another time through the beamsplitter to the detector. A compensating plate (C) is used so each beam has passed twice through the same optical length.[71]

At the detector, due to the difference in path, the beams will present a path difference δ called the retardation and its magnitude will depend on the position of the movable mirror. The two rays will interfere constructively or destructively. A smooth change in δ will cause the detected signal to behave as a cosine function.

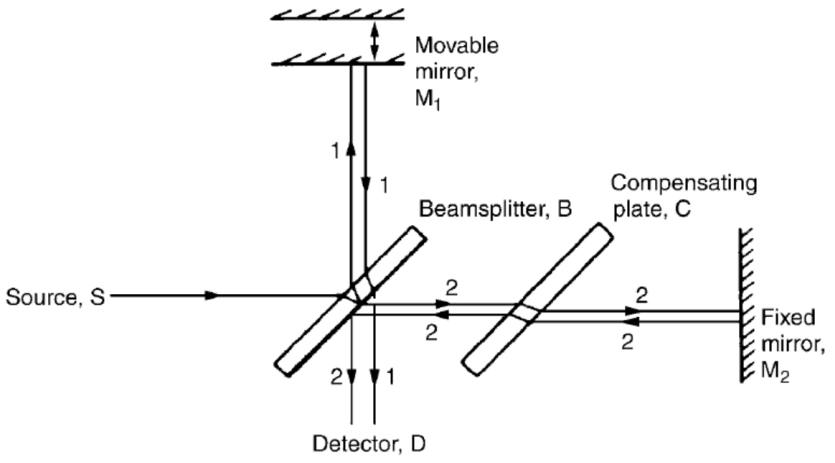

Figure 3.4: Scheme of a Michelson interferometer.[71] The source is split in two components and their path difference creates interference.

The true emission source will contain many wavelengths such that the signal intensity recollected by the detector is due to many consine wavelengths and it is of the form:

$$I(\delta) = 2\int_0^\infty B(\nu)cos(2\pi\nu\delta)d\nu \tag{3.1}$$

where $B(\nu)$ is the source intensity at ν, the wavenumber of the radiation.

A plot of these two quantities is the dispersed spectrum of the source and is obtained by a Fourier transformation (FT) which allows us to go from the path difference domain spectrum $I(\delta)$ to the frequency domain one $B(\nu)$:

$$B(\nu) = 2\int_0^\infty I(\delta)cos(2\pi\nu\delta)d\delta \tag{3.2}$$

The infrared source, as stated previously, will emit in a wide range of wavenumbers so the final result will be the addition of many cosine waves of different wavelengths. For this reason, the resulting interferogram (the plot of $I(\delta)$ versus δ) will present a large signal at $\delta = 0$ where all the waves are in phase. The signal is partially cancelled elsewhere due to the waves being out of phase. Due to a slight dispersion by the beamsplitter there will be an asymmetry at the center because even the waves at $\delta = 0$ will not be perfectly in phase. The features of the spectrum will be recollected in the interferogram as these waves are not cancelled out.

The transformation operated by the computer is limited in the number of data points so the user can choose whether to neglect the outer regions of the interferogram (wider wavenumber range, lower resolution) or having the points more distanced (higher resolution, narrower range).

The resolution $\Delta\nu$ depends on the maximum displacement of the mirror M_1 and consecutively on the inverse of δ_{max}.

The Rapid Scan option which will be set on the Vertex v80 spectrometer implies the activation of a higher scanner velocity, increased to a maximum of 320 kHz.[70] This parameter refers to the speed of the movable mirror M_1, responsible for waves phasing and thus the speed of point acquisition in the interferogram.

Another important feature illustrated in the User Manual is that the acquisition should take place in the form of interferometers in order to guarantee the maximum temporal resolution. This is due to the time spent by the computer to convert the interferograms into flux measurements which would obviously slow down the acquisiton. In the dynamic setting, we will first acquire a set of interferograms and the data processing will be operated after the measurement.

3.4 Theoretical aspects

As the implementation of the Rapid Scan has been achieved, it is now time to theoretically describe the measurement method and the data treatment necessary to overcome some of the main issues which could possibly be present.

The most important issue is the possible spectral distortion during measurement since the sample is continously and rapidly changing its temperature during the cooling. The main point of the instrumental setup is that it is based on the characterization of heat fluxes emitted by the sample by acquiring interferograms continuously (see figure 3.5).

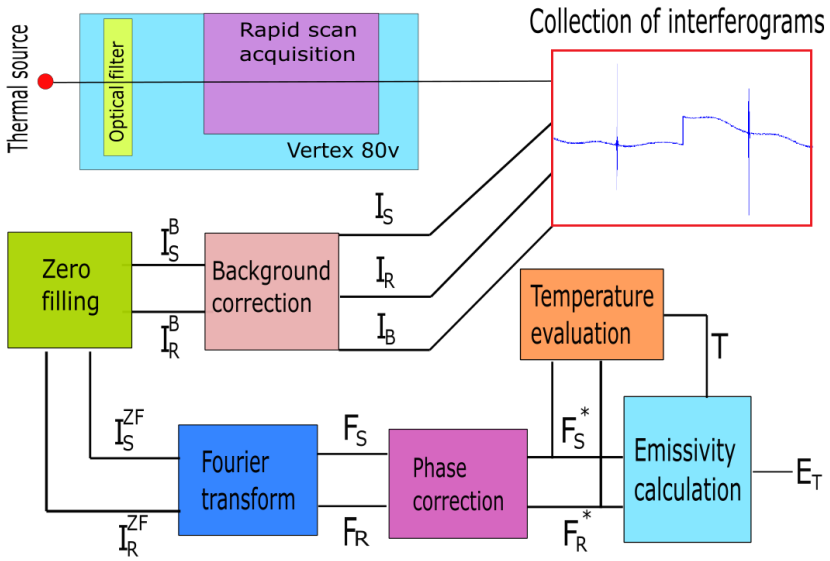

Figure 3.5: Graphical scheme of a Rapid Scan aquisition method and data treatment. The collection of interferograms are related to the source (S), the background (B) and the reference (R). The interferograms are then transformed in fluxes after the FT and finally the emissivity E_T is retrieved after the temperature has been evalued from the reference.

However, this update has to take into consideration the time dependence of the measurements, so also the theoretical approach of the technique will be affected. A rediscussion in deeper details is thus mandatory to understand how measurements are performed.

The main step is the aquisition of flux measurements emitted by a blackbody reference at a fixed temperature and the one coming from the heated sample. Another flux originating from the background is considered as it will be used to correct the fluxes. These measurements are performed consecutively and not simultaneously to have the time necessary to turn the table and align the optical system for proper flux recollection.

As for the background surrounding the sample, it is assumed that the enclosure produces a blackbody radiation and is given by the relation:

$$F_B = F_0 + fP^{T_B} \tag{3.3}$$

where F_0 is a flux contribution external from the closure, f is the transfer function of the measurement system and P^{T_B} is the intensity emitted by a blackbody at background temperature T_B, given by the Planck function P^T:

$$P^T(\bar{\nu}) = \frac{C_1\bar{\nu}^3}{e^{\frac{C_2\bar{\nu}}{T}} - 1} \tag{3.4}$$

with $C_1 = 2hc^2$ and $C_2 = \frac{hc}{k}$, $\bar{\nu}$ is the wavenumber and T is the temperature.

Similarly, the flux signal aquired from the blackbody reference at a temperature T_R is given by:

$$F_R = F_0 + fP^{T_R} \tag{3.5}$$

Both of these flux measurements should suffer no change in temperature during the aquisition process.

As for the flux emitted by the sample, the time dependence in temperature T(t) becomes mandatory in the Planck function and reflects itself in the flux measurement given by:

$$F_S(t) = F_0 + f(\varepsilon^{T(t)}P^{T(t)} + \rho^{T(t)}P^{T_B} + \tau^{T(t)}P^{T_B}) \tag{3.6}$$

In this time changing case, the temperature dependence is also found in the hemispherical directional spectral reflectance ($\rho^{T(t)}$) and transmittance ($\tau^{T(t)}$) of the sample as well as in the normal spectral emittance $\varepsilon^{T(t)}$.[72,73]

However, the Kirchhoff law and energy balance $\varepsilon^{T(t)} = 1 - \rho^{T(t)} - \tau^{T(t)}$ can still be used to simplify the relation if the sample will still possess a given temperature at a given time, a necessary prerequisite since temperature has to be defined during the cooling:

$$F_S(t) = F_0 + f(\varepsilon^{T(t)}(P^{T(t)} - P^{T_B}) + P^{T_B}) \tag{3.7}$$

Up to now, the discussion has been focused on the actual quantity we are

probing: the heat flux. Even though this is true from an human point of view, we should now shift our attention on the spectrometer's point of view which is recollecting the fluxes in the form of interferograms.

During the time of our acquisition, the spectrometer is acquiring N points of an interferogram which will also present a time dependence and temperature gap from the first point to the last due to the changes occurring in the thermal flux. This is because it is impossible to capture instantaneously the N points of the corresponding interferogram.

Since the thermal flux will change during the time interval (Δt) of the acquisition, what is really measured is a composite interferogram ($I^*_{\Delta t}$). Each recorded point ($I_{i,i}$) displayed in figure 3.6 corresponds to the value recorded by the interferogram of the flux emitted at a particular time ($t_i = (i-1)\Delta t/N - 1$), path difference and at a specific temperature (T(t_i)).

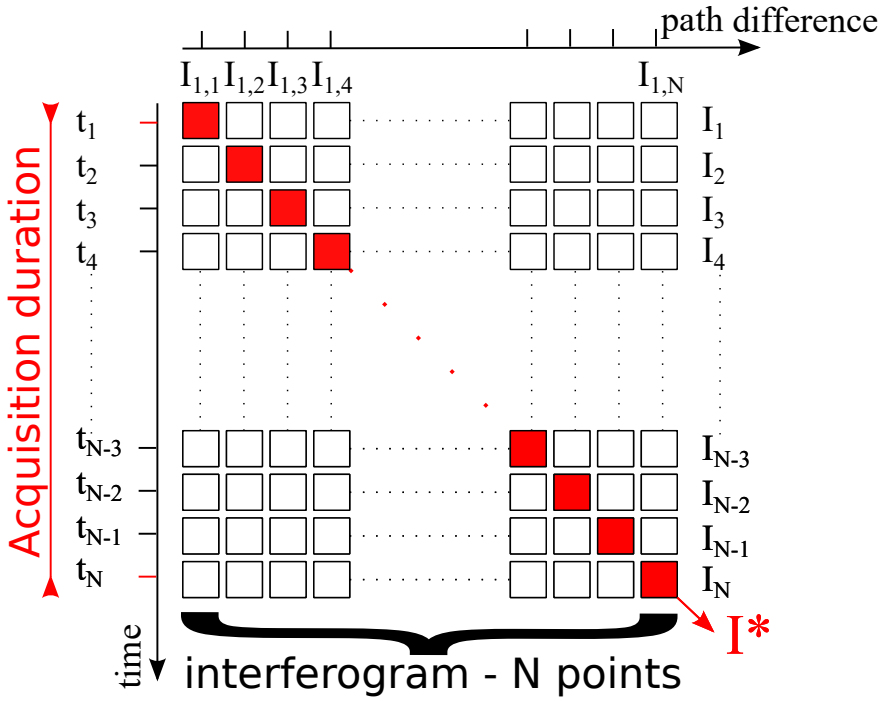

Figure 3.6: Composite interferogram during acquisition. The N points are acquired at different times for the whole duration of acquisition. The composite interferogram I^* illustrates this collection.

Therefore, the serie of N points obtained during a complete scan (I*) do not coincide with a conventional interferogram of a constant source. It is a set of values that correspond to the diagonal elements of a square matrix composed by the NxN points of a set of N interferograms.

In other words, the composite interferogram is the end product of a time-changing acquisition in which all the points are acquired in different times while the source is undergoing some changes, so at the end we will obtain a result that is inherently dynamic.

As the path difference increases (mimicking the movement of the M_1 mirror), the N points are being acquired at an always increasing time so that the source will be in a more diverse state at the maximum path difference if compared to shorter path differences. This concept is evident considering that the changes in our sample are occurring with time. The problems arising with this fact are multiple and they will be addressed in the next section.

As for now, we will consider the set of interferograms obtained and illustrate the process to compute the spectral emittance which is given by:

$$E_T = \frac{FT(I_S - I_B)}{FT(I_R - I_B)} \frac{P^{T_R} - P^{T_B}}{P^{T(t)} - P^{T_B}} E_R \tag{3.8}$$

where FT is the Fourier Transform and I_x are the interferograms of the fluxes originating from the sample (S), the blackbody reference (R) and the instrumental background (B), and E_R is the emissivity of the blackbody reference.[?]

A FT on the interferograms allows us to retrieve the fluxes, which were previously background corrected (refer to figure 3.5 for the complete scheme):

$$E_T = \frac{F_S - F_B}{F_R - F_B} \frac{P^{T_R} - P^{T_B}}{P^{T(t)} - P^{T_B}} E_R \tag{3.9}$$

The last step to obtain the spectral reflectivity is the consideration that the samples used are opaque in the IR range so it is possible to use:

$$R_T = 1 - E_T \tag{3.10}$$

3.4.1 Simulation test of the data analysis chain

This section will address the evaluation of the impact of possible sources of error related to temperature variations during data acquisition and processing. The main point to be discussed is whether the interferogram acquired could be trusted as a reliable measurement.

As explained previously, as we acquire data at different times, the interferograms might not reflect the sample at a fixed temperature but during a

time interval. These time intervals would reflect onto temperature intervals of different magnitude fixed by the speed of cooling. Hence the acquired signal would consist of a mixture or an average of the flux emitted by the material during the mirror's displacement time window, making the technique possibly unsuitable for our purpose.

In order to proceed, it was mandatory to study the nature of a composite interferogram to understand how the acquisition would take place. For this reason, a quantification of spectral distortion has been done by numerically simulating all the steps involved in data acquisition and processing, starting from the generation of a fictive material emissivity curve.

This fictive material is set to be used in a numerical simulation which mimics the kinetic process of the cooling from molten state. After the fictive cooling, the interferograms generated will be processed following the standard steps mainly encountered in FT-IR techniques.

At the end, it will be possible to make a comparison between the original curve and the processed one to estimate the distortion. The fictive material has been modeled with a 2 phonon model in the interval 400-1600 cm^{-1}, similarly to the ones commonly observed in the molten state of non conductive materials, as seen in figure 3.7.

Two phonons contributing to the dielectric function are chosen to have a transversal frequency ω_{TO_j} of 600 and 1100 cm^{-1} and a damping γ_{TO_j} of 80 and 120 cm^{-1} and the dielectric strengths $\Delta\varepsilon_j$ are set at 0.5 and 1, respectively. The choice of these values mimic real silica IR data and they take place in the Lorentz model of the dielectric function (see Chapter 4 for a detailed explanation), expressed in the following formula:

$$\varepsilon(\omega) = \varepsilon_\infty + \sum_j \frac{\omega_{TO_j}^2 \Delta\varepsilon_j}{\omega_{TO_j}^2 - \omega^2 - i\omega\gamma_{TO_j}} \tag{3.11}$$

The high frequency dielectric constant ε_∞ is set at 3, respecting the values typical of these materials.

The emissivity and the reflectivity are then retrived by using:

$$E(\omega) = 1 - R(\omega) = 1 - \left| \frac{\sqrt{\varepsilon(\omega)} - 1}{\sqrt{\varepsilon(\omega)} + 1} \right|^2 \tag{3.12}$$

The first step in the simulation is the generation of a set of composite interferograms having N points (with values compatibles to the 2^P factor used in FT) corresponding to temperature differences which can be also encountered

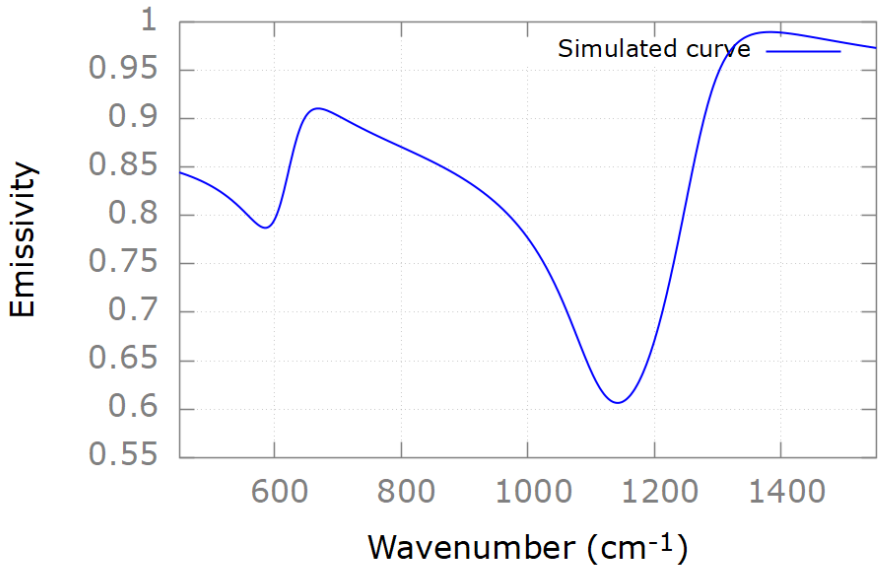

Figure 3.7: Emissivity of the simulated material.

in experimental data. In other words, the generated interferograms should represent all the possible temperature gaps to properly mimic the entirety of the cooling phenomenon.

In order to do so, the cooling speed has to be known such that it would be possible to establish a maximum and minimum value. To model our experiment, the highest temperature was set at 2500 K, the maximum temperature difference ΔT at 50 K, and the temperature steps each $\frac{(n-1)\Delta T}{N-1}$ with n from 1 to N. The choice of these values is made to encompass conditions met during measurements.

The spectral distortion is higher during faster temperature changes i.e. at the fastest cooling rates observed experimentally (841 K/s for Al_2O_3 and 696 K/s for SiO_2) so a upper limit of 1000 K/s was chosen for the simulation to cover all situations. Consequentely, $\Delta T_{max} = 50K$ for a measurement (Δt=0.05 s). It could be noticed that in order to choose the proper values, test measurements had already been performed to be able to get reference values to run the simulation. Figure 3.8 illustrates the cooling curves from which the beforementioned values have been extracted.

The testing materials have been chosen for three main reasons:

- Both materials have been extensively studied in a wide temperature range,

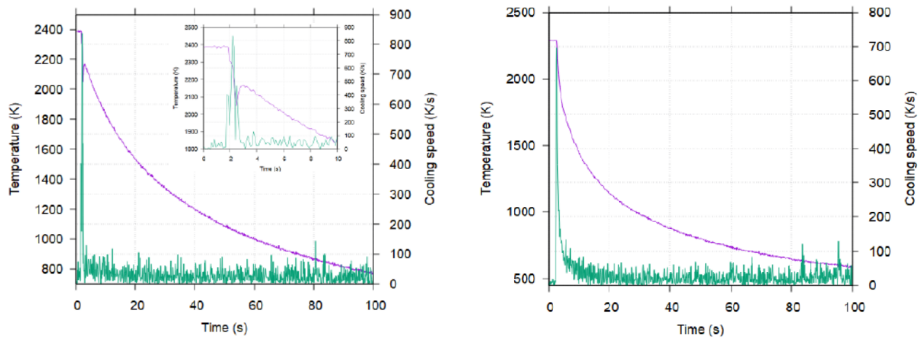

Figure 3.8: Free cooling curves of the tested materials: (Left) Al_2O_3, (Right) SiO_2. The cooling speed has been extracted from a second order derivative. The parameters set in the simulation are chosen to cover all the situations: since Al_2O_3 and SiO_2 have the most different fragility indexes and solidification behaviour, all the aluminosilicates that will be used in the study will fall in the middle of these two categories.

both with FT-IR and with other techniques, such that their properties are already well known.[74–83]

- Their cooling mechanisms are not the same: liquid Al_2O_3 crystallizes and liquid SiO_2 vitrifies. This difference will result in very diverse cooling speeds and curves.
- Al_2O_3 and SiO_2 present a difference in liquid behaviour during cooling since they are classified as "fragile" and "strong", respectively. This classification indicates the sensitivity of the liquid structure to temperature changes and point toward the degree of reorganization of particle orientation and coordination states.[84]

As the experimental parameters had been set, it is time to discuss the "digital" parameters. The most important of them is the resolution of the spectrum which is directly correlated to the number of points acquired by the interferometer. For this reason, the simulated N points also respect the standard conditions for points aquisition at a specific resolution. This value can be changed by the user and the simulation can be launched again to test the impact of this choice on the final spectrum.

The resolutions tested will be used to determine the best conditions during the experiment and are the usual ones used for high temperature measurements (16, 8 or 4 cm^{-1}) since other values would provide no advantages. The reason for this point will be rediscussed at a later time.

The temperature decrease between the recording of the first and last point of the interferogram is linear by hypothesis, which is a fairly good approximation

given their temporal proximity of 0.05 s (time of a single scan) that corresponds to a temperature change less than 50 K in the worse investigated experimental conditions so the linear approximation is sufficient for such small temperature change.

Each numerical composite interferogram is evaluated by extracting the I_{ii} elements of the NxN dimensional matrix I_{kj} corresponding to specific acquisition conditions (temperature, cooling rate, aquisition speed and resolution).

These data allow to compute the associated flux within the limits of the Nyquist frequency ($\omega_{max}/2$ where ω_{max} is the instrumental wavenumber limit) by applying the Fourier transform.

In order to do this, a conversion from the standard N points to wavenumbers is performed within the details of the chosen resolution by using:

$$\Delta\nu = \frac{1}{N\Delta x} \tag{3.13}$$

and

$$\omega_{max} = \frac{N}{2}\Delta\nu \tag{3.14}$$

This conversion is the same performed by the Discrete Fourier Transform which is used to go from an interferogram to a spectrum.

Apodisation using a Blackman Harris 3 terms, spectral ordering and zero filling to the next power of 2 is performed before using a Fast Fourier Transform.[85]

Moreover, the interferograms need to be corrected to eliminate their intrinsic asymmetry, as discussed in section 3.3, with an additional asymmetry originating from the dynamics of our measurements.

Phase correction is a method used to eliminate the asymmetry and extract a physical flux (real function) from the complex FT output we obtained. The type of phase correction performed on the data is the Mertz method, used to extract the amplitude spectrum from a complex output.

Let us consider a general FT transformed interferogram $S(\nu)$:

$$S(\nu) = A(\nu)exp(i\phi(\nu)) \tag{3.15}$$

where A is the amplitude spectrum and the complex exponential apply to the phase function (ϕ).

The extraction of A can be performed by taking the real part of the product of $S(\nu)$ and the inverse of the phase exponential, as seen in:

$$A(\nu) = Re[S(\nu)exp(-i\phi(\nu))] \tag{3.16}$$

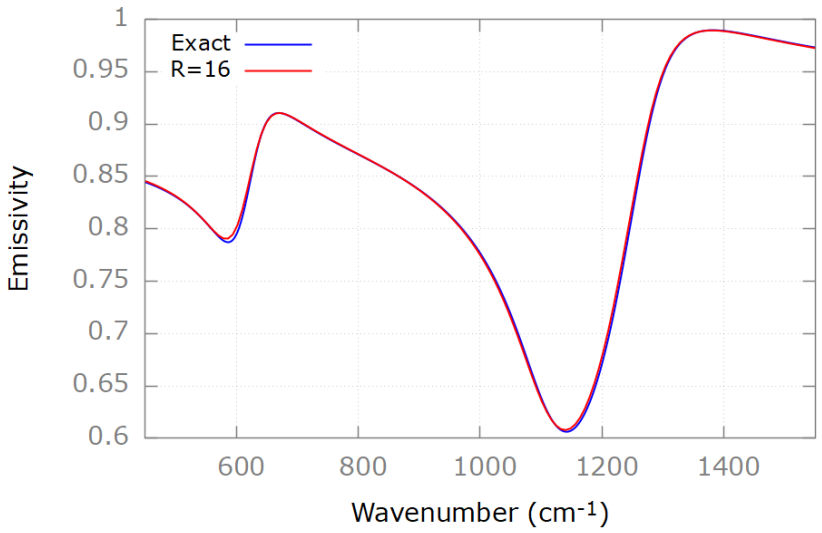

Figure 3.9: Exact (R=0) emissivity curve (blue) and the computed one (red) with a cooling rate of 1000 K/s at R=16 cm^{-1}. The error on resolution is small.

In our case, A is the phase corrected signal which represents the thermal flux emitted by the sample during the time of acquisition of the composite interferogram.

This standard data processing is routinely performed on all kinds of FT-IR data to correct the spectral artifacts originating from the usage of a discrete transformation.[85]

Having acquired the fluxes, the last step is to process them into emissivity data by taking into consideration that the emission reaches one at the Christiansen wavenumber so it can be used as a reference point to compute emissivity spectra, completing the entirety of data processing steps. This last point will be explained in more details in the next section about measurement procedure.

As the data has been acquired and processed, we can now evaluate and estimate the impact of the sources of error evidenced by the simulation tests. The first source of error is the interferogram distortion caused by the fast changes in sample temperature and its structure being out-of-equilibrium and changing rapidly, as explained previously. Figure 3.9 illustrates the highest time-induced deviation case: the cooling rate is maximum and the resolution is the lowest. Even in this case, the deviation is not as important and it does not prevent good data acquisition. Moreover, after phase correction, the relative error due

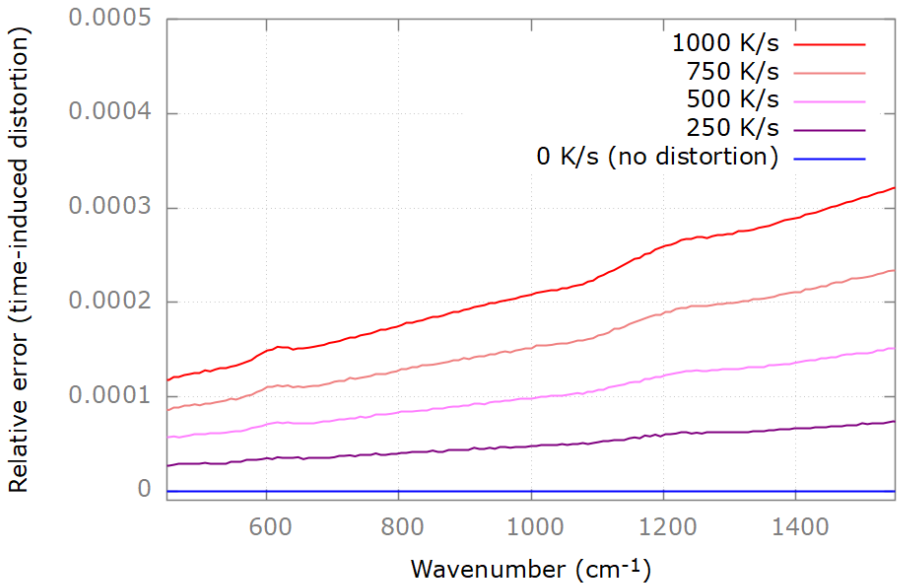

Figure 3.10: Emissivity relative error due to time-induced distorsion during the acquisition of a scan obtained by data simulated at different cooling rates (R=16)

to the distortion in the interferogram is estimated as being less than 0.04% from the highest to the lowest temperature reached during the acquisition process (see figure 3.10).

For this reason, we can assume that the application of the Mertz method is enough to account for it, since for our setting the cumulative error when performing a conventional measurement is estimated to be 2%[69] so the supplementary contribution due to the interferogram's distortion we encountered is not a major one.

As the simulation has been performed using different resolution values, it is also possible to quantify the impact of this parameter. Resolution (R) showed itself as being the main source of error (<1.2%) but, as seen in the second graph of figure 3.11 which illustrates the emission curves' deviation due to resolution when compared to the exact one, it can be neglected if compared to the total signal. It is important to evidence that the exact curve has R=0, meaning that the N points are theoretically infinite, such that an acquisition at R=0 would actually employ infinite time and infinitesimal mirror displacements to be performed. This scenario is obviously not practically attainable.

Table 3.1 presents the error estimation from the analysis of the computed data. It is also expected that almost all the smooth features present in the spectra

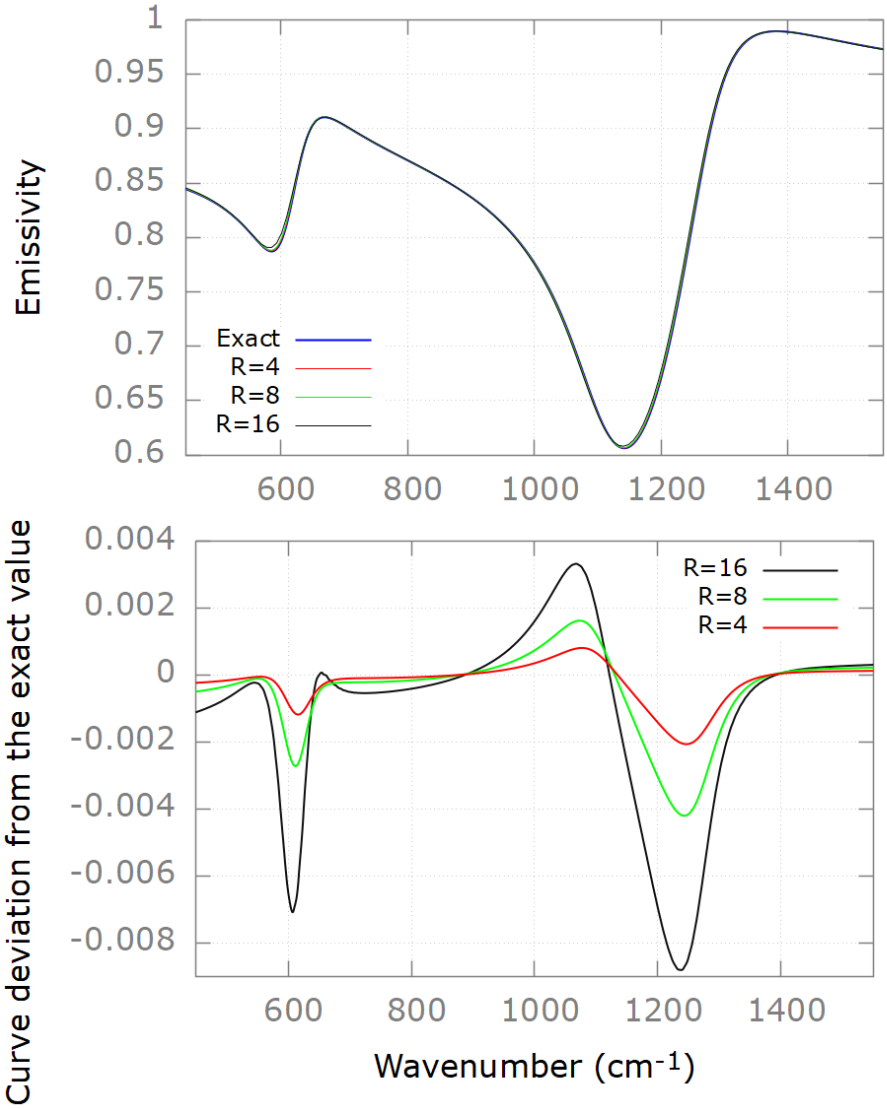

Figure 3.11: (Top) Effect of resolution on the emissivity spectrum at different resolutions: Exact (blue), R=4 (red), R=8 (green) and R=16 (black). (Bottom) Curve deviation from the exact value using different resolutions.

Error estimation (%)		
R	Error at 0 K/s	Error at 1000 K/s
16	0.8	1.2
8	0.4	0.6
4	0.2	0.3

Table 3.1: Error estimation at different resolutions (R) and for exact and highest cooling speed measurements

are acquired at times close to the moment when the mirror finds itself placed at the zero path difference, thus avoiding possible artifacts and meaning that the computed (measured) spectra reflect an image of the sample in a brief time window, making the observation in real time at a specific temperature that is the average temperature during the Δt time interval.

3.5 Measurement procedure

The samples are prepared by pressing powders or glasses to produce circular pellets with 13 mm of diameter and various thicknesses, ranging from 5 to 7 mm. The aim of this is having thicknesses which are sufficient to self contain a molten pool created by laser heating the sample from above. This is because the depth of the molten pool will determine the amount of liquid created. This amount of liquid will reflect itself in the length of the plateau, if crystallization occurs.

Laser heating is performed with a CO_2 laser, usually until reaching 100 K above the melting point and the pool of molten material will be created in the center of the pellet (around 8 mm of diameter).

As the starting temperature has been reached, the laser power is shutdown to observe the free cooling phenomenon by the continuous acquisition of the forwards and backwards interferograms of the heat flux originating from the sample.

In order to obtain the emissivity or reflectivity spectra, a program has been developed. The input data are the interferograms of the sample, the reference set at 1280 K and the background at room temperature (295 K). Since we focus on oxide ceramics and glasses the real temperature of the sample can be directly computed by using the Christiansen point of the material because at this peculiar wavelength the emissivity of the material is comparable to the one of a blackbody.[86,87]

In our case, the studied materials possess this feature and the high reliablity of this physical property is beneficial. The temperature dependence of the point was taken into account by allowing the program to automatically search for the Christiansen point into a range and the emissivity value is fixed at 0.998. The wavelength range can be modified freely by the user and in this case it was set to take into account the temperature shift commonly observed for the material.

Before continuing with the description of the standard settings which will be used during our study, it is important to give a more detailed explanation of how the temperature is measured and determined.

3.5.1 Temperature determination by Christiansen point

Sample temperature is a crucial parameter in the study of solidification processes or phase transitions.

For this reason, a reliable and fast method to determine the real sample temperature is very important. Usually, a pyrometer is employed to obtain this quantity, restricting the user to probe temperature ranges that depend on the wavelength of the pyrometer. Moreover, in order to use a pyrometer it is necessary to know the emissivity of the material at its wavelength, which is most of the times not possible, as it is in the case of our measurements. Another tool to monitor the temperature is a pyroreflectometer that uses two different, but close, wavelengths to determine the convergence temperature that is assumed to be identical to the true temperature. This has been used to determine the surface temperature of metals.[88] In our case, we will study oxide ceramics and glasses such that we can use another method to obtain the real sample temperature.

As discussed previously, our experiment consist in the acquisition of two heat fluxes: the normal spectral emittance E(σ,T) can be retrieved simply by the ratio of the flux emitted by the sample and by a blackbody furnace.

If we consider a homogenous and non-scattering sample of thickness d then:

$$E(\sigma,T) = \frac{(1-\rho(\sigma,T))(1-exp(-4\pi k(\sigma,T)d))}{1-\rho(\sigma,T)exp(-4\pi k(\sigma,T)d)} \tag{3.17}$$

with k(σ,T) extinction coefficient of the material and ρ(σ,T) the reflectivity at the interface air/material.

The Fresnel relation define $\rho(\sigma,\mathrm{T})$ by:

$$\rho(\sigma,T) = \left|\frac{\mu(\sigma,T)-1}{\mu(\sigma,T)+1}\right|^2 \tag{3.18}$$

where $\mu(\sigma,\mathrm{T})$ is the complex refractive index ($\mu(\sigma,\mathrm{T})$=n(σ,T)+ik(σ,T)).

The Christiansen wavelength λ_c is defined as the wavelength where $\rho(\sigma_c,\mathrm{T})\simeq 0$. If the exponential term tends to zero (due to the optical thickness of the material) then $\mathrm{E}(\sigma_c,\mathrm{T})\simeq 1$, meaning that at this wavenumber the material is emitting electromagnetic waves as a blackbody would. Due to this fact, σ_c is useful for the retrieval of the spectral emittance and the temperature determination by using the interferometer as a pyrometer working at this specific wavenumber.

The Christiansen wavenumber is localized after the highest wavenumber of the phonon range and it shifts slightly to lower wavenumbers with increasing temperature because of anharmonicity effect and thermal dilatation.[86]

Nonetheless, this temperature dependence is not very strong so we can now justify the use of it and the setting of a wavelength range to be able to extract temperature information during the entire cooling process.

3.5.2 Detectors specifics, filtering and additional settings

The number of spectra acquired for the blackbody reference and the background was set to 1024 to allow a high signal-to-noise ratio and the sample is scanned 1000 times to be able to cover a wide temperature range. The data is visualized and processed with the OPUS software. Several tests have been performed to find the best compromise between aquisition speed and data resolution. The use of a Rapid Scan technique at the highest acquisition speeds causes a need to limit the spectral range of acquisition. Since the extreme temperatures induce thermal radiation in a very wide spectral range, it is thus mandatory to remove the contribution that is outside the range of interest to avoid signal aliasing during the Fourier transform computation. To block the unwanted radiation, optical filters (F311-H or F321-H) are included in the optical path inside the Vertex spectrometer. The use of these filters allow to reduce the acquisition bandwith below 2000 cm^{-1} or 4000 cm^{-1} (see figure 3.12) and theoretically to enhance temporal resolution. In this study we employed an F311-H and set the Nyquist frequency at 3950 cm^{-1} since no significative change in acquition time was observed by reducing the Nyquist frequency below 2000 cm^{-1}. Additional

Detectors specifics			
	DLaTGS	Bolometer	MCT (LN-Wide)
Spectral range (cm^{-1})	350-4000	10-500	420-7500
Detectivity (logD*[cm HZ/W])	8.7	11.5	12
Maximum speed (kHz)	80	160	320

Table 3.2: Specifics of the tested detectors

electronic low-pass filters have been tested (5, 10 and 20 kHz) to improve acquistion.

The best parameters to perform this measurement, with a DLaTGS detector, are found to be 80 kHz for the acquisition speed, a resolution of 16 cm^{-1} and 2 scans (forward-backward) at each mirror movement, allowing the acquisition up to 20 spectra per second. Due to the high acquisition speed, this parameters are best suited to be employed to study fast phenomena.

Other configurations are possible, depending on the purpose of the study: by lowering the acquisition speed, it is possible to use higher resolutions to improve the quality of the spectra. Obviously this is convenient at lower temperatures where the cooling rate is not very high (in our case, 4.2 K/s at 500 K compared to the maximum observed in the range from 2400 K to 2050 K of up to 841 K/s). A good DLaTGS configuration for these cases is 40 kHz for the acquisition speed, a resolution of 8 cm^{-1} and 2 scans at each mirror movement.

The Bolometer is able to reach a measurement speed of 160 kHz so it is possible to acquire twice the number of spectra during the same timeframe as DLaTGS (when the other parameters are in the same conditions).

An MCT detector (D316) had also been tested and, thanks to the 100 times higher detectivity compared to the DLaTGS, 160 kHz was reached but it is unsuitable for our study since its low limit acquisition starts at 700 cm^{-1} so a lot of microstructural information would be missing, denying a complete characterization. For this reason, it will not be used in this work. Another MCT (LN-Wide) has been tested, and the maximum speed reached has been 320 kHz.

The main features of the detectors can be found in table 3.2.

The purpose of this preliminary study was multiple:

1. Studying the fastest temperature changes, since the laser is shutdown so the temperature difference will be elevated

2. Searching for the best instrumental parameters to employ the method

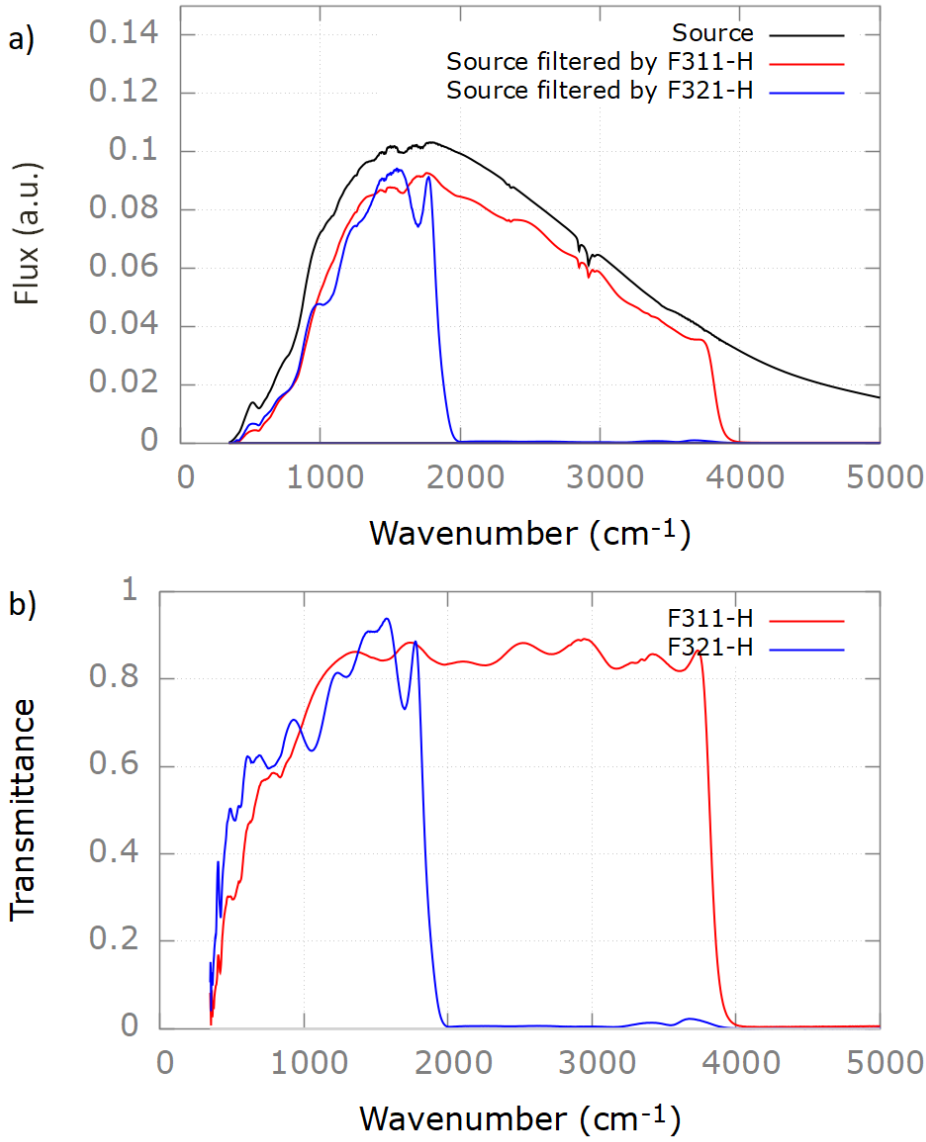

Figure 3.12: a) Flux measurement with (S) and without filtering (Sref). b) Retrieved transmittance (S/Sref) of the filters used to limit the aquisition range (DLaTGS/KBr detector, Ge/KBr beamsplitter, tungsten lamp source)

3. Identifying possible sources of distortion and errors in order to obtain reliable data.

To summarize, the possible performances of the setup are various and it allows to study fast occurring phenomena and unquenchable phases by reaching a maximum acquisition speed of 60 spectra per second and a maximum temperature of almost 2700 K.

3.5.3 Reliability of the method

In order to show the reliability of the technique, high temperature static measurements were conducted to be able to compare and validate the results obtained (figure 3.13). The purpose of this study is to acquire static data both with the classical setting and with the Rapid Scan to further prove the reliability of the technique. Up to this point the only validation we obtained has been through the numerical simulation so it is time to test it in practice.

As illustrated before, the samples used are Al_2O_3 and SiO_2 to be able to extend the method to a vast variety of oxide materials which present differences in their cooling process and their structures.

The experimental conditions for the two double sets are kept the same, as well as the samples used and the laser parameters to achieve a very close temperature for comparison. The data processing has also been the same.

The only difference is the acquisition parameters being the standard classical one compared to the best choice made for DLaTGS at high temperatures. The main parameters that distinguish the two measurements procedures are again the acquisition time, the speed of the moving mirror and the resolution.

The measurements were conducted at 5 kHz, 64 scans were averaged and the acquisition time is more than 1 min in classic conditions and, as for Rapid Scan, the parameters changed to 80 kHz, 2 scans and 0.1 s to complete the acquistion. The doubled time is due to the averaging of a backward and forward scans. The sample, in this case, is not compared when it is in dynamic conditions due to the changes in structure that can occur, especially in the case of fragile liquids like Al_2O_3.

The scans selected for comparison are directly extracted from the total kinetic measurement.

It is of fundamental importance to state that this test has the purpose of providing a comparison to further prove the reliability of spectra acquired at

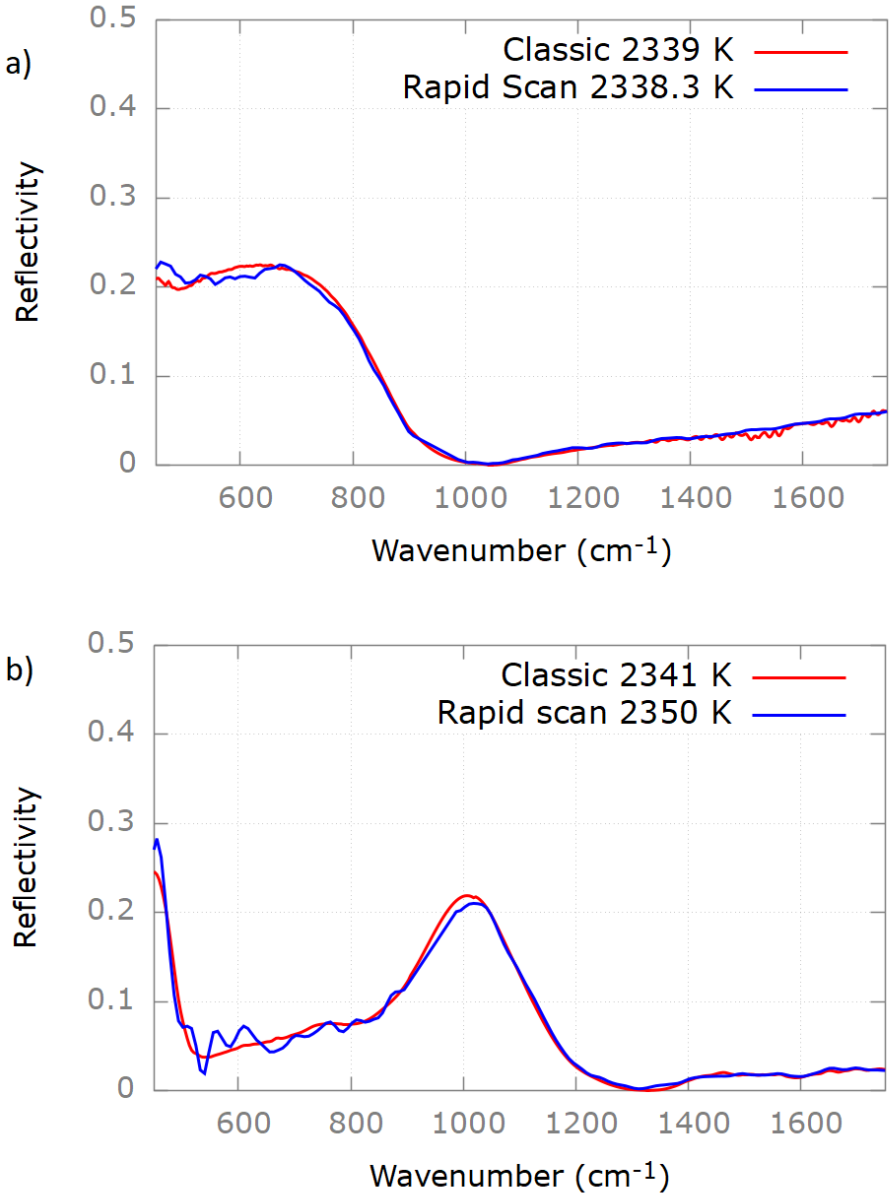

Figure 3.13: Spectra comparison of molten a) Al_2O_3 ,b) SiO_2. Both sets of data show good agreement even though the resolution used in the Rapid Scan acquisition option is 4 times lower (R=16) than the one used for the classic measurements (R=4). The speed of acquisition of the kinetic sets is 20 spectra/s.

the same temperature in the liquid which is, in this case even during Rapid Scan acquisition, acquired in equilibrium conditions before the laser power is shutdown.

The spectra acquired in real-time present obviously a lower signal-to-noise ratio but it does not pose a big problem in the global spectrum as the quality is enough to perform spectra decomposition for structural studies. This is due to the values of resolution employed, the classical measurements are commonly acquired at 4 cm^{-1} while the resolution value selected for Rapid Scan is 16 cm^{-1}, as well as the spectral averaging.

Other optimal parameters to perform Rapid Scan were also tested and the same result has been obtained thus confirming that the technique is able to operate at very high speed and still provide spectra that are correct and reliable.

We will see that due to the differences in sample's nature and structure, it will be possible to use the technique as it is or perform spectra averaging to obtain higher quality spectra.

Spectra averaging is not convenient during the dynamical measurement due to the obvious doubling of the acquisition time, but as the cooling rates become slower at lower temperatures, it will provide higher quality data. This decision will depend on the acquired data itself and on how fast and how much the structure is evolving.

3.5.4 Additional measurement possibilities and spectral analysis

The presented spectra have been acquired during the free cooling of the samples but the technique has the possibility of being extended to allow the performance and observation of phenomena at different cooling speeds.

Indeed, the laser heating system can be considered as a "controllable temperature provider", meaning that the changes in temperature can be controlled directly by it so also the cooling rate and the relaxation time given to the sample.

In other words, the temperature and the timeframe of the heating can be directly decided by operating the laser, allowing the user to decide the speed of heating or cooling. This feature will be employed during our study to observe how different cooling speeds affect the final structure of the material.

The possibility to control and establish a cooling path will be one of the fundamental points regarding this technique.

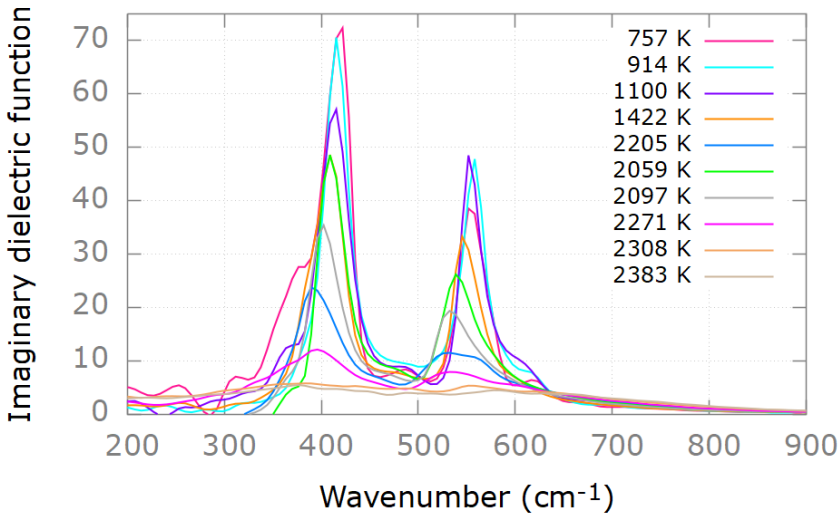

Figure 3.14: Imaginary dielectric function evolution of Al_2O_3 using the Kramers-Kronig method. In order to perform this method it is important to acquire the full spectral range of phonon contributions. Due to the detectors' acquisition range, two detectors are required to cover this range (from FIR to MIR).

The laser used is capable of sustaining a power of 500 W so it is possible to reach higher temperatures (in the previously reported experiments the output laser power was approximatively 120 W). The maximum temperature reachable with this setting depends also on the thickness of the sample.

A brief analysis is performed on a few reflectivity spectra of Al_2O_3 to highlight the evolution of the imaginary part of the dielectric function which is important to evaluate and distinguish the (group) vibrations. The acquisition of a spectral range enough wide to contain all phonon contributions allows also the use of Kramers-Kronig[89] relations to perform this data analysis (figure 3.14).

More information regarding data analysis are presented in the next chapter.

4

IR spectroscopy, theories of molten state and phase formation

Contents

4.1 Observation of structural changes during solidification

As stated previously, the objective of the study is to illustrate structural changes during phase transition and the possible creation of metastable phases during the solidification process. The importance of this observation is evidenced when considering the different polymorphs that could be created by solidifying from the liquid state.

During solidification, the structure is forced to reorganize itself to adapt to temperature changes. When this phenomenon starts from the liquid, a status in which the atoms are freerer due to the breaking of bonds, the variety of polymorphs and possible structural recombinations grows vaster. For this reason, it is crucial to observe the conditions leading to the formation of a particular structure.

This observation will be possible thanks to the previously presented experimental setup. The technique used for this characterization is infrared spectroscopy which is a branch of spectroscopy based on the study of emission, reflection or absorption of electromagnetical waves by a material. The spectrum retrieved at the end of this physical phenomenon is characteristic of the material. Normal spectral emittance can be used to obtain the optical properties from the dielectric function of the material and its evolution in temperature. The analysis of the imaginary dielectric function and the bands that form part of it is enough to understand and point out structural differences and changes with temperature during the solidification process.

Our study will be focused on oxide materials belonging to the ternary system M_xO_y-Al_2O_3-SiO_2. M_xO_y is an oxide that will be replaced while maintaining the aluminosilicate part fixed (SrO and ZrO_2). This choice is due to the importance and the high possibilities that the aluminosilicate network offers. Compositions obtained in these systems demonstrate high chemical stability and mechanical resistance. They are also used in the design of high-temperature sealants,[90] transparent ceramics,[91] bioactive glasses,[92] dielectric and refractory glass-ceramics,[93] photoactive glasses and glass-ceramics,[94] radio-transparent ceramics[95] and many others.

This chapter presents an overview of the theoretical means for data analysis and some basic concepts on the nature of the molten state and phase formation.

4.2 Infrared spectroscopy for material studies

The electromagnetic radiation spectrum, shown in figure 4.1, contains the infrared (IR) region. The typical unit to express wavenumber is reciprocal centimeters (cm^{-1}).

Vibrational infrared is mostly located in the region 4000-625 cm^{-1}. In our study we will also refer to the region 625-50 cm^{-1}, the far infrared.

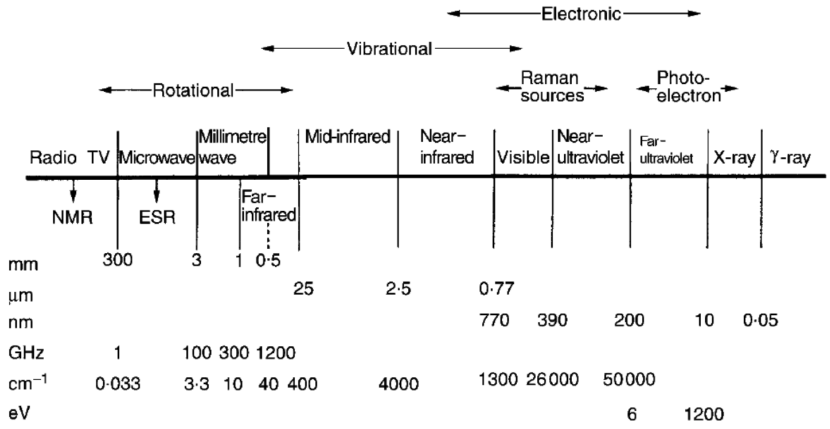

Figure 4.1: Electromagnetic spectrum scheme. The infrared region of the spectrum is located in the middle and it corresponds to the region in which the vibrational motions are observed.[71]

An IR spectrum is obtained after FT of an interferogram and it corresponds to a plot of the signal intensity versus the wavenumber. The analysis of the reflectivity spectra will yield some information about the vibrations occurring in chemical bonds.

Bond vibrations can be of different types: the fundamental ones are stretching (asymmetrical or symmetrical) and bending (in-plane and out-of-plane).

Strecthing vibrations are motions in the direction of the bond. When there is a change in bond angle it is a bending motion. Since it takes more energy to stretch a bond rather than to bend it, stretching vibrations generally occur at higher frequency (refer to figure 4.3 for a scheme).[96]

Each chemical bond is associated to a characteristic vibrational frequency approximated as proportional to $\sqrt{k/\mu}$ where k is the bond strength and μ is the reduced mass, so the radiation absorbed will be of a particular wavelength.

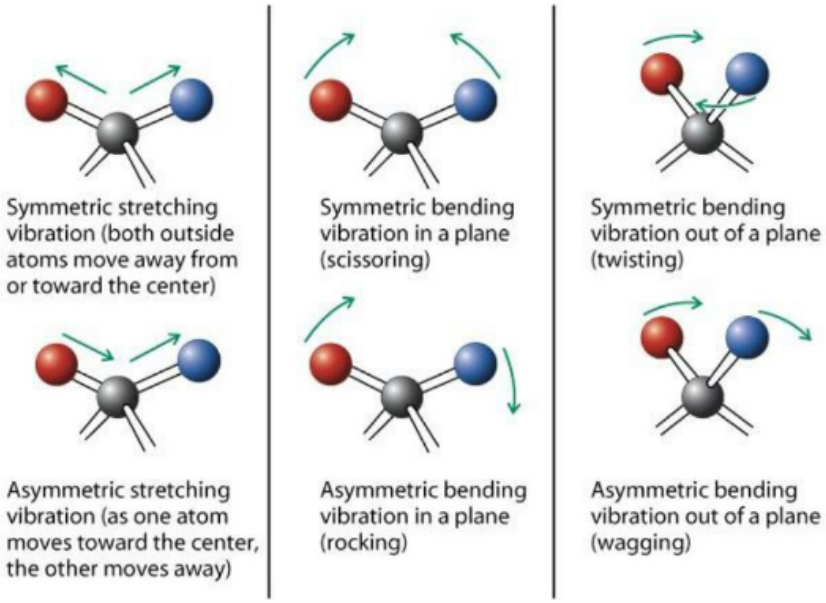

Figure 4.2: Scheme of bending and stretching motions. Stretching motions cause a change in bond length and bending changes the bond angle. All of these vibrational modes are detected by IR.

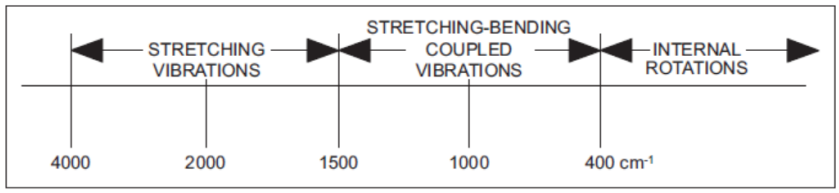

Figure 4.3: General frequency range of stretching and bending vibrations. Each studied material will present different peak locations due to its chemical bonds' properties (bond lengths or strengths).[96]

The dependence on the bond strength causes stronger bonds to vibrate at higher frequencies. Moreover, due to the dependence on the inverse of the reduced mass of the atoms involved in the vibration, heavy atoms will vibrate at lower frequencies compared to lighter atoms. For this reason, the correlation bond-frequency is the basis for the determination of structural and chemical features.

Nevertheless, not all the modes are IR active, meaning that some vibrations are not observable. The observability of vibrations depends on the symmetry (or lack of it) of the molecule studied. In general, detection is possible when the electric dipole moment changes when atoms are displaced. Group theory is the application of symmetry concepts to vibrational spectroscopy and it allows to classify molecules by a point group through the symmetry elements it presents and to classify the vibrational modes giving rise to an electric dipolar moment and thus active in IR, according to symmetry selection rules.

In our case, the structural properties will be evidenced by using a dielectric function model so the next sections will be dedicated to it, starting from the basics of the interaction light-matter.

4.2.1 Interaction light-matter

The behaviour of an electromagnetic wave interacting with dielectric matter is described by Maxwell's equations:

$$\vec{\nabla} \cdot \vec{D} = 0 \qquad \vec{\nabla} \cdot \vec{B} = 0 \qquad \vec{\nabla} \times \vec{E} = -\frac{\partial \vec{B}}{\partial t} \qquad \vec{\nabla} \times \vec{H} = \frac{\partial \vec{D}}{\partial t} \tag{4.1}$$

where $\vec{D}$ is the electric displacement field, $\vec{B}$ is the magnetic field, $\vec{E}$ the electric field and $\vec{H}$ the magnetizing field.

A polarization $\vec{P}$ is induced by the interaction such as:

$$\vec{P} = \varepsilon_0 \chi \vec{E} \tag{4.2}$$

with χ being the electric susceptibility and ε_0 the permittivity of free space.

The electric displacement field can then be expressed as:

$$\vec{D} = \varepsilon_0 \vec{E} + \vec{P} = \varepsilon_0 \varepsilon \vec{E} \tag{4.3}$$

where ε=1+χ represents the dielectric function of the material.

As stated previously, the dielectric function is a fundamental quantity in infrared spectroscopy due to the possibility of the retrieval of quantitative information on the structure of the material. It is possible to obtain this quantity directly from the infrared spectra by choosing and using a model.

4.2.2 Dielectric function and models

The dielectric function is a complex quantity with its real part representing dispersion through the material and the complex part the absorption at the same wavenumber. If the measurements are performed at an almost normal angle (at normal incidence), it is possible to obtain this quantity from a reflectivity spectrum of a smooth plane interface delimiting vacuum and a semi-infinite medium (opaque material) through the Fresnel equation:

$$R(\omega) = \left| \frac{\sqrt{\varepsilon(\omega)} - 1}{\sqrt{\varepsilon(\omega)} + 1} \right|^2 \tag{4.4}$$

The dielectric function can be determined using either the Kramers-Kronig (KK) relations or the dispersion analysis.

In the first case, the KK relations are directly applied to the reflectivity data ($R(\omega)$) through the calculation of the phase shift($\phi(\omega)$):

$$\phi(\omega) = \frac{\omega}{\pi} \int_0^\infty \frac{ln(R(\omega')) - ln(R(\omega))}{\omega^2 - \omega'^2} d\omega' \tag{4.5}$$

At this point, it is possible to employ the Fresnel equation to calculate the index of refraction $n(\omega)$ and the extinction coefficient $k(\omega)$ from which the real and the imaginary parts of the dielectric function can be retrieved.

If we consider $\varepsilon(\omega)$=$\varepsilon_1(\omega) + i\varepsilon_2(\omega)$, then:

$$n(\omega) = \frac{1 - R(\omega)}{1 + R(\omega) - 2\sqrt{R(\omega)} cos\phi(\omega)}$$

$$k(\omega) = \frac{2\sqrt{R(\omega) sin\phi(\omega)}}{1 + R(\omega) - 2\sqrt{R(\omega)} cos\phi(\omega)}$$

$$\varepsilon_1(\omega) = n^2(\omega) - k^2(\omega) \qquad \varepsilon_2(\omega) = 2n(\omega)k(\omega) \tag{4.6}$$

In order to do so, the total vibrational spectrum is needed because the unmeasured spectrum can have a large effect on the calculated values of $\phi(\omega)$, possibly leading to negative values of ε_2. These errors can cause problems in interpretation and subsequent calculations.

For this reason, a more efficient tool for quantitative analysis is using a model for the dielectric function and calculating the optical properties from it. This method is called dispersion analysis and the parameters modelled are obtained by fitting the calculated reflectivity spectrum to the experimentally measured one. Problems arising from a limited data set can still arise but they can be overlooked upon if the model is adequate and if all the strongest resonances are contained in the measured region.

The reflectivity $R(\omega)$ at normal incidence can be expressed as:

$$R(\omega) = \frac{(n(\omega)-1)^2 + k(\omega)^2}{(n(\omega)+1)^2 + k(\omega)^2} \tag{4.7}$$

As seen in equation (4.6), n and k are linked to ε, so it is possible to express them as:

$$\begin{aligned} n(\omega) &= \left[\frac{1}{2}(\sqrt{\varepsilon_1^2(\omega)+\varepsilon_2^2(\omega)} + \varepsilon_1(\omega))\right]^{1/2} \\ k(\omega) &= \left[\frac{1}{2}(\sqrt{\varepsilon_1^2(\omega)+\varepsilon_2^2(\omega)} - \varepsilon_1(\omega))\right]^{1/2} \end{aligned} \tag{4.8}$$

If the model used for the dielectric function is a simple damped harmonic oscillator then:[97,98]

$$\varepsilon(\omega) = \varepsilon_\infty + \sum_j \frac{N_j e^2}{m_j} \frac{1}{(\omega_j^2 - \omega^2) - i\Gamma_j\omega} \tag{4.9}$$

with N_j being the product of the oscillator strength and number of oscillators, ω_j is the resonant frequency, Γ_j the damping factor and m_j the mass of the j-th oscillator, respectively. The damping term will originate a Lorentzian dielectric function model due to the homogeneous line broadening.

The solutions obtained are analytical and they are:

$$\begin{aligned} \varepsilon_1(\omega) &= \varepsilon_\infty + \sum_j \frac{N_j e^2}{m_j} \frac{\omega_j^2 - \omega^2}{(\omega_j^2-\omega^2)^2 + \Gamma_j^2\omega^2} \\ \varepsilon_2(\omega) &= \sum_j \frac{N_j e^2}{m_j} \frac{\Gamma_j\omega}{(\omega_j^2-\omega^2)^2 + \Gamma_j^2\omega^2} \end{aligned} \tag{4.10}$$

This model is also called the Classic dispersion analysis (CDA) and it is appropriate for crystalline systems in which the local environment is the same for all oscillators.

In amorphous materials and glasses, the local environment is not uniform and it creates an inhomogeneous broadening of the resonance line-widths which is not considered in this model. For this reason, a more appropriate model would be treating the absoption bands as a Gaussian distribution of homogeneously broadened Lorentzian oscillators.

Starting from this model, an approximation can be made if the inhomogenous broadening is much larger than the homogeneous linewidth, such that the absorption bands can be uniquely considered as Gaussian distributions. This technique is the Gaussian dispersion analysis (GDA) and it is based on the expression of the complex dielectric function as a sum of Gaussian terms that correspond to separate oscillations such that:

$$\varepsilon_2(\omega) = \sum_j \frac{A_j}{\sqrt{2\pi\Delta\omega_j}} exp(-\frac{1}{2}\left[\frac{(\omega-\omega_j)}{\Delta\omega_j}\right]^2) \tag{4.11}$$

where the subscript j refers to the j-th resonance mode, A_j is the amplitude, $\Delta\omega_j$ the standard deviation of the mode and ω_j is the center frequency of the resonance.

It is possible to use the KK relation to obtain the real part:

$$\varepsilon_1(\omega) = \varepsilon_\infty + \frac{2}{\pi}\int_0^\infty \frac{\omega'\varepsilon_2(\omega')}{\omega'^2-\omega^2} d\omega' \tag{4.12}$$

Since the expression of ε_2 in this model can represent the entire spectrum, the application of KK will not affect the data as discussed previously.[99] In this work, the reflectivity data will be fitted using the GDA method.

4.3 Crystals and Glasses: Theoretical overview

The solidification processes that will be observed are either the crystallization or the vitrification of our sample starting from the molten state.

This section is dedicated to a theoretical discussion on the main differences observed from a structural point of view, as well as the dynamics of phase transition.

4.3.1 Liquids and solidification paths

Liquids have the ability to flow and change their shape according to the container they are set in. The structure of a melt is inherently dynamically disordered even though local order could be found in some melts at several positions during small time durations. During solidification, the melt becomes solid and the structure reorganizes itself by forming new chemical bonds.

As seen in figure 4.4, there are different paths that can be achieved during this process and the key factor to obtain a different path is by changing the speed of cooling.

A slow cooling allows the melt to crystallize at thermal equilibrium and the end product will be a crystal or a mixture of several crystalline phases (depending on chemical composition). A crystal is a well-ordered structure composed of periodic crystal lattices extending in all directions. This transformation is accompanied by a big decrease in volume.

In some cases, a fast cooling results in the formation of a glass, after a state of undercooling (a temperature region just below the melting point), characterized by the absence of long range order, contrary to a crystal. In this case, the high viscosity precludes structural rearrangement at long distances. The process can be described as a loss of mobility until the structure "freezes" and the glass has been obtained, after a particular temperature called the glass transition temperature (Tg).

Tg can differ if the cooling rate is different due to a different degree of undercooling,[100] in any case, the final structure can still be a glass if the cooling has been performed fast enough to avoid crystallization.

Another important feature of liquids is their fragility. As mentioned in the previous chapter, the choice of the testing materials has been also determined by this factor.

Angell[84] describes this property as the sensitivity of a liquid to temperature changes. Fragile liquids can adopt different structural reorganizations and a variety of coordination states. Strong liquids, on the other hand, tend not to reorganize even over wide ranges of temperatures.

This distinction is illustrated in figure 4.5. It is seen that the behaviour of the viscosity differs for the two types of liquids: strong liquids display a linear change, while fragile liquids are more affected with temperature. Generally, strong inorganic liquids have the ability to form glass while high fragility liquid can not and only crystallize.

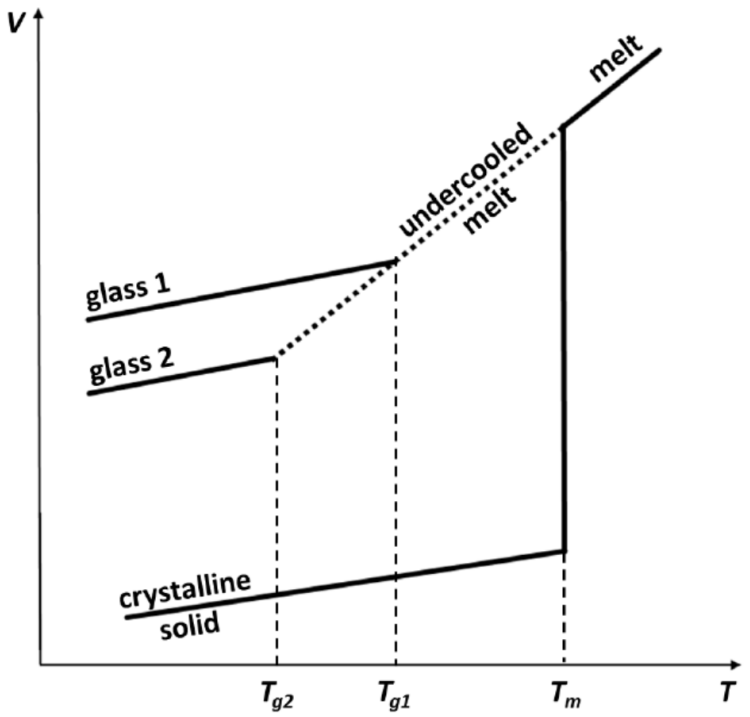

Figure 4.4: Volume-temperature diagram for glasses and crystalline solids. The formation of the two materials are characterized by differences in their cooling path from molten state.[101]

In our study, all of the studied aluminosilicate compositions will lie in the intermediate region. The nature of the liquid will also determine its ability to crystallize or vitrify.

4.3.2 Nucleation theory and crystal growth

Crystallization can be divided in two steps: nucleation and growth.

Nucleation is the process in which a solid nuclei reaches a critical size and becomes stable in the liquid (volume vs surface energy) as described below. Then the growth can occur and the nuclei can increase in size.[102]

The nucleation process is entirely described by the Classic Nucleation Theory (CNT), although this theory fails to predict efficiently the evolution of the system leading to a critical nucleus. Alternative theories have been proposed,

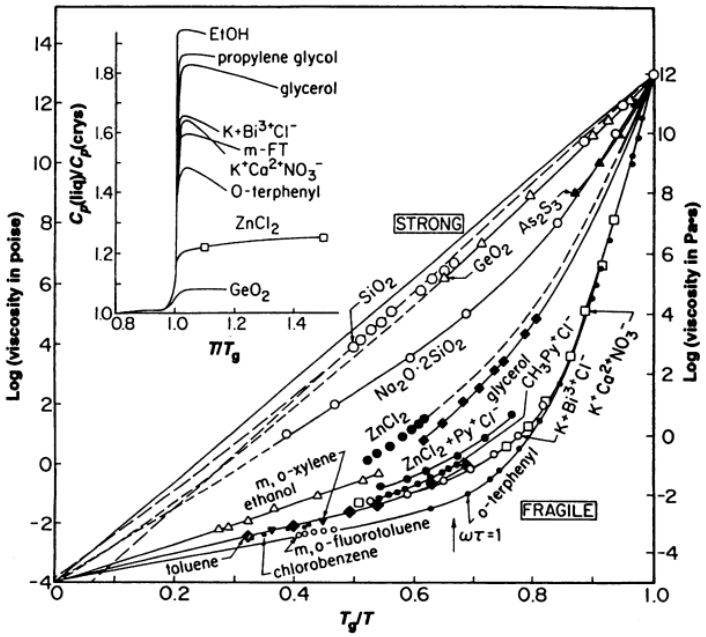

Figure 4.5: Viscosity data scaled by Tg values.[84] The strong/fragile liquid behaviour is illustrated.

yet CNT remains the easiest to understand the physical mechanisms driving the nucleation process.

CNT describes the stationary nucleation rate $I(T)$, the number of nuclei per time unit at a given temperature, as:

$$I(T) \propto exp\left[-\frac{\Delta G_D}{k_B T}\right] exp\left[-\frac{W^*}{k_B T}\right] \tag{4.13}$$

where k_B is the Boltzmann constant and T is the temperature.

The first exponential describes the kinetic passage of an atom from the liquid to the surface of the crystal with activation energy ΔG_D. The second exponential illustrates the thermodynamic process, with W^* being the critical work of formation of a cluster having a critical radius r^*.

The formation of a nucleus requires energy and it is expressed by:

$$W = \frac{4\pi r^3 \Delta G_V}{3} + 4\pi r^2 \gamma \tag{4.14}$$

with ΔG_V difference in free energy, γ interfacial energy corresponding to the

creation of a surface and r the radius of the cluster.

If a cluster has a size larger than the critical radius r^* then the nucleus becomes energetically stable. These considerations are represented in figure 4.6 and expressed by:

$$r^* = -\frac{2\gamma}{\Delta G_V} \qquad W^* = \frac{16\pi}{3}\frac{\gamma^3}{(\Delta G_V)^2} \tag{4.15}$$

In the CNT theory, no information of the pathways leading to critical nucleus

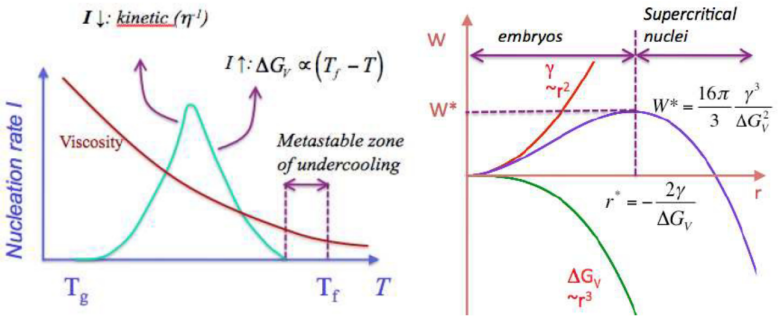

Figure 4.6: (Left) Nucleation rate, function of temperature. (Right) Work of formation, function of radius for CNT theory.[102]

formation is given as it is simply assumed that random fluctuations occur in the liquid corresponding to clustering of atoms.

The Generalized Gibbs Approach (GGA)[103,104] was introduced to account for a change in composition of the nucleus α. The critical parameters are now:

$$r^* = -\frac{2\gamma}{c_\alpha \Delta G_V} \qquad W^* = \frac{16\pi}{3}\frac{\gamma^3}{(c_\alpha \Delta G_V)^2} \tag{4.16}$$

with c_α the volume concentration of the new forming phase.

The consequence of this introduction is that the size of the nucleus is changed until the critical value with few changes in composition compared to the initial state. Allowing compositional and structural fluctuations during nucleation can also explain the phenomenon of phase separation[102−105] in which a liquid solidifies two or more different phases with different structures and compositions.

4.3.3 Phase transformations, polymorphs and metastable phases

The main interest of this work is the observation of the cooling phenomenon, so the sample will be followed through a large range of temperatures. The implication of this is the occurence of different phase transitions which can be observed as the temperature is changed.

In order to refer at different phases, there should be at least one physical property of the material which is different. That means that the first step to understand and describe the transition is the identification of said property.

If we consider only one phase, the values of said property can continously change but if a finite discontinous change is observed, it will evidence that a transformation has occurred as well as which are the transition point and factors that caused the phenomenon.

There are also properties that do not change quantitatively but qualitatively. The latter are defined as a difference in symmetry. In this case, the transition point can be defined by the occurrence of a symmetry change which leaves chemical bonds unchanged but only slightly change their length and orientation (second order transitions) or break bonds (first order transitions).[106]

First order transitions imply the reorganization of the network to give rise to a different microstructure whilst maintaining the chemical composition unaltered. This is the case of polymorphs.

Some materials seem to possess a wide variety of polymorphs that can only be distinguished by microstructural organization differences.

A polymorph can be a stable phase of matter, meaning that its network and its properties are bound to be unaltered in time, or a metastable phase that has a lifetime and will eventually get reorganized to reach the stable phase. The possible formation of intermediate metastable phases was first predicted by Ostwald et al.[108] Due to the short lifetime of these phases, their observation is complicated and requires an adequate setting and conditions.

An example of polymorphism is illustrated in figure 4.7. Most of the silica polymorphs are crystalline. α-quartz is stable until 573 °C, when it transforms to its β-phase. An increase in temperature causes the formation of tridymite and crystobalite forms until reaching 1700 °C which causes it to melt. β forms of the polymorphs are only stable at high temperatures and their respective α phase can be obtained by slow cooling. In this case, the β forms can be considered metastable polymorphs since they can not exist at different temperature conditions.

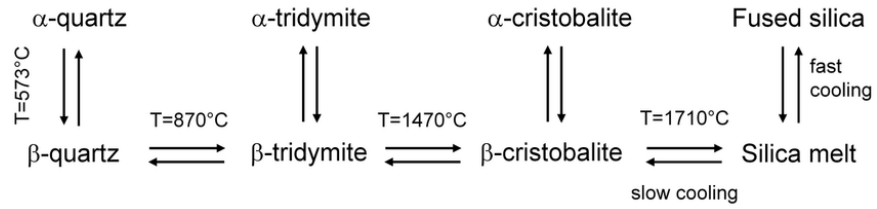

Figure 4.7: Diagram of the phase transition of silica polymorphs. In this example, the β phases are metastable due to their inexistence at different temperatures, excluding the ones of their formation. The cooling path used can allow to solidify the corresponding α phase from the metastable one. The first distinction from the melt is drawn in terms of fast or slow cooling, with the fast path leading to glass formation.[107]

4.3.4 Glass theory

There have been a lot of theories to describe glass structure. The discussion of the complete history concerning the theoretical formation of glass is out of the scope of this work except for the classification of cations' role in a glass and the notion of coordination number, as well as some basic theories. However, it is also important to describe the subdivision of a glass network, since its structure is not regular and not organized as a crystal. In fact, the main distintion between a glass and a crystal is that the former presents a lack of long range order meaning that the structure does not repeat itself periodically.

We can differenciate three ranges of organization at different length scales:[109]

- Short range order (<3 Å): Structural units in the network
- Medium range order (3-10 Å): Connectivity and angles between structural units, ring structures
- Long range order: Fluctuations of composition or density

And we can classify cations considering their role in the formed network as:

- Network formers: can form a glass network
- Network modifiers: modify the network by breaking bonds between the network formers and the oxygens
- Intermediates: do not form glass on their own but are able to do so in the presence of modifying oxides, can either reinforce or break the network

Classification of cations according to Dietzel's field strength (W. Vogel, Glass Chemistry, Springer-Verlag, 1992).

Element	Valence Z	Ionic radius	Coordination number	Ionic distance	Field strength Z/a^2	Function in glass structure
K	1	0.133	8	0.277	0.13	Network-modifiers $Z/a^2 \approx 0.1–0.4$
Na	1	0.098	6	0.230	0.19	
Li	1	0.078	6	0.210	0.23	
Ba	2	0.143	8	0.286	0.24	
Pb	2	0.132	8	0.274	0.27	
Sr	2	0.127	8	0.269	0.28	
Ca	2	0.106	8	0.248	0.33	
Mn	2	0.091	6	0.223	0.40	
Fe	2	0.083	6	0.215	0.43	
Mn	2	0.083	4	0.203	0.49	
Mg	2	0.078	6	0.210	0.45	Intermediates $Z/a^2 \approx 0.5–1.0$
			4	0.196	0.53	
Zr	4	0.087	8	0.228	0.77	
Be	2	0.034	4	0.153	0.86	
Fe	3	0.067	6	0.199	0.76	
			4	0.188	0.85	
Al	3	0.057	6	0.189	0.84	
			4	0.177	0.96	
Ti	4	0.064	6	0.196	1.04	
B	3	0.020	4	0.150	1.34	Network-formers $Z/a^2 \approx 1.3–2.0$
Ge	4	0.044	4	0.166	1.45	
Si	4	0.039	4	0.160	1.57	
P	5	0.034	4	0.155	2.1	
B	3	0.020	3		1.63	

Figure 4.8: Classification of cations from their function in the glass structure. Network-modifiers modify the glass network created by network-formers and intermediates can have different roles depending on their CN.

This is due to differences in valence and field strengths of these elements. Network formers present high field strengths (Z/a^2), high valence numbers (3,4 or 5^+ cations) and their radii are small. Network modifiers have low field strengths, low valence and bigger ionic radii. Elements displaying these characteristics generally belong to alkaline and alkaline earth. Intermediates can have different values for those quantities yet they mainly lie in the middle between the two groups.

This distinction allows to determine the coordination number that is a quantity used to obtain informations on the microstructural motifs present in the network. The coordination number (CN) is determined by how many anions can be packed around a given cation, and it is defined as the cation/anion ratio.

As illustrated in the table in figure 4.8, networks formers mainly present a CN of 4, while network modifiers have CN$\geq$6. Intermediates can present differences in their CN depending on their role in the network, a CN=4 reinforces the network whilst CN$\geq$6 breaks it further.

In this work, we will consider oxide materials so the anions coincide with oxygens. The CN will illustrate how many oxygens are linked to the cation.

Figure 4.9 presents the main theories on the structure of glass. In the Continous

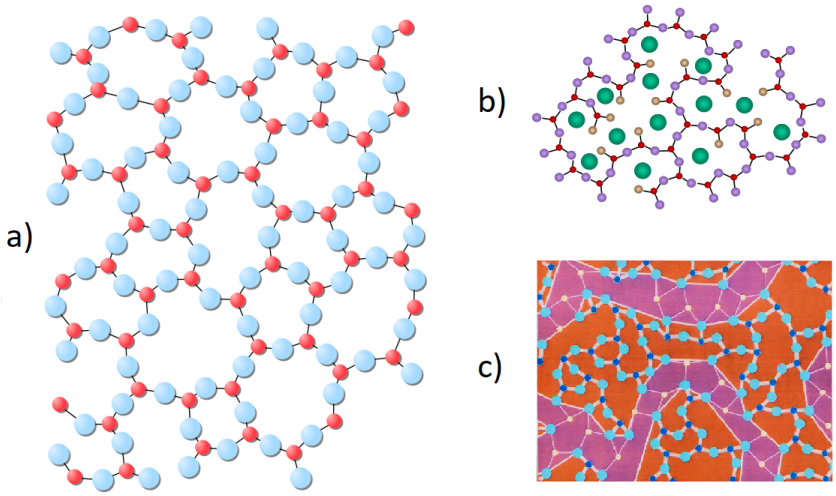

Figure 4.9: Main theories regarding glass structure. a) Zachariasen's model of silica glass (Continous Random Network). The blue dots represent Si and the red dots O.[110] b) Modified Random Network. This theory takes into account the addition of cations (green) in the glass structure, creating BOs (red) and NBOs (yellow).[111] c) Percolation Channels. In this case, a separation of zones rich with network modifiers and zones rich with network formers is illustrated.[112]

Random Network's description of oxide glasses,[110] they can be described as a network of TO_3 and TO_4 units linked by corner sharing to form a continous network. In the Modified Random Network,[111] the addition of network modifiers causes the creation of NBOs. More recent descriptions of glass networks are those of Percolation Channels.[112]

4.3.5 Silicate and aluminosilicate glasses structural description

The ternary system studied in this work is M_xO_y-Al_2O_3-SiO_2 so it is important to illustrate how an aluminosilicate network is formed, starting from the silicate one.

If we do not take into account the existence of a very small amount of defects in the glass network, vitreous silica is composed of interconnected corner-sharing SiO_4 tetrahedra, meaning that each SiO_4 is linked to other four tetrahedra. All of the oxygens are linking only two tetrahedra, thereby satisfying the charge balance principle between tetravalent cations Si^{4+} and divalent O^{2-}, and they can be referred to as bridging oxygens (BOs). This kind of network is said to be fully polymerized. When a modifier oxide is introduced in the network,

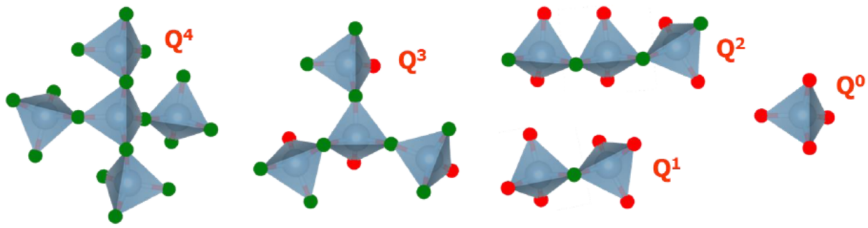

Figure 4.10: Schematic representation of Q^n species[113,114]

some linkages will be destroyed, creating non-bridging oxygens (NBOs). This phenomenon is referred to as depolymerization.

In order to differenciate between these structures and to quantify the degree of depolymerization of a network (how many inter-tetrahedral linkages have been broken by the modifying oxide), the Q^n species notation has been introduced (where n is the number of BOs per SiO_4 tetrahedron). In the previous case, the silicate network can be considered as a Q^4 network and each NBO created by the breaking of the connection will reduce n, figure 4.10 illustrates these structures.

In the melt, Q^n species are present and created by a disproportional reaction:

$$2Q^n \iff Q^{n-1} + Q^{n+1} \tag{4.17}$$

The proportion of this creation is controlled by the equilibrium constant K_n:

$$K_n = \frac{x(Q^{n-1})x(Q^{n+1})}{x(Q^n)^2} \tag{4.18}$$

where $x(Q^n)$ is the mole fraction of the Q^n species.

The value of K_n depends on the cation's nature and temperature.

In the case of aluminosilicate compounds, a silicon tetrahedron can be linked to other silicon tetrahedra or aluminium tetrahedra, as well as a mixture of both. Al is an intermediate cation and it can enter the network by forming tetrahedral or octahedral units depending on composition.[115–117] The notation of Q^n_m species is introduced to distinguish between these different environments. In general $n \geq m$ because n still refers to the number of BOs and m is the number of aluminium tetrahedra connected to the silicon one. It can be noted that this notation just adds supplementary information to the Q^n notation. Some examples are shown in figure 4.11.

The structure described refers to the short range ordering in aluminosilicate glasses. In medium range there are larger structural units involving ring forma-

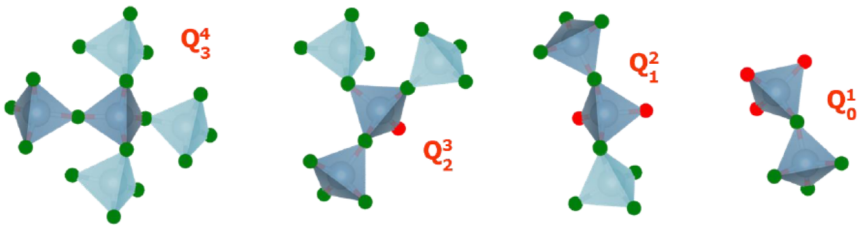

Figure 4.11: Schematic representation of Q_m^n species[114]

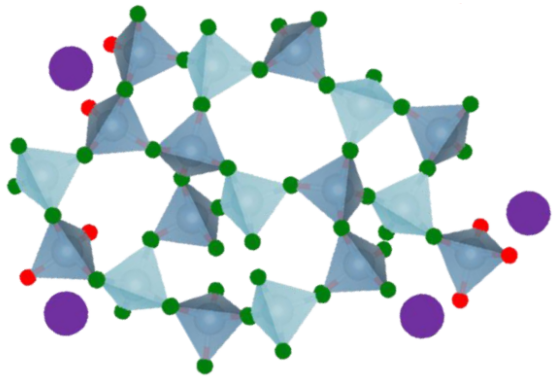

Figure 4.12: Schematic representation of an aluminosilicate glass network including metal cations and ring structures[114]

tion, for example (figure 4.12). Al^{3+} set in tetrahedral AlO_4^- require charge compensation to achieve charge neutrality in the system. For this reason, the addition of non-network forming cations will either provoke a depolymerization of the network or assume a charge compensating role. This difference in behaviour depends on their positioning in the network and whether they can be found close to NBOs or to negatively charged aluminium tetrahedra.

In addition to these structures, in alkali and alkaline earth aluminosilicate glasses there are also probably oxygen triclusters[118−120] which designate an oxygen shared by three tetrahedra at the same time, departing from simple structural models as those depicted in figure 4.9(a,b).

5

SiO_2

Contents

5.1 The prototypical glass-forming material

SiO_2 has been given a very important role in the foundation of glass science. This material is still considered the prototypical glass due to its chemical simplicity.

Nonetheless, silica has been the main subject of a lot of studies. The reason to this is easily found in its simplicity, even though this is just an apparent quality as silica, in reality, is structurally complex and its properties can present anomalies. Controversies on its behaviour and on the models that can be used to predict it are still present as most of them are inadequate of fully describing it.[121]

Due to its historical importance and its chemical simplicity, additional work probing its structure is mandatory as the understanding of its behaviour and structure can shed some light on the nature of the glassy state. If this is reached, these considerations can then be used to understand more chemically complex glasses and thus allow more research to be made.

In this chapter we will discuss the structure of silica from molten state to the solid glass phase. In order to do this, a comparison between the static and the kinetic measurements has been made. The congruity of the results obtained allow us to validate our real-time technique and further prove its ability to extract dynamical but reliable structural information. As we performed static heating and dynamic cooling of silica glass, we can consider the measurements as part of a circle since the end result is the starting point of the next study and viceversa.

The choice of SiO_2 as a reference material is obvious if taken into account the low fragility of its liquid phase, a property that describes how influent the temperature-induced structural changes are in the network.[84]

As seen previously, the structure of silica glass is solely composed of SiO_4 tetrahedra forming a fully polymerized network containing ring structures of different sizes.[122] This fact makes this material the perfect candidate for our study, as its dynamic changes will be subtles but still providing valuable insight on the mechanisms of glass transition and vitrification.

Thanks to the possibility of following the cooling at various temperatures, it is possible to observe the glass transition region closely to explore the dynamics of vitrification. A "frozen" dynamic structure has been encountered in different measurements at almost 100 K below the transition temperature and it will be discussed at the end of the chapter.

5.2 Structural studies and controversies, state of art

SiO_2 is mainly considered as the prototypical oxide glass former.

Its structure is comprised of corner-sharing tetrahedral SiO_4 structures interconnected by bridging oxygens, as seen in figure 5.1. This glass has an high network connectivity. SiO_2 is also found in crystalline forms such as quartz and cristobalite.

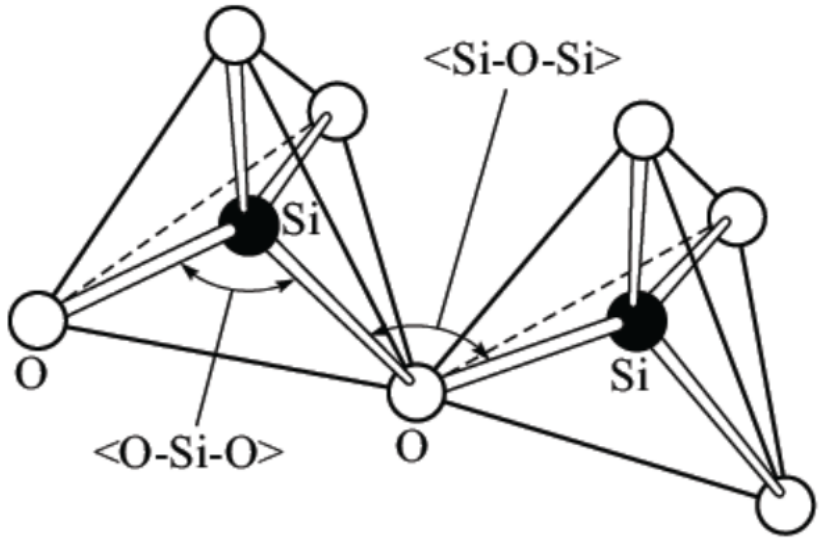

Figure 5.1: SiO_4 tetrahedra[123]

The first measurements of silica glass have been performed in 1938 using XRD.[124] The results obtained confirmed the tetrahedral structure where each silicon is surrounded by 4 oxygens at a distance of 1.62 Å and show a random orientation of tetrahedral neighboring groups, two characteristics that confirmed the Random Network theory prevalent in those years.

From these results, the interest in models concerning glass structure increased[125] as there was a great difficulty in expressing the experimental data into a defined atomic model. Another difficulty arose from the formulation of sets of rules to determine atomic positions.[126]

In 1969, the experimental conditions improved allowing the measurement on the Si-O-Si bond angles that displayed a wide distribution of angles (from 120°

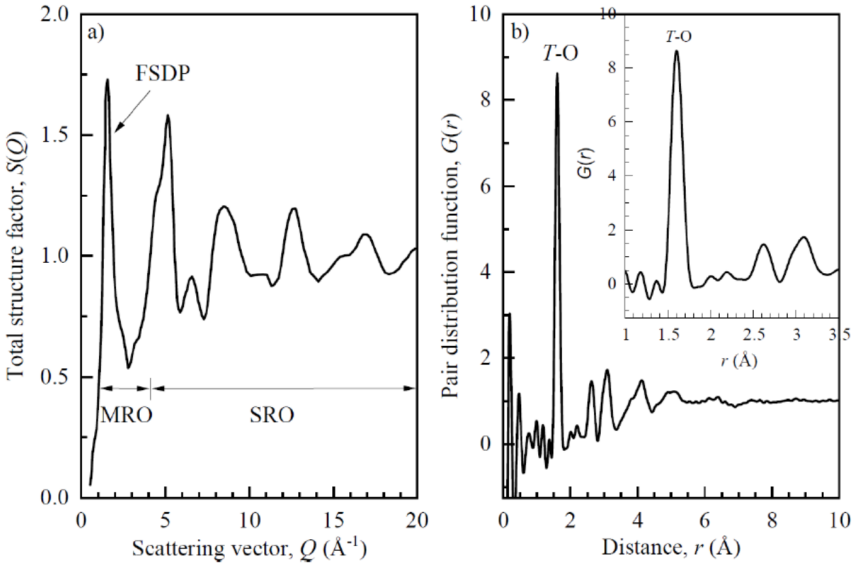

Figure 5.2: XRD measurements for SiO_2 glass[129]

to 180°), defining a very important distinction between the vitreous and the crystalline forms of silica.[127] This result was later disproved by comparing XRD data with NMR and neutron diffraction data.[128]

More recent XRD measurements of silica glass are shown in figure 5.2, mostly concerning the more complicated medium range order. As observed in the figure, the $G(r)$ for pure silica glass presents a first peak at 1.60 Å and a second peak at 2.61 Å which respectively correspond to Si-O and O-O distances of neighboring atoms in a tetrahedron. Calculating the O-Si-O angle from these distances shows a good correspondance to the value of a perfect intratetrahedral angle. After distances greater than 6 Å the $G(r)$ appears featureless due to the lack of long range ordering, as expected in a glass.

For this measurement of $S(q)$ it is possible to distinguish the first sharp diffraction peak at $q_1 = 1.55$ Å^{-1}, a peak observed in many glasses which is a signature of medium range order (MRO) in the glass with periodicity $2\pi/q_1$.[130–132]

In real space, the distance in which the MRO persist is calculated by $2\pi/\Delta q_1$ with Δq_1 being the full width at half maximum of the peak.[132] For this reason, the position of q_1 gives information on how much this order is preserved and a sharper peak means a MRO persisting for a longer distance.[43]

In SiO_2 the first peak is attributed to tetrahedral units in ring arrangements.[43] Information on the ring structures and the full nature of MRO is mainly

quantified using simulation methods.[133] The local structural ordering is found in the oscillatory features at high-q rate. This is confirmed by the peaks in real-space of $G(r)$ at the characteristic interatomic distances of short-range chemical bonds.

Another technique used for the determination of the Si-O-Si bond angle is NMR[134] due to the dependency on the ^{29}Si chemical shift.[135] More recent NMR studies employ ^{17}O two-dimensional studies[136] and in this case, the existence of an unexpected positive correlation between the Si-O-Si angle and Si-O distance only in the glass, and not present in crystalline forms, has been suggested.

The Raman spectra of SiO_2 polymorphs is shown in figure 5.3.[137] The glass spectrum in the region below 1000 cm^{-1} can be linked to the MRO of the silica glass and it is typically related to Si-O-Si breathing modes from SiO_4 tetrahedra in ring arrangements.[138−147]

The Boson Peak (BP) at 80 cm^{-1} can be attributed to the signature of a longer-range vibrational structure and the "R" peak at 440 cm^{-1} corresponds to bending vibrations of intertetrahedral Si-O-Si angles in rings having more than 5 members.

Peaks D_1 and D_2 are instead associated to the bendings of Si-O-Si in 3 and 4 membered rings, and the remaining asymmetric peaks found at 800 cm^{-1} and 1080 cm^{-1} illustrate the Si-O stretching vibrations in SiO_4.[147]

In addition, other probing techniques like atomic resolution microscopies made possible the observation of thin films of silica,[148−150] as shown in figure 5.4. In this case, a very strong parallelism with the structure depicted by Zachariasen[110] in the early days has been spectacularly obtained.

High temperature molecular simulations of SiO_2 have also been performed to acquire more insight into the structure.[151−155] In this case, in order to explain how the structure of silica and its density changes due to temperature, a model based on structures called "structons" has been developed.[151] Following this model, vitreous silica would be comprised of static alpha and beta structures, shown in figure 5.5 as a) and b), meanwhile the liquid would instead present all the 4 kinds of structons. As the temperature changes, the proportion of these structures would change.

More recent simulations evidence the presence of SiO_5 units in the liquid, appearing as transient states and that can justify the dynamics of the viscous flow.

Computational work has focused on finding the best models to describe silica and its polymorphs.[155] This is due to the fact that not all the properties and

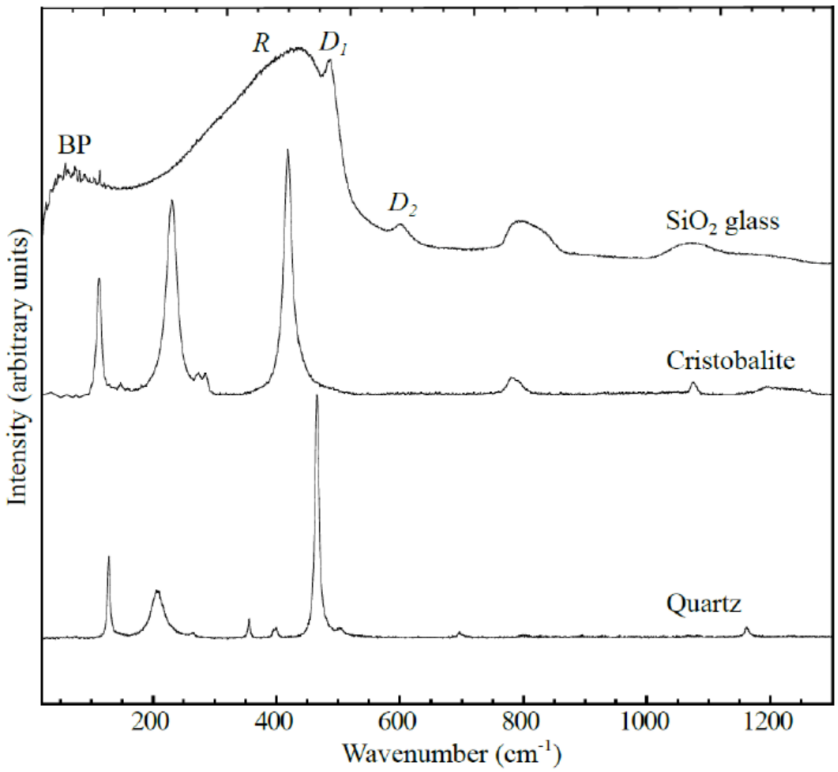

Figure 5.3: Raman measurements for SiO_2 glass, cristobalite and quartz[137]

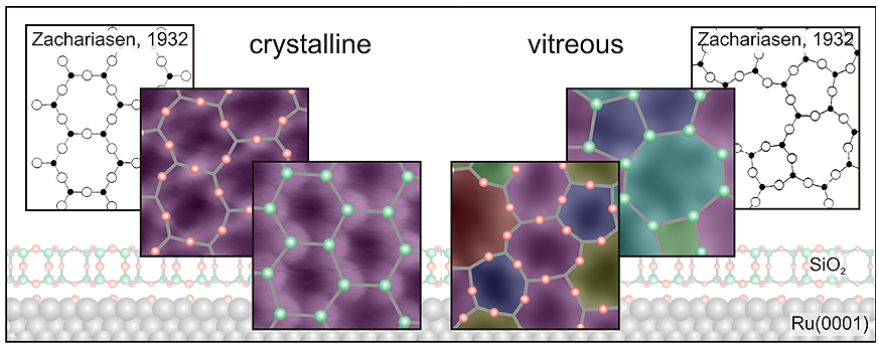

Figure 5.4: Atomic structure of vitreous and crystalline regions of a thin silica film through noncontact atomic force microscopy (nc-AFM) and scanning tunneling microscopy (STM).[150]

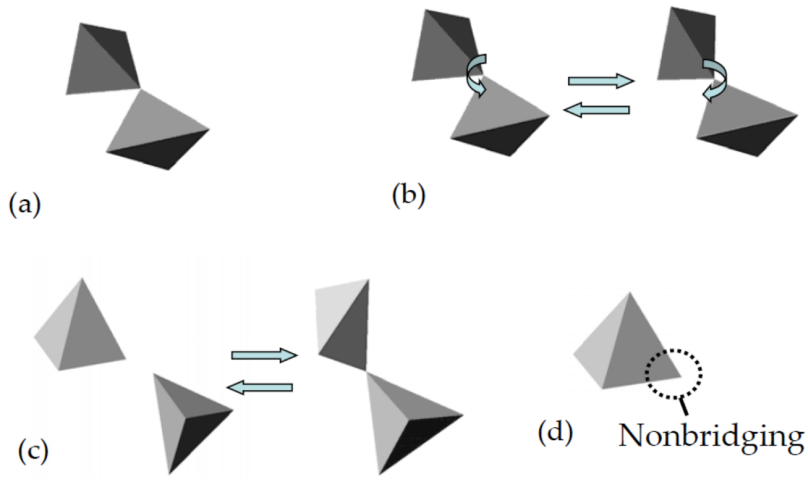

Figure 5.5: Scheme of the structures used in the structon model[151]

transitions observed experimentally are easily covered by the use of a potential and the large number of polymorphs is due to the many ways of linking silica tetrahedra.[157] In this work, we will focus on the kinetic vitrification of silica from molten state using FT-IR, a study that has not yet been conducted.[121]

Another issue that arose in the previous years is centered on band interpretation of silica glass. Due to the history-dependent properties of glasses, it is difficult to explain its vibrational spectral features by using the properties of equilibrium parallels.[158]

The IR spectrum of silica is mainly composed of three regions:

1. A broad peak centered at 1070-1120 cm^{-1}
2. Another broad band at 400-600 cm^{-1}
3. A small band at 800 cm^{-1}
4. A small shoulder band at 950 cm^{-1}
5. A shoulder band at 1180-1200 cm^{-1}

Band 1 has been initially assigned to the stretching motion of Si-O-Si bond and band 3 to the BO stretching vibrations through theoretical calculations.[159,160] Later, band 1 is assigned to asymmetric BO stretch and band 3 to the symmetric one.[161] Band 2 has been described as the BO bending. These assignments have then been used ever since.[162–164]

Band 4 has been the most controversial by far, initially attributed to the vibration of Si-O of NBOs,[165] even though more recent MD calculations suggest

that the contributions from NBO-only are quite small.[166] In this case, this band could still be assigned to BO network vibrations with a red-shift from band 1 due to the connectivity of the network being disrupted by the NBOs.

Band 5 is often referred to as the LO mode,[167−170] nonetheless, the concept of TO-LO splitting is defined for phonon modes of crystals that possess long-range periodicity,[171] yet a glass does not possess that feature, so it would be not applicable to noncrystalline glass networks.[158]

The frequent approach to assign glass' modes is to compare their vibrational features with those of crystalline materials with the same or a similar chemical composition. The compositional similarity is actually not enough to guarantee spectral similarity due to differences in allowed or forbidden modes in crystals that are not encountered in amorphous materials. In addition, the glass presents broader distributions of bond lengths and angles.

Moreover, mode assignment was also originally based on theoretical calculations based on connected tetrahedral units[161,172−175] that did not consider the non-existence of long-range order and the three-dimensional network connectivity of glass so the accuracy of the results is reduced by this over-simplification of the problem.

5.3 Static heating of SiO_2

We start our discussion on silica by performing static heating measurements on a high-purity Saint Gobain silica glass from very low temperature to the high temperature liquid phase.

Figure 5.6 illustrates the temperature dependence of the normal spectral reflectivity between 4 K and 2505 K. The stabilization times at each temperature are nearly 10 minutes and the experimental setting used coincides with the so-called classic conditions discussed previously.

The largest temperature dependence of silica is found in the high-frequency band. This is due to a wider separation of bands in this region and from this observation we decide to focus on it for simplicity.

As discussed in the previous chapter, glass is a disordered material and this is observed clearly in the vibrational spectra as the broad peaks are still present at low temperatures. The strong remnant disorder of the glass is seen as there is very little difference between the spectrum at 4 K and the one at room temperature.

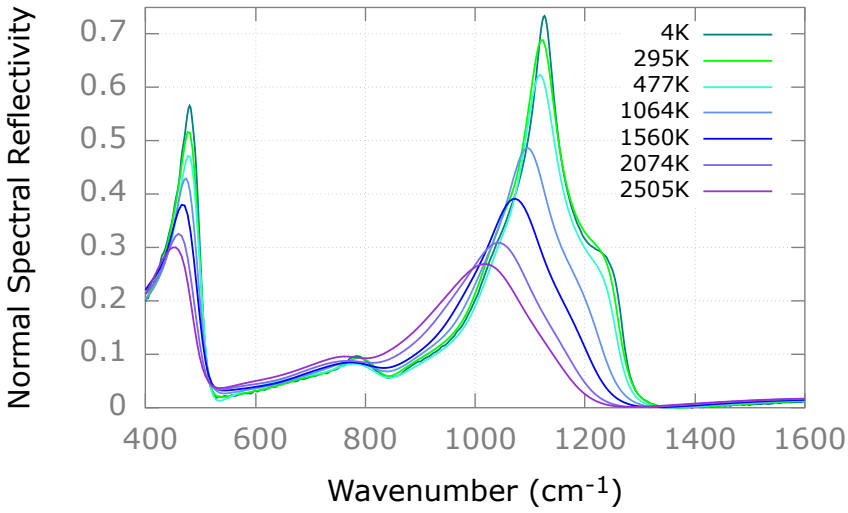

Figure 5.6: Normal spectral reflectivity obtained during static heating of silica glass at various temperatures (from 4 K to 2505 K). The results show a clearer separation of the stretching motions (1000-1300 cm^{-1}) compared to the bending ones (400-550 cm^{-1}). The spectra at high temperature (and especially in the liquid) present a wider broadening.

As the data has been acquired, it is important to choose carefully the number of bands and the parameters used for the fit.

Up to now, the vibrational properties of silica are not completely understood due to controversies on band indexing and their nature.[?] The choice of the number of components is thus crucial for a correct interpretation.

From the analysis of silicate glasses by De Sousa Meneses et al.[176] and the temperature dependence observed, it seems necessary to include at least four bands in the spectral range between 1000-1300 cm^{-1}. This assumption will be further justified later in this chapter yet it is important to discuss it beforehand by using the results obtained on the silicate network.

The authors study the structural modifications of the silicate network following the addition of different percentages of K_2O into it, as illustrated in figure 5.7. As K_2O is introduced in the network, structural modifications occur and new structures such as Q_3 (ν_{10}) and Q_2 (ν_9) are created. These new structures will have an impact on the silica structure by decreasing the number of Q_4 units originally present in the network. This way, the band representing Q_4 is automatically recognized as ν_{11}.

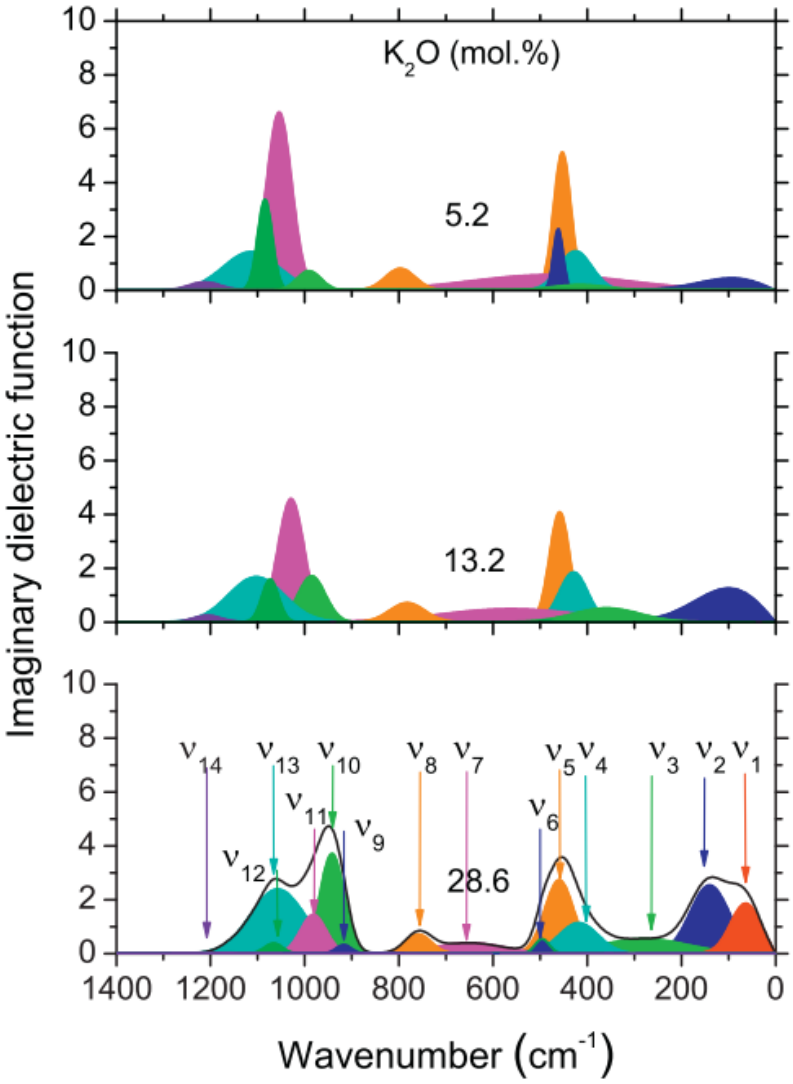

Figure 5.7: Decomposition of the imaginary part of the dielectric function with increasing inclusion of K_2O content.[176] The four bands observed starting from ν_{11} to ν_{14} belong to SiO_2. This band interpretation is useful to be applied later to understand their temperature evolution.

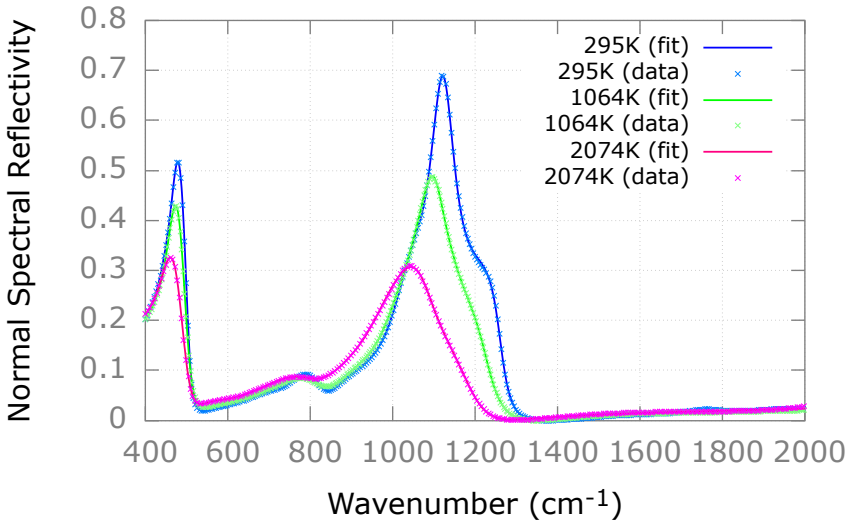

Figure 5.8: Example of fit of experimental reflectance spectra of SiO_2 to the Gaussian dielectric function model at different temperatures: 295 K (blue), 1064 K (green) and 2074 K (pink). It is observed that the model and the number of gaussians used is capable of reproducing the data in the whole temperature range.

Next we consider another band that changes greatly with increasing addition of K_2O. The dramatic decrease of ν_{12} has to be linked to the depolymerization of the network as well, even though its decrease is not area linked as the Q_4 band is. The decrease of this band is found to be composition dependent meaning that it is linked to the connectivity of the system as K_2O is introduced.

From their work, it is also observed that ν_{11} and ν_{13} are correlated as tetrahedral motions in static and dynamic disorder. ν_{14} is a band that has already been observed in crystalline forms of silica.

Following these assumptions, we can now consider four bands (ν_{11} to ν_{14}) to fit the spectra in the stretching regions (10 bands for the total spectrum).

The results of the fits are shown in figure 5.8 and the quality of the fit at different temperatures confirms the presence of at least these four modes. The real and imaginary part of the retrieved dielectric function are illustrated in figure 5.9.

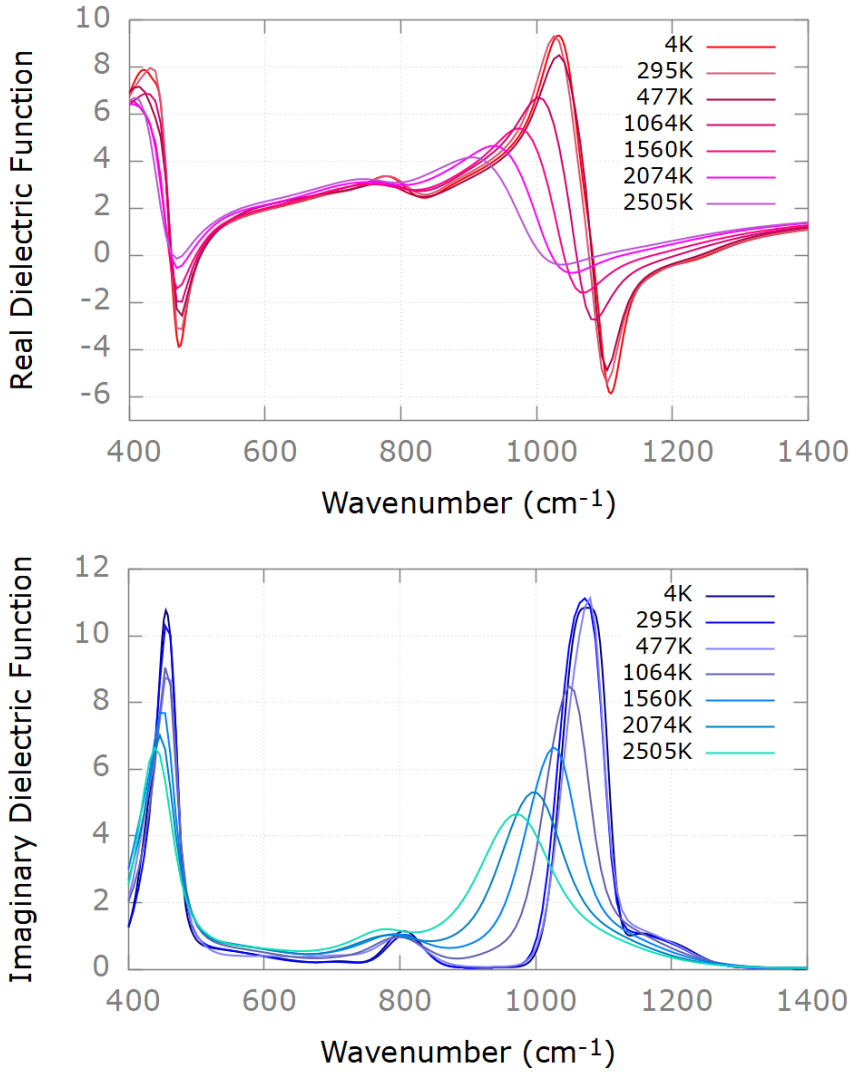

Figure 5.9: Temperature dependence of the a) real part and b) imaginary part of the dielectric function of silica glass at different temperatures (from 4 K to 2505 K). It is yet again observed that a bigger degree of separation between bands is present in the stretching region.

5.4 Kinetic cooling of SiO_2

Figure 5.10 presents the entirety of data acquired during the cooling of silica from molten state and the time vs temperature graph is shown in figure 5.11.

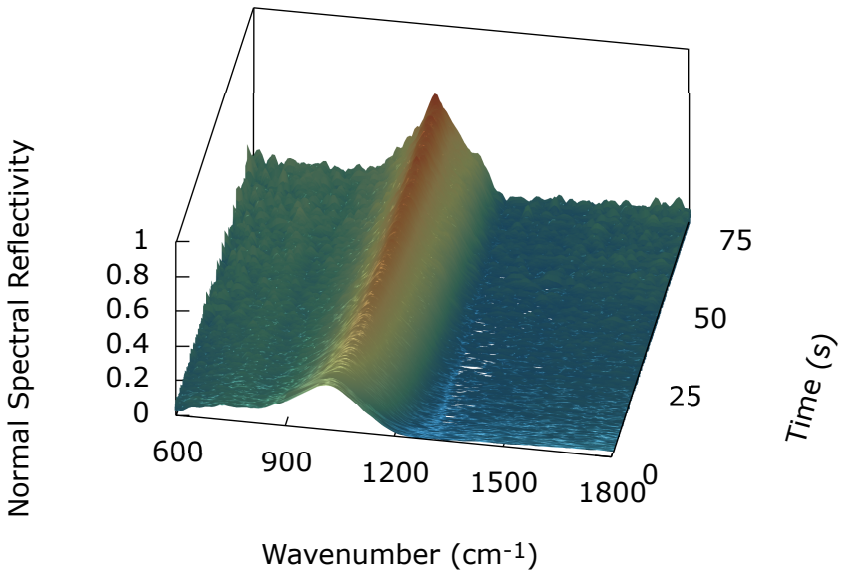

Figure 5.10: Kinetic data acquired during the cooling from molten state of SiO_2 from 2516 K to 643 K. The first dozen of spectra are acquired in static conditions in liquid state while the remaining ones show the process of vitrification (refer to figure 5.11 for the cooling curve) and the progressive decrease of the broadening effect as the temperature is lowered.

The cooling curve is obtained from temperature determination of each spectrum at the Christiansen point.

The experimental parameters used for the acquisition are the ones previously discussed, the speed of acquisition is thus 0.1 s for a double scan (20 spectra/s). The data acquisition is set to start some seconds before the laser shutdown such that equilibrium spectra in the liquid can also be acquired.

In this case, the starting material is yet again a glass, produced from high purity silica powder and converted into small beads through aerodynamic levitation. The small beads are then crushed and a pellet is produced.

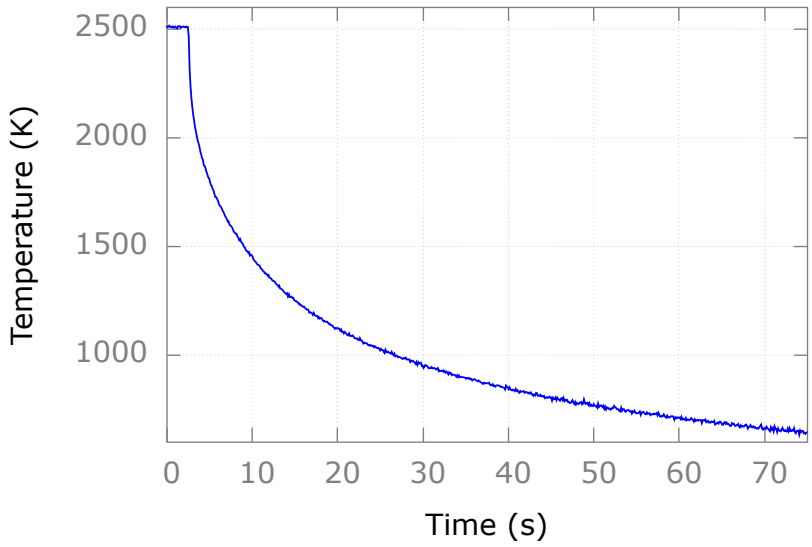

Figure 5.11: Temperature vs time graph illustrating the vitrification process of SiO_2. This graph also illustrates the total duration of the experiment (75 s).

The sample is heated up to 2516 K to allow a starting point for comparison with the static study and the acquisition ends at 643 K.

Figure 5.12 illustrates a comparison between the static and the dynamic data. It can be noticed that the dynamic data present a lower resolution (4 times coarser) but the results are in good agreement even though the acquisition method is not the same.

This observation allows us to consider the two sets of data as one, since the information provided at equal temperature will be the same. In order to be sure of this, both data sets have to be fitted using the same model.

Due to the high number of spectra, a selection has to be performed for the fitting and it has been limited to 1000 K due to the increase in signal-to-noise ratio.

An example of the data fits can be seen in figure 5.13. The next section presents the results and the interpretation of the bands through their temperature evolution.

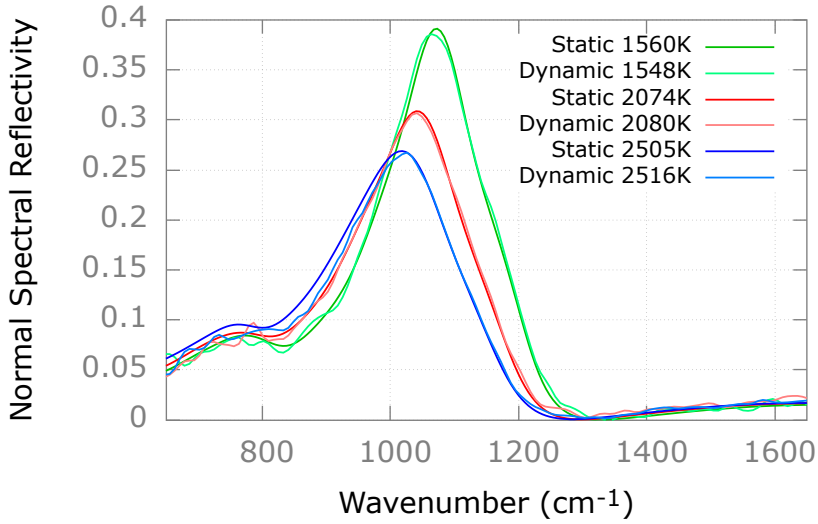

Figure 5.12: Comparison between static and dynamic data. The data show a good agreement, taken into account the lower signal-to-noise ratio of the kinetic measurements due to the lower resolution.

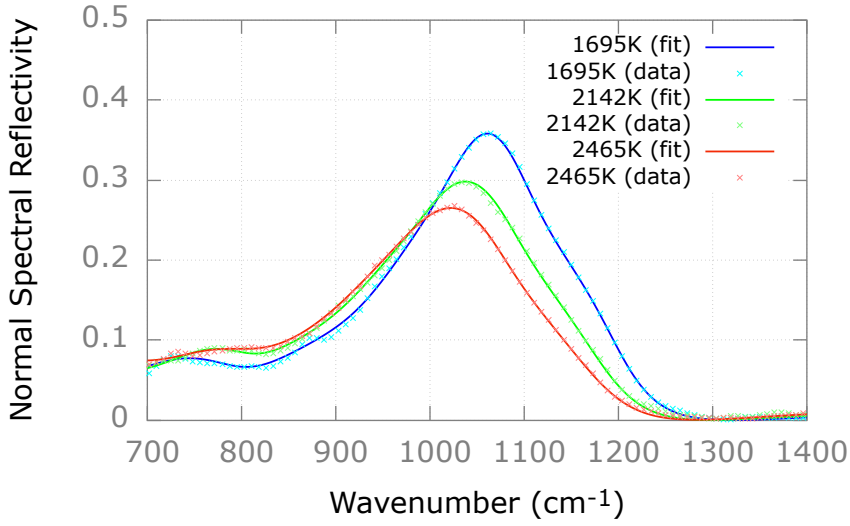

Figure 5.13: Example of fit of kinetic data at different temperatures: 1695 K (blue), 2142 K (green), 2465 K (red). The model and the number of gaussian components used for the fit is yet again sufficient to reproduce the three spectra.

5.5 Interpretation of the vibrational bands and discussion

A fitting model based on Gaussian components has already been used to reproduce satisfactorily reflectivity spectra of glasses.

As discussed at the beginning of this chapter, qualitative assignment of the vibrational bands of vitreous silica is still a source of controversy, particularly regarding the substructure inside the big composite band between 1000 and 1200 cm^{-1}.

In this work, we will explain the temperature dependence of the infrared properties of the material by using what is already known from literature studies and mainly from the data presented on K_2O addition, presented previously.

As usual when dealing with polar materials, infrared-active vibrations can be categorized into bending or stretching in character. Here, we only discuss the stretching components above 800 cm^{-1}, assuming they contain duplicate and equivalent information on the structure and dynamics of the material.[176]

The assignments of the five stretching modes are summarized in Table 7.1.

Mode (ref.[176])	Assignment
P_0 (ν_8)	Symmetric Si-O-Si stretching
P_1 (ν_{11})	Asymmetric Si-BO stretching (regular tetrahedra)
P_2 (ν_{12})	External mode (connectivity)
P_3 (ν_{13})	Asymmetric Si-BO stretching (dynamic disorder)
P_4 (ν_{14})	High-frequency localized mode

Table 5.1: Qualitative assignments of the five stretching bands used in the analysis.[176]

The stretching region of the spectrum consists of two well-separated regions.

First, a mode numbered as P_0 is found around 800 cm^{-1} at room temperature. This mode is well known to correspond to a symmetric stretching of Si-O-Si bridges, with dominant Si character.[177] The breaking of long-range order allows this mode to be IR active.

The rest of the stretching modes, which are linked to asymmetric vibrations, are located close to each other in a characteristic shape. There is significant evidence supporting the picture of two TO asymmetric stretching vibrations in this region.[178] However, these are usually assigned as in-phase and out-of-phase vibrations.

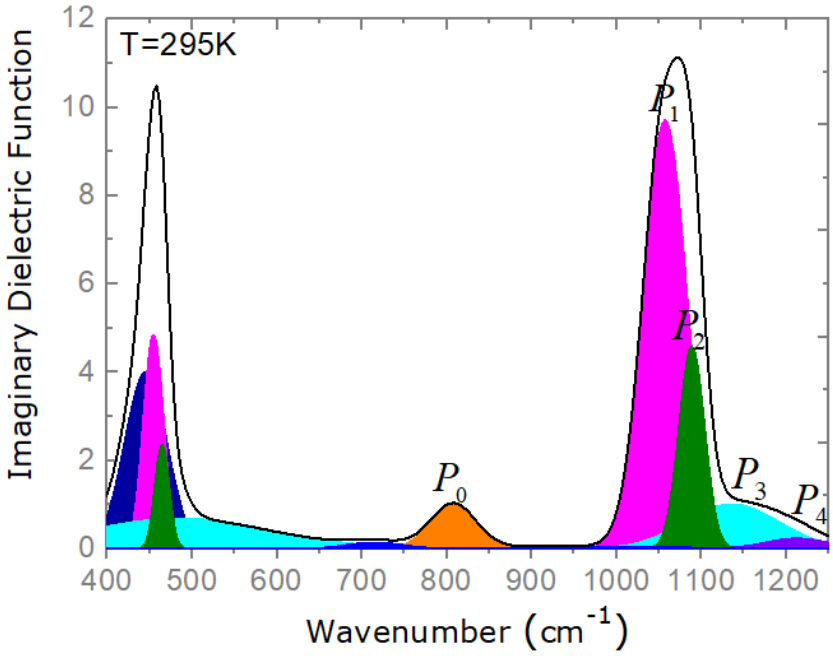

Figure 5.14: Gaussian components used to fit the room temperature reflectivity spectrum of silica. The main components that are discussed in this chapter are P_i with i=1,..,4. Table 7.1 presents their assignment.

Here, we suggest that the higher-frequency band corresponds to the internal stretching of tetrahedra participating in dynamic disorder. The main consequence of this is that temperature changes will induce a transfer of spectral weight between the modes.

Finally, the two remaining modes are attributed to external modes, not intrinsically related to the internal modes of the SiO_4 tetrahedron. P_2 was observed to correlate well with the degree of connectivity between Q_4 structural units in alkali silicate glasses,[176] whereas P_4 can be linked to high-frequency weak modes in crystalline versions.[179]

The proposed phenomenological model is not only useful to retrieve the dielectric function of the material, but also as a tool to investigate its structure and dynamics.

Through the qualitative assignment discussed previously, the temperature dependence of certain properties of the material can be quantitatively tracked by representing the amplitude, position and full width at half maximum (FWHM) of each P_i stretching mode as a function of temperature, as illustrated in figure 5.15.

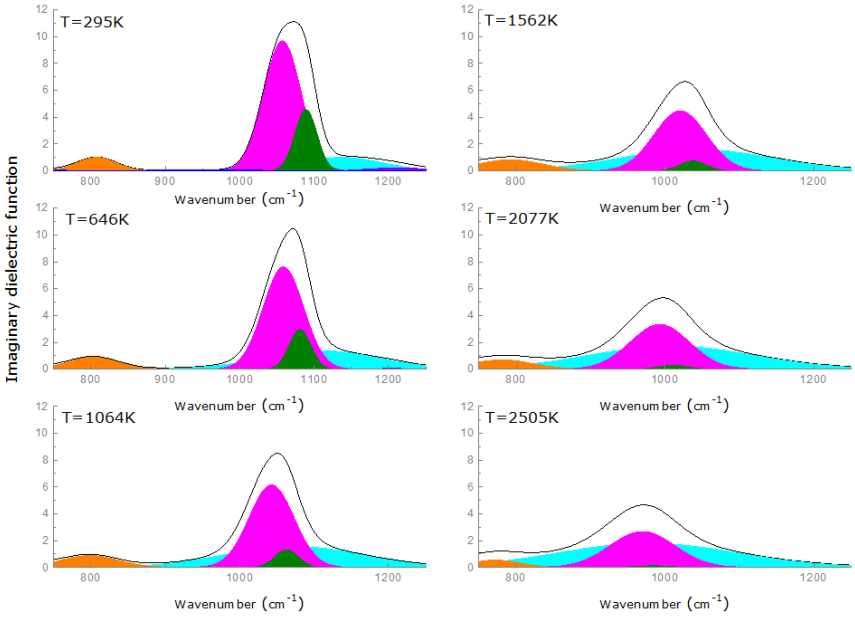

Figure 5.15: Temperature dependence of the P_i Gaussian components in static heating conditions from 2505 K to 295 K. The temperature evolution of the modes is reported in figure 5.16.

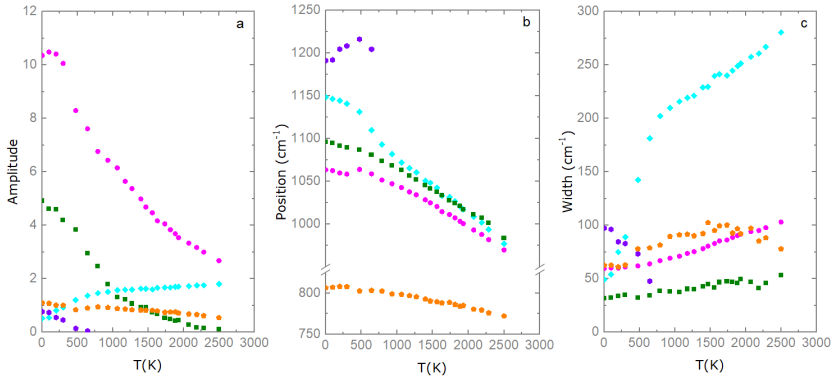

Figure 5.16: Temperature dependence of the a) amplitude, b) position and c) FWHM of the Gaussian components corresponding to the stretching vibrations of the silica network (P_0 - pentagons, P_1 -circles, P_2 - squares, P_3 -diamonds, P_4 -hexagons).

Each band follows a clearly-defined continuous evolution with temperature. The high-frequency P_4 contribution quickly becomes undetectable; P_3, which is linked to the degree of dynamic disorder, increases spectacularly in width and total area; and the other three modes experience a redshift (i.e. toward lower frequencies) and a decrease in total area.

The features observed qualitatively at discrete temperatures in figure 5.15 can be better appreciated in figure 5.16, where all the fitting results are plotted as a function of temperature. Many interesting features are immediately obvious from these phenomenological parameters.

As indicated before, all modes except P_4 experience a clear redshift. This anomalous component is almost undetectable above 600 K and the assignment of this band is consistent with the disappearance of a similar mode in cristobalite above its $\alpha - \beta$ phase transition at 543 K.[180]

Regarding the other modes, we can observe in more detail the same behaviors that were discussed above. These features are even more evident for the area of the modes (figure 5.15) where sudden changes are observable near 800 K, around the glass transition temperature T_g (1480 K) and the melting temperature T_m (considered as 1993 K).[181]

Increasing temperature leads to spectral weight transfer. The areas of modes P_1 and P_2 drastically decrease and the mode P_4 is even more affected since it disappears around the first evidenced anomaly near 800 K. On the contrary, the weight of the components P_0 and P_3 is strengthened in the same temperature range.

For higher temperatures, the same tendencies are observed, with the exception of the mode P_0, whose area seems to be relatively constant up to T_g and starts decreasing above this temperature.

Another remarkable feature that occurs exactly at the glass transition temperature is the crossing of the areas of modes P_1 and P_3, as shown in figure 5.17. This feature will be analyzed in more details through the dynamic study.

5.5.1 Temperature evolution of internal and external modes

As discussed previously, modes P_1 and P_3 have the same infrared activities and certainly the same microscopic origin.

The FWHM of P_3, about three times higher than that of P_1, indicates that P_3 vibrations are influenced by a far more disordered environment which is

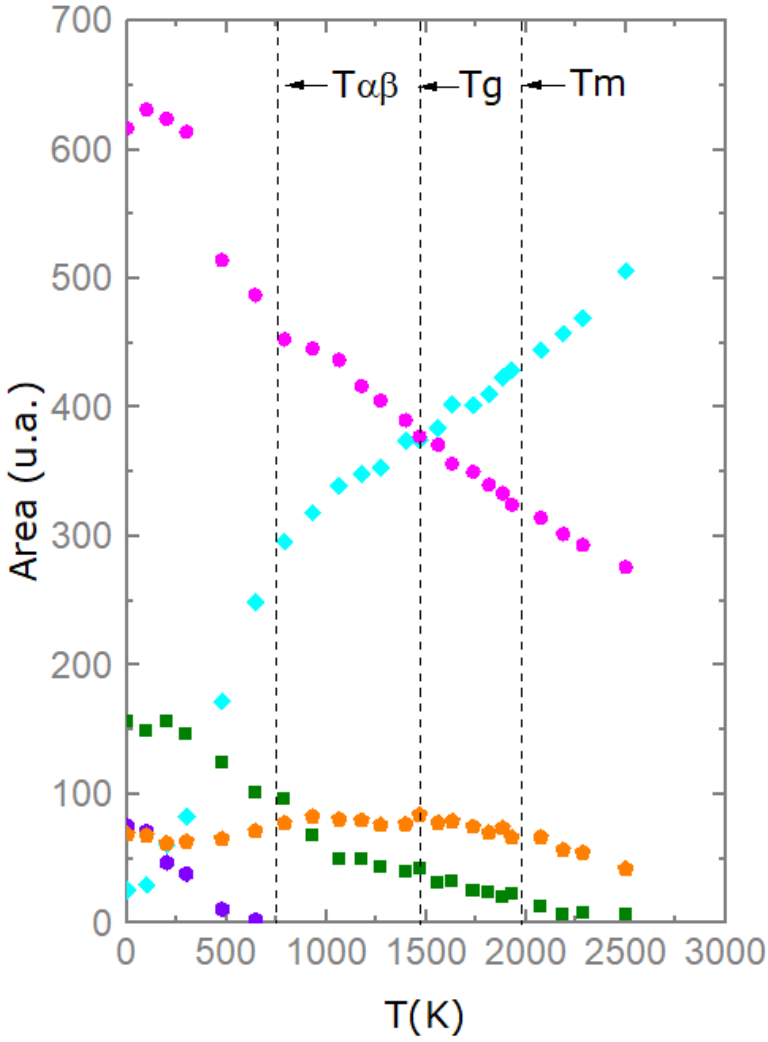

Figure 5.17: Temperature dependence of the P_i Gaussian components in static heating conditions. The figure evidences the spectral weight transfer occurring between P_1 and P_3 and their change of slope at $T_{\alpha\beta}$. These modes also present an area crossing at T_g. Mode P_4 appears after $T_{\alpha\beta}$.

also in agreement with its strengthening with increasing disorder at higher temperatures. The above results show that these modes behave as localized ones, i.e. as internal modes of the same structural units present in both solid and liquid states but experiencing different surroundings.

To sum up these first results, we can say that the trend of these two modes shows that at low temperature the dynamics of the structural units of silica contribute essentially to the P_1 peak. With increasing temperature there is a continuous transfer of the spectral weight towards the P_3 state due to the activation of dynamical disorder.

Following this assignment, it is striking to notice that the temperature for which the occupancy of the two modes are equal corresponds to the glass transition temperature T_g. Above this temperature, P_3 keeps increasing at the expense of P_1, as shown in figure 5.17.

After dealing with the two more prominent modes, it is tempting to see if the other two modes P_0 and P_2 are also related in some way and we can make the hypothesis that these modes are also of the same nature and that their infrared activities are similar. To better understand the origin of these modes let us reconsider the structure of silica.

Silica is composed of a network of corner shared SiO_4 tetrahedra, the degrees of freedom of the structure leads to vibrational modes that can be distributed between internal modes, i.e. localized inside a single tetrahedra and external ones, i.e. vibrations involving the Si-O-Si bridges.

The number of internal modes must not change between 0 K up to the boiling point since the number of structural units is preserved. This is why P_1 and P_3 components are attributed to internal modes corresponding to asymmetric stretching of the silicate tetrahedra.

Modes involving more than one tetrahedron are more sensitive to temperature, as their existence requires the preservation of Si-O-Si bonds. With increasing temperature, bond loosening and breaking between SiO_4 tetrahedra due to the activation of dynamical disorder must result in a decrease of these spectral components. Indeed, the temperature dependence of P_0 and P_2 presents effectively this kind of behavior, indicating that these peaks can be attributed to external (inter-tetrahedral) components.

Figure 5.18 presents the division of modes in these two families: internal and external modes. It is observed that the internal modes display a linear behaviour in temperature, as the structural units should be preserved. The external modes decrease progressively and would disappear completely at the estimated boiling point (extrapolated at around 3150 ± 20 K and compatible with a reported value of 3070 ± 75 K[182]). If one goes now more finely in

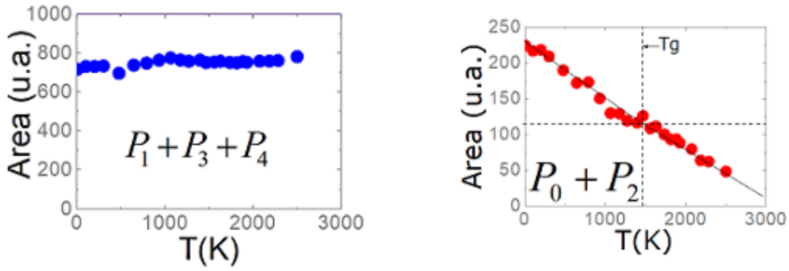

Figure 5.18: (Left) Internal and (Right) external modes evolution in temperature. In the first case, the sum of the areas of the modes (P_1, P_3 and P_4) remains constant in temperature, as the number of structural units should be preserved even when the increase in temperature causes a network breakdown. In the second case, the sum of the areas of the modes (P_0 and P_2) decreases with increasing temperature, a sign that these modes contribute to the connectivity of the network and the bond breaking phenomenon causes their decrement. It is also observed that their areas would reach zero at the boiling point.

the description and considers that the P_1 peak originates from asymmetric stretching of the SiO_4 tetrahedra that does not contain loosened bonds due to dynamical disorder nor broken bonds and that P_3 is the same kind of vibration but in a tetrahedron having loosened or broken bonds, one can relate the disappearance of half of the external modes ($P_0 + P_2$) at the glass transition to the fact that at this temperature half of the internal modes contribute to the P_3 peak.

Another interesting result arising from the fit is the value of the FWHM of the P_2 component. The rather small value suggests that this delocalized mode reflects the existence of medium-range order in the structure of vitreous silica at low temperature.[176] The loosening of bonds with increasing temperature has a deep impact on the medium range order of the structure which explains the rapid decrease of this peak.

At first, the progressive disappearance of medium-range order favors the increase of the P_0 component but when bond breaking starts to become very effective above T_g both components disappear progressively.

Even if no definitive answers can be given on the interpretation of the structural evolution of silica, these results show clear changes on the dynamics of silica at several characteristic temperatures and these modifications have been evaluated in a quantitative way by using a dielectric function model.

The kinetic results confirm yet again the temperature evolution of the modes, as the qualitative evolution of the four stretching components looks indistiguishable. The only difference reported in this case is the difficulty of locating and determining small area modes due to the lower resolution. In any case and

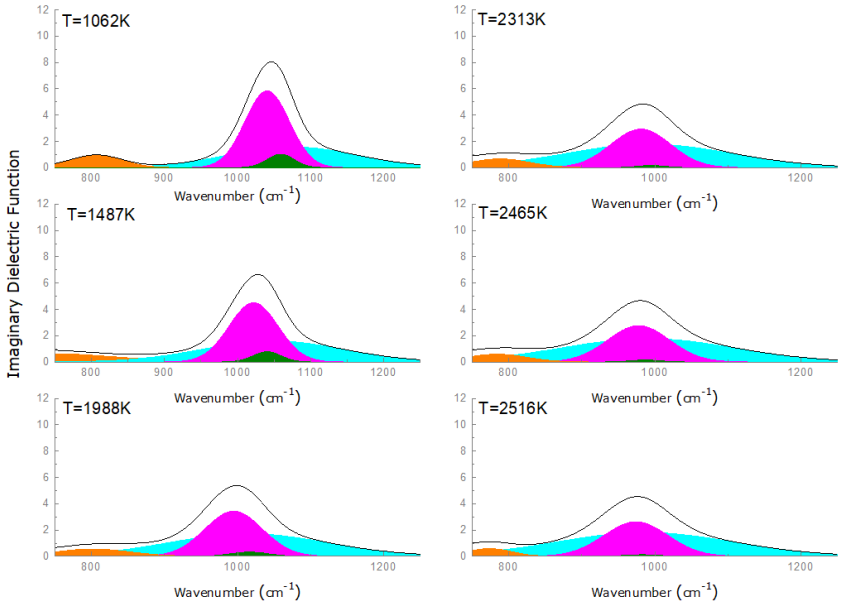

Figure 5.19: Temperature dependence of the Gaussian components corresponding to the stretching vibrations of the silicate tetrahedra (dynamic conditions). The results are in agreement with the static ones shown in figure 5.15.

as stated previously, the compromise between speed and resolution has been achieved since a full mode characterization has been possible.

5.6 Dynamical disorder and glass transition temperature

As the comparison between the static and the dynamic study has been conducted in a successful way, it is now time to investigate possible new features that could be evidenced only through a high speed study.

Selected temperature regions of interest are determined by their importance for the material. In our case, a more detailed study can be performed on the region nearing the glass transition (T_g) temperature, thanks to the 0.1 s acquisition speed. For this reason we will now consider a portion of spectral acquisition to be able to explain the mechanisms and structural changes taking place during the transition to glass. This set of data is presented in figure 5.22.

From this measurement it is evident that the structural evolution of silica must present some changes in this region due to the discontinous reflectivity spectral

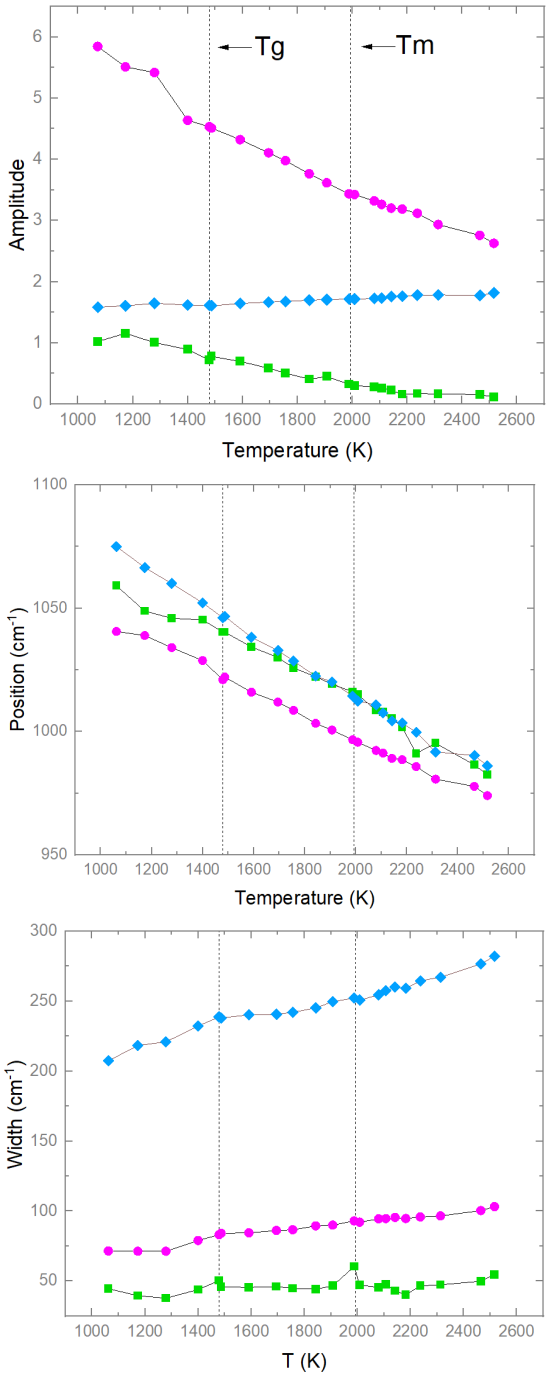

Figure 5.20: Temperature dependence of the amplitudes, positions and widths of stretching components P_1 (pink), P_2 (green) and P_3 (blue). The results are in agreement with the static ones (previously reported and shown in figure 5.16).

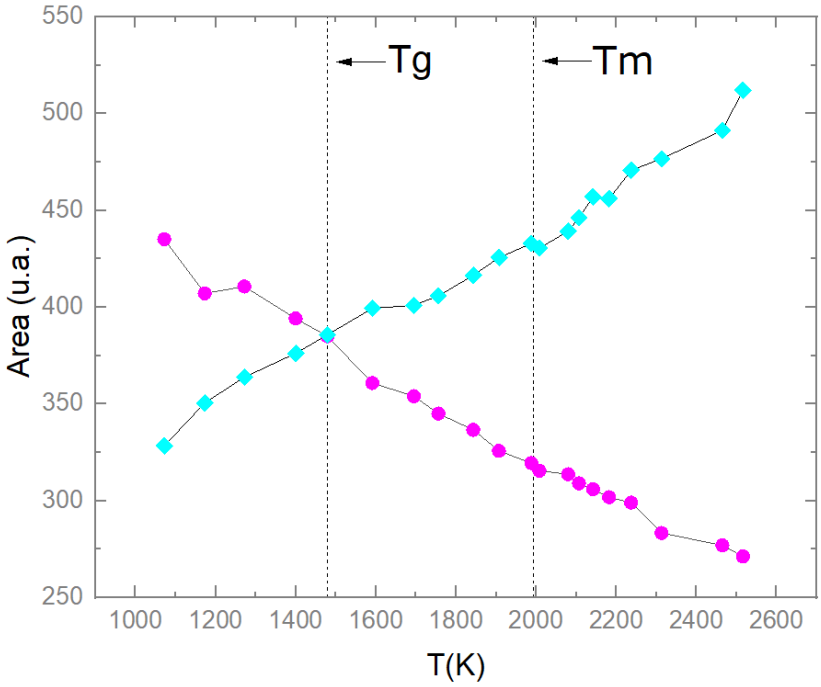

Figure 5.21: Temperature dependence of the area of modes P_1 (pink) and P_3 (cyan) in dynamic conditions. Yet again, the crossing at T_g is observed, as seen in static conditions (figure 5.17).

growth. As seen previously, the evolution in temperature is characterized by a continous increase in reflectivity, yet it seems that this region does not provide the same result.

Figure 5.23 illustrates a comparison between static and kinetic area calculations of the two main modes P_1 and P_3. The areas calculated were retrieved from spectral fitting, following the same model used up to now. A plateau region in the area evolution of the P_3 mode is evidenced from 1518 K to 1470 K where Tg=1480 K. As seen in the graph, this feature was already observed in static heating condition yet the fast spectra acquisition through Rapid Scan seems to confirm the assumption and provide a better defined region in which the phenomenon takes place.

Even though this feature is anomalous, a similar version of this phenomenon has already been observed in the P_3 component of quartz just above the phase transition alpha to beta at 843 K.[183]

To summarize their result and explanation, a plateau region in the evolution of P_3 is observed just above the alpha to beta transition until 1300 K as the

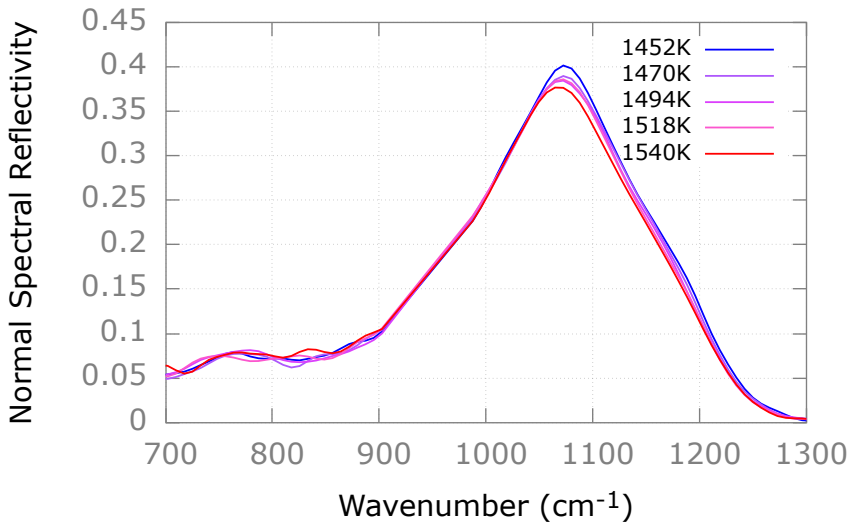

Figure 5.22: Dynamic data acquired near T_g. The retrieved spectra report different temperatures even though those nearing T_g at 1518 K, 1494 K and 1470 K (shades of violet) are almost indistiguishable.

beta phase is less prone to develop more dynamical disorder due to its better configurational stability inside this temperature range. P_3 gets reactivated above 1300 K due to the increase of thermal energy and the emergence of an ill defined state that promotes the number of degrees of freedom of the network and progressively enhances the amount of oxygen atoms impacted by dynamic disorder.

In our case, the plateau in P_3 area is observed just above Tg and even though its appearance is not due to the same exact process, some similar conclusions can be drawn. As illustrated previously, the viscosity of silica above Tg lowers drastically upon heating meaning that Si-O bonds start to breakdown and the degrees of freedom are not limited anymore by the structural configuration of the glass network. This phenomenon is illustrated through the increase of dynamical disorder corresponding to the P_3 band well above Tg after the plateau. Below Tg, Si-O bond breaking is not possible so the degrees of freedom of the silica network are imposed by the glass structure produced during the cooling phase. The temperature dependence of the dynamic disorder is imposed by the available degrees of freedom and thermal energy. At low temperatures, there is less thermal energy and consequently lower dynamical disorder due to the progressive saturation of the degrees of freedom. This is preserved until bond breaking cause the increase of dynamic disorder and the appearance of

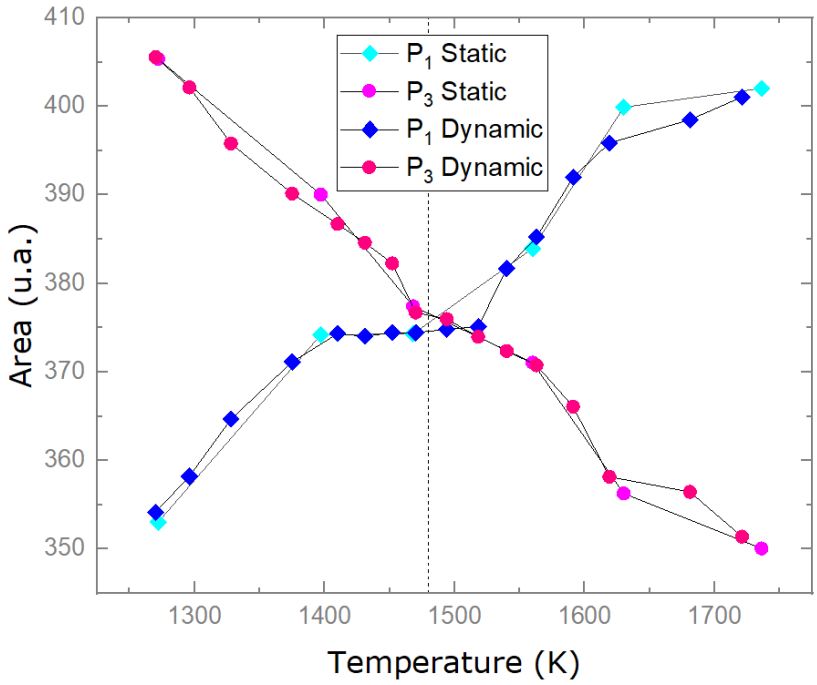

Figure 5.23: Area comparison of data acquired near T_g in both conditions for P_1 and P_3. The kinetic conditions allowed a faster acquisition and thus the retrieval of more spectra nearing T_g. The areas of the bands retrieved from the spectra illustrated in figure 5.22 are also illustrated and it is seen that the three spectra represented in violet shades present nearing areas for the two bands.

new degrees of freedom.

Inside the temperature range corresponding to the plateau, there is enough thermal energy to activate all the available degrees of freedom (allowed by the fixed configuration of the silicate network). A saturation regime of the dynamic disorder is achieved and thus the area of P_3 is constant in this region due to the percentage of Si-O bond breaking being very limited in this temperature range so the increase of the number of degrees of freedom in this temperature range is not enough important to impact significantly the dynamic disorder close to Tg.

The huge evolution of the viscosity above Tg is compatible with the fast change of dynamic disorder after the plateau since the number of supplementary degrees of freedom (due to bond breaking) quickly becomes of the same order of that already available in the glass state.

In other words, the glass transition phenomenon seems to be closely linked to the dynamic disorder and it is visible through a temperature region in which

the number of degrees of freedom of the network are not enough even though there is enough thermal energy for their activation. This description suggests the existence of a metastable state in which the network is still evolving from a state to another yet it can not fully transform in the glass structure due to the presence of additional degrees of freedom. The disappearance of these additional degrees of freedom can be seen here experimentally through the increase of the P_1 component, representing the tetrahedral structures, such that additional Si-O bonds have been recreated from their breakdown in the high temperature region.

Accordingly, another explanation of the observed phenomenon could be related to transient thermal effects since a similar plateau at the glass transition temperature of 1480 K has been observed through drop calorimetry experiments on SiO_2.[184]

6

Al_2O_3

Contents

6.1 The rise of a new structure

In the previous example dealing with the vitrification of SiO_2 we observed that the tetrahedral SiO_4 environment in the molten state is preserved to give rise to the silica glass network. In this chapter we show instead the crystallization of Al_2O_3 to illustrate the observation of the change of local structure and coordination number from liquid to solid.

Indeed, the cooling phenomenon leads to the creation of the stable $\alpha - Al_2O_3$ phase which exhibits a crystalline structure built of octahedral units which can be face-, edge- and corner-sharing. In contrast, the structure of molten Al_2O_3 is mainly four-coordinated.[185] Structural modifications are evidenced through the reorganization of matter from a disordered undercooled liquid state to an ordered crystal lattice.

This chapter will present the informations recollected to identify the phenomenon and the evidence obtained through IR studies dealing with the formation of $\alpha - Al_2O_3$.

The main questions we will try to solve are how and when the system reaches the solid stable phase and whether a metastable phase has been formed meanwhile. In order to do so, our experimental setting will be used in extreme temperature conditions and at its maximum speed. Various runs are needed to try and obtain a big amount of data to be able to extract the maximum amount of information on this compound.

Al_2O_3 will also force us to change our experimental approach by changing the initial conditions of the acquisition. This aspect is important to evidence the versatility of the Rapid Scan technique and the various possibilities offered. As discussed previously, the laser power allows to control the temperature of the initial liquid.

The crystallization signature will be evidenced through the time-temperature graph where the exothermic nature of the process is clearly shown as a temperature increase in the undercooling region. Room temperature data is also acquired to allow a comparison between alumina polymorphs and to identify the main peaks contributing to the formation of $\alpha - Al_2O_3$. These measurements are important to assign the observed bands to structural motifs.

Finally, features that could demonstrate the presence of metastable γ-Al_2O_3 during cooling are evidenced and reported only thanks to the fast kinetic acquisition condition.

6.2 Polymorphism of Al_2O_3, liquid structure and state of art

Aluminium oxide (Al_2O_3) can exist in a variety of polymorphs, aside from the thermodynamically stable form of corundum (α-Al_2O_3).[186]

The historical importance of this material, being used as a standard for pyrometers' calibration[187–191], as well as its many industrial applications in its solid as cements, ceramics, abrasives, and high-temperature crucibles[186] as well as in its molten form for the production of sapphire crystals[192–196] or to analyze the behaviour of rocket motor effluents,[197–199] highlights the need to investigate the phase forming mechanisms in order to promote stable scale formation. This can be reached when the transformation mechanisms and the conditions which lead to the formation of a peculiar metastable polymorphic struture are well known.[186]

Aside from the stable α phase (corundum), several polymorphs can be obtained from different precursors, as shown in figure 6.1. If we consider boehmite (aluminium oxide hydroxide $\gamma - AlO(OH)$) as an example, we can see that a deshydroxilation mechanism causes the formation of $\gamma - Al_2O_3$ at 450 °C, then $\delta - Al_2O_3$ at 750 °C and finally $\theta - Al_2O_3$ at 1000 °C. All of these metastable phases transform ultimately into $\alpha - Al_2O_3$ above 1200 °C. The same transition sequence has been theorized for the solidification from molten state, at different temperatures.[186] The differences between polymorphs is evidenced by their structure, as seen in figure 6.2, as well as their differences in CN of their structural motifs. $\alpha - Al_2O_3$ is composed only of AlO_6 units, however the metastable phases present a mixture of AlO_6 and AlO_4 in different proportions.

Skinner et al.[185] investigated the structure of liquid Al_2O_3 by means of neutron and X-ray diffraction data using the reverse Monte Carlo method starting from a molecular dynamics model. Their study pictures the alumina melt as composed primarily of AlO_4 and AlO_5 structural units and the majority of Al-O-Al connections are corner-sharing, consistent also with NMR data[202–205] and the observed density decrease,[206,207] explained by a breakdown of the AlO_6 units observed in solid corundum. In that process, the microstructure of Al_2O_3 undergoes a process of reorganization following a structural pattern during the state change, as the oxygen linkages rearrange to form a new network.

Molecular dynamics simulations have shown that alumina might present a first-order phase transition in the liquid[208] even though a continous change in structure is observed with increasing pressure.[209–212] It has been reported

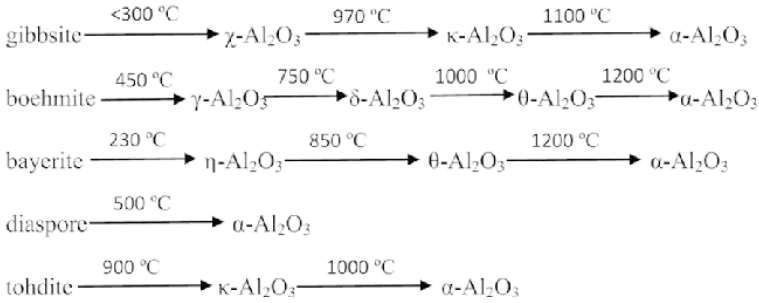

Figure 6.1: Phase trasformation of alumina starting from different precursors.[200]

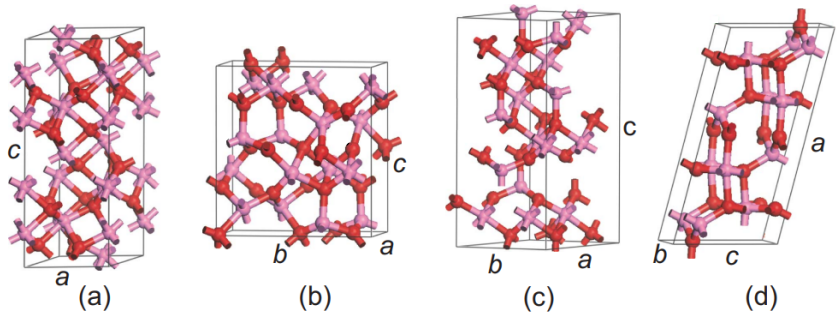

Figure 6.2: Polymorphism of Al_2O_3. (a) $\alpha - Al_2O_3$ (hexagonal), (b) $\kappa - Al_2O_3$ (orthorhombic), (c) $\gamma - Al_2O_3$ (triclinic), (d) $\theta - Al_2O_3$ (monoclinic).[201]

by Levin et al.[186] that the passage from molten alumina to α-alumina should include the formation of metastable γ then δ or θ before solidification. This hypothesis is supported by quenching experiments because very high cooling rates ($>10^5$ K s^{-1}) from the melt results in phases containing tetrahedrally coordinated aluminum. Experimental work has confirmed the tetrahedral coordination of liquid aluminum oxide using X-ray,[213−214] neutron diffraction[215] and high temperature NMR.[?−?] Nonetheless, different studies propose different values for the relative proportions of AlO_x polyhedral units in the liquid.[208−212,216−218]

The crystallization of alumina in free-cooling conditions has already been observed through time-resolved ^{27}Al NMR by Florian et al.[56] They observed a cohexistence of the liquid with the growing crystal, bound to start nucleation of the α phase. It is thus expected to observe a CN change during solidification and it probably should occur in the undercooling region, where nucleation of the AlO_6 units would take place. It should also be mentioned that a transition from α to γ-like tetrahedral structure before melting, when heating from room temperature, has been evidenced by Brun et al.[219] through IR emission measurements.

	peaks in $S(Q)$			peaks in $G(r)$		coordination number
T (K)	Q_1 (Å^{-1})	Q_2 (Å^{-1})	Q_3 (Å^{-1})	r_1 (Å)	r_2 (Å)	CN (±0.5)
X-ray Results: Liquid Al_2O_3 in Argon						
2126	2.10	4.47	7.71	1.80	3.16	4.46
2312	2.11	4.45	7.73	1.80	3.14	4.53
2415	2.10	4.44	7.74	1.80	3.16	4.31
2415	2.10	4.44	7.74	1.80	3.16	4.30
2499	2.10	4.47	7.74	1.80	3.12	4.38
X-ray Results: Liquid Al_2O_3 in Oxygen						
2002	2.09	4.54		1.80	3.12	4.48
2571	2.09	4.50		1.80	3.14	4.55
MD Results						
2350	2.00	4.57	8.00	1.75	3.14	4.23

Figure 6.3: Structural results on liquid aluminum oxide evidencing the obtained CN through different techniques.[215]

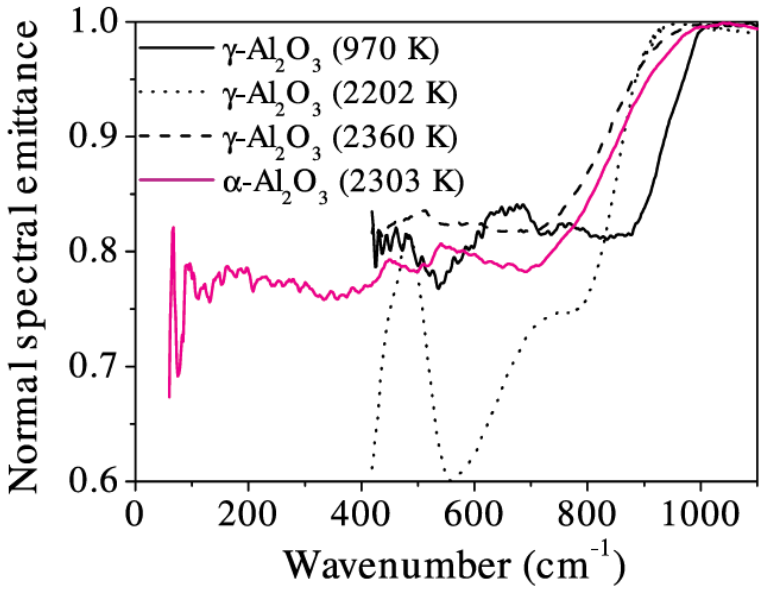

Figure 6.4: Normal spectral emittance of a single crystal of α-Al_2O_3 compared to the normal spectral emittance of a plasma sprayed pellet of γ-alumina.[219]

6.3 A fast dynamic study into the formation of $\alpha - Al_2O_3$

The solidification of Al_2O_3 has been observed from a temperature of 2380 K in free-cooling conditions. The starting temperature is in the liquid since the melting point of alumina is reported to be 2327 K.[220]

The a) and b) part of figure 6.5 present the reflectivity data, while c) shows the temperature vs time of the previous data, with each point corresponding to the temperature extracted from each spectrum. d) presents a selection of spectra amongst the ones acquired. The temperature vs time curve show a recalescence phenomenon characteristic of crystallization with an exothermic signature. This is defined as the undercooled liquid region. With the configuration discussed in section 2, the data acquisition speed (20 spectra/s) is enough to capture the entirety of the cooling process as well as the undercooling zone. The choice of showing a selection in the data set was made to highlight the undercooling region in d) (maximum time 1 s, up to 20 spectra acquired) and show the transformation from liquid to solid, corresponding to the zoomed in part that can be seen in the inset of c).

The undercooling region actually represents the most important part of our acquisition because it represents a transient state of matter preceding the solidification. For this reason, the spectra presented correspond to a small part of the total acquisition yet the most important since it illustrates a fast and metastable phenomenon. It is expected that the coordination change would occur during this small timeframe as this region appears below the fusion temperature of alumina.

Nonetheless, it can be noticed that the crystallization temperature retrieved from our measurement clearly does not correspond to the melting temperature, as it was evidenced through aerodynamic levitation studies on crystallization. This effect is clearly explained by the way our measurements are performed. The pool of molten material created in the middle of the sample is microstructurally interconnected and, even though the information on temperature and the spectra is only acquired in a small spot, the effect of thermal conductivity from neighbouring regions could have caused this result. Due to a too low volume of liquid in the molten bath, the release of energy occurring during the crystallization step is not significant enough to counterbalance the radiative and conductive heat losses for a time interval greater than the time required to achieve a well-defined solidification plateau at the melting temperature of alumina. In any case, this does not represent an obstacle to our certainty and reliability of our measurements since this effect is real and not observed through

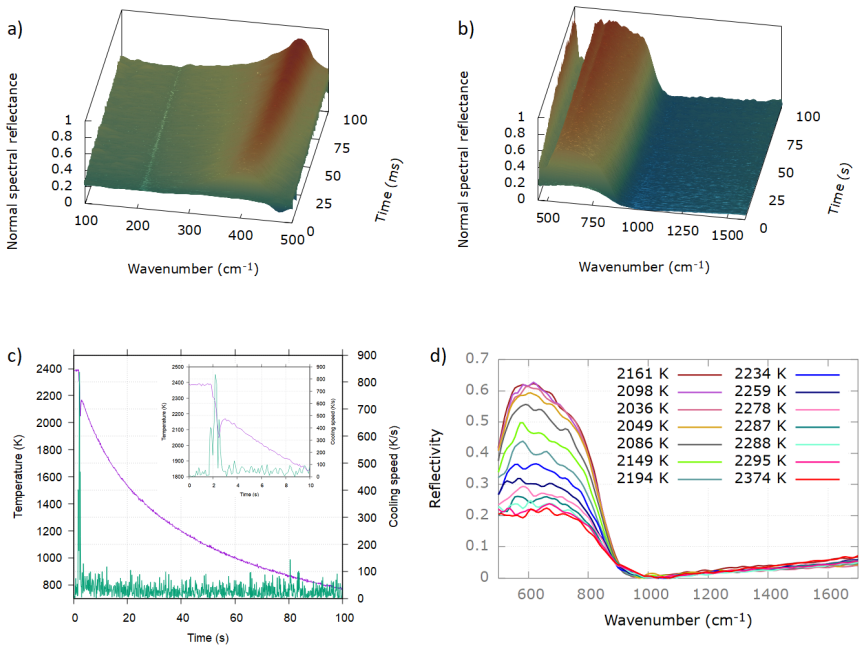

Figure 6.5: Crystallization of Al_2O_3. a) Rapid Scan measurement during free-cooling in FIR, b) Rapid Scan measurement during free-cooling in MIR, c) Cooling speed and inset of undercooling region, d) Selection of reflectivity spectra in the undercooling region.

levitation only due to the complete isolation of the sample and a comparatively higher volume of liquid since the entire sample is liquid. Moreover, this effect has already been observed and it has been linked to the depth of the molten pool[221] which in our case is probably not enough to obtain a well defined plateau at the crystallization temperature.

The data has been acquired in the middle infrared (MIR) and the far infrared (FIR) regions because both contain all the signatures of vibrational motions in Al_2O_3 and thus this is the spectral region of interest to study structural modifications from solid to liquid. Full spectra combining the data acquired by the two detectors are presented in figure 6.6. The importance of a full acquisition is due to the necessity of a complete spectra for fitting since all the bending motions of Al_2O_3 are in the FIR region.

From the measurements we observe that the solidifcation process can be divided into 4 regions due to differences in their evolution, evidenced in figure 6.7 and visible through the obtained spectra illustrated in figure 6.8:

1. Liquid: this disordered state is mainly formed of tetrahedral AlO_4 and

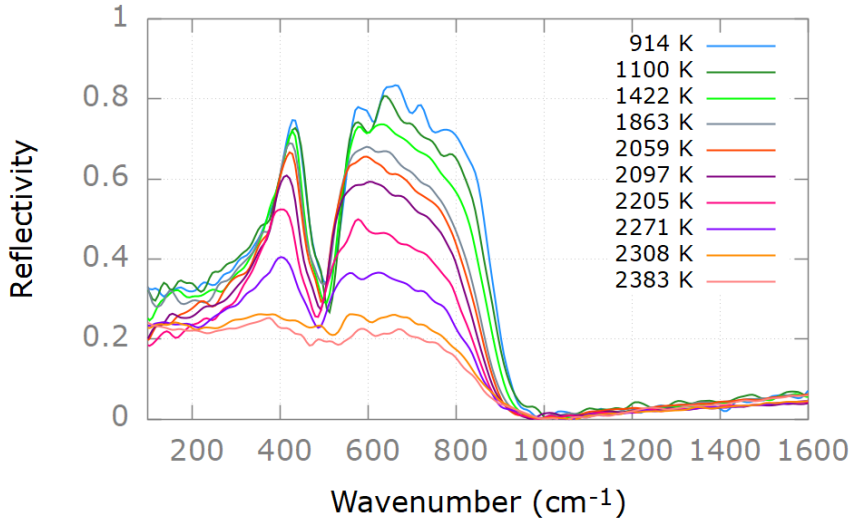

Figure 6.6: Full spectra acquired with DLaTGS detector in MIR and Bolometer in FIR selected from the runs displayed in figure 6.5

AlO_5 structures

2. First region: start of the cooling process (after laser shutdown) and undercooled liquid before the exothermic reaction.

3. Second region: increase of temperature indicating that crystallisation is in progress

4. Solid: ordered crystalline state composed of octahedral AlO_6 units

The choice of this repartition is due to the appearance of an additional peak during the exothermic reaction and illustrated in figure 6.8.

The spectra acquired in these regions have been averaged to obtain a better signal-to-noise ratio and allow the study of the dynamics of structural changes and they are illustrated in figure 6.8. Even though spectra averaging causes a loss of kinetic information in time, in this case it is important to perform it to obtain more reliable data and to focus only on the main features that are common to all the spectra acquired in a specific region.

This procedure also allows to obtain average spectra that are more defined and clearer to interpret, taking into account that an advantage of FT-IR is that the areas of the peaks in a spectrum are proportional to concentration so lower noise level allows to determine more accurately these quantities.[222]

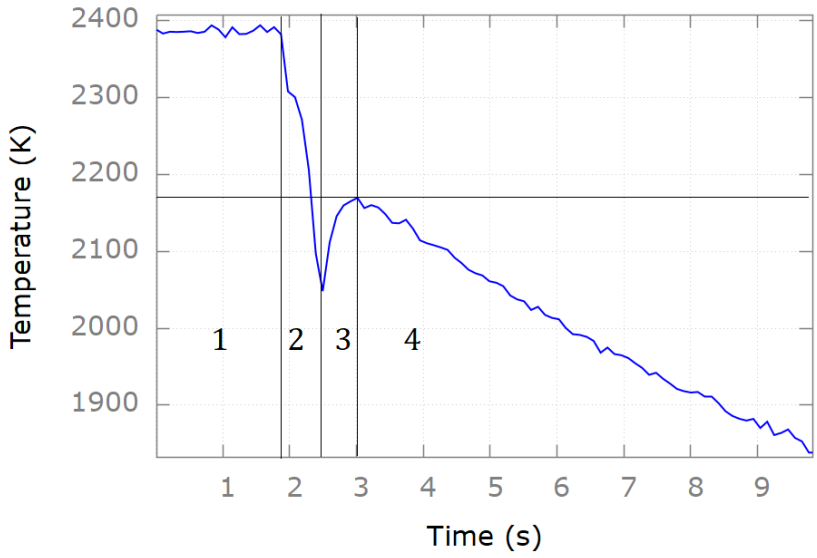

Figure 6.7: Structural modification Regions: 1. Liquid, 2. First Region, 3. Second Region, 4. Solid. This classification of Regions has been adopted to observe spectra evolution with important changes in Regions 2 and 3 while the variations in 1 and 4 are small. The crystallization temperature retrieved here is evidenced to illustrate that the undercooled liquid has been split in two Regions.

Another possibility would have been to use a slower scanner velocity, but at the price of a higher spectral distortion of the resulting composite spectra and no fine control on the probe of the structural modification regions.

Due to the absence of other sources of kinetic IR data illustrating the crystallization of $\alpha - Al_2O_3$, it is important to recall information obtained through previous studies focusing on the formation of Al_2O_3.

There are different precursors that result in the ultimate formation of $\alpha - Al_2O_3$.[223] Most of these processing routes involve thermal treatment of the precursor resulting in the formation of metastable alumina phases that resemble the lattice found in their precursor.[224]

Pecharromán et al.[224] studied the thermal evolution of transitional aluminas through infrared spectroscopy. In their work, they obtain reflectance spectra of aluminas through the thermal decomposition of bayerite and they evidence the formation of the α phase through the appearance of a mode located at 637 cm^{-1}. This is noticeably a resolved mode of $\alpha - Al_2O_3$ that becomes predominant in the structure after thermal treatment.

Another fact to consider is the starting structure from which the α phase

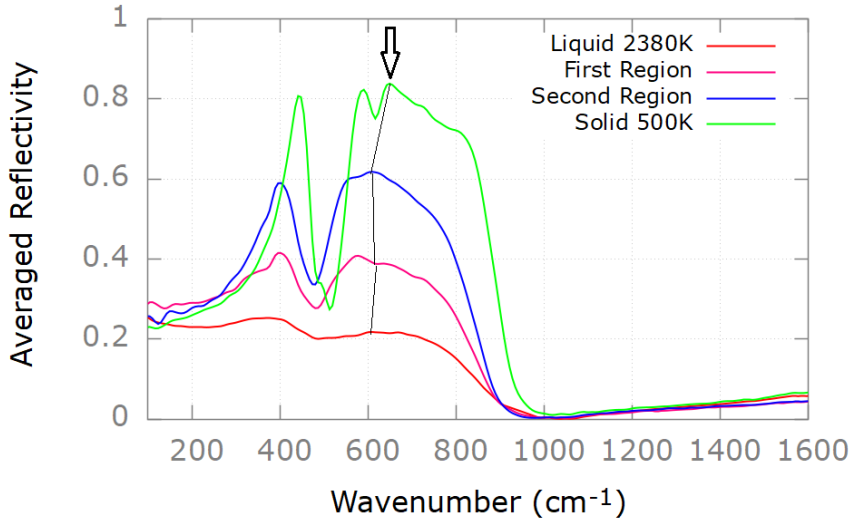

Figure 6.8: Main structural modification regions evinced from the study. The spectra displayed have been averaged to minimize signal-to-noise ratio. The appareance of an additional mode in the Second Region that stays present in the solid is evidenced and displayed through an arrow and lines that represent where the mode should have been found in the previous regions taken into account the shift caused by temperature.

originates. This is due to the fact that the mechanisms that allow the formation of the stable phase might be different if the original structure is not the same. In this case, they assume a spinel structure due to the formation of the γ phase.

Parallelism between our work and the aforementioned study can be found if we consider that Brun et al.[219] proved the appearance of γ-like tetrahedral structure just before melting the sample.

If we consider the passage between the First and the Second Region (illusrated in figure 6.7 as 2 and 3), it is noticeable that the peaks which dominate the latter are the ones encountered in the region 550-650 cm^{-1}. Taken into account the temperature shift of these peaks, as well as their obvious presence in the solid spectrum, we can assume that they should represent octahedral sites or, more generally, vibrations involving octahedral units.

From this, it is possible to propose these two peaks located at 575 cm^{-1} and 610 cm^{-1} in the Second Region (also observed in the solid α phase, red shifted) as the initiators of the network reorganization. We will refer to these peaks as $A_{\alpha 1}$ and $A_{\alpha 2}$.

If now we go further and consider the temperature shift, we can assume that the resolved α peak observed by Pecharromán et al.[224] corresponds to $A_{\alpha 2}$. As seen in figure 6.6, the peak starts to be visible right after the start of the cooling process but dominates the structure only at the end of the transient state.

For the previously illustrated reasons, the dynamics of $A_{\alpha 1}$ and $A_{\alpha 2}$ will be more closely observed to gain insight into the formation of $\alpha - Al_2O_3$.

We will rediscuss this observations after reiteration of the cooling measurement with different parameters.

6.3.1 An even faster dynamic study

Al_2O_3 is a fast changing material due to its liquid fragility and for this reason, we implemented the MCT-Wide detector to improve the temporal resolution and obtain more scans due to the higher sensitivity of the instrument.

Dynamic data has been acquired during solidification each 0.04 s, allowing the acquisition of 50 scans/s. This has been possible thanks to the higher sensitivity (10 times higher) of the detector which allowed to reach a mirror speed of 320 kHz (maximum speed achievable with the Rapid Scan option). The resolution value has been left at 16 cm^{-1}, as discussed in Chapter 3.

The following presented data focus on the evolution and appearance of $A_{\alpha 1}$ and $A_{\alpha 2}$ as their dominance in the spectra can signify the creation of the stable phase, as hypothesized previously. The displayed runs were thus performed at a mirror speed of 320 kHz and a starting temperature of 2340 K (13 K above the melting point).

As it can be seen from the data reported in figure 6.9, the two experiments are basically equivalent. The width of the undercooling region is almost equal (1.5 s for Run 1 ans 1.6 s for Run 2) due to the similarity of the cooling conditions. This statement is of fundamental importance if we consider that the cooling is totally and solely determined by the starting temperature, independently from the time that the sample spends in liquid conditions, which is almost double in Run 2. Moreover, Run 2 has been performed right after the cooling observed in Run 1, demonstrating the possibility of the technique to be iterated and allowing to easily verify the reproducibility of the result.

Figure 6.10 illustrates the spectra acquired in the undercooling regions of both runs. This choice has been made due to the importance of this region for the observation of the creation of the α phase, as discussed previously.

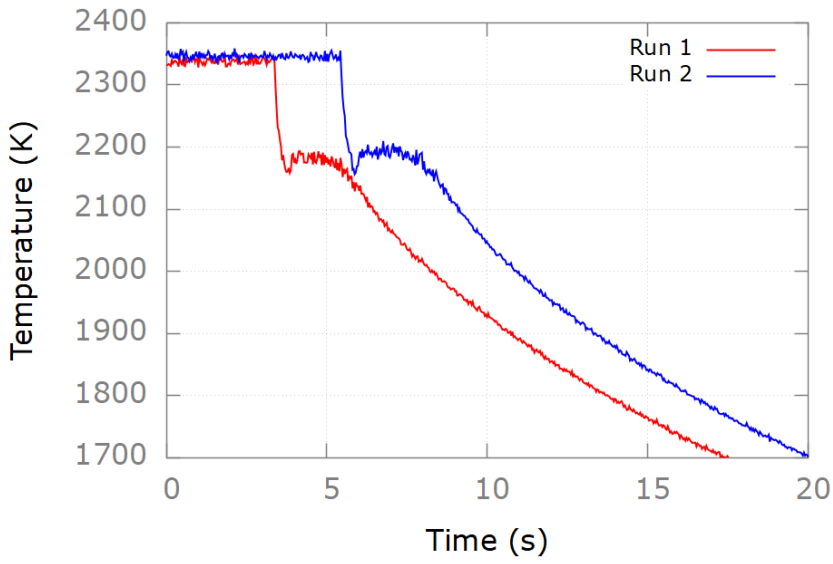

Figure 6.9: Time-temperature curves for Run 1 and 2 with an acquisition speed of 0.04s using LN-Wide MCT detector.

As seen in the figures, the dominance of $A_{\alpha 2}$ is clear just in the last spectra but its appearance is more difficult to predict. Due to the dynamic nature of this peak, it seems like there could be spectral transfer between it and its neighbour $A_{\alpha 1}$.

From these measurements, it seems clear that these peaks are present in the liquid form as well and their redistribution is only due to the cooling phenomenon. This means that the signature of the structural motifs could be present in the liquid as well, and the kinetic organization of matter dependent on temperature will only be caused by the prevalence of one structure on another.

In these cases, at a temperature of almost 2160 K, $A_{\alpha 2}$ has definitively established its presence in the network, leading to the formation of the stable phase.

6.4 Band assignment and discussion, γ-like structure

In order to understand the mechanisms that cause the formation of the octahedrally coordinated α-alumina, it is time to discuss the band assignment.

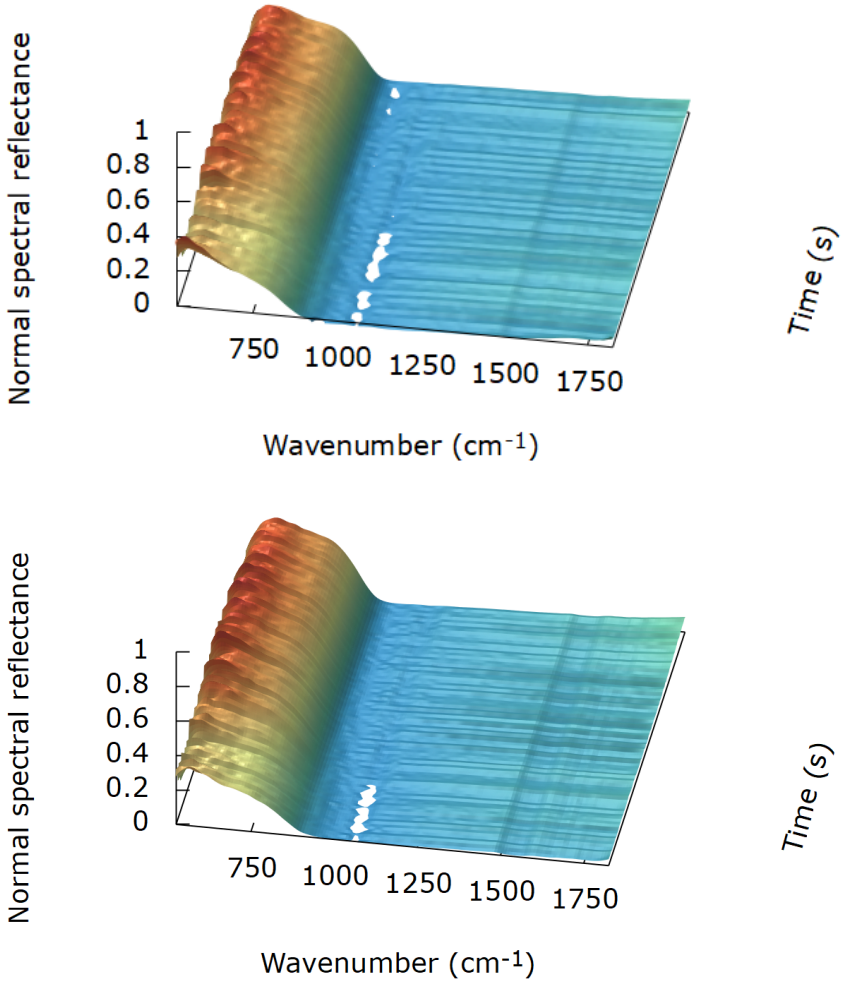

Figure 6.10: Undercooling regions observed during the cooling of alumina from molten state, modes $A_{\alpha 1}$ and $A_{\alpha 2}$ seem to be linked together by some exchanging mechanisms.

This way, it would be possible to understand the role of $A_{\alpha 1}$ and $A_{\alpha 2}$ and the structural information they hold. The mechanisms leading to the change in coordination number would then be explained consecutively.

To discuss this, room temperature reflectivity spectra of α-alumina and γ-alumina have been acquired and shown in figure 6.11. Ab-initio numerical calculations can also be used to help mode assignment of experimental data.[225]

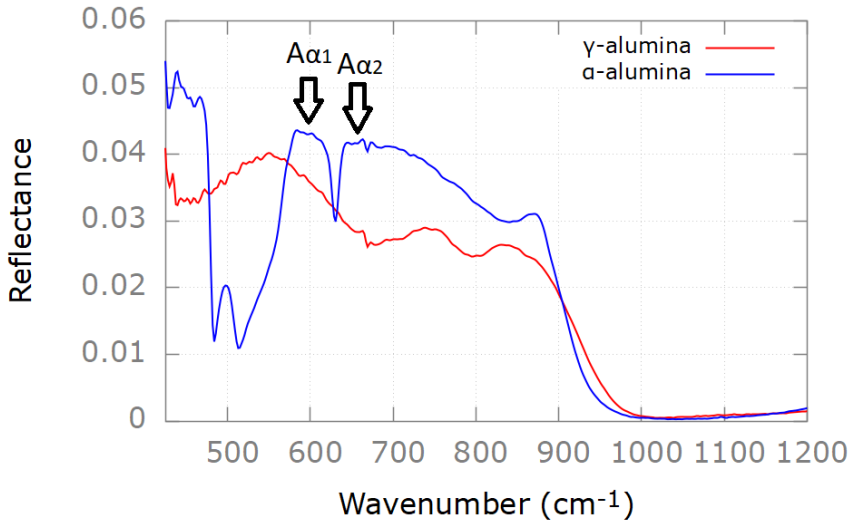

Figure 6.11: Room temperature reflectance spectra of compressed powders of α- and γ-alumina.

Taking into account the temperature shifts of $A_{\alpha 1}$ and $A_{\alpha 2}$ and since the number of peaks in the undercooling region coincides with the number of peaks of room temperature α-alumina, they have to be correlated to octahedral structures.

$A_{\alpha 2}$ is the fastest growing peak from molten state and due to this, it seems reasonable to assign it to a mixed contribution of stretching motions of all coordinance Al and O atoms.

$A_{\alpha 1}$ is then automatically assigned to the stretching motions of AlO_6. In this case, the two modes could be automatically paired since the octahedral network is formed among the other coordinances, so it is expected to find the decrease of the AlO_4 mode.

AlO_4 stretching is mainly encountered[226] nearing 750 cm^{-1} and it is shown clearly in the spectrum of γ-alumina. It can be observed that this peak is also visible in the First region, and it is almost undetectable in the Second region (taking into consideration the temperature shift to lower frequencies).

This mechanism of spectral weight transfer could be used to explain the change of coordination number in alumina: as the AlO_6 units begin to nucleate, the number of AlO_4 is automatically reduced.

Spectral fitting through a dielectric function model can help shed light on the identification of these bands and the structural motifs they represent.

Liquid alumina should be composed mainly by 4-fold coordinated structures, with a smaller presence of other coordinations. The wide bands encountered in this state (Liquid Region (1 in figure 6.7)) originate from the presence of a wide distribution of bond angles and lengths in the liquid leading to a strong spectral broadening making their resolution more complicated. Four broad bands are evidenced from fitting, as illustrated in figure 6.12. Among these, 3 bands (G2, G3 and G4) are illustrated in the 250-1200 cm^{-1} range, corresponding to $(AlO_4)^-$. G1, instead, is observed in a range that has been frequently assigned to vibrational motions of cations involved as network modifiers or charge compensators.[176,227] In our case, we can suppose that Al^{3+} cations are created in the liquid to charge compensate for the negatively charged $(AlO_4)^-$ units forming a network of corner-sharing tetrahedra.

If we consider $Al_2O_3 \rightarrow 1{,}5(AlO_2)+0{,}5Al$ and then assume the negatively charged 4-fold coordination Al: $Al_2O_3 \rightarrow 1{,}5(AlO_4)^- + 0{,}5Al^{3+}$. This distribution is also found through area comparison and thus confirmed. Figure 6.13 illustrates some additional examples that display this phenomenon.

In this framework, the liquid could be interpreted as a corner-sharing tetrahedral network in which the long Al-O distances cause higher CN sites, which are not due to higher coordination AlO_x species that would require the presence of oxygen triclusters, but rather occupied by the Al^{3+} cations.

As the cooling starts, some new structures start to arise from the disordered liquid state: this can be seen from the higher number of bands needed to fit the next spectra. These new bands show the signature of the formation of solid crystalline structures from the liquid because they appear narrower and smaller.

Figure 6.14 illustrates the imaginary dielectric function obtained from the fit of the First Region spectrum (2 in figure 6.7). In this case, we can consider the three bands at 514, 540 and 623 cm^{-1} as the main contributions to the stretching motions that originate from the liquid. It is safe to assume that the band at 540 cm^{-1}, due to its importance, could represent stretching motions

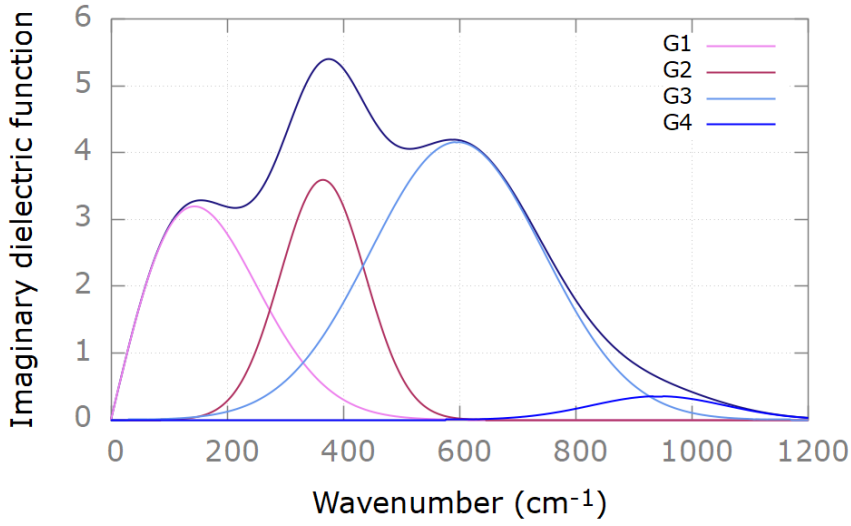

Figure 6.12: Imaginary dielectric function of liquid alumina spectrum shown in figure 6.8. All of the bands belong to the liquid and it is clearly seen by their broadening due to wide distribution of structural motifs, bond lengths and angles.

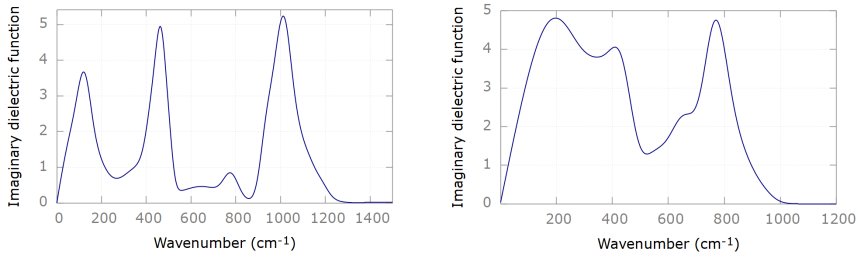

Figure 6.13: Imaginary dielectric function of glasses with compositions 29%BaO-71%SiO_2 (Left) and 60%CaO-40%Al_2O_3 (Right). In the spectrum on the left the feature at 100 cm^{-1} is assigned to Ba^{2+} cations vibrational motions, 500 cm^{-1} contains the bending motions of SiO_4 and the stretching at 1000 cm^{-1}. On the right we observe Ca^{2+} cation vibrational motions at 200 cm^{-1}, bending and stretching motions of $(AlO_4)^-$ at 400 and 800 cm^{-1}. These examples are illustrated to allow a comparison with our observations in the liquid structure of Al_2O_3.

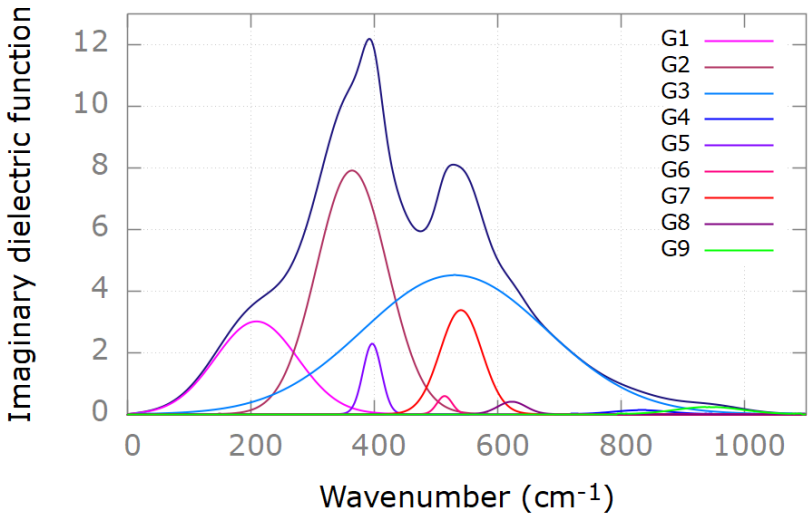

Figure 6.14: Imaginary dielectric function of the First Region spectrum shown in figure 6.8. The appearance of solid-like (smaller, narrower) bands is evidenced.

of all coordinances (mainly 4-folds at this stage). The band at 623 cm^{-1} has been assigned to stretching motions of AlO_4 as it is completely vanished in the Second Region and afterwards due to the formation of α-Al_2O_3. Nonetheless, the presence of these 3 new bands and their positioning in the spectra can suggest a defect spinel structure, such as the IR spectra simulated to depict the γ-phase.[228]

Figure 6.15 illustrates the fit of the Second Region (3 in figure 6.7) and only the bands corresponding to the octahedral units are present as we have now formed α-Al_2O_3. The band at 514 cm^{-1} seen in the First Region has been assigned to the stretching motions of AlO_6 as it is still present in the Second Region, shifted at 519 cm^{-1}. Stretching motions of all coordinations are still present, represented by the band now located at 523 cm^{-1}. More importantly, the nature of its shift suggests that AlO_4 units must have disappeared from the network such that this band now only represents octahedrally linked Als. This can also be proved by the total area of the peak assuming the same IR activity for the two structures.

As for the first point, subtracting the area of the AlO_4 peak to this peak encountered in the First Region gives exactly the area of the peak in Second Region, as AlO_4 units have disappeared.

Lastly, the shift observed is towards lower wavenumbers which is not correct if we

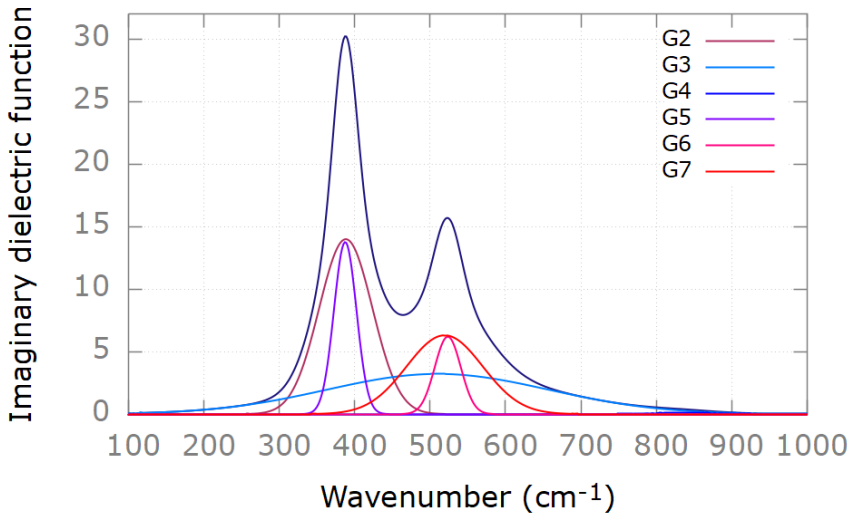

Figure 6.15: Imaginary dielectric function of the Second Region spectrum shown in figure 6.8. The bands obtained in the liquid have either disappeared or have started to shrink and become less impactful. The solid G8 band has disappeared.

only consider the shift due to temperature. Nonetheless, if we consider this peak as a mean between the region of AlO_4 and AlO_6, the shift is easily explained by the loss of AlO_4 that are generally encountered at higher wavenumbers.

The shift observed is mainly due to the absence of the 4-fold coordinated and for this reason, its shift would be abnormal if only the temperature condition is considered. Yet, these considerations may not be entirely true due to the different IR activity and ionicity of the bonds belonging to the two species. It is possible to retrieve the ratio of the IR activity for these two bands by considering two spectra that present both bands and by comparing their areas.

To further confirm these assumptions and retrieve the IR activity of the species, a spectrum belonging to the region lying between the First and the Second Region has been fitted. This spectrum is at a temperature of 2086 K. What is obtained is that the tetrahedral structures have a 61% of activity if compared to a detection of a 100% of octahedral structures. So, in our case, the detection of AlO_4 units is more complicated, yet, the Al-O-Al bonds increase in number and probably contained also these structures.

In this case, what is observed is a different proportion of tetrahedral and octahedral units and a predominance of octahedrals. This is due to the fact that in the First Region the percentage of AlO_4 and AlO_6 are almost equal

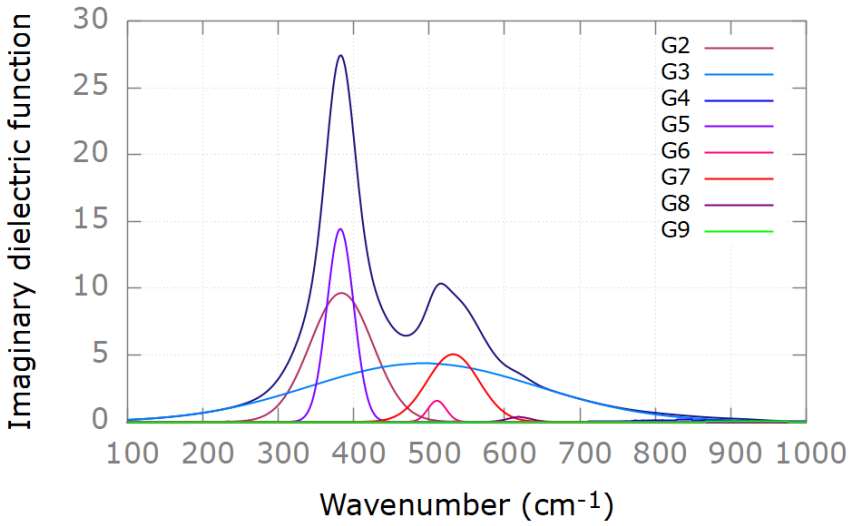

Figure 6.16: Imaginary dielectric function of a spectrum lying between the First and the Second Region (Intermediate Region T=2086 K). The interpretation of solid and liquid bands is reinforced by this fit that illustrates an intermediate situation between the two regions.

Mode	Assignment
G_1	Al^{3+} Cation Vibrational Motions (Liquid)
G_2	$(AlO_4)^-$ Bending (Liquid)
G_3	$(AlO_4)^-$ Stretching (Liquid)
G_4	Additional Mode (Liquid)
G_5 $(A_{\alpha 1})$	Bending Motion (Solid)
G_6 $(A_{\alpha 2})$	AlO_6 Stretching (Solid)
G_7	Stretching Motion of AlO_x units x=4,5,6 (Solid)
G_8	AlO_4 Stretching (Solid)
G_9	Additional Mode (Solid)

Table 6.1: Qualitative assignments of the bands used in the analysis.

Region	CN_1	CN_2
First Region (Averaged)	4.82	4.58
Second Region (Averaged)	6	6
Intermediate Region (Single spectrum at T=2086 K)	5.54	5.34

Table 6.2: Coordination numbers in different regions assuming the same IR activity for the two structural units (CN_1) and assuming the retrieved IR activity (CN_2).

(56% and 43%) but there is still a majority of tetrahedral structures. The areas calculated for this fit allow us to estimate a 77% of AlO_6 and a 23% of AlO_4 which is coherent with the rest of the data. If we now consider the IR activity, these estimates show a larger number of AlO_4 that were probably less detected (assuming the retrieved IR activity: 68% of AlO_4 and 32% of AlO_6 in the First Region, 67% and 33% for the Intermediate Region). In any case, we can estimate the average CNs (shown in Table 6.2) and compare them with the table reported in figure 6.3. From this comparison we can see that the values obtained in the First Region are compatible with the other studies whilst the values obtained in the Intermediate Region are not compatible with the CN measurements at this temperature but it closely resembles the predicted CN of transitional aluminas.[229]

Nonetheless, our suppositions and species quantification seems to be supported again by the observation of the same type of shift observed previously in the Second Region. As the number of AlO_4 has decreased, we should yet again expect a shift of the peak corresponding to all coordinations. This assumption is yet again confirmed by its presence at 531 cm^{-1}. For these reasons, we assume our peak assignment to be fairly reliable.

The suppositions and the consecutive assignments are supported by molecular simulations in the liquid and by literature studies on Al_2O_3 and aluminate networks, as illustrated previously. Nonetheless, the proposed assignments are not definitive so the best conclusion for this discussion is that additional solid bands are detected in the undercooling region and they can be associated with the first nucleation centers causing the formation of α-alumina.

In order to allow a deeper knowledge of this phenomenon, the material could be considered as an effective medium composed of a liquid matrix and solid inclusions[230,231] and thus studied by applying this theory.

The question that still remains unsolved is whether there is an actual formation of metastable phases before formation of the α-phase from liquid. The structure before melting was already investigated by Brun et al.[219] by high temperature IR emission measurements in static heating conditions. The authors suggest a possible transition from the α phase to a γ-like structure before melting. They

propose a transition sequence of the form: $\gamma \rightarrow \alpha \rightarrow \gamma$ between 970 and 2200 K for the first transition and between 2200 K to the liquid for the second.

As seen previously, we observed a γ-like spinel structure in the First Region, a region that contains both the liquid and the solid due to spectra averaging before the undercooling region starts, and in the Intermediate spectrum. Moreover, the two-phase nature of this region has already been reported in heating and free-cooling conditions.[232,233] The transition sequence of formation of $\alpha - Al_2O_3$ from liquid has been reported in literature as:[186]

Melt$\rightarrow\gamma\rightarrow\delta,\theta\rightarrow\alpha$

In our case, we surely observe a spinel structure composed of 3 solid-like bands reminiscent of γ but the signature of δ and θ phases has not been reported. In order to determine whether these phase transition could have occured, it is important to understand the reason lying behind this theoretical proposition. The transformation from γ and δ is known to occur by ordering of tetrahedra.[223] The difference between these two phases lies in the degree of order of tetrahedral sites, more disordered than octahedral ones in γ[229] and totally ordered in δ.[234]

Nonetheless, there is no clear evidence of the formation of multiple metastable phases so it is rather risky to assume that. In addition, the NMR study on cooling from molten state by Florian et al.[56] evidenced only one discontinuity at the crystallization point. As we described phase transformations as the detection of discontinuous change in a property for first order transitions, and this type of transition has been predicted,[208] this result seem to exclude the formation of these two intermediate phases. Another possibility is that the technique is not able to properly draw a clear distinction between γ and δ or θ phases.

From the liquid, the process that has been observed nearing the crystallization point is an exchange between tetrahedral and octahedral units as the peak fluctuations encountered in the MCT measurements seem to point out a dynamic evolution of the network as well as the appearance of solid-like features that point out to a possible formation of a spinel γ structure in the undercooling region. These observations seem to be also confirmed by the retrieved CN in the Intermediate spectrum, a value that corresponds greatly to the one obtained for metastable aluminas.[229]

In conclusion, the study of the cooling of molten alumina allowed the retrieval of important information on the crystallization process and the mechanisms causing the coordination change from a 4-fold to a 6-fold coordinated structure. The process involved in coordination change seems to be linked to a fast and dynamic exchange between the structural motifs and the gradual appearance

and growth of the number of octahedral motifs due to nucleation. In addition, the presence of a γ-like structure in the undercooling region before the exothermic reaction has been also observed and the structure of the liquid is illustrated as a dynamic structure in which the negatively charged (AlO_4^-) are charge balanced by Al^{3+} cations possessing higher coordination, among a fraction of higher coordinated AlO_x.

7

$SrO - Al_2O_3 - SiO_2$

Contents

7.1 Creation of polymorphs through cooling rate control

The ternary system $SrO - Al_2O_3 - SiO_2$ has been studied for the variety of structural polymorphs that it presents. This chapter illustrates the results of controlled cooling operated on specific composition known to be able to heavily rely on the cooling rate to form specific phases.

The possibility of forcing a cooling path on the sample originates from the laser heating technique. In this case, instead of a complete shutdown of the laser power, a progressive decrease at different timesteps will be used. Time steps will be described through the concept of BPM (Beats Per Minute) to allow an equal time division. From this concept, it will be possible to extract the speed of cooling of the obtained cooling curves through its derivative. Another way to control and modify the cooling rate is through the initial temperature since it is greatly dependent on it.

The composition selected correspond to feldspars which present congruent melting and solidification, possess a wide variety of crystalline polymorphs and can form glasses. In order to investigate this material, a series of different experiments has to be conducted to retrieve information on the two forms of controlled cooling. These cooling methods will be then compared to get an insight on their differences in speed and in phase formation.

At the end of each cooling, the structural nature of the sample is confirmed through XRD measurements.

An important exploration for this material would be that of analyzing whether and what kind of structural change occurs through a difference in cooling rate. For this reason, most of the study will be focused again on the undercooling region as the most changes can be found in this metastable region, as seen by the previous results on Al_2O_3.

Moreover, metastable phase creation and stabilization will be attempted to illustrate the cooling conditions deemed necessary, if found.

This chapter has the aim of illustrating additional possibilities of the experimental setting as a meaningful tool for material engineering and design. That is due to the completeness of the information acquired during the cooling measurement that could then be employed to solidify the material in its preferred structure.

7.2 Ternary systems M_xO-Al_2O_3-SiO_2 with x=1,2

Ternary aluminosilicate systems involve the presence of different domains of the phase diagram distinguished by how the network will be formed as a function of the basic structural units and their connectivity. We restrict our discussion on alkaline and alkaline earth aluminosilicates (M_xO with x=2,1) due to their wide glass forming regions and the presence of well studied crystalline compounds (such as feldspars).

We define the ratio R=M_xO/Al_2O_3 with x=1,2 to describe their differences.

- Domain of silicates R=∞: Depolymerized network (presence of NBOs produced by introduction of modifying oxides in the network)
- Peralkaline domain R>1: Excess of cations, depolymerization of the network. The cation can act as a charge compensator or as a network modifier in the glass and the structural units present in the network are mainly four-coordinated Al and Si.
- Charge compensated/Tectosilicate join R=1: Fully polymerized network in which metal cations act as charge compensators. Silicon and alumunium tetrahedra are interconnected.
- Peraluminous domain R<1: Highly polymerized network in which the excess of Al_2O_3 causes the formation of high-coordinated AlO_x sites for charge compensation.

An example of a ternary phase diagram is shown in figure 7.1.

Alkaline or alkaline earth cations can act as network modifiers or as charge balancers. If the composition and the role of the cation in the network is known, the polymerization of the network can be calculated and translated in different Q^n units as building blocks in the network (as seen previously). The relative abundance of Q^n units in a glass depends on various factors: mainly on the R ratio but also influenced by the nature of the M cation depending on its value, coordination and M-O bond strength.[227] T_g is also dependent on the chosen cation in the aluminosilicate system, as seen in figure 7.2.

Some of the most studied ternary systems containing alkaline earth cations are $CaO-Al_2O_3-SiO_2$ (CAS),[236–240] and $BaO-Al_2O_3-SiO_2$ (BAS).[241,242]

The CAS glasses are widely studied due to their optical qualities with the drawback of their low glass stability.[243,244] Changes in the frequency of the tetrahedral stretching mode with polymerization have been observed and related

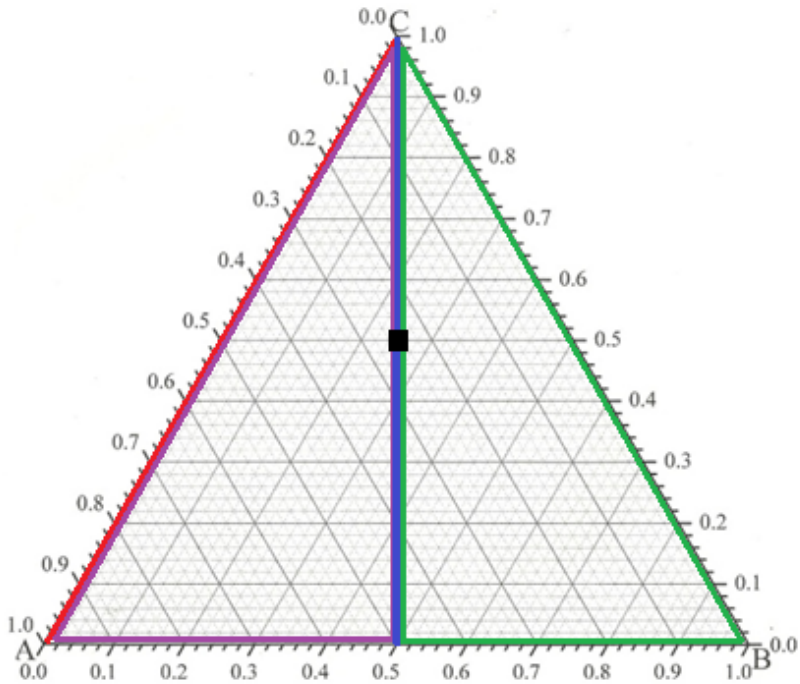

Figure 7.1: Ternary phase diagram. In our case: A=M_xO with x=1,2; B=Al_2O_3; C=SiO_2; Red line: R=∞; Violet triangle: R>1; Blue line: R=1; Green triangle: R<1; Black square: Feldspar composition.

to the fact that the presence of a larger amount of alkaline earth modifiers led to the formation of species with larger amount of NBOs.[227] Low-silica compositions show a wide variation of the distribution of tetrahedral aluminate species, dependant on composition,[243] with Si and Al occupying tetrahedral sites and Ca in octahedral sites.[244] In this case, Al is distributed in Q^2, Q^3, and Q^4 species.[245]

In glasses at high-calcium content, Al and Si partecipate as depolymerized Q^2 and Q^3 units and five- and six-fold coordinated aluminums have been detected in the peraluminous glasses in agreement with the deficit of charge compensators.[246] Variations in the glass transition temperature depending on composition have also been reported.[247]

As stated previously, these systems also present crystalline polymorphic forms. For example, CAS presents anorthite and BAS can be found as celsian, paracelsian and hexacelsian. These crystalline forms are classified as feldspar minerals ($MOAl_2O_32SiO_2$) which are the most abundant minerals in the Earth's crust[248] and are important materials for glass and ceramics industries.[249–252]

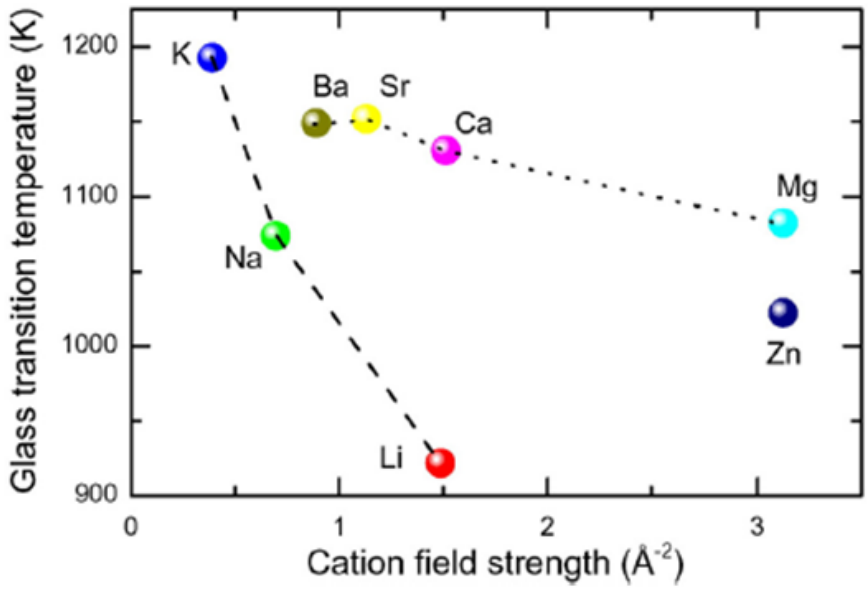

Figure 7.2: Glass transition temperature T_g as a function of the cation field strength for glasses of identical composition belonging to the systems M_xO_y-Al_2O_3-SiO_2[235]

These crystalline materials possess a high melting point,[248,253−256] low thermal expansion,[253,257,258] good oxidation resistance and high temperature phase stability.[259] Due to these characteristics, they are used as matrix of fiber-reinforced ceramics composites, refractories, protective coatings and electro-ceramics.[260−266]

The $MAl_2Si_2O_8$ aluminosilicate feldspar structures are built of corner-sharing SiO_4 and AlO_4 tetrahedral (TO_4) units. The basic building units of the framework are 4-member [T_4O_8] rings linked together to form double crankshaft chains of TO_4 tetrahedra. These crankshaft chains are then connected to form different framework topologies depending on the rotational orientation of the chains and the M^{2+} cations are located in the interstices of the framework to balance the charge of AlO_4^- tetrahedra.[267]

The different frameworks can be distinguished according to orientations of tetrahedra pointing up (U) or down (D) in the 4-membered rings along the chain extension. The crankshaft chains are made of [UDUD] [DUDU] 4-member rings for the celsian feldspar topology and of [UDDU] [UDDU] 4-member rings for the paracelcian one. In both cases, the chains are connected to form 3D networks consisting of 4-, 6-, and 8-membered rings with the M^{2+} cations being located in the larger rings. The crankshaft chains in the celsian feldspar structure are twisted compared to those in the paracelsian one (figure 7.3). For the hexacelcian structure, the crankshaft chains are made of [UUUU] [DDDD]

4-member rings such that two tetrahedra are flipped in each ring with respect to the previous cases. This breaks the 3D connectivity of the network to give rise to a 2D structure alternating cationic layers and aluminosilicate ones containing 4- and 6-member rings.

The degree of order of the feldspars compositions has long been studied[268–271] and it is still subject of discussion to these days[272] because an important point in the description of these crystalline structures concerns the distribution of Si and Al in the tetrahedral sites of the framework. Completely ordered structures satisfy Lowenstein's rule (avoidance of Al-O-Al bonds) and involve only Al-O-Si bonds.[273] Nonetheless, Lowenstein[273] illustrated this phenomenon as a non-random ordering in which a maximum of 50% of aluminum ions can substitute silicon in tetrahedral position. It may be noted that this complete ordering has been observed in feldspar and paracelcian structures, whereas hexacelcian structures are described with mixed TO_4 site occupancy and thus Si/Al disorder.[274,275] In addition, it is well known that the Al/Si ordering in the tetrahedral site of aluminosilicate network depends on thermal history.[276,277]

The celsian feldspar,[278] paracelsian[279] and hexacelsian[274] topologies adopted by the $BaAl_2Si_2O_8$ crystalline polymorphs are illustrated in figure 7.3

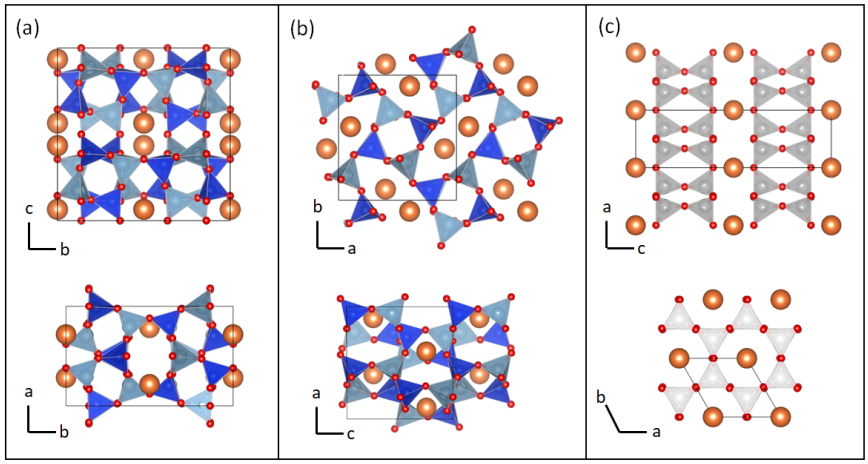

Figure 7.3: Views of the (a) celsian feldspar monoclinic struture (I2/c, a =8.622 b=13.078 c=14.411 β=115.1 ICSD 27528), (b) paracelsian monoclinic structure ($P2_1/a$, a =9.072 b=9.588 c=8.577 β=90.2 ICSD 40530) and (c) hexacelsian hexagonal structure ($P6_3/m$, a =5.292 c=15.557 ICSD 46116) of the $BaAl_2Si_2O_8$ polymorphs. In (a, b), the structure display full Al/Si ordering and dark- and light-blue tetrahedra correspond to SiO_4 and AlO_4 units, respectively. In (c), the structure displays an Al/Si mixed occupancy in TO_4 tetrahedra. Orange spheres correspond to Ba atoms.[280]

7.2.1 The ternary system $SrO - Al_2O_3 - SiO_2$

The ternary system $SrO - Al_2O_3 - SiO_2$ has received less attention compared to other alkaline earth aluminosilicates despite showing a high number of applications as transparent ceramics,[275] high-temperature sealants[281] and refractory materials.[282–284]

The tectosilicate join of $SrO - Al_2O_3 - SiO_2$ glasses and melts has been investigated.[285,286] MD simulations performed by Charpentier et al. with two different potentials describe the structure of aluminum ions as mainly fourfold coordinated and mixing with the silicon network favoring the Al/Si mixing in terms of Al-O-Si linkages.[286] Novikov et al. show differences in the T_g values by changing the amount of silica content.

A relation to the amount of detected AlO_5 units in the structure (mainly observed for high-silica contents and reaching 4-5%) seems to have a correlation with T_g as the miminum of T_g is found when AlO_5 content is maximum. Decrease in AlO_5 units is linked to a decrease of the number of different structural units causing the system to become more ordered since the species that contribute to the structure are similar. Nonetheless, the amount of AlO_5 has been reported to be lower in Sr-based than for analogous Mg- and Ca-based aluminosilicate glasses as well as a difference in CN that is observed to be close to 9 for Sr which is higher than that of Mg and Ca for analogous compositions.[245]

The presence of AlO_5 units in these systems is supported by MD[286] showing that they preferentially adopt a small ring configuration and link to tricoordinated oxygen atoms.

In this chapter we present some results on $SrAl_2Si_2O_8$. The feldspar $SrAl_2Si_2O_8$ congruent melting and crystallization makes this compound able to adopt different polymorphic structures which are known as celsian feldspar (I2/c, a =8.379 b=12.973 c=14.245 β=115.5), paracelsian ($P2_1/c$, a =8.329 b=9.375 c=8.893 β=90.2) and hexacelsian ($P6_3/m$, a=5.197 c=15.199).[287] The celsian phase is mainly used as a matrix material for high-temperature ceramic composites and it is also reported to be the stable one.[288] The paracelsian phase was reported as natural mineral. Hexacelsian is instead a metastable phase of these compositions, only obtainable by quenching of a superheated melt.[287] It can also be formed by annhealing a parent glass (with the same composition) at 1020°C for 3 hours.[275] The formation of the hexacelsian phase should be avoided for high-temperature applications due to its high thermal expansion.[257]

For these reasons, the mechanisms of phase formation and transformation from celsian, paracelsian and hexacelsian and their structrural differences have been an important subject of study.[287,289–291]

7.3 Polymorphism of $SrAl_2Si_2O_8$: NMR and Reflectance

As discussed previously, $SrAl_2Si_2O_8$ can form different polymorphs that possess different structural features (3D network or 2D layered arragement) and degrees of Al/Si ordering. In order to investigate in-situ the formation of solid phases from the high temperature liquid we have first characterized the IR vibrational signature of the different polymorphs with variable degrees of Al/Si order.

For that purpose, three samples were selected: a fully ordered celsian, a disordered celsian and a disordered hexagonal phase. The hexagonal-$SrAl_2Si_2O_8$ sample was obtained by congruent crystallization at 1050°C for 3 h of the parent glass. The fully-ordered monoclinic celsian $SrAl_2Si_2O_8$ sample was obtained by heating the parent glass at 1450 °C for 2h. The disordered monoclinic celsian sample was recovered from the surface of the sample after free-cooling emissivity measurements. The samples used in free-cooling conditions were cylindrical compressed pellets of the parent $SrAl_2Si_2O_8$ glass. The glass was synthesized by melting a stochiometric mixture in a platinum crucible, introduced in a 1700 °C preheated electric furnace, left for 10 min, and heated up to 1750 °C for 10 min and back to 1700 °C for 30 min before quenching the crucible in water.[275]

The structure of the crystalline samples was carefully checked by powder X-Ray diffraction and their respective degree of Al/Si ordering was measured by ^{29}Si Magic Angle Spinning (MAS) NMR.

The NMR experiments were carried out on a Bruker Avance III spectrometer operating at a magnetic field of 9.4 T (^{29}Si Larmor frequency of 79.5 MHz). The powdered samples were packed in a ZrO_2 rotor (4 mm diameter) and spun at the magic angle with a spinning frequency of 12.5 kHz. The ^{29}Si MAS spectra were recorded using a flip angle of 15° (corresponding to a RF pulse duration of 1 µs) and a recycle delay of 60 s. The quantitativity of the obtained spectra was carefully checked experimentally (by recording spectra with longer recycle delay up to 120 s).

The results of the deconvolution of NMR spectra are presented in figure 7.4.

It can be seen that the ordered celsian (monoclinic) depicted in figure 7.4 a) displays two narrow peaks corresponding to the two inequivalent Si sites

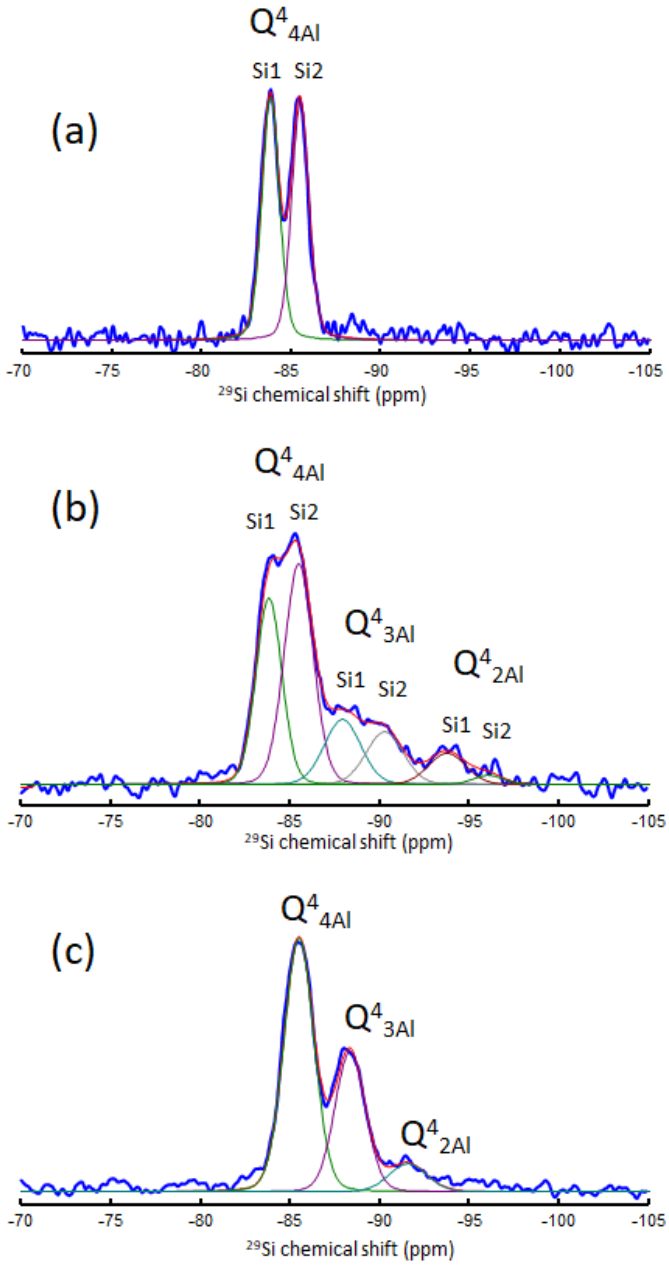

Figure 7.4: ^{29}Si solid-state magic angle spinning (MAS) NMR spectra of (a) ordered paracelsian, (b) disordered paracelsian and (c) disordered hexacelsian forms of $SrAl_2Si_2O_8$, recorded at 9.4 T with a spinning frequency of 12.5 kHz.

of the structure, arranged in Q^4_{4Al} units. Nonetheless, the higher degree of disorder of the disordered celsian (figure 7.4 b)) is revealed by the appearance of additional peaks that can be assigned to Q^4_{3Al} and Q^4_{2Al} units in the structure, with an higher probability to find these new structures in the first (Si1) site. Hexacelsian, instead, possess a single Si crystallographic site due to its high symmetry and its degree of disorder is yet again found by the presence of Q^4_{3Al} and Q^4_{2Al} units in addition to the expected Q^4_{4Al} .

In order to be able to distinguish phase formation in-situ with the Rapid Scan technique, we acquire room temperature reflectance spectra on compressed circular pellets made of these powdered samples.

The results of these measurements are shown in figure 7.5. While the spectra show similarities in the region 800-1000 cm^{-1} except the higher broadness observed for the hexagonal phase, the structure appearing at 1100 cm^{-1} is only retrieved for the monoclinic polymorph. This band is present in the spectra of other celsians and paracelsians[292] but totally absent in the spectrum of the hexagonal phase.

The disappearance of the band at 1100 cm^{-1} has to be related to a change of the structure's symmetry and the related distortion of tetrahedral units and thus we attribute its absence to a degeneracy of the tetrahedral vibrational modes in the high-symmetry hexagonal phase. Regarding the study of the polymorphism of $SrAl_2Si_2O_8$, the disappearance of the aforementioned band will be associated to the formation of the hexagonal 2D-layered structure and this direct fingerprint can be used to identity the polymorph formed in-situ at high temperature or during the cooling from the high temperature liquid. The structure at 1050 cm^{-1} probably is due to an artefact linked to the heterogeneous nature of the pellet sample (porosity and surface rugosity) that can be probably explained by an effective medium theory like those of Maxwell-Garnett. It does not appear in homogenous samples having a smooth surface. The Rapid Scan spectra that will be reported in the following sections confirm this hypothesis since they do not present this feature and showcase instead a wide connected band with no decrease in that wavenumber region.

Another difference is reported at 650-750 cm^{-1} where the appearance of 3 features is only observed in the monoclinic forms. In this case, the shape of these modes with much lower infrared activity are as expected less impacted by the effective medium effect. The disordered monoclinic presents an additional broadening, probably due to an higher network disorder related to the Al/Si inversion phenomenon. Anyways, it is strickingly clear that the two polymorphs present entirely different spectra, even though the NMR measurements illustrated a similar distribution of structural units for the two disordered structures.

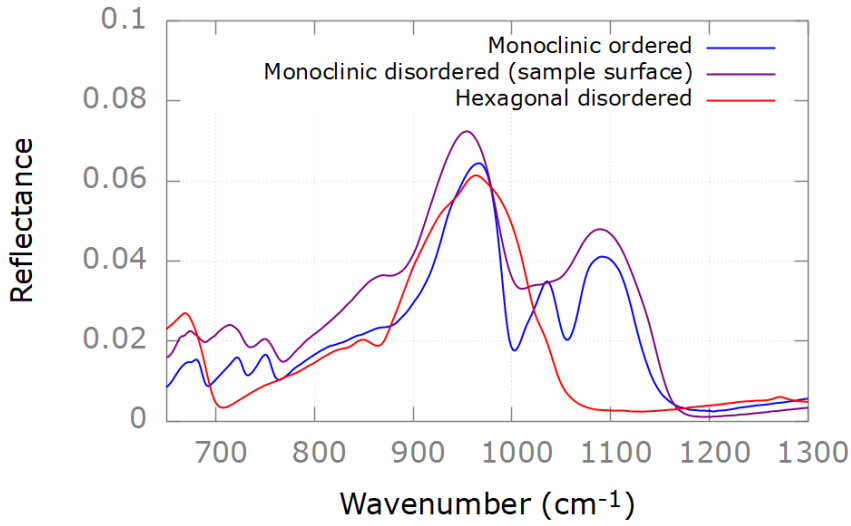

Figure 7.5: Reflectance spectra of pellets of $SrAl_2Si_2O_8$.

7.4 Controlled cooling of $SrAl_2Si_2O_8$: liquid temperature

The first results that we report for this composition are those observed through cooling control by setting the liquid temperature from which the solidification starts. The data is reported in figure 7.6 and obtained with a DLaTGS detector with a resolution of 16 cm^{-1} (20 spectra/s). All the curves reported display an exothermic phenomenon during solidification that is characteristic of a crystallization process, as seen in the case of Al_2O_3. This means that with our experimental conditions, the vitrification process does not occur. It can be noticed that this liquid possesses an intermediate fragility found inbetween the strong SiO_2 and the fragile Al_2O_3 liquids. This suggests that the cooling speed achievable or the experimental conditions used are not suited to produce a $SrAl_2Si_2O_8$ glass.

By controlling the starting temperature we are able to observe that the end of crystallization temperature becomes slightly higher with increasing liquid temperature. Another factor that can be observed is that the exothermic feature increases in length and size, showing that a wider metastable area can be created just by increasing the liquid temperature before the start of the solidification process. This result is in accordance to the discussion aforementioned in the

Al_2O_3 chapter as a higher liquid temperature in our experimental conditions has to create a deeper molten pool and thus a more defined plateau and a rise in the retrieved crystallization temperature maximum.[221]

The values of the crystallization temperature maxima and transformation duration for each run are reported in table 7.1.

Starting liquid (T_0)	Crystallization maximum (T_M)	Transformation duration (T_D)
T_0=2471 K	T_M=1863 K	T_D=2.40 s
T_0=2437 K	T_M=1855 K	T_D=2.14 s
T_0=2388 K	T_M=1852 K	T_D=1.90 s
T_0=2324 K	T_M=1847 K	T_D=1.67 s
T_0=2240 K	T_M=1831 K	T_D=1.53 s

Table 7.1: Table comparing starting liquid temperature, crystallization temperature maxima and transformation durations. Both of these last two quantities decrease with decreasing starting temperature.

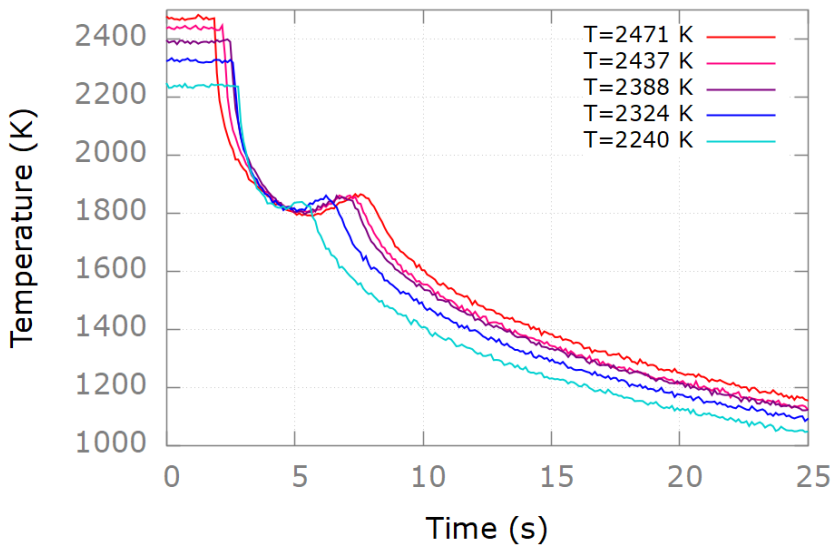

Figure 7.6: Controlled cooling through starting temperature control. It can be noticed that the crystallization temperature slightly changes as well as the length of the transformation duration with increasing liquid temperature.

A selection of data from the highest and the lowest temperature runs are presented in figure 7.7. It can be observed that overall the phase formation occurs in the same way for the two experiments and lead to the formation of the celsian monoclinic phase as evidenced by the bands around 1100 cm^{-1}. Nonetheless, these spectra show slight differences in their broadening. However, the signal-to-noise ratio remains limited making difficult a detailed analysis

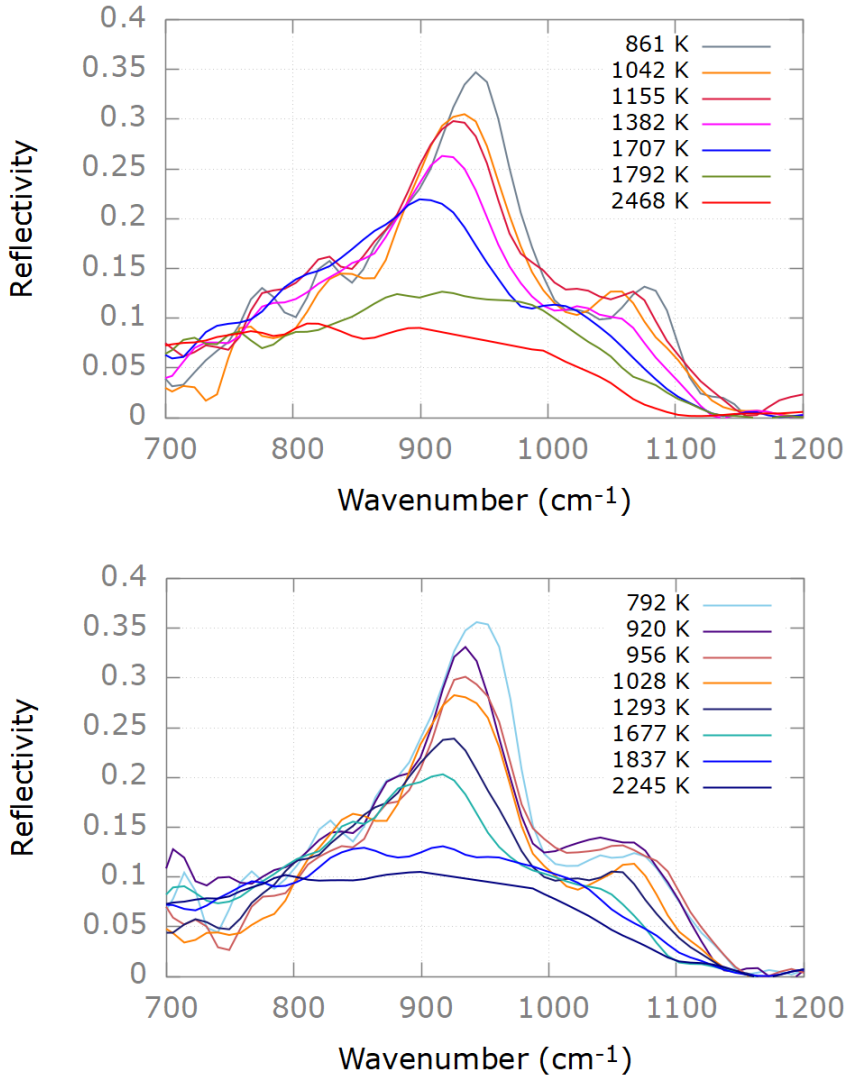

Figure 7.7: Selection of spectra from the highest temperature run (Top) and the lowest temperature run (Bottom). These measurements are performed in Rapid Scan mode using the DLaTGS detector with a resolution of 16 cm^{-1} (20 spectra/s). It is shown that the cooling process does not proceed totally equally even though they both solidify as monoclinic structures.

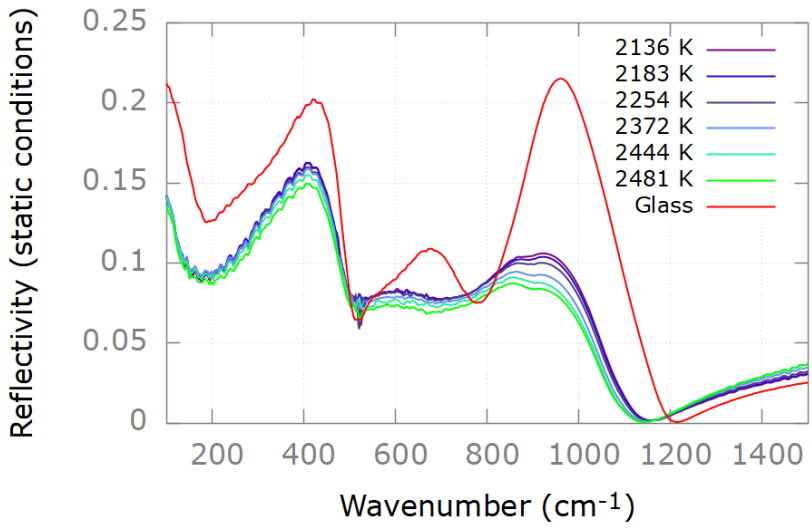

Figure 7.8: Reflectivity spectra obtained from high temperature reflectivity measurements of $SrAl_2Si_2O_8$ in static heating conditions. Room temperature reflectivity of a glass of the same composition (shown in red).

of these individual spectra. To go further in the characterization of the high temperature liquid, we perform additional static measurements to improve the signal-to-noise ratio and extend the frequency range to the FIR, as shown in figure 7.8. The spectra of the glass obtained by quenching the high temperature liquid is also shown for comparison.

If now we recall the reference spectra shown in figure 7.5, it can be seen that the spectrum of the glass includes all the features seen for the monoclinic reference with an additional broadening due to a strong disorder in the glass. Moreover, we can also observe a strong similarity between the spectra of the liquid and the glass, taking into account the temperature shift. This suggests that the structure of the liquid is a 3D polymeric network of tetrahedral units.

From these classic measurements, the signatures of Sr^{2+} cations vibrational motions can also be found below 200 cm^{-1}. Due to their similarity, one can assume that the Sr^{2+} cations have mostly the role of charge compensators in both the glass and the liquid structures. Nonetheless, the high level of broadening illustrated by these spectra do not allow to easily confirm or discard the possible presence of a low amount (few %) of higher coordinated Al species (AlO_5) (oxygen triclusters or NBOs) as suggested by Novikov et al.[245]

7.4.1 Cooling speed determination I

In order to observe the impact of the cooling speed on the sample after the previously reported runs, we extract it from its derivative. The results from the highest, the medium and the lowest starting temperature are presented in figure 7.9. Only three curves will be reported to guarantee an easier visualization and interpretation of the data.

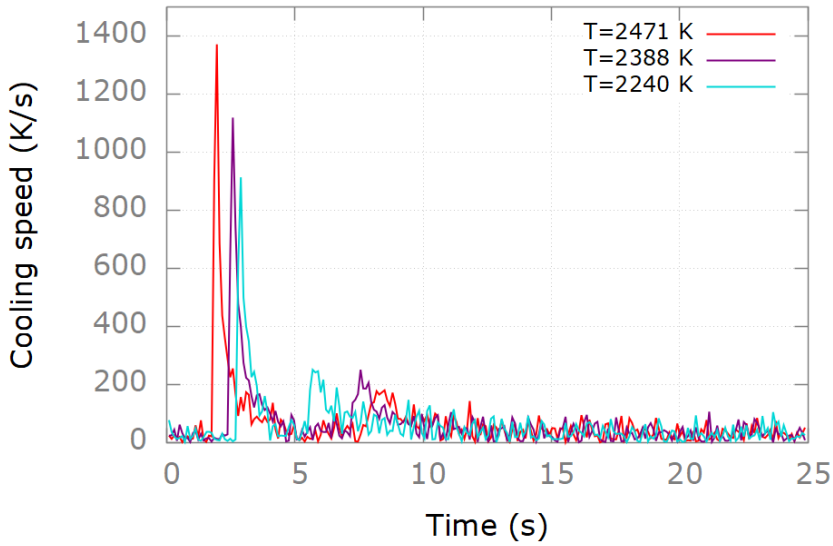

Figure 7.9: Cooling speed at different starting temperatures. Highest (T=2471 K, red), medium (T=2388 K, violet) and lowest (T=2240 K, light blue) starting temperatures. It is observed that the maximum cooling speed is retrieved at the highest starting temperature, making it an efficient way to control the maximum cooling speed in free-cooling conditions.

We can observe that except the highest points that correspond to the laser shut-down, the rest of the cooling has approximatively the same rate. Nonetheless, we have observed structural differences in the degree of disorder during cooling and for this reason we confirm that the effect of thermal history and cooling rate (even when slightly different) can cause differences in the solidification process and in the solidified material. This effect has also been due to the differences in the amount of liquid created before cooling.

7.4.2 Exothermic peak region analysis and comparison

Due to the observation of differences in the exothermic reaction region and the retrieved crystallization temperature, we will focus our analysis on the spectra acquired in this region to observe microstructural changes.

The data is presented in figure 7.10 as averaged spectra in the Second Region (as seen in the chapter on Al_2O_3) to minimize signal-to-noise ratio. 24 spectra have been averaged for the highest temperature run at T=2471 K and 15 spectra for the lowest temperature run at T=2240 K due to their different transformation durations.

Two totally different structural scenarios taking place in this temperature region are thus observed. In the case of the highest temperature, the appearance of an additional feature at 920 cm^{-1} when compared to the liquid spectra illustrated in figure 7.8 symbolizes the nucleation sites of Q^n units. This is not the case for the lowest temperature as this feature is still undetectable and hidden by the broadened structure of the liquid.

The 500-700 cm^{-1} region that usually represents the network linkages between structural units is found in the solid monoclinic state as three features which are perfectly compatible to those observed in the lowest temperature spectrum. The highest temperature spectrum seems to present broader features, probably due to a wider distribution of bond angles and lengths.

All of the data aquired solidified into monoclinic structures but, from these observations, we can conclude that the amount of liquid sample has a deep influence on the mechanisms of phase formation. In our case, the mechanism that seems to take place is a narrower distribution of Q^n units, giving rise to the feature at 920 cm^{-1} due to a more pronunced local ordering of Si/Al in the case of a bigger molten pool. Smaller pools, instead, seem to display a more developed topological order. Nonetheless, our technique is able to probe only the surface of the molten pool such that this phenomenon could also be related to differences in surface solidification due to the differences in depth of the molten pools created.

If that is correct, metastable phase stabilization through the undercooled region could give rise to crystalline structures with more complicated networks due to the differences in bond lengths.

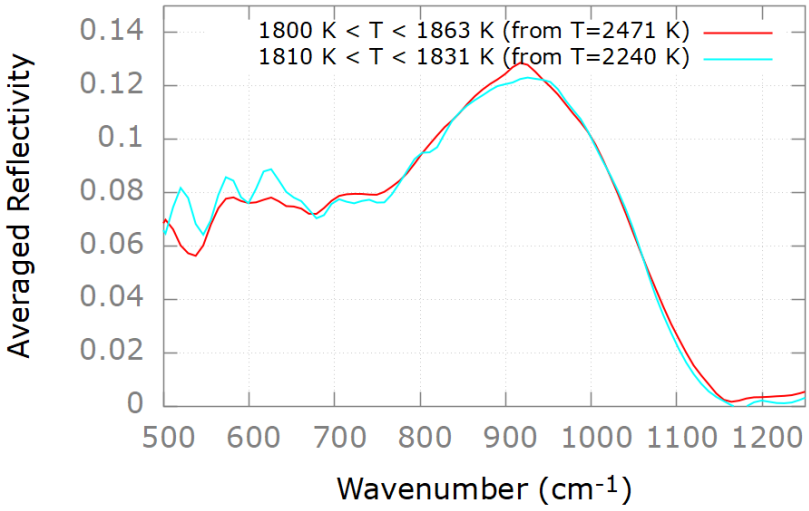

Figure 7.10: Averaged reflectivity of Second Region for the highest temperature (T=2471 K, in red) and the lowest temperature (T=2240 K, in light blue). Various differences are reported before the crystallization process is complete.

7.5 Controlled cooling of $SrAl_2Si_2O_8$: laser power

The previous section illustrated the impact of cooling on the mechanisms of phase formation. Indeed, we were not able to evidence clearly the structural differences on the sample and their link to disorder due to the similarity of cooling speeds. For this reason, another cooling method used for this sample is a controlled cooling at the same starting temperature.

In this set of measurements, we decide to maintain the same starting temperature to guarantee the same amount of liquid at the start of the measurements. This is due to the fact that the previous measurements were affected by the depth of the molten pool and the amount of liquid in the sample. In these measurements, instead, the amount of created liquid before solidification is approximatively the same due to the same starting temperature. In order to observe the differences that might arise through a cooling speed difference, a free cooling measurement is also performed for comparison.

As illustrated in figure 7.11, the starting liquid temperature remains unaltered whilst the cooling rate changes its speed depending on the timestep used. In this

case, we will operate on laser power through knobstep movements temporally spaced.

The concept used to be able to divide time through equally spaced timesteps is the BPM (Beats Per Minute). BPM is a temporal division mostly employed in the music sector. It is commonly seen in orchestral music sheets and gives information on the so called "tempo" of the composition. The number of BPMs equals the number of divisions of a minute. It is now evident that a speed of 60 BPMs is equivalent to a timestep of 1 second.

The tool used to measure BPMs is called a metronome and we will use it to have a solid reference for the experimental timesteps needed to control the cooling rate. In parallel to the music sector, the employed values are multiples or quotients to the other such that there is also a complementariety between the timesteps. In this case, the retrieval of the cooling rate will illustrate whether this complementariety is reflected through speed as well.

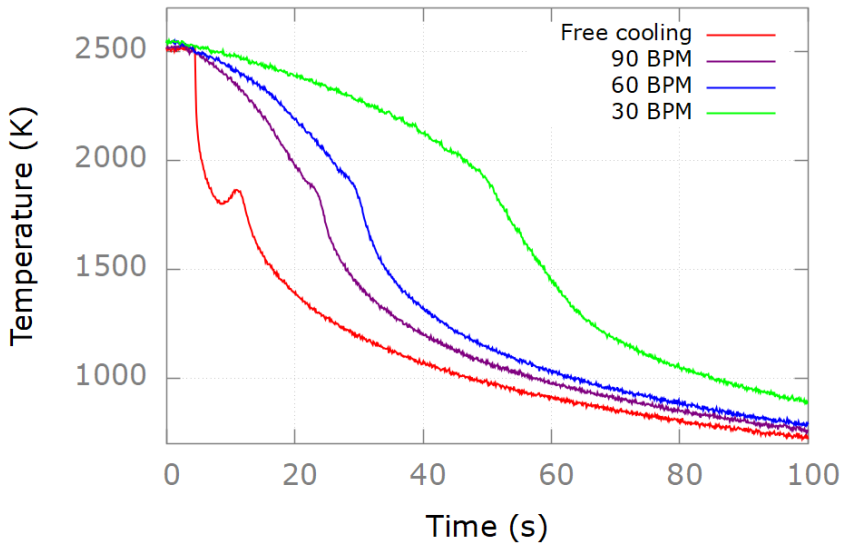

Figure 7.11: Controlled cooling of $SrAl_2Si_2O_8$ at different laser power knob timesteps.

In all of the tested speeds the final polymorph is seen to be monoclinic. This means that regardless of the cooling speed, the final structure has stayed unaltered, at least from an XRD point of view, a technique that has no possibility of distinguishing more subtle changes.

As discussed previously, the same polymorph can still possess site inversion while staying the same polymorph, from a purely structural point of view. Yet,

in that case, the nature and the number of T-O-T linkages present might not be the same.

7.5.1 Cooling speed determination II

In order to determine the cooling speed obtained by the curve, it is possible to extract it through a derivative. The results are presented in figure 7.12.

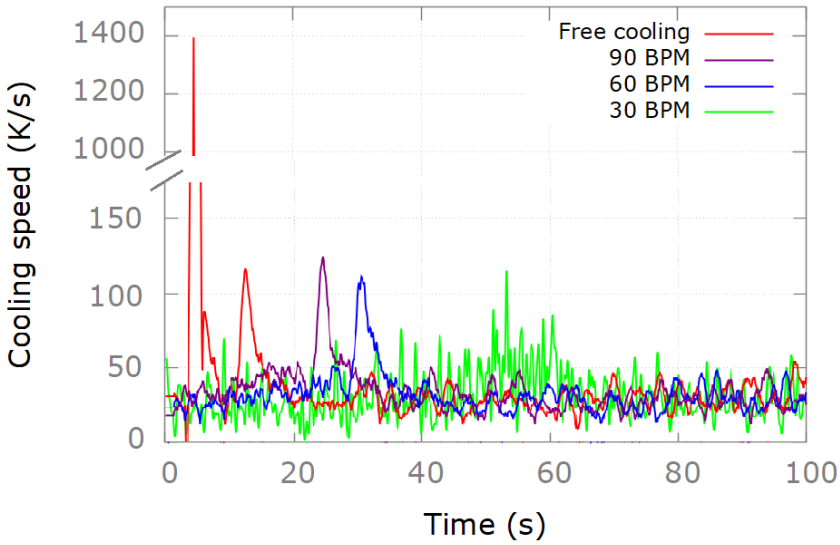

Figure 7.12: Cooling speed obtained from the respective cooling curves illustrated in figure 7.11. The data has been cut from 200 to 1000 in the y-axis to improve the readability of the results.

The free cooling curve reaches a maximum of 1400 K/s after the laser shutdown while the controlled cooling ones reach their maximum value (nearing 90 K/s) in the exothermic peak region. Moreover, the data obtained shows the displacement in time of the transformation duration as well as its increase. These conditions are expected to create structural differences in network formation. Nonetheless, due to the fast acquisition, the differences in temperature of consecutive spectra is minimal making the differences more easily observed directly in figure 7.11.

7.5.2 Al/Si inversion phenomenon

In order to investigate the differences regarding network formation at different cooling speeds, two spectra at 1000 K have been selected. One of them has been obtained from the data acquired during free-cooling meanwhile the other has been extracted from the run performed at 30 BPM. They are illustrated in figure 7.13. It is easily noticed that the two spectra are very similar, with

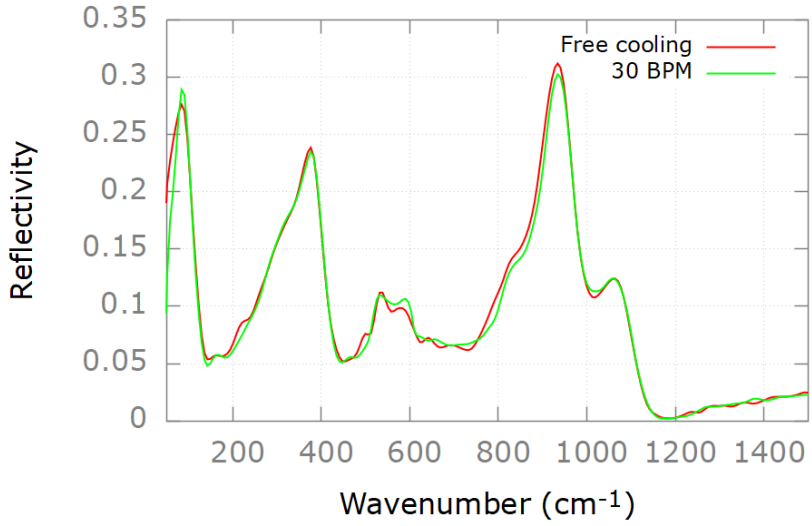

Figure 7.13: Reflectivity spectra extracted from the runs at 1000 K. Red - Free Cooling, Green - 30 BPM. It is observable that even though the starting liquid temperature has been kept the same for both measurements, the spectra present some differences especially in the broadening of the features reported.

most of their differences located in the region 500-800 cm^{-1}. The proposed imaginary dielectric function obtained from the fit of these spectra are shown in figures 7.14 and 7.15.

The fitted dielectric functions show differences at the same temperature, indicating that the cooling speed has an impact on the final structure of the solid. However, XRD analysis of the samples at all cooling rates reveal that they all crystallized in the monoclinic form. Thus, differences in the vibrational response are related to subtle variations of the intermediate range ordering in the structure. The spectra have been fitted with a dielectric function model and with 15 Gaussian components Gx. In order to propose a quantitative

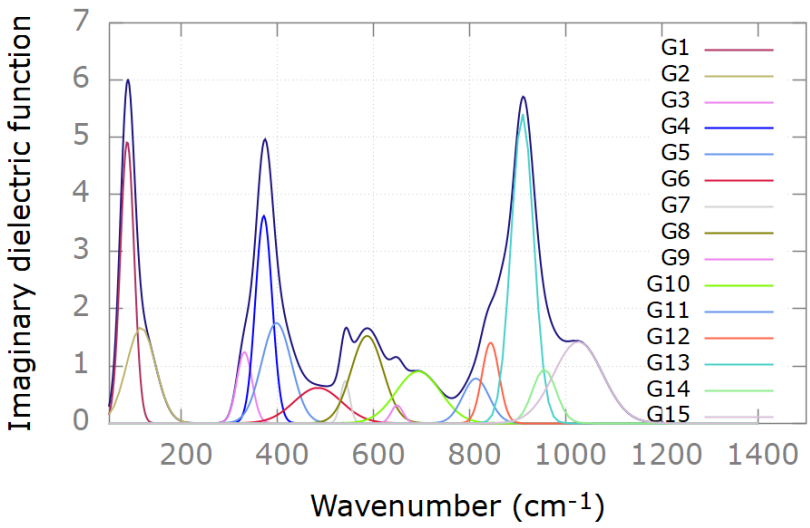

Figure 7.14: Imaginary dielectric function obtained through fit of the 1000 K spectrum in free cooling conditions and illustrated in figure 7.13. The modes are displayed to allow a comparison with figure 7.15 and illustrate the difference in the degree of ordering of the structure.

interpretation for these spectra we will use the results obtained by Mabrouk et al.[293] on aluminoborosilicate glasses as a guide. We assign the region below 300 cm^{-1} to vibrational motions of strontium cations.

The bending movements of tetrahedra are reported in the region extending from 300 cm^{-1} to 500 cm^{-1}. Between 500 cm^{-1} to 900 cm^{-1} we observe different bands assigned to the stretching motion of the building blocks as well as network linkages between these units.

Lastly, the components appearing after 900 cm^{-1} are assigned to Q^4_{xAl} with x=2,3,4. The last band has already been discussed previously and interpreted as a distortion of tetrahedral Q^4_{xAl} units that cause a change in symmetry.

The bands that present the most differences are G9, G11, G12 and G13. The position of the G9 band suggests to assign it to the Si-O-Al band, while the rest belong to tetrahedral stretching modes of Q_4^{xAl} SiO_4 units involving different numbers of Si-O-Al and Si-O-Si bonds. It is observed that G9 increases greatly in the controlled slow cooling spectrum. This evidences a process of replacement of Si-O-Si by Si-O-Al bonds in the strontium aluminosilicate glass network.

This process reflects the ordering of the network and the replacement observed is energetically more favorable, in agreement with the Lowenstein rule reported for

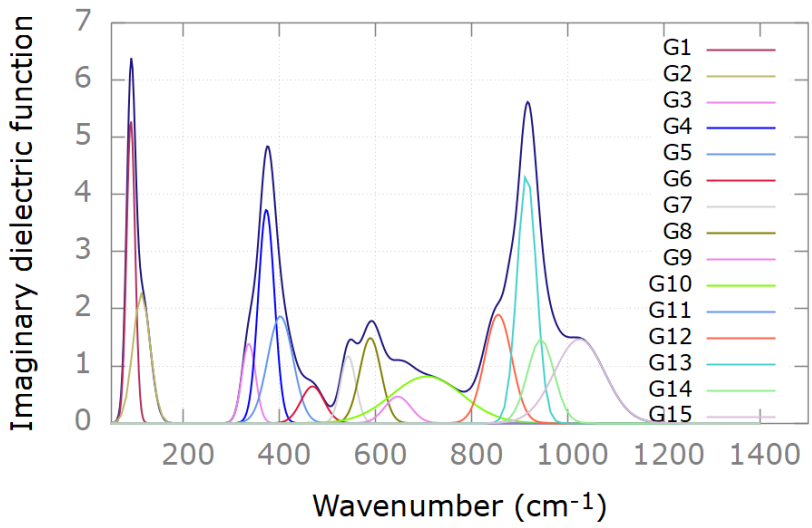

Figure 7.15: Imaginary dielectric function obtained through fit of the 1000 K spectrum in controlled cooling conditions (30BPM) and illustrated in figure 7.13. The modes are displayed to allow a comparison with figure 7.14 and illustrate the difference in the degree of ordering of the structure.

aluminosilicates.[273] Nonetheless, the sample has been kept at the same starting temperature and probed in the same point for both Rapid Scan measurements, so the differences observed are only due to the different cooling speed and not to a difference in the amount of liquid created prior solidification. Band assignment is heavily complicated by the 3D structure of the monoclinic phase and the distortion of tetrahedral units, as well as a possible overlap between bands.

Even though an assignment of Q_4^{xAl} units is extremely difficult in this case, the minimalist model employed is still able to show differences in the ordering phenomenon. This is due to the fact that most of the bands retrieved in the controlled cooling spectrum present sharper features when compared to the free-cooling one and thus illustrating a lower degree of disorder.

In order to confirm our results, we extract other spectra at 900 K and we focus on the stretching region and the Q_{xAl}^4 units. It can still be observed that the controlled cooling showed an higher degree of ordering, illustrated by the wider features observed in the free-cooling spectrum.

In conclusion, we have proven that the cooling speed and the thermal history of this composition strongly influence its final microstructure and that slower speeds allow the formation of more ordered networks. Attempts at solidifying

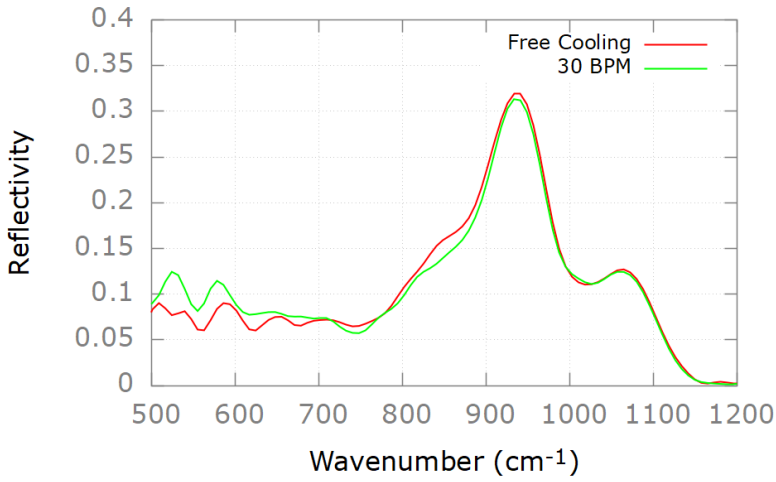

Figure 7.16: Reflectivity spectra extracted from the runs at 900 K. Red - Free Cooling, Green - 30 BPM. These spectra also present differences in their broadening, as observed at 1000 K (figure 7.13).

an hexagonal structure on the surface did not succeed but still, the possibility of the setup to follow and quantify the degree of disorder on phase creation through controlled cooling has been illustrated.

8

Additional measurements on the impact of cooling conditions on more complex systems with industrial applications

Contents

8.1 Application of the technique to complex systems

The solidification from molten state of systems with higher complexity can give rise to an higher variety of solid and metastable phases, compared to single or binary systems.

This is due to the higher number of possible network formations due to the reorganization of the structural motifs and the migration of species in the liquid, due to chemical affinities or oppositions that could cause phase separation.

In order to demonstrate the potential application of the in-situ Rapid Scan emissivity approach developed previously, example measurements have been performed on kaolinite $Al_2Si_2O_5(OH)_4$ and a composition belonging to the $ZrO_2 - Al_2O_3 - SiO_2$ ternary system. This will allow us to evaluate the additional experimental challenges and future developments required for an accurate and appropriate characterization of such systems.

Kaolinite is a natural aluminosilicate clay mineral (phyllosilicate family) widly used in ceramic industries as raw material. Compositions belonging to the AZS system are widely used for industrial applications as refractory materials.

These samples will be tested in free-cooling and controlled cooling conditions and with different starting liquid temperatures. The data obtained will illustrate the importance of cooling rate and starting temperature on the material.

From this study it will be possible to obtain a framework from the acquired data that could serve as an example to draw some final perspectives on the future use of the technique to monitor the solidification of complex materials as well as some new ideas on which new options could be implemented to further improve the experimental setting.

8.2 $Al_2Si_2O_5(OH)_4$: Incongruent solidification

The chosen composition for this study is Kaolinite $Al_2Si_2O_5(OH)_4$ due to its importance in ceramic industries as well as the possibility to form a liquid with equal amount of Al_2O_3 and SiO_2 from the starting composition. This compound presents a triclinic layered structure made of octahedral AlO_6 sheets linked to tetrahedral SiO_4 sheets.[294]

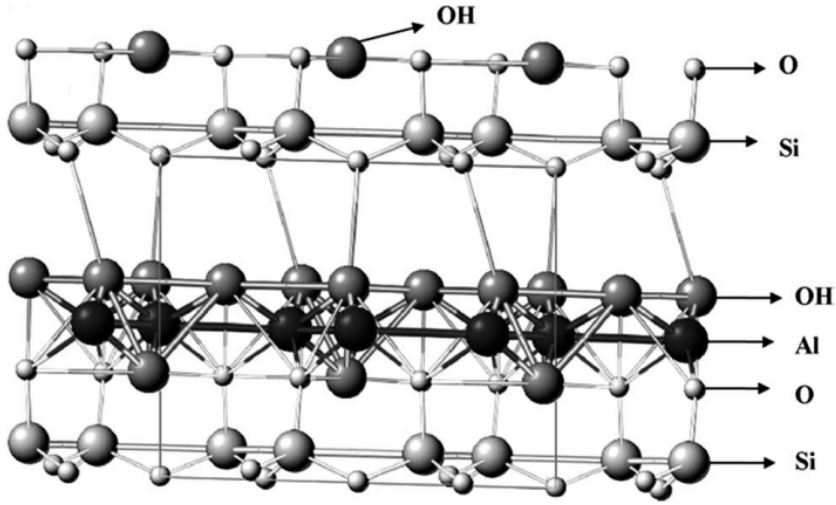

Figure 8.1: Scheme of the structure of $Al_2Si_2O_5(OH)_4$.[294]

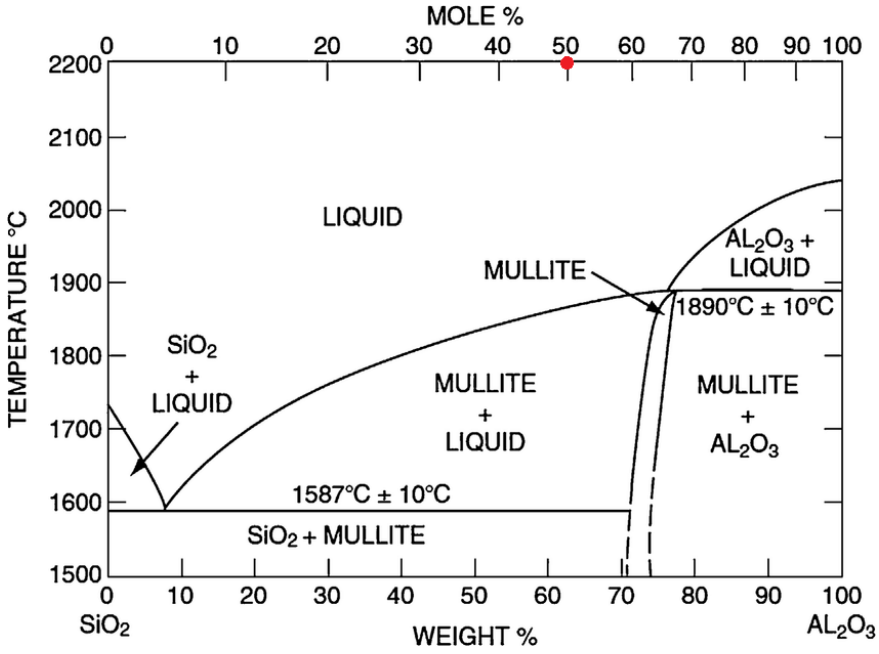

Figure 8.2: High temperature phase diagram of $Al_2O_3 - SiO_2$ showing the incongruent solidification of the chosen composition (illustrated by a red dot).[295]

The thermal transformation of Kaolinite has been widely studied.[296–302]

The first mechanism is the dehydroxylation at 400-600°C and it leads to the formation of the metakaolinite amourphous phase by the loss of structural water, the delamination of the structure, loss of crystallinity and reorganization of the local environment due to variations in $Si-O$ and $Al-O$ bond lengths. The appearance of lower coordinated Al species have been detected during dehydroxylation.[303] The importance of the knowledge regarding the mechanisms of dehydroxylation made this process a candidate to be studied by different techniques.[304–307]

This process leading to the formation of metakaolin is described as:[308]

$$Al_2Si_2O_5(OH)_4 \rightarrow Al_2O_32SiO_2 + 2H_2O \tag{8.1}$$

At higher temperatures (until 1100°C) transformation of metakaolin to spinel or γ-alumina with amorphous silica is observed, yet still under investigation.[308]

After 1100°C, the formation of mullite phase is observed along with the transformation of amorphous silica into crystalline cristobalite. As it can be seen in figure 8.2, melting above 1850 °C forms a liquid with a composition Al_2O_3-SiO_2 that is able to form various phases. In order to observe if there was a difference during solidification, we consider the free-cooling curves retrieved with Rapid Scan, presented in figure 8.3.

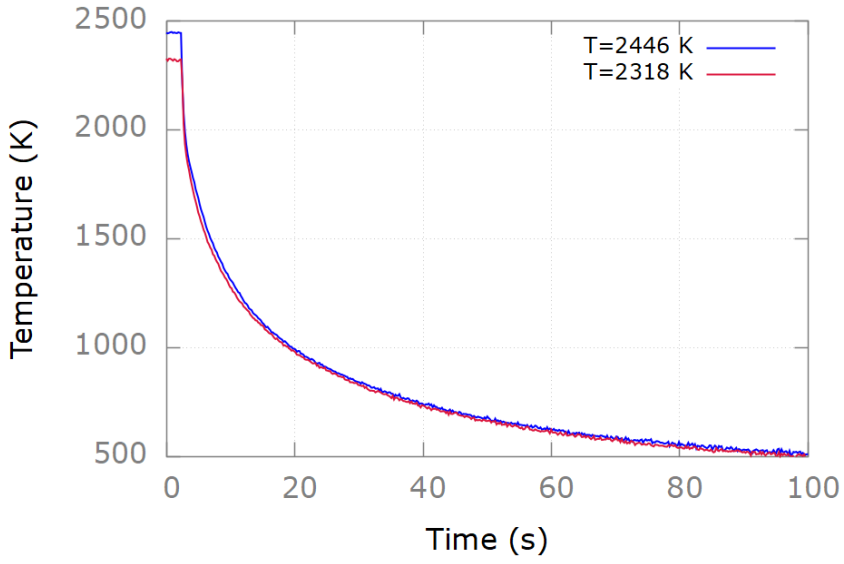

Figure 8.3: Rapid Scan free-cooling curves of Runs performed at different starting liquid temperatures at starting temperatures of 2446 K (blue) and 2318 K (red).

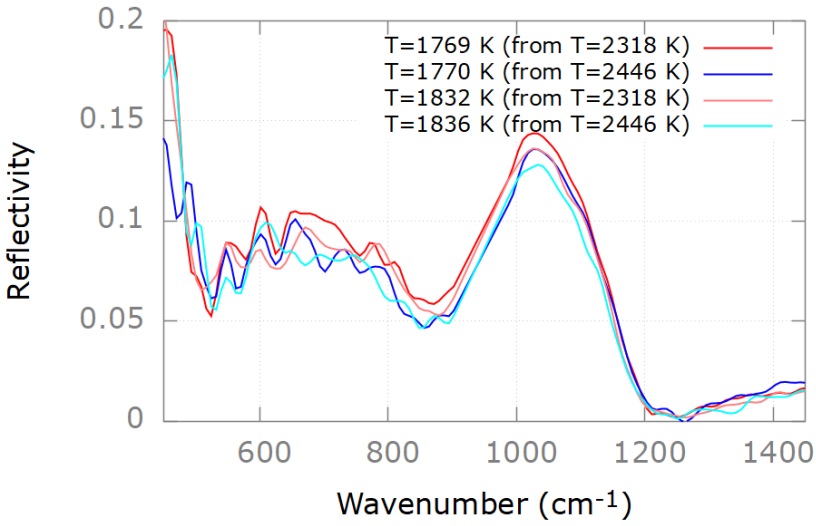

Figure 8.4: Spectra at similar temperatures extracted from the Runs displayed in figure 8.3

It is noticeable that the higher temperature curve displays the slowest cooling, and there is a departure from the other curve at a temperature of 1800 K. We have seen in the previous chapter that the temperature of crystallization of corundum lies near this value, as well as the one of cristobalite. From this result, it seems like the highest temperature allowed the formation of a bigger variety of phases.

It is also noticeable from figure 8.4 that the silica content should be inferior in the higher temperature run as the region from 1000 cm^{-1} has lower intensity and it is related to silica streching motions, as seen in the SiO_2 chapter. The alumina content seems to be preserved in a similar quantity, seen by the region of 600-800 cm^{-1} that has been reported in the Al_2O_3 chapter. Nonetheless, the spectra at similar temperature report various differences, leading us to consider that possibly multiple phases have been formed.

After the cooling, the sample displayed macroscopical differences by forming coloured rings. This observation suggested us to perform a post-mortem analysis on the surface to investigate if and which phases have been obtained during the cooling due to the thermal gradient across the sample surface due to laser heating.

Nonetheless, due to the complexity of this study, its analysis should be done using more complex theories due to the presence of multiple phases.

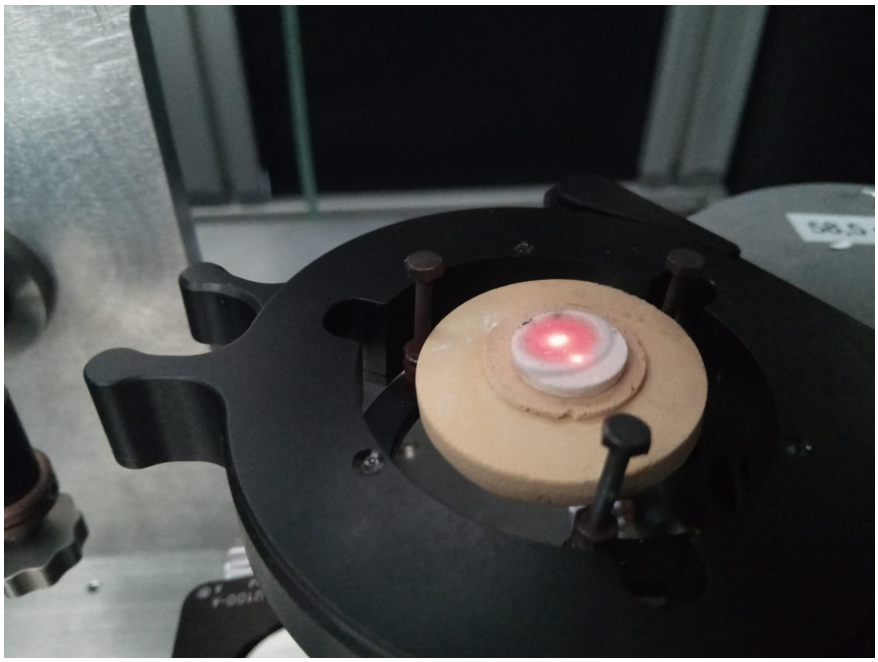

Figure 8.5: Sample displaying macroscopical differences after the Runs displayed in figure 8.3. These differences are shown as consecutive rings, suggesting that their appareance has to be due the thermal gradient across the sample surface during laser heating.

An XRD study has been conducted post-mortem to allow us to understand which networks have been formed after the free cooling from molten state of an equimolar Al_2O_3-SiO_2 mixture starting from a Kaolinite sample. The results are shown in figure 8.6 and it shows the formation of four different polymorphs from an homogeneous liquid containing the same proportion of Al_2O_3 and SiO_2:

- Mullite ($3Al_2O_3$ $2SiO_2$ or $2Al_2O_3$ SiO_2)
- Corundum (Al_2O_3)
- Cristobalite (SiO_2)
- Silica glass (SiO_2)

The presence of silica glass is evidenced by the wide peaks present in the XRD diagram.

As Kaolinite is composed of almost the same proportion of Al_2O_3 and SiO_2, we can assume that their general proportion will stay the same even after cooling. This means that since a mullite network is found, in a compositional

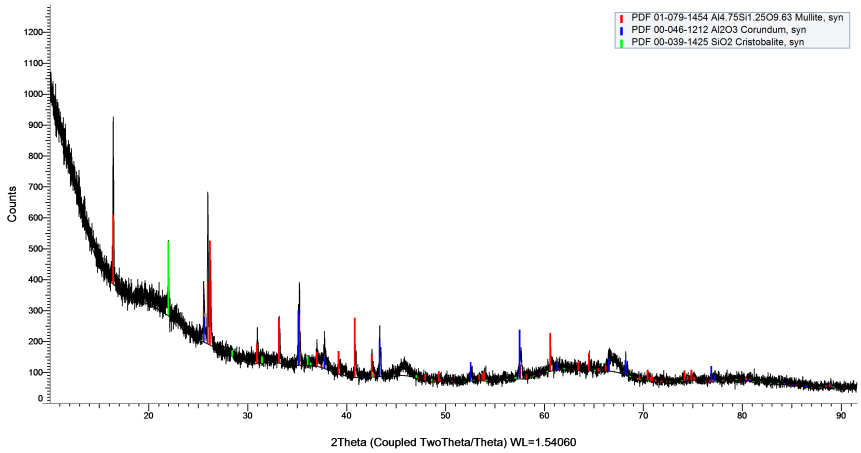

Figure 8.6: Post-mortem study on the polymorphs created by free cooling of Kaolinite

region that sees the prevalence of Al_2O_3 ($3Al_2O_3$ $2SiO_2$ or $2Al_2O_3$ SiO_2), we can expect SiO_2 to be present as a 1/3 more though its two polymorphs, if compared to corundum alone.

The newtork topology is also different as the only disordered structure is the one of the silica glass, the rest are crystalline: corundum has a trigonal geometry, cristobalite is tetragonal and mullite is orthorhombic.

It is also expected to find different structural motifs such as SiO_4 and AlO_4 tetrahedra as well as AlO_6 octahedra units. Both polymorphs of silica present only SiO_4 structures, corundum has AlO_6 units and mullite is composed of tetrahedra of both species.

Ideally, a concentric subdivision of regions can be postulated, based on the macroscopical differences observed on the surface of the sample:

- Center Ring: this region is the one probed by Rapid Scan, it has the fastest cooling rate and the highest temperature (it has reached the liquid)
- First Ring: Intermediate region lying between the liquid and the next ring
- Second Ring: Intermediate region lying between the previous ring and the solid
- Third Ring: Solid region

These results are obtained on a measurement on the whole surface of the sample, thus it contains regions in which the maximum temperature reached as well as the speed of cooling have not been homogenous. We can assume that the center of the sample is the part that reached the highest temperature and solidified faster than the rest.

A Raman cartography on the surface of the sample has been performed to observe how phase formation occurred from the liquid state.

These two cartographies were performed on a Renishaw Qontor microRaman. A Cobolt 514nm laser and a 1800l/mm grating were used. The LiveTrack options allowed the setup to keep the focus on the whole analysed area, even if the sample surface presented a strong inhomogeneity.

The first step is to observe the Center Ring, corresponding to the the highest temperature region with the fastest cooling rate, through a "hot area analysis". The "hot area analysis" is a cartography on a 91x57 spectra area, with a 1x1 µm spatial resolution. A 100x 0.85 NA microscope objective was used.

From this measurement we can conclude that this ring saw the formation of mullite and silica glass, as predicted by other studies.[309] Figures 8.7 and 8.8 show the results obtained after a comparison to reference spectra available on the RRUFF database.[310]

It is also observed that the two images are almost precisely inversed and thus complementary, meaning that the sample formed regions of silica glass and others of mullite. Nonetheless, yet only from a qualitative point of view, the silica content appears to be dominant if compared to that of mullite, showing its signature peaks even in high mullite content regions. Other phases obtained by XRD have not been found in this Ring. Due to the presence of the same amount of Si and Al atoms in the initial composition, the remnant alumina content is supposed to be located in other Rings. If this is correct, the thermal gradient across the sample could have caused a flux of matter, thus explaining the compositional differences retrieved.

Another explanation to this phenomenon is yet again related to the molten pool and the inhomogeneity of the liquid of this composition. The solidification of this material does not occur congruently and, for this reason, the solidification of crystals can occur also through a mechanisms of crystal sedimentation on the depth of the molten pool. In this case, the corundum crystals could have sedimented such that the surface (which is probed by the cartography) displays an higher silica content.

Nonetheless, we have observed that the solidification phenomenon can cause compositional differences in the surface and the depth of the sample due to the incongruent melting phenomenon.

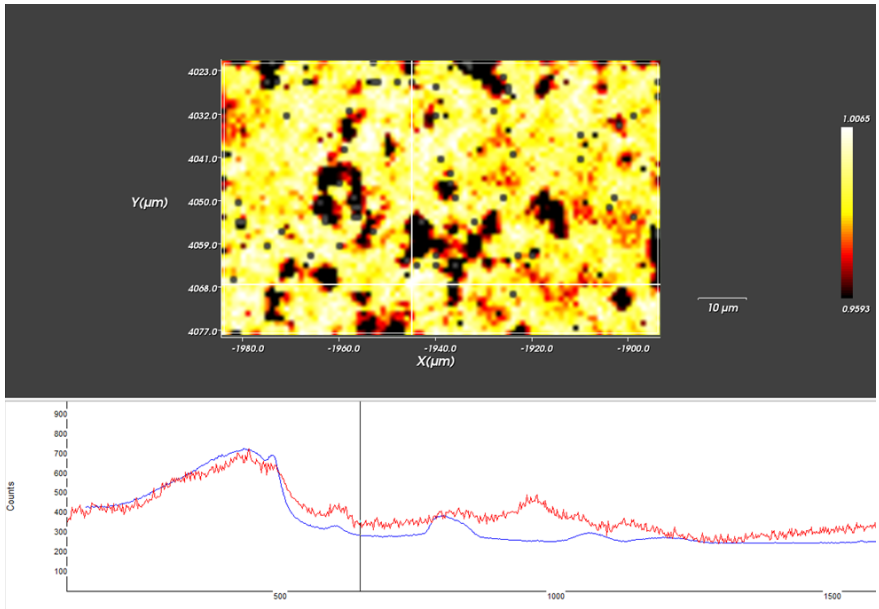

Figure 8.7: Center Ring cartography result on the likeliness of silica glass formation and spatial distribution through comparison to a reference spectra

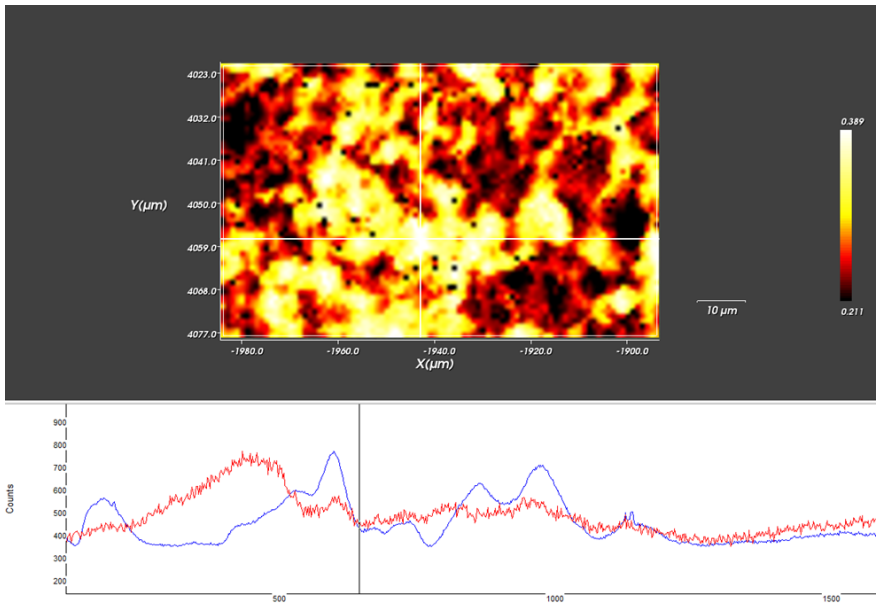

Figure 8.8: Center Ring cartography result on the likeliness of mullite formation and spatial distribution through comparison to a reference spectra

In light of the previously discussed results, Rapid Scan measurements are conducted through light beam displacement. This is due to the fact that our experimental setting is able to probe the surface of the material but not its depth but the region of acquisition can be selected. This displacement will make us able to acquire data at different distances from the heating laser beam since the data is recollected where the data acquisition beam is set. These new experiments will be conducted while keeping the same conditions from the first standard measurement that produced the compositional and structural differences in the sample. The aim of this observation is to establish the parameters that produced these phases, whether possible.

The beam displacement will impact the way the measurement is performed by changing two main conditions that are mutually connected:

- Starting temperature: at greater distances, the sample reaches a lower liquid temperature

- Cooling speed: at lower starting temperatures, the cooling speed is slower

The obtained cooling speeds and starting temperatures are displayed in figure 8.9.

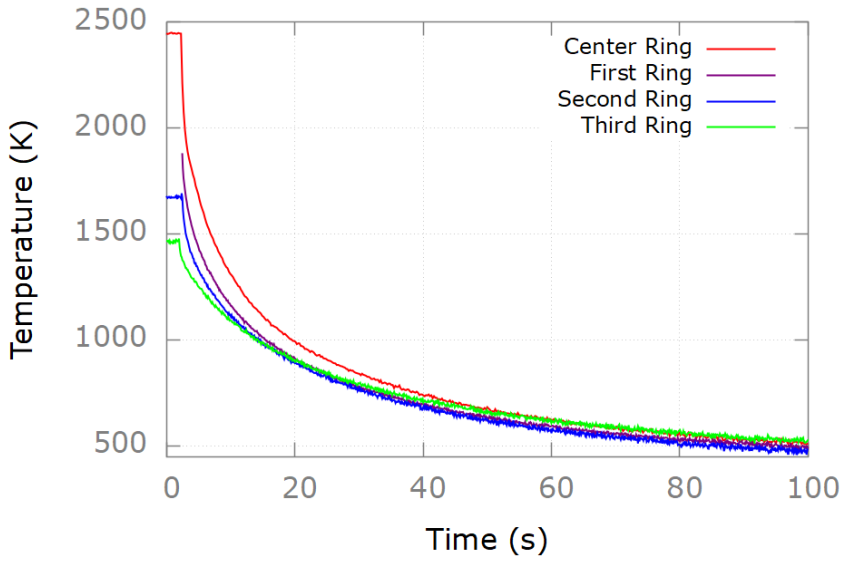

Figure 8.9: Possible cooling speeds and starting temperature of the observed Rings. The measurement in the First Ring with the laser on has not been possible due to the high interference of the laser beam in the surface of the sample that prevented us to retrieve the starting temperature of the sample before the cooling.

As illustrated, the Center Ring displays the highest temperature with a value compatible to the one necessary to produce both silica glass and mullite. The First Ring measurement has been the most challenging due to the observed laser beam reflections in the spectra acquired before the shutdown. Due to the high level of noise in the spectra, it has not been possible to retrieve the starting temperature of this region. Nonetheless, through repetition of the measurement, it has been possible to acquire a spectrum still presenting a noisy signal but at a lesser degree. It is observed that this spectrum has been acquired precisely at the moment of the laser shutdown, when only the reflected beams are present. Due to the high value of the speed of light, if compared to our acquisition, we can estimate the starting temperature to be nearing 1900 K. The Second Ring reached a maximum value of around 1650 K and the Third Ring 1485 K. The temperatures retrieved are enough to allow the formation of all discussed phases.

These results seem to point out that an even bigger compositional difference in the sample has to be found in the depth of the material, more than the surface. Nonetheless, the possibility of controlling the depth of the molten pool by adjusting the starting liquid temperature could minimize this effect.

Moreover, the dimensions of this sample are small when compared to industrially produced materials such that in the case of big blocks, the effect of thermal gradient on the surface could be more noticeable. In addition, if the composition chosen does not present crystals that could provoque a sedimentation on the depth of the molten pool, a surface measurement could suffice to observe the effect of radial migration of material due to thermal gradient. In conclusion, the monitoring of the thermal gradient could make possible the observation of phase formation outside the high temperature liquid area and could be important for these more complex compositions.

8.3 AZS36: Polycrystalline solidification

The complex composition chosen as an example is AZS36 and it belongs to the ZrO_2-Al_2O_3-SiO_2 ternary system. The study of the phase diagram of the ternary system $ZrO_2 - Al_2O_3 - SiO_2$ is very important for many industrial applications. Fused cast refractories containing ZrO_2 are used in glass tanks construction due to their high resistance to corrosion.[311,312] This high resistance is due to the interlocking of alumina and ZrO_2 crystals and the glassy matrix.

AZS36 is composed of 47.6% of Al_2O_3, 29.1% of ZrO_2 and 23.3% of SiO_2 (corresponding to 49.3%w Al_2O_3, 36.5%w ZrO_2, 14.2%w SiO_2). Due to the

very high melting point, this composition was created through aerodynamic levitation and the produced beads were then crushed to form a pellet that is homogeneous in composition. It is known from the ternary diagram that the liquid system for these compositions solidifies to form different crystalline phases: baddeleiyte (monoclinic zirconia), corundum (Al_2O_3) and mullite, making this system an highly complex one. AZS36 has been observed using free-cooling and controlled cooling (30 BPM) conditions at the same starting liquid temperature in order to maintain the same amount of liquid in the sample, as illustrated in figure 8.10.

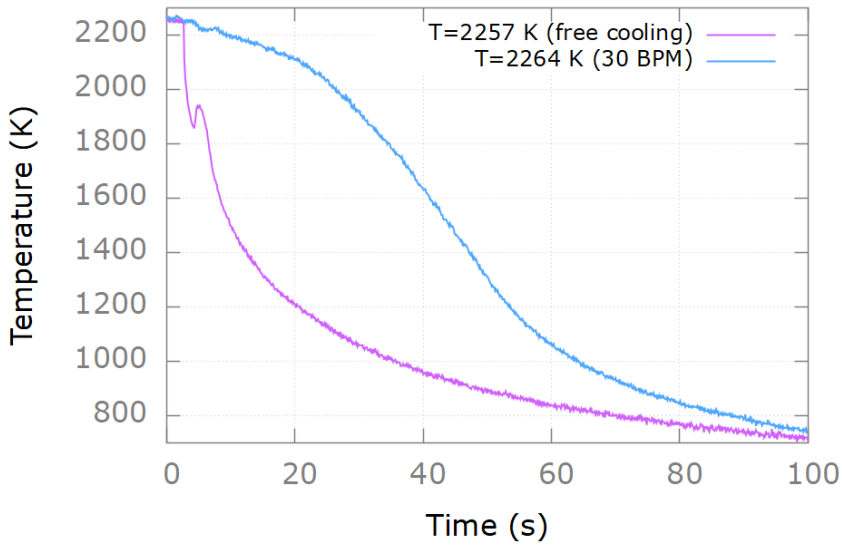

Figure 8.10: Cooling curves of AZS36: the starting temperature has been kept almost equal to guarantee the same amount of liquid prior to solidification.

We compare XRD data obtained after cooling at the higher speed and at the slowest at the same starting temperature. The results are displayed in figure 8.11. These diffractograms show intense peaks characteristic of metallic lead which was used to block the unmolten part of the sample during the measurements.

In addition to these, the figure also presents lower intensity peaks that can be indexed to the compounds retrieved in the final solids. It can be observed that the cooling speed has a crucial impact on phase formation as mullite is only retrieved after free-cooling conditions while corundum and vitreous silica is present only in controlled cooling conditions.

Moreover, it can be observed in figure 8.12 that the two coolings proceed very differently. The free cooling spectra show a continous evolution and seem to

preserve the same evolution through solidification. This is not the case for the controlled cooling. Indeed, we notably observe the appareance of narrow bands characteristic of the formation of a crystalline phase and their disappearance upon cooling. The remaining part of the spectra evolution is relatively similar to the one reported in free cooling conditions except for the apparance of an additional band at 1050 cm^{-1}, reminiscent of the signature of vitreous silica (or an aluminosilicate glass). This leads to a red shift of 150 cm^{-1} in the Christiansen point. This observed Christiansen point shift could have been taken into account due to the possibility of choosing a range for its detection. An accurate determination of the Christiansen point is essential in order to obtain reliable temperature values during the whole cooling phenomenon. Through this example we have shown that the technique is able to follow complex cooling mechanisms.

The AZS36's case illustrates here the importance of the real-time acquisition process for capturing a phenomenon occurring during a very short time frame throughout the cooling. Under controlled cooling conditions this allows us to observe the formation and disappearance of a metastable phase right before the start of solification.

In addition, it is also evident that the shift of the Christiansen point occurs right after the disappearence of the additional narrow features, so it is likely possible that the formation of the silica (or aluminosilicate) glass and the nature of the metastable phase could have something in common either from a compositional or from a kinetic point of view.

In conclusion, we have observed that the importance of the cooling speed on phase formation is crucial, especially in high complexity materials that can present incongruent or polycrystalline solidification. It is important to state that, in order to study systems of higher complexity, a more careful interpretation and analysis is required to be able to describe properly the mechanisms of multiple phase formation.

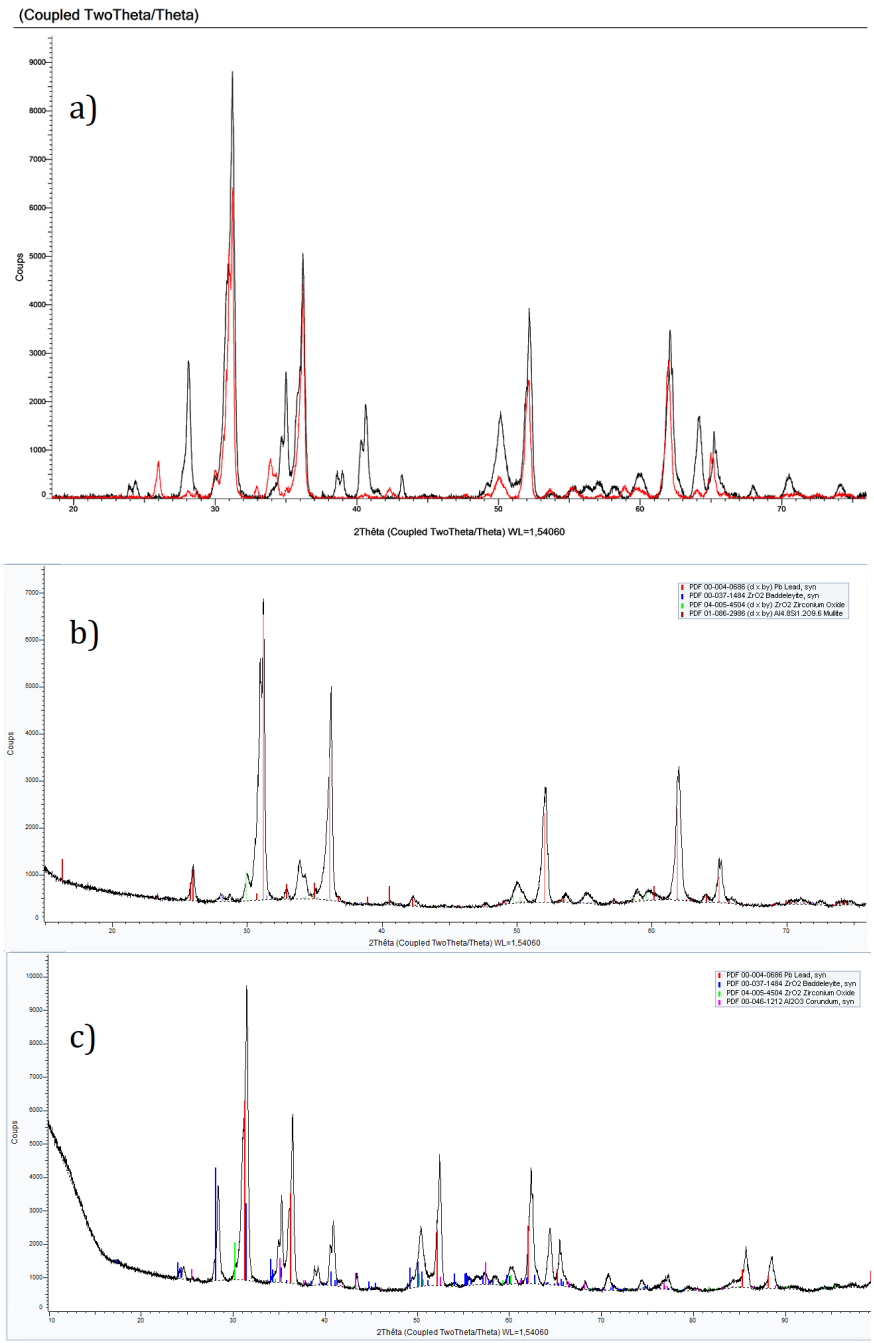

Figure 8.11: a) XRD of post cooling of AZS36 at the fastest free-cooling (Red) and the slowest controlled cooling (Black). Except for the four predominant peaks belonging to Lead, the final structures appear to be different. Peak assignment of the final structure after b) free-cooling and c) controlled cooling. It can be observed that some phases are not present in both spectra, confirming the importance of the cooling speed used to perform solidification.

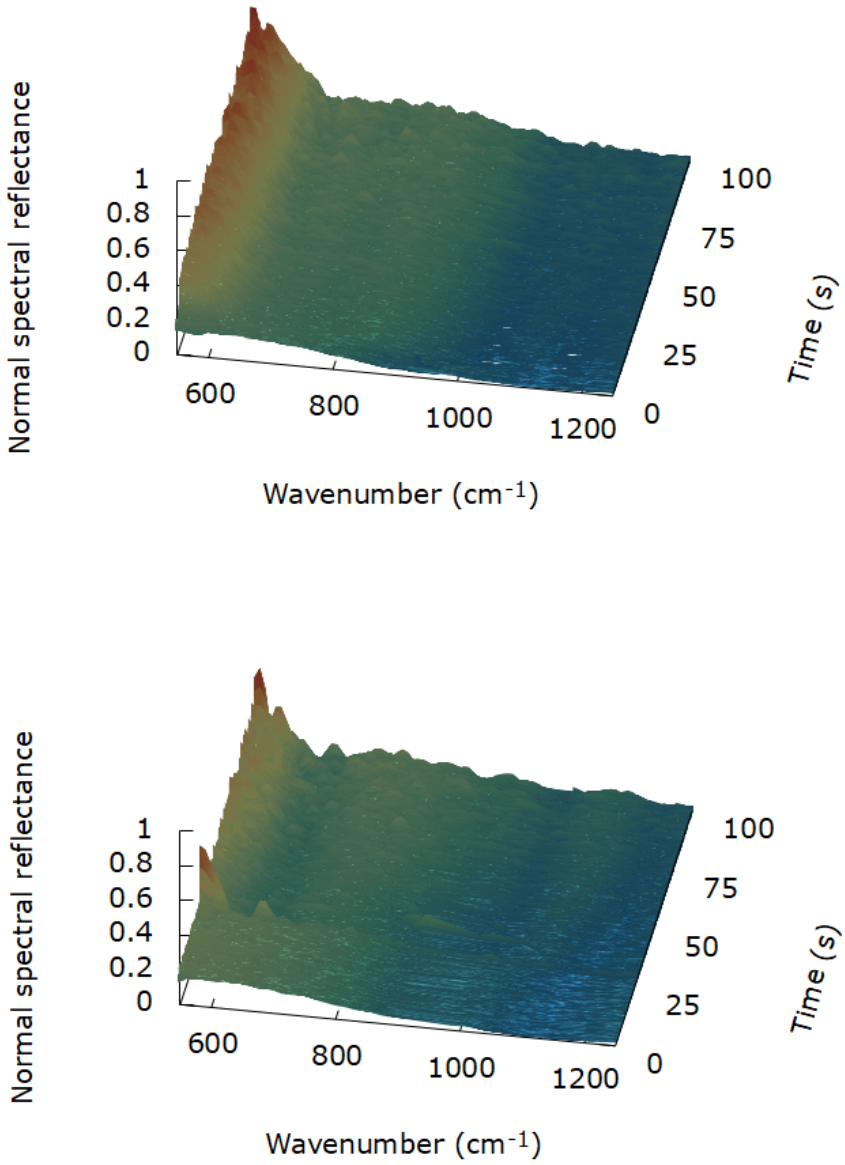

Figure 8.12: Reflectivity spectra collected during free cooling (top) and controlled cooling (bottom). It is evident that the cooling does not proceed in the same way with additional features appearing in the controlled cooling and maybe related to the appearance of metastable phases.

9

General conclusion and perspectives

Contents

9.1 Conclusion

The study of the solidification process from molten state is very important to allow a better understanding of the mechanisms of phase formation. This knowledge is needed to be able to create and engineer materials by design. In order to reach this goal, in-situ real-time experimental setups should be developed and paired with the ability to observe materials in extreme temperature conditions.

The implementation of a Rapid Scan feature on an emissometer designed to probe materials at extreme temperatures allowed the observation of solidification from molten state in real-time conditions. The kinetic nature of this phenomenon has been taken into consideration to be able to obtain precise information on structural modifications and temperature.

Real-time IR spectra and temperature evolution of cooled down molten materials have been acquired, showing differences in their solidification process. The versatility of this new experimental setup is thus shown through its application for various studies.

The first example is SiO_2 that has been used to validate the real-time technique through comparison to static measurements in a wide temperature range. Moreover, the possibility of acquiring spectra each 0.1 s in out-of-equilibrium conditions allowed the investigation of the dynamics of glass formation.

Al_2O_3 is then analyzed to observe the structural changes occuring in the undercooled metastable region. 20 spectra have been acquired to capture the metastable phenomenon that only lasts 1 second, showing a coexistence of liquid and solid until the start of the solidification.

$SrAl_2Si_2O_8$ is presented to illustrate the control of the speed of cooling through its starting temperature in the liquid and laser power operation. The results show differences in the degree of ordering of the sample during solidification.

Systems with higher complexity are finally presented to address hypothetical new features that could be implemented on the setting to allow an easier operation of the device and additional updates that could allow material engineering and design by a total control of the mechanisms of solidification.

This last section presents these hypothetical new features that, if implemented, would allow to obtain an easier control on the measurement procedure and a fuller characterization of the studied material. Among these, the implementation of an aerodynamic levitation system is discussed as it would simplify the

study of complex systems. A similar setting could also provide an additional control on the cooling speed as it could be easily operated with different gas flows that have an impact on the cooling rate during solidification from molten state.

9.2 Perspectives on additional instrumental developments

From the examples reported, it is possible to discuss some hypothetical instrumental and theoretical developments. As for the theoretical ones, it is important to highlight that in this work we only used the GDA (Gaussian Dispersion Analysis) method to analyse our spectra but yet, other more complex dielectric function theories could be employed.

The next sections present the main options that could be implemented in the setting.

With these implementations, the user would command the cooling speed, obtain temperature data before the start of the acquisition and observe and control different regions of the sample by a fully automated control on the experiment.

9.2.1 Additional implementations on the original setup

- **Automated laser control**
  As seen in this work, laser control has been a main point of the study. Nonetheless, the profile of the laser is not entirely linear so the BPM procedure that was operated on the power knob may have not given rise to the same output power during each step.

  In addition, the manual control of the laser heavily depends on the user response time to acoustic stimuli and the ability to rotate the knob without mistakes.

  The implementation of an automated system operating on laser power calibrated on the true power output curve would provide more affidability by avoiding user mistakes and by providing uniform decrease in steps or in a constant continuum.

In order to do this, the output power of the laser should be known in the used range as well as the establishment of a connection between the laser and a user interface to command the execution of a particular power decrease. If this profile is known, it could be used to calibrate the laser power to allow uniform controlled cooling speed. However, the procedure used previously was not completely unrealiable due to the possibility of retrieving the cooling speed directly from the cooling curve.

Yet, the determination is entirely post measurement such that the user is not able to know the cooling speed steps beforehand as well as the temperature reached by the sample.

- **Laser-linked calibrated pyroreflectometer(s)**
  The possibility of prolonging fast phenomena by restarting the laser during measurement is an incredibly complicated task that would require the user to memorize the time conditions and laser settings and have the ability to react accordingly fast, also taking into account the delay time of the experimental setup.

  The implementation of a laser-linked calibrated pyroreflectometer coupled with an automated laser power system would open the gates to this possibility.

  The pyroreflectometer would provide the user with the real time temperature of the sample before the start of the experiment and at any time during the acquition. The implementation of a pyroreflectometer would also allow the characterization of materials that do not possess a Christiansen point in the probed range.[313]

  Moreover, if the pyroreflectometer is connected to the automated laser power option, it would be possible to trigger the laser automatically with the known settings and at the right time (except the delay of pyroreflectometer temperature detection) to extend mestastable phases and observe more closely how the metastable phase behaves when its structure is reached and maintained for a longer time.

  In this case, the delay of temperature detection from the pyroreflectometer could be obtained to start the process beforehand such that the laser would be on again when the sample is at the temperature set by the user.

  The study and creation of materials belonging to complex systems is highly temperature dependent such that circular temperature regions are frequently capable of forming different structures.

The ability to form these polymorphs depends on the temperature reached by the sample and the amount of liquid and solid-liquid created during heating.

These phenomenas could be motitored by the implementation of a set of pyroreflectometers that can be directly displaced diametrically on the surface of the heated sample.

If that is the case, one could be fixed at the acquisition point and a set of movable pyroreflectometers could allow the user to control the sample temperature in different diametrically distant regions. The number of needed pyroreflectometers would be set to a maximum that depends on the diameter of the samples used and the possibile temperature threshold known for phase formation in that material.

- **Detection of multiple data within the same run**
  With the hypothetical implemented setting presented up to now, the spectra acquisition and the cooling information would be just retrieved at the center so in order to further expand the study new detection systems should be implemented.

  In order to do obtain information in other regions, a multiple acquisition at the same time would be necessary. These detection systems should be coupled and controlled by the user that sets a starting time common to all the acquisitions.

  In addition, the possibility of aligning the acquisition point with the pyroreflectometer would allow the observation of the desired region that will form the polymorph. In this case, multiple and interesting sets of data with known temperatures during the whole cooling process and automated by the control of the laser linked to the pyroreflectometers would be obtained in the same run.

  Nonetheless, all of this is possible only if the pyroreflectometers used can estimate the temperature as fast as the Rapid Scan acquisition of cooling phenomenon which, at least with the technology available now, is not the case.

9.2.2 Implementation of an aerodynamic levitator

- **Surface and in-depth thermal gradient minimization**
  We have seen in the previously illustrated example that the complexity of the phase diagram in study can lead to the formation of different phases.

A similar conclusion as been drawn from the example of kaolinite, in which differences in thermal treatment across the sample created structural and compositional inhomogeneities after cooling from molten state.

Both of these examples highlight that a less degree of complexity during the study could be achieved by minimizing these two factors. In order to achieve this, it is important to consider that both of these factors depend mostly on the size of the sample.

In our study, we employed a self-containing liquid sample to avoid chemical contamination with a container. For this reason, a thermal gradient across the sample is created both on the surface and in depth which can lead to increasing inhomogeneities.

A solution to this could be by using smaller samples, yet this can cause the liquid to escape its self-container or fall from the absence of enough solid surrounding material.

In order to use smaller samples and preserve the uncontaminating nature of the setup, the implementation of an aerodynamic levitator could be beneficial.

Aerodynamic levitation is a technique capable of performing laser heating on a sample that is suspended in air. Through this, small beads at very high temperature are created.

This technique can also be easily combined to other analytical techniques due to its simplicity and compactness.

- **Additional cooling speed control through gas flow**
  In this work, we have controlled the cooling speed of the sample through laser power operation. Nonetheless, this is not the only way to perform this task. It has been shown that the type of gas flow used in aerodynamic levitation experiments has an impact on the cooling speed.[314]

  If that is certain, a double control on cooling speed could be obtained, allowing an even more precise choice of the solidification path and, consequently, the creation of materials that display the desired optical and macroscopical properties in their solid form.

10

Exploration dynamique des systèmes $M_xO_y - Al_2O_3 - SiO_2$ depuis le milieu fondu jusqu'à basse température

Résumé en français. Les principaux concepts et résultats de l'étude sont mis en évidence et liés aux chapitres présents dans la thèse, par ordre chronologique

Introduction: Temps, causalité et processus naturelles

La recherche scientifique est fortement corrélée et motivée par le développement de la civilisation et la nature curieuse de l'humanité. La nature consciente de l'être humain conduit inévitablement à la recherche de réponses et d'explications aux questions concernant la nature et les phénomènes naturels.

D'un point de vue physique, le lien entre l'espace et le temps a été établi depuis longtemps par la théorie de la relativité restreinte,[1] conduisant au remplacement de l'espace euclidien tridimensionnel par l'espace de Minkowski quadridimensionnel[2] qui inclut le temps comme quatrième dimension.

Cette découverte, associée au développement de la mécanique quantique, a rapidement provoqué un changement de paradigme[3] d'abord dans la communauté scientifique, puis dans le grand public. Ce concept est fondamental en philosophie des sciences : une discipline qui recoupe la métaphysique, l'ontologie et l'épistémologie dans le but d'explorer la relation entre science et vérité.

La science est principalement menée à l'intérieur d'un paradigme, un ensemble logiquement cohérent de règles connues, alors que lorsque des révolutions scientifiques se produisent, le paradigme « change » et un nouveau cadre est utilisé pour les recherches ultérieures. Le choix d'un paradigme change complètement les visées et les interprétations de la science. Que ce choix soit fait ou non dépend de justifications tant rationnelles que sociales.

Cet argument illustre le lien fort existant entre la métaphysique et la physique, ainsi que leur influence mutuelle. Cela est dû au fait que l'interprétation métaphysique de la nature et de ses lois affecte la pratique scientifique et vice versa.

L'exemple du philosophe spéculatif Alfred North Whitehead est peut-être l'un des meilleurs pour décrire ce phénomène. Whitehead a fait ses études de mathématicien, mais ses œuvres les plus célèbres concernent principalement la métaphysique et l'ontologie, du point de vue de la philosophie des sciences.

Dans son livre "Processus et Réalité",[4] considéré comme la pierre angulaire de la métaphysique des processus,[5] il décrit deux types d'existence d'une entité. Les entités réelles font référence à celles qui existent réellement dans la nature en tant que processus et événements étendus spatio-temporellement. Le monde, selon lui, est une multiplicité d'entités réelles et leurs corrélations. Les entités abstraites sont abstraites ou dérivées d'entités réelles : un principe qui peut donner une forme particulière à une entité réelle[6]

Dans ce cas, l'existence réelle est considérée comme un processus de devenir, fortement lié au concept de temps, car chaque entité réelle possède intrinsèquement sa dimension respective de temps. Le principe de causalité est bien

respecté puisque chaque entité actuelle est causalement consécutive à celles qui la précèdent dans le temps et a pour conséquences causales celles qui suivent. On constate aisément que cette approche métaphysique de la nature est parfaitement cohérente avec le point de vue de la théorie de la relativité restreinte d'Einstein et avec la géométrie de Minkowski de l'espace-temps. Le travail de Whitehead a été influent parmi les scientifiques, notamment le chimiste physique Ilya Prigogine, le biologiste Conrad Hal Waddington et les généticiens Charles Birch et Sewall Wright, illustrant une fois de plus l'influence mutuelle de la science et de la philosophie.

La citation choisie comme ouverture de cet ouvrage s'inscrit parfaitement dans son contenu, tant l'aspect dynamique et son rapport au temps y sont fondamentaux. L'objectif est de développer un appareil en temps réel pour pouvoir observer la transition de phase à partir de l'état fondu et étudier les changements microstructuraux qui s'y produisent. Afin d'atteindre cet objectif, il est important de considérer attentivement un autre facteur clé : le temps.

La principale caractéristique de cette étude est la possibilité d'effectuer des mesures dynamiques en temps réel. Pourtant, il est extrêmement difficile de définir ce que signifie « temps réel » et s'il s'agit d'un instant ou d'un intervalle de temps.

Le concept de cône de lumière dans l'espace de Minkowski illustre clairement que la causalité relie les événements et grâce à ce principe, il est possible de distinguer les événements passés et futurs. Dans cet exemple, le présent est désigné par l'événement unique se produisant à un instant de temps t_0, illustré par un point. L'hypersurface du présent contient tous les autres événements à t_0 qui ne sont pas corrélés à cet événement.

Dans ce cadre, nous pouvons voir que le temps réel coïncide avec le présent et plus précisément avec t_0. D'un point de vue mathématique et logique, cette définition est théoriquement la meilleure possible mais d'un point de vue humain ce concept est inaccessible et même inutile à l'application.

L'intervalle de temps théoriquement mesurable le plus court est le temps de Planck correspondant approximativement à 5,39 x 10^{-44} s.

Tous les processus physiques se produisent à des échelles de temps plus longues. Les unités supérieures à 10^{-3} s commencent à impliquer la vie humaine et notre perception de celle-ci.

Les échelles de temps plus longues impliquent la durée de vie des espèces biologiques et les temps géologiques.. Tous les temps au-delà de 10^{15} s sont théoriques car ils dépassent la durée de vie de l'univers.

Tous les phénomènes naturels et physiques décrits ont leur propre échelle de temps et leur classification en phénomènes rapides ou lents repose entièrement sur la perspective humaine puisque nous en sommes les observateurs. On peut facilement considérer que tous les phénomènes se produisant à des échelles de temps plus courtes que notre perception (10^{-3} s) sont rapides, et vice versa.

Néanmoins, il est toujours important de réfléchir à la manière de bien décrire le temps réel d'un point de vue plus humain et pratique. Tout d'abord, nous devons tenir compte des limites imposées par la technologie, en la limitant à 10^{-6}. Enfin, la description du temps réel doit être liée à la façon dont nous percevons le moment présent. Il a été constaté que la perception humaine du moment présent est intrinsèquement liée à des informations perceptives qui peuvent être stockées jusqu'à 10^{-3} . Passé ce délai, l'information a été stockée et appartient donc au passé. Cela signifie également que le temps n'est pas vécu directement.

En conclusion, il semble y avoir un énorme décalage entre la nature scientifique et l'existence du temps et notre expérience de celui-ci. Cette question métaphysique ne sera pas discutée plus avant, car elle sort du cadre de ce travail.

Les chapitres suivants présentent les grandes lignes et la motivation de l'étude, l'état de l'art et enfin quelques résultats et discussion.

Techniques d'acquisition pour l'ingénierie des matériaux

La quête de l'acquisition de données à grande vitesse est toujours en cours en raison de la nécessité de l'amélioration de l'instrumentation pour pouvoir observer des phénomènes rapides. En effet, l'apparition et l'étude d'états transitoires, métastables ou des phases hors équilibre sont encore une question ouverte en science, forçant les scientifiques à trouver de nouvelles façons rapides de sonder les matériaux. La production industrielle à grande échelle est également affectée puisque la plupart de ces phénomènes rapides se produisent sous forme de processus à haute température lors de la solidification. Les domaines de recherche dans le secteur industriel sont variés mais ceux qui nous intéressent dans cette étude sont ceux impliqués dans la conception des matériaux et concernent les diagrammes de phase, les effets sur le matériau par les impuretés et la stabilisation des polymorphes. Il a été démontré que le refroidissement rapide des matériaux en phase liquide supprime la croissance et la nucléation, si la vitesse est suffisante. Lorsque les deux phases solidifiées présentent des différences microstructurales, ce fait doit être recherché dans la voie de solidification. En effet, les propriétés mécaniques et physiques d'un matériau dépendent fortement des paramètres impliqués dans sa production par refroidissement à partir de l'état liquide, même lorsque sa composition chimique reste inchangée. Grâce à la connaissance complète et au contrôle de

la température et du taux de refroidissement d'un matériau, il est possible de modifier sa microstructure, ce qui entraîne différentes propriétés macroscopiques à l'état solide. Cette approche stratégique de la conception des matériaux combinée aux connaissances acquises par des études à haute température, la formation de phases et les propriétés microstructurales, contribueront à la fois à l'amélioration de matériaux applicables bien connus et le développement de nouveaux matériaux avec des propriétés améliorées. Afin d'observer les matériaux dans des conditions extrêmes, il est nécessaire de développer des configurations instrumentales capables d'effectuer ces mesures. L'importance d'une approche multitechnique dans le domain de la science des matériaux s'explique facilement par le fait que les informations extraites seront différentes selon la technique employée.

Ce chapitre présente les principaux problèmes concernant la production industrielle des matériaux par solidification à partir de l'état liquide et les principaux thèmes de recherche impliqués dans cette discussion. Il illustre également les principales techniques utilisées pour sonder les matériaux et les avancées instrumentales en termes de vitesse d'acquisition. L'accent est mis sur les études à haute température et l'observation du phénomène de refroidissement.

FT-IR en temps réel au cours du refroidissement

Le concept d'équilibre est fondamental lorsqu'il s'agit des sciences. La matière se transforme et se réorganise pour créer de nouvelles structures lorsqu'elle est modifiée par un agent externe, tout cela pour atteindre l'énergie minimale. Comme la matière a atteint un équilibre donné par les conditions extérieures, ses propriétés ne changent pas puisqu'il y a un échange entre l'environnement et la matière. Cette situation est la plus courante et permet aux expériences scientifiques d'être effectuée : pour quantifier une propriété de la matière, il faut lui donner un temps suffisant pour stabiliser ladite propriété afin d'obtenir des mesures précises, parce que la matière ne réagit pas toujours instantanément lorsque l'environnement est modifié.

Indépendamment de ce qu'il se passe pendant la transformation, l'approche la plus courante pour mesurer une propriété est de la quantifier dans deux états d'équilibre. Pourtant, cette approche ne considère pas un aspect très important : comment cette propriété particulière a changé au cours du phénomène. Afin de comprendre les conditions qui déterminent si la matière est transformée d'une manière ou d'une autre, un suivi de la région de déséquilibre est à faire pour permettre une compréhension plus profonde.

Pour se faire, l'instrumentation doit évoluer pour atteindre des vitesses d'acquisition et une qualité spectrale plus élevées : deux exigences qui s'opposent en raison des limitations imposées par l'électronique.

Ce chapitre illustre les spécificités utilisées pour mettre à niveau l'instrumentation afin d'effectuer des experiences d'émissivité infrarouge résolue en temps pour pouvoir suivre le refroidissement en temps réel à partir de l'état fondu.La mise en place d'une technique Rapid Scan sur un émissomètre capable de résister à des conditions extrêmes de température a permis d'atteindre une vitesse d'acquisition de 60 scans/s. La nouvelle méthode a été testée sur deux oxydes présentant diverses différences de fragilité à l'état liquide et de leur processus de solidification. Les aspects théoriques de cette implémentation sont discutés et les causes d'erreur quantifiées et minimisées via des simulations numériques à différentes températures. Le système d'acquisition est présenté ainsi que la technique de mesure qui sera adoptée dans la majeure partie de cette étude : l'arrêt du laser chauffant l'échantillon permettant l'observation du refroidissement libre à partir du liquide.

Etudes statiques et cinétiques: changements structurels

Lors de la solidification, la structure est obligée de se réorganiser pour s'adapter aux changements de température. Lorsque ce phénomène part du liquide, état dans lequel les atomes sont plus libres du fait de la rupture des liaisons, la variété des polymorphes et des recombinaisons structurales possibles s'élargit. Pour cette raison, il est crucial d'observer les conditions conduisant à la formation d'une structuration particulière.

Cette observation sera possible grâce au montage expérimental présenté précédemment. La technique utilisée pour cette caractérisation est la spectroscopie infrarouge qui est une branche de la spectroscopie basée sur l'étude de l'émission ou de l'absorption d'ondes électromagnétiques par un matériau. Le spectre récupéré à l'issue de ce phénomène physique est caractéristique du matériau. L'émittance spectrale normale permet d'obtenir les propriétés optiques à partir de la fonction diélectrique du matériau et de son évolution en température. L'analyse de la fonction diélectrique imaginaire et des bandes qui en font partie suffit à comprendre et souligner les différences structurelles et les changements avec la température pendant le processus de solidification.

Notre étude porte sur les matériaux oxydes appartenant au système ternaire $M_xO_y - Al_2O_3 - SiO_2$. M_xO_y est un oxyde qui sera remplacé tout en maintenant fixe la partie aluminosilicate. Ce choix est dû à l'importance et aux grandes possibilités qu'offre le réseau aluminosilicate. Les compositions obtenues dans ces systèmes présentent une stabilité chimique et une résistance mécanique élevées. Ils sont également utilisés dans la conception de mastics haute température, de céramiques transparentes, de verres bioactifs, de vitrocéramiques diélectriques et réfractaires, de verres photoactifs et de vitrocéramiques, de céramiques radiotransparentes et bien d'autres.

Ce chapitre présente un aperçu des moyens théoriques d'analyse des données et l'état de l'art au moment de la rédaction. La méthode utilisée pour l'ajustement des données via la fonction diélectrique imaginaire est basée sur l'utilisation de modèles de mélanges gaussiens (GDA: Gaussian Dispersion Analysis) en raison de l'élargissement des modes à haute température. L'affectation des composantes aux modes vibrationnels est basée sur les régions spectrales dans lesquelles ils se trouvent dans la littérature.

La théorie de la structure vitreuse, ainsi que des concepts tels que la nucléation et les transformations de phase, sont décrits pour faciliter la compréhension des résultats. Les principaux résultats concernant les systèmes $M_xO_y - Al_2O_3 - SiO_2$ à l'état liquide et leurs différentes morphologies en utilisant différentes techniques.

SiO_2: Le matériau vitrifiant prototype

Le SiO_2 s'est vu attribuer un rôle très important dans la fondation de la science du verre. Ce matériau est toujours considéré comme le verre prototype et a fait l'objet de nombreuses études. La raison en est facilement trouvée dans son apparente simplicité, mais en réalité, elle est structurellement complexe et ses propriétés peuvent présenter des anomalies.

Les controverses sur son comportement et sur les modèles qui peuvent être utilisés pour le prédire sont toujours présentes car la plupart d'entre eux sont insuffisants pour le décrire complètement. En raison de son importance historique et de sa simplicité chimique, des travaux supplémentaires sondant sa structure sont obligatoires car la compréhension de son comportement et de sa structure peut éclairer sur la nature du verre. Ainsi ces considérations peuvent alors être utilisées pour comprendre des verres plus complexes chimiquement et permettre d'approfondir les recherches.

Dans ce chapitre, nous discutons de la structure de la silice de l'état fondu au solide. Pour ce faire, une comparaison entre les mesures statiques et cinétiques a été effectuée. La congruence des résultats obtenus nous permet de valider notre technique dynamique en temps réel et de prouver davantage sa capacité à extraire des informations structurelles fiables. Comme nous avons effectué un chauffage statique et un refroidissement dynamique du verre de silice, nous pouvons considérer les mesures comme faisant partie d'un cercle puisque le résultat final est le point de départ de l'étude suivante et vice versa.

Le choix de SiO_2 comme matériau de référence est évident si l'on tient compte de la faible fragilité de sa phase liquide, une propriété qui décrit l'influence des changements structurels induits par la température sur le réseau. Ainsi, la structure de la silice est uniquement composée de tétraèdres SiO_4 qui peuvent former des structures cycliques de différentes tailles. Cela fait de ce matériau le

candidat idéal pour notre étude, car ses changements dynamiques seront subtils mais fourniront toujours des informations précieuses sur les mécanismes de la transition vitreuse et de vitrification. Selon notre interprétation, le phénomène de vitrification peut être interprété comme le passage d'un état de désordre dynamique à un état de désordre statique. Grâce à la possibilité de suivre le refroidissement à différentes températures, il est possible d'observer de près la région de transition vitreuse pour explorer la dynamique de la vitrification. Une structure dynamique "gelée" a été rencontrée dans différentes mesures à près de 100 K en dessous de la température de transition vitreuse et représentant un phénomène de relaxation.

Al_2O_3: L'essor d'une nouvelle structure

La cristallisation de Al_2O_3 est illustrée pour mettre en évidence l'observation du changement de nombre de coordination du liquide au solide. Ceci est dû au fait que le phénomène de refroidissement conduit à la création d'une structure basée sur des octaèdres (coordinence six) $\alpha - Al_2O_3$ à partir d'un état fondu composé de tétraèdres (coordinence 4). Les modifications structurales sont mises en évidence par la réorganisation de la matière d'un état désordonné à un réseau cristallin ordonné.

Ce chapitre présente les informations recueillies pour identifier le phénomène et les preuves obtenues à travers les études IR portant sur la formation du $\alpha - Al_2O_3$. Les principales questions que nous essayons de résoudre sont de savoir comment et quand le système atteint la phase stable solide et si une phase métastable s'est formée entre-temps. Pour se faire, notre dispositif expérimental est utilisé dans des conditions extrêmes de température et à sa vitesse maximale. Plusieurs runs sont nécessaires pour essayer d'obtenir une grande quantité de données afin de pouvoir extraire le maximum d'informations sur ce composé.

Al_2O_3 va aussi nous obliger à changer notre approche expérimentale en changeant les conditions initiales de l'acquisition. Cet aspect est important pour mettre en évidence la versatilité de la technique Rapid Scan et les diverses possibilités offertes. Comme discuté précédemment, le chauffage laser permet de contrôler la température du liquide initial. La signature de la cristallisation est mise en évidence par le graphique temps-température où la nature exothermique du processus est clairement indiquée comme une augmentation de température dans la région de sous-refroidissement. Cette caractéristique est présente lorsque le refroidissement est effectué à partir de l'état fondu.

Des données de température ambiante sont également acquises pour permettre une comparaison entre les polymorphes d'alumine et pour identifier les principaux pics contribuant à la formation de $\alpha - Al_2O_3$ et, en raison de la rareté des résultats cinétiques à grande vitesse, les bandes IR associées à la formation

de la phase α observées lors du chauffage des précurseurs ont été aussi prises en compte. Ces mesures sont importantes pour identifier et attribuer également les bandes observées aux motifs structuraux. Le chapitre se termine par une discussion des informations recueillies sur cette structure en constante évolution et donne un aperçu du processus de cristallisation.

$M_xO_y - SiO_2 - Al_2O_3$: Création de polymorphes

Les systèmes ternaires $M_xO_y - Al_2O_3 - SiO_2$ ont été étudiés pour la variété des polymorphes structuraux et ses applications. Ce chapitre illustre les résultats d'un refroidissement contrôlé opéré sur une composition spécifique connue pour pouvoir former différents polymorphes cristallins ou vitrifier en fonction de la vitesse de refroidissement du liquide. La possibilité de forcer un chemin de refroidissement sur l'échantillon est également étudiée.

Dans ce cas, au lieu d'un arrêt complet de la puissance du laser, une décroissance progressive à différents pas de temps sera utilisée. Les pas de temps seront décrits à travers le concept de BPM (Beats Per Minute) pour permettre une division égale du temps. A partir de ce concept, il sera possible d'extraire la vitesse de refroidissement des courbes de refroidissement obtenues grâce à la dérivée. Une autre façon de contrôler et de modifier la vitesse de refroidissement est d'utiliser la température initiale puisqu'elle en dépend fortement.

Les échantillons utilisés pour ce test présentent un haut degré de polymorphisme et ils sont étudiés par les méthodes de refroidissement décrites précédemment. Pour ce faire, une série d'expériences différentes doit être menée pour récupérer des informations sur les deux formes de refroidissement contrôlé. Ces méthodes de refroidissement sont ensuite comparées pour avoir un aperçu de leurs différences de vitesse et de formation de phase. A la fin de chaque refroidissement, la nature structurale de l'échantillon est confirmée par des mesures DRX.

Une exploration importante pour ce matériau consisterait à analyser si et quel type de changement structural se produit par une différence de vitesse de refroidissement. Pour cette raison, la majeure partie de l'étude se concentre à nouveau sur la région de surfusion car la plupart des changements peuvent être observés dans cette région métastable, comme le montrent les résultats précédents sur Al_2O_3.

Ce dernier chapitre a pour but d'illustrer les possibilités supplémentaires du cadre expérimental en tant qu'outil significatif pour l'ingénierie et la conception des matériaux. Cela est dû à l'exhaustivité des informations acquises lors de la mesure de refroidissement qui pourrait ensuite être utilisée pour solidifier le matériau dans sa structure préférée.

Systemes complexes

La solidification à partir de l'état fondu de systèmes plus complexes peut donner lieu à une plus grande variété de phases solides et métastables, par rapport aux systèmes simples ou binaires.

Afin d'illustrer l'intérêt de notre approche de spectroscpie rapide in-situ pour des systèmes plus complexes, des exemples de mesures sont présentés dans le cas d'un liquide de composition Al_2O_3-SiO_2 et d'une composition appartenant au système $ZrO_2 - Al_2O_3 - SiO_2$ largement utilisée pour des applications industrielles comme matériaux réfractaires.

Ces expériences seront conduitent dans des conditions de refroidissement libre mais aussi de refroidissement contrôlé. Les données obtenues illustreront l'importance de la vitesse de refroidissement et de la température de départ sur le chemin de solidification et la nature des différentes phases solides formées à l'issu du refroidissement.

Elles nous permettrons également de dresser des perspectives sur l'utilisation future de cette technique pour surveiller in-situ et en temps réel la solidification de matériaux complexes et de définir de nouvelles options qui pourraient être mises en œuvre pour améliorer encore le cadre expérimental.

Conclusion generale et perspectives

L'étude du processus de solidification à partir de l'état fondu est très importante pour permettre une meilleure compréhension des mécanismes de formation des phases. Ces connaissances sont nécessaires pour pouvoir créer et concevoir des matériaux. Afin d'atteindre cet objectif, des configurations expérimentales in situ en temps réel doivent être développées et associées à la capacité d'observer les matériaux dans des conditions de température extrêmes.

La mise en œuvre d'une fonction Rapid Scan sur un émissomètre conçu pour sonder les matériaux à des températures extrêmes a permis d'observer la solidification à partir de l'état fondu dans des conditions en temps réel. La nature cinétique de ce phénomène a été prise en compte pour pouvoir obtenir des informations précises sur les modifications structurelles et la température.

Des spectres IR en temps réel et l'évolution de la température des matériaux fondus refroidis ont été acquis, montrant des différences dans leur processus de solidification. La polyvalence de ce nouveau dispositif expérimental est ainsi démontrée à travers son application à diverses études.

Le premier exemple est SiO_2 qui a été utilisé pour valider la technique en temps réel par comparaison avec des mesures statiques dans une large plage

de températures. De plus, la possibilité d'acquérir des spectres toutes les 0,1 s dans des conditions hors équilibre a permis d'étudier la dynamique de la formation du verre.

Al_2O_3 est ensuite analysé pour observer les changements structuraux se produisant dans la région métastable surfondue. 20 spectres ont été acquis pour capturer le phénomène métastable qui ne dure qu'une seconde, montrant une coexistence du liquide et du solide jusqu'à la fin de la solidification.

$SrAl_2Si_2O_8$ est présenté pour illustrer le contrôle de la vitesse de refroidissement via la température initiale du liquide ou bien une diminution progressive et controlée de la puissance du laser. Les résultats montrent des différences dans le degré d'ordonnancement de l'échantillon lors de la solidification.

Des systèmes plus complexes sont enfin présentés pour aborder d'hypothétiques nouvelles fonctionnalités qui pourraient être implémentées sur le terrain et permettre un fonctionnement plus facile du dispositif. Ces mises à jour supplémentaires seront une étape vers un dispotitif pemettant l'ingénierie et la conception des matériaux via un contrôle total des mécanismes de solidification. La dernière section présente ces nouvelles fonctionnalités hypothétiques qui, si elles étaient mises en œuvre, permettraient d'obtenir un contrôle plus facile de la procédure de mesure et une caractérisation plus complète du matériau étudié. Parmi celles-ci, la mise en œuvre d'un système de lévitation aérodynamique est discutée car elle simplifierait l'étude de systèmes complexes. Cette méthode de lévitation pourrait également fournir un contrôle supplémentaire sur la vitesse de refroidissement lors de la solidification à partir de l'état fondu en jouant sur le flux et la nature du gaz de lévitation.

Bibliography

[1] A. Einstein, Zur Elektrodynamik bewegter Körper, Annalen der Physik 17: 891 (1905).

[2] D. Morin, Introduction to Classical Mechanics, Cambridge University Press, Cambridge, 11, Appendix I (2007) ISBN 1-139-46837-5.

[3] T.Kuhn, The Structure of Scientific Revolutions (1962).

[4] A. N. Whitehead, Process and Reality, New York: Macmillan (1929).

[5] N. Rescher, Process Metaphysics: An Introduction to Process Philosophy, SUNY Press (1996).

[6] M. Weber, After Whitehead: Rescher on Process Metaphysics, Frankfurt / Paris / Lancaster, Ontos Verlag (2004) (ISBN 3-937202-49-8).

[7] M. Planck, Über irreversible Strahlungsvorgänge. Sitzungsberichte der Königlich Preußischen Akademie der Wissenschaften zu Berlin (1899). 5: 440–480.

[8] G. Hooft and S. Vandoren, Time in Powers of Ten: Natural Phenomena and Their Timescales, World Scientific (2014).

[9] P.A. White, The perceived present: What is it, and what is it there for?, Psychonomic Bulletin & Review (2020) https://doi.org/10.3758/s13423-020-01726-7.

[10] P. Castany, F. Diologent, A. Rossoll, J.-F. Despois, C. Bezençon, A. Mortensen, Influence of quench rate and microstructure on bendability of AA6016 aluminum alloys, Materials Science and Engineering: A, 559 (2013) 558-565, https://doi.org/10.1016/j.msea.2012.08.141.

[11] Y. Tomita and K. Okabayashi, Effect of quench rate on microstructure and tensile properties of ALSL 4320 and 4340 steels. Metall Trans A 18, 115–121 (1987). https://doi.org/10.1007/BF02646228.

[12] K.H. Eckelmeyer et al., The effect of quench rate on the microstructure, mechanical properties, and corrosion behavior of U-6 wt pct Nb. Metall Trans A 15, 1319–1330 (1984). https://doi.org/10.1007/BF02648560.

[13] D. Ehrt, Photoactive glasses and glass ceramics, IOP Conf. Ser. Mater. Sci. Eng. 21 (2011), 12001. doi:10.1088/1757-899X/21/1/012001.

[14] A. Goel, S. Kapoor, A. Tilocca, R.R. Rajagopal, J.M.F. Ferreira, Structural role of zinc in biodegradation of alkali-free bioactive glasses. J. Mater. Chem. B 1, (2013) 3073. doi:10.1039/c3tb20163e.

[15] G. Kaur, P. Sharma, V. Kumar, K. Singh, Assessment of in vitro bioactivity of $SiO_2 - BaO - ZnO - B_2O_3 - Al_2O_3$ glasses: An optico-analytical approach. Mater. Sci. Eng. C 32, (2012) 1941–1947. doi:10.1016/j.msec.2012.05.034.

[16] M. Boyer et al., Enhanced Transparency through Second Phase Crystallization in $BaAl_4O_7$ Scintillating Ceramics. Cryst. Growth Des. 16 (2016), 386–395. doi:10.1021/acs.cgd.5b01374.

[17] X.L. Duan et al., Preparation and characterization of Co^{2+}-doped $ZnO\breve{}Al_2O_3\breve{}SiO_2$ glass-ceramics by the sol–gel method. Mater. Res. Bull. 38 (2003), 705–711. doi:10.1016/S0025-5408(03)00009-6.

[18] N. Najafizadeh et al., Selection of solidification pathway in rapid solidification processes, Physical Review Materials, 7 (2023) 23403. 10.1103/PhysRevMaterials.7.023403.

[19] J. Ulrich, P. Frohberg, Problems, potentials and future of industrial crystallization, Frontiers of Chemical Science and Engineering 7 (2013) 1-8.

[20] A. Kroupa, Modelling of phase diagrams and thermodynamic properties using Calphad method – Development of thermodynamic databases, Computational Materials Science 66 (2013) 3-13, https://doi.org/10.1016/j.commatsci.2012.02.003.

[21] H. Xiong et al., A generalized computational interface for combined thermodynamic and kinetic modeling. Calphad (2011) 35(3): 391–395.

[22] S. Al-Jibbouri, C. Strege, J. Ulrich, Crystallization kinetics of epsomite influenced by pH-value and impurities. Journal of Crystal Growth, (2002) 236(1–3): 400–406.

[23] K. Sangwal, On the nature of supersaturation barriers observed during the growth of crystals from aqueous solutions containing impurities. Journal of Crystal Growth, 2002, 242(1–2): 215–228.

[24] L. Dang, H. Wei, J. Wang, Effects of ionic impurities (Fe^{2+} and SO_4^{2-}) on the crystal growth and morphology of phosphoric acid hemihydrate during batch crystallization. Industrial & Engineering Chemistry Research (2007) 46(10): 3341–3347.

[25] C.-H. Gu, et al., Stabilization of a metastable polymorph of sulfamerazine by structurally related additives, Journal of Crystal Growth 235.1-4 (2002): 471-481.

[26] M.-G. Song et al., Stabilization of gamma alumina slurry for chemical–mechanical polishing of copper, Journal of Colloid and Interface Science, 300, 2 (2006) 603-611, https://doi.org/10.1016/j.jcis.2006.04.046.

[27] P. Duwez et al., Stabilization of zirconia with calcia and magnesia, Journal of the American Ceramic Society 35.5 (1952): 107-113.

[28] S. Grdanovska, Characterization of radiation damage to a novel photonic crystal sensor, (2015) 10.13016/M2BZ0D.

[29] R. Purohit and P. Venugopalan, Polymorphism: an overview. Reson (2009) 14(9): 882–893.

[30] Z.Q. Yu et al., Recent advances in crystallization control: an industrial perspective. Chemical Engineering Research & Design (2007) 85(7): 893–905.

[31] L. Yu et al., Crystallization and polymorphism of conformationally flexible molecules: problems, patterns, and strategies. Organic Process Research & Development (2000) 4(5): 396–402.

[32] A.Y. Lee, Crystal polymorphism in chemical process development, Chem Biomol Eng (2011) 2(1): 259–280.

[33] J.S. Capes and R.E. Cameron, Contact line crystallization to obtain metastable polymorphs, Crystal Growth & Design (2006) 7(1): 108–112.

[34] N. Zencirci et al., Crystallization of metastable polymorphs of phenobarbital by isomorphic seeding, Crystal Growth & Design, (2009) 9(8): 3444–3456.

[35] H-P. Cheng et al., Quantum, classical, and multi-scale simulation of silica-water interaction: Molecules, clusters, and extended systems. Journal of Computer-Aided Materials Design 13 (2006) 161-183. 10.1007/s10820-006-9009-x.

[36] P. Duwez, R. H. Willens, and W. Klement Jr., Continuous series of metastable solid solutions in silver-copper alloys, J. Appl. Phys. 31, 1136 (1960).

[37] W. Klement Jr., R. H. Willens, and P.O.L. Duwez, Non-crystalline structure in solidified gold–silicon alloys, Nature 187, 869 (1960).

[38] H. Jones, Rapid solidification of metals and alloys, The institution of metallurgists, London, UK, (1982).

[39] W. Kurz and R. Trivedi, Rapid solidification processing and microstructure formation, Mater. Sci. Eng.: A 179, 46 (1994).

[40] R. Mehrabian, Rapid Solidification, Int. Mater. Rev. 27, 185 (1982).

[41] O. Fisette et al., Synergistic Applications of MD and NMR for the Study of Biological Systems, Journal of Biomedicine and Biotechnology (2012), 254208 doi:10.1155/2012/254208.

[42] F. Foglia et al., Decoupling polymer, water and ion transport dynamics in ion-selective membranes for fuel cell applications, Journal of Non-Crystalline Solids: X. 13, (2021) 100073. 10.1016/j.nocx.2021.100073.

[43] J. W. E. Drewitt et al., From Short to Medium Range Order in Glasses and Melts by Diffraction and Raman Spectroscopy, Reviews in Mineralogy and Geochemistry (2022).

[44] A.P. Sokolov, V. Garcia Sakai, Experimental techniques for studies of dynamics in soft materials, in: V. Garcia Sakai, C. Albana-Simionescu, S.-A. Chen (Eds.), Dynamics of Soft Matter, Springer USA (2012) pp. 1–23. ISBN: 978-1-4614-0727-0.

[45] L. Hennet et al., Application of time resolved x-ray diffraction to study the solidification of glass-forming melts, High Temp.-High Press. 40 (2011) 263–270.

[46] L. Hennet et al., Fast x-ray scattering measurements on molten alumina using a 120° curved position sensitive detector, Review of Scientific Instruments 73, 124 (2002); https://doi.org/10.1063/1.1426228.

[47] H.E. Fischer, A.C. Barnes, P.S. Salmon, Neutron and x-ray diffraction studies of liquids and glasses. Rep Prog Phys 69: 233–299 (2006) doi:10.1088/0034-4885/69/1/R05.

[48] P. Zeeman, On the influence of magnetism on the nature of the light emitted by a substance, Philosophical Magazine 5th series, 43 (262): (1897) 226–239. doi:10.1080/14786449708620985.

[49] A. Abragam, The Principles of Nuclear Magnetism, Clarendon, Oxford (1961).

[50] K. J. D. MacKenzie and M. E. Smith, Multinuclear Solid State NMR of Inorganic Materials. Pergamon Press: Oxford (2002).

[51] E.R. Andrew et al., Removal of dipolar broadening of nuclear magnetic resonance spectra of solids by specimen rotation. Nature (1959), 183 (4678), 1802-1803.

[52] I.J. Lowe, I. J., Free induction decays of rotating solids. Phys. Rev. Lett. (1959), 2 (7), 285-287.

[53] D. Massiot et al., Structure and dynamics of oxide melts and glasses: A view from multinuclear and high temperature NMR. J. Non-Cryst. Solids (2008), 354 (2), 249-254.

[54] J. Jeener et al., Investigation of exchange processes by two-dimensional NMR spectroscopy, J. Chem. Phys. (1979) 71 (11), 4546-4553.

[55] I. Farnan and J.F. Stebbins, The nature of the glass transition in a silica-rich oxide melt. Science (1994) 265 (5176), 1206-1209.

[56] P. Florian, D. Massiot, B. Poe, I. Farnan, J.-P. Coutures, A time resolved ^{27}Al NMR study of the cooling process of liquid alumina from 2450 °C to crystallisation, Solid State Nuclear Magnetic Resonance 5 (1995) 233-238, https://doi.org/10.1016/0926-2040(95)01188-X.

[57] M. Yoshizawa and M. Kurosawa, Femtosecond time-resolved Raman spectroscopy using stimulated Raman scattering, Phys. Rev. A 61, 013808 (1999).

[58] M. Kühnel et al., Time-resolved study of crystallization in deeply cooled liquid parahydrogen, Physical review letters vol. 106,24 (2011): 245301. doi:10.1103/PhysRevLett.106.245301.

[59] M. Gonzalez, Force fields and molecular dynamics simulations. École thématique de la Société Française de la Neutronique. 12. 169-200. (2011) 10.1051/sfn/201112009.

[60] M.Salanne et al., Including many-body effects in models for ionic liquids, Theor Chem Acc (2012) 131:1143,10.1007/s00214-012-1143-9.

[61] M. Salanne and P. A. Madden, Polarization effects in ionic solids and melts, Molecular Physics: An International Journal at the Interface Between Chemistry and Physics, (2011) 109:19, 2299-2315.

[62] M. Salanne et al., Conductivity-Viscosity-Structure: Unpicking the Relationship in an Ionic Liquid, J. Phys. Chem. B (2007) 111, 4678-4684.

[63] A. Pedone et al., A New Self-Consistent Empirical Interatomic Potential Model for Oxides, Silicates, and Silica-Based Glasses, J. Phys. Chem. B (2006) 110, 11780-11795.

[64] T. Karmakar et al., Collective variables for the study of crystallisation, Molecular Physics 119.19-20 (2021): e1893848.

[65] A. Hasmy, S. Ispas, Simona and B. Hehlen, Percolation transitions in compressed SiO_2 glasses. Nature. 599. 62-66 (2021).

[66] J. Matthew, D. Lane, Cooling rate and stress relaxation in silica melts and glasses via microsecond molecular dynamics, Phys. Rev. E 92, 012320 (2015).

[67] Z. Zhang, W. Kob and S.Ispas, First-principles study of the surface of silica and sodium silicate glasses, Phys. Rev. B 103, (2021) 184201.

[68] H. Jabraoui et al., Behaviors of sodium and calcium ions at the borosilicate glass–water interface: Gaining new insights through an ab initio molecular dynamics study; The Journal of Chemical Physics 156.13 (2022).

[69] D. De Sousa Meneses, P. Melin, L. del Campo, L. Cosson, P. Echegut, Apparatus for measuring the emittance of materials from far infrared to visible wavelengths in extreme conditions of temperature, Infrared Phys. Technol. 69 (2015) 96–101, http://dx.doi.org/10.1016/j.infrared.2015.01.011.

[70] Option for Rapid Scan, Time-Resolved Spectroscopy (TRS) using a FT-IR Spectrometer of the VERTEX Series, S129 User Instructions, Bruker Optik.

[71] J.M. Hollas, Modern spectroscopy, Wiley (2004).

[72] D. De Sousa Meneses, P. Melin, L. del Campo, O. Rozenbaum, L. Cosson, Probing high temperature thermal emissive properties of energy materials and coatings with emission spectroscopy augmented by in situ reflection, Infrared Phys. Technol. 108 (2020) 103329, http://dx.doi.org/10.1016/j.infrared.2020.103329.

[73] J.R. Howell, M.P. Menguc, R. Siegel, Thermal Radiation Heat Transfer, fifth ed., CRC Press, Boca Raton (2010) http://dx.doi.org/10.1201/9781439894552.

[74] P.H. Zhang, R.Z. Chang, Z. Wei, H. Cao and X.N. Zhou, The melting point, latent heat of solidification, and enthalpy for both solid and liquid α-Al_2O_3 in the range 550-2400 K, Int. J. Thermophys. 7 (1986) 811–819.

[75] M. Schubert, T.E. Tiwald and C.M. Herzinger, Infrared dielectric anisotropy and phonon modes of sapphire, Phys. Rev. B 61 (12) (2000) 8187–8201, http://dx.doi.org/10.1103/PhysRevB.61.8187.

[76] J.Y. Yang, M. Xu and L.H. Liu, Infrared radiative properties of alumina up to the melting point: A first-principles study, J. Quant. Spectrosc. Radiat. Transfer 184 (2016) 111–117, http://dx.doi.org/10.1016/j.jqsrt.2016.07.006.

[77] V. Petrov and A. Vorobyev, Spectral emissivity and radiance temperature plateau of self-supporting alumina melt at rapid solidification, High Temp.- High Press. 35/36 (2003) 321–329, http://dx.doi.org/10.1068/HTJR141.

[78] H. Sakate et al., Observation of Al_2O_3 melting and freezing plateaus using a cavity-type tungsten crucible, Metrologia 32 (2) (1995) 129.

[79] I.G. Polyakova, The Main Silica Phases and Some of their Properties, De Gruyter (2014) 197–268, http://dx.doi.org/10.1515/9783110298581.197.

[80] P.F. McMillan, B.T. Poe, P.H. Gillet and B. Reynard, A study of SiO_2 glass and supercooled liquid to 1950 K via high-temperature Raman spectroscopy, Geochim. Cosmochim. Acta 58 (17) (1994) 3653–3664, http://dx.doi.org/10.1016/0016-7037(94)90156-2.

[81] D. Huang, C. Guo, M. Zhang and L. Shi, Characteristics of nanoporous silica aerogel under high temperature from 950 °C to 1200 °C, Mater. Des. 129 (2017) 82–90, http://dx.doi.org/10.1016/j.matdes.2017.05.024.

[82] B. Vessal, M. Amini, D. Fincham and C.R.A. Catlow, Water-like melting behaviour of SiO_2 investigated by the molecular dynamics simulation technique, Philos. Mag. B 60 (6) (1989) 753–775.

[83] J. Kubicki and A. Lasaga, Molecular dynamics simulations of SiO_2 melt and glass: Ionic and covalent models, Am. Mineral 73 (1988) 941–955.

[84] C. A. Angell, Formation of glasses from liquids and biopolymers. Science 267,(1995) 1924–1935, doi: 10.1126/science.267.5206.1924.

[85] W. Herres and J. Gronholz, Understanding FTIR data processing part 1: Data acquisition and Fourier transformation 1, (2007).

[86] B. Rousseau, J. Brun, D. Meneses and P. Echegut, Temperature measurement: Christiansen wavelength and blackbody reference, Int. J. Thermophys. 26 (2005) 1277–1286, http://dx.doi.org/10.1007/s10765-005-6726-4.

[87] J. Manara et al., Long wavelength infrared radiation thermometry for non-contact temperature measurements in gas turbines, Infrared Phys. Technol. 80 (2017) http://dx.doi.org/10.1016/j.infrared.2016.11.014.

[88] D. Hernandez, A. Netchaieff and A. Stein, True temperature measurement on metallic-surfaces using a two-color pyroreflectometer method, Rev. Sci. Instrum. 80(2009) 094903, http://dx.doi.org/10.1063/1.3208011.

[89] J.M. André, K. Le Guen, P. Jonnard, N. Mahne, A. Giglia, et al., On the Kramers-Kronig transform with logarithmic kernel for the reflection phase in the Drudemodel, J. Mod. Opt. 57 (16) (2010) 1504, http://dx.doi.org/10.1080/09500340.2010.506015.

[90] A. Arora, K. Singh, O.P. Pandey, Thermal, structural and crystallization kinetics of $SiO_2\check{}BaO\check{}ZnO\check{}B_2O_3\check{}Al_2O_3$ glass samples as a sealant for SOFC. Int. J. Hydrogen Energy 36, (2011) 14948–14955. doi:10.1016/j.ijhydene.2011.03.036.

[91] X.L. Duan et al., Preparation and characterization of Co^{2+}-doped $ZnO\check{}Al_2O_3\check{}SiO_2$ glass-ceramics by the sol–gel method, Mater. Res. Bull. 38, (2003) 705–711. doi:10.1016/S0025-5408(03)00009-6.

[92] G. Kaur, P. Sharma, V. Kumar and K. Singh, Assessment of in vitro bioactivity of $SiO_2 - BaO - ZnO - B_2O_3 - Al_2O_3$ glasses: An optico-analytical approach, Mater. Sci. Eng. C 32, (2011) 1941–1947. doi:10.1016/j.msec.2012.05.034.

[93] G.H. Beall, Refractory glass–ceramics based on alkaline earth aluminosilicates, J. Eur. Ceram. Soc. 29, (2009) 1211–1219. doi:10.1016/j.jeurceramsoc.2008.08.010.

[94] D. Ehrt, Photoactive glasses and glass ceramics, IOP Conf. Ser. Mater. Sci. Eng. 21, (2011) 12001. doi:10.1088/1757-899X/21/1/012001.

[95] G.V. Lisachuk, Ceramic radiotransparent materials on the basis of $BaO-Al_2O_3-SiO_2$ and $SrO - Al_2O_3 - SiO_2$ systems. Epa. - J. Silic. Based Compos. Mater. 67, (2015) 20–23. doi:10.14382/epitoanyag-jsbcm.2015.4.

[96] J.M. Thompson, Infrared spectroscopy, Pan Stanford (2018).

[97] A.M. Efimov and E.G. Makarova, Dispersion equation for the complex dielectric constant of vitreous materials and the dispersion analysis of their reflection spectra Fiz. Khim. Stekla (Sov. J. Glass Phys. Chem.) 11 (1985) 385.

[98] E.I. Kamitsos, Y.D. Yiannopoulos, C.P. Varsamis and H. Jain, Structure-property correlation in glasses by infrared reflectance spectroscopy, Journal of Non-Crystalline Solids 222, (1997) 59-68, https://doi.org/10.1016/S0022-3093(97)90097-1.

[99] S. A. MacDonald, C. R. Schardt, D. J. Masiello and J. H. Simmons, Dispersion analysis of FTIR reflection measurements in silicate glasses, Journal of Non-Crystalline Solids, 275 (2000) 72-82, https://doi.org/10.1016/S0022-3093(00)00121-6.

[100] C.T. Moynihan, A.J. Easteal, J. Wilder and J. Tucker, Dependence of the glass transition temperature on heating and cooling rate. J. Phys. Chem. 78 (1974) 2673–2677. doi:10.1021/j100619a008.

[101] W. Vogel, THE DEVELOPMENT OF THE CLASSICAL STRUCTURE THEORIES, in: Structure and Crystallization of Glasses. Elsevier, (1971) 14–20. doi:10.1016/B978-0-08-006998-2.50005-0.

[102] L. Cormier, Nucleation in Glasses – New Experimental Findings and Recent Theories, Procedia Materials Science 7 (2014) 60-71, 2211-8128, https://doi.org/10.1016/j.mspro.2014.10.009.

[103] J.W.P Schmelzer, G.S. Boltachev and V.G. Baidakov, Classical and generalized Gibbs' approaches and the work of critical cluster formation in nucleation theory. J. Chem. Phys. 124 (2006) 194503.

[104] J.W.P. Schmelzer, A.R. Gokhman and V.M. Fokin, Dynamics of first-order phase transitions in multicomponent systems: a new theoretical approach. J. Colloid Interface Sci. 272 (2004) 109-133.

[105] M. Grant and C. Sagui, Theory of nucleation and growth during phase separation, Phys. Rev. E 59, 4175-4187 (1999). 59. 10.1103/PhysRevE.59.4175.

[106] C. Boulesteix, Diffusionless phase transitions and related structures in oxides, Trans Tech (1992).

[107] K. Mishchik, Ultrafast laser-induced modification of optical glasses : a spectroscopy insight into the microscopic mechanisms (2012).

[108] W. Ostwald, Studien über die bildung und umwandlung fester körper. Z. Phys. Chem. 22 (1892) 289-330.

[109] G. Lucovsky, Specification of medium range order in amorphous materials, Journal of Non-Crystalline Solids, 97–98,1 (1987) 155-158, https://doi.org/10.1016/0022-3093(87)90036-6.

[110] W.H. Zachariasen, The atomic arrangement in glass, J. Am. Chem. Soc. (1932) 54, 10, 3841–3851.

[111] B.E. Warren, Summary of work on atomic arrangement in glass. Journal of the American Ceramic Society 24.8 (1941): 256-261.

[112] G.N. Greaves, Random network models. In: Defects and disorder in crystalline and amorphous solids. Dordrecht: Springer Netherlands (1994) 87-122.

[113] L.G. Engelhardt, D. Zeigan, H. Jancke,W. Wieker and D. Hoebbel, ^{29}Si-NMR spectroscopy of silicate solutions. 2. On the dependence of the structure of silicate anions in water solutions from the Na:Si ratio. Zeitschrift für Anorg. und Allg. Chemie 418, (1975) 17–28, doi:10.1002/zaac.19754180103.

[114] A. Novikov, Structure and dynamics of aluminosilicate glasses and melts, Thèse de doctorat Science des matériaux Orléans (2017).

[115] D.R. Neuville, L. Cormier, A.M. Flank, V. Briois and D. Massiot, Al speciation and Ca environment in calcium aluminosilicate glasses and crystals by Al and Ca K-edge X-ray absorption spectroscopy. Chem. Geol. 213, (2004) 153–163. doi:10.1016/j.chemgeo.2004.08.039.

[116] J.F. Stebbins, S. Kroeker, S.K. Lee and T.J. Kiczenski, Quantification of five- and six-coordinated aluminum ions in aluminosilicate and fluoride-containing glasses by high-field, high-resolution ^{27}Al NMR, J. Non. Cryst. Solids 275, (2000) 1–6. doi:10.1016/S0022-3093(00)00270-2.

[117] M.J. Toplis, S.C. Kohn, M.E. Smith and I.J.F. Poplett, Fivefold-coordinated aluminum in tectosilicate glasses observed by triple quantum MAS NMR. Am. Mineral. 85, (2000) 1556–1560. doi:10.2138/am-2000-1031.

[118] E.D. Lacy, Aluminium in glasses and in melts. Phys. Chem. Glas. 4, (1963) 234–238.

[119] M.J. Toplis, D.B. Dingwell, T. Lenci, Peraluminous viscosity maxima in $Na_2O - Al_2O_3 - SiO_2$ liquids: The role of triclusters in tectosilicate melts. Geochim. Cosmochim. Acta 61, (1997) 2605–2612. doi:10.1016/S0016-7037(97)00126-9.

[120] M.J. Toplis, D.B. Dingwell, Shear viscosities of $CaO - Al_2O_3 - SiO_2$ and $MgO - Al_2O_3 - SiO_2$ liquids: Implications for the structural role of aluminium and the degree of polymerisation of synthetic and natural aluminosilicate melts. Geochim. Cosmochim. Acta 68, (2004) 5169–5188. doi:10.1016/j.gca.2004.05.041.

[121] B. Hehlen, A century of structural and vibrational spectroscopy in vitreous silica: A short review, International Journal of Applied Glass Science 13 (2022) 10.1111/ijag.16572.

[122] F.L. Galeener, Planar rings in vitreous silica. J Non-Cryst Solids 49:53-62 (1982) doi:10.1016/0022-3093(82)90108-9.

[123] I. Polyakova, The Main Silica Phases and Some of Their Properties, (2014) 10.1515/9783110298581.197.

[124] B.E. Warren and J. Biscce, THE STRUCTURE OF SILICA GLASS BY X-RAY DIFFRACTION STUDIES, Journal of the American Ceramic Society 21 (1938): 49-54.

[125] D. Evans and S. King, Random Network Model of Vitreous Silica. Nature 212, 1353–1354 (1966). https://doi.org/10.1038/2121353a0.

[126] R. Bell and P. Dean, Properties of Vitreous Silica: Analysis of Random Network Models. Nature 212, 1354–1356 (1966). https://doi.org/10.1038/2121354a0.

[127] R. L. Mozzi and B. E. Warren, The structure of vitreous silica. J. Appl. Cryst. 2, (1969) 164–172.

[128] J. Neuefeind and K. D. Liss, Bond angle distribution in amorphous germania and silica. Berichte der Bunsengesellschaft für physikalische Chemie, 100: (1996) 1341-1349. https://doi.org/10.1002/bbpc.19961000812.

[129] S. Kohara and K. Suzuya, Intermediate-range order in vitreous SiO_2 and GeO_2, J Phys: Condens Matter 17:S77-S86 (2005) doi:10.1088/0953-8984/17/5/009.

[130] D.L. Price et al., Intermediate-range order in glasses and liquids. J Phys: Condens Matter 1:1005-1008 (1989) doi:10.1088/0953-8984/1/5/017.

[131] S. Elliot, Medium-range structural order in covalent amorphous solids. Nature 354:445–452 (1991) doi: 10.1038/354445a0.

[132] P.S. Salmon, Real space manifestation of the first sharp diffraction peak in the structure factor of liquid and glassy materials. Proc R Soc Lond A 445:351-365 (1994) doi:10.1098/rspa.1994.0065.

[133] S.Jahn, Molecular Simulations of Oxide and Silicate Melts and Glasses, Reviews in Mineralogy and Geochemistry 87(1):193-227 (2020) doi:10.2138/rmg.2022.87.05.

[134] E. Dupree and R. Pettifer, Determination of the Si-O-Si bond angle distribution in vitreous silica by magic angle spinning NMR. Nature 308, 523–525 (1984). https://doi.org/10.1038/308523a0.

[135] R.F. Pettifer, R. Dupree, I. Farnan and U. Sternberg, NMR determinations of Si-O-Si bond angle distributions in silica, Journal of Non-Crystalline Solids 106, 1–3, (1988) 408-412, https://doi.org/10.1016/0022-3093(88)90299-2.

[136] T.M. Clark et al., Correlated structural distributions in silica glass, Phys. Rev. B 70, (2004) 064202.

[137] D.R. Neuville, Advances in Raman Spectroscopy Applied to Earth and Material Sciences. In: Spectroscopic Methods in Mineralogy and Materials Sciences, Henderson GS, Neuville DR, Downs RT (eds) Rev Mineral Geochem 78:509-541 (2014) doi:10.2138/rmg.2013.78.13.

[138] S.K. Sharma, J.F. Mammone, M.F. Nicol, Raman investigation of ring configurations in vitreous silica. Nature 292:140-141 (1981) doi:10.1038/292140a0.

[139] F.L. Galeener, Planar rings in glasses. Solid State Commun 44:1037–1040 (1982) doi:10.1016/0038-1098(82)90329-5.

[140] F.L. Galeener, A.J. Leadbetter and M.W. Stringfellow, Comparison of the neutron, Raman, and infrared vibrational spectra of vitreous SiO_2, GeO_2, and BeF_2. Phys Rev B 27:1052-1078 (1983) doi:10.1103/PhysRevB.27.1052.

[141] R.A. Barrio, F.L. Galeener, E. Martínez and R.J. Elliot, Regular ring dynamics in AX_2 tetrahedral glasses. Phys Rev B 48:15672-15689 (1993) doi:10.1103/PhysRevB.48.15672.

[142] P.F. McMillan, B.T. Poe, P. Gillet,B. Reynard, A study of SiO_2 glass and supercooled liquid to 1950 K via high-temperature Raman spectroscopy. Geochim Cosmochim Acta 58:3653-3664 (1994) doi:10.1016/0016-7037(94)90156-2.

[143] A. Pasquarello and R. Car, Identification of Raman defect lines as signatures of ring structures in vitreous silica. Phys Rev Lett 80:5145-5147 (1998) doi:10.1103/PhysRevLett.80.5145.

[144] P. Umari and A. Pasquarello, Modeling of the Raman spectrum of vitreous silica: concentration of small ring structures. Physica B 316-317:572-574 (2002) doi:10.1016/S0921-4526(02)00576-8.

[145] P. Umari, X. Gonze and A. Pasquarello, Concentration of Small Ring Structures in Vitreous Silica from a First-Principles Analysis of the Raman Spectrum. Phys Rev Lett 90:867-755 (2003) doi:10.1103/PhysRevLett.90.027401.

[146] A. Rahmani, M. Benoit and C. Benoit, Signature of small rings in the Raman spectra of normal and compressed amorphous silica:A combined classical and ab initio study. Phys Rev B 68:184202 (2003). doi:10.1103/PhysRevB.68.184202.

[147] A.G. Kalampounias, S.N. Yannopoulos and G.N. Papatheodorou, Temperature-induced structural changes in glassy, supercooled, and molten silica from 77 to 2150 K. J Chem Phys 124:014504 (2006) doi:10.1063/1.2136878.

[148] L. Lichtenstein et al., The Atomic Structure of a Metal-Supported Vitreous Thin Silica Film. Angew. Chem. Int. Ed., 51: (2012) 404-407. https://doi.org/10.1002/anie.201107097.

[149] P. Y. Huang et al., Direct Imaging of a Two-Dimensional Silica Glass on Graphene, Nano Letters 12, 2 (2012) 1081-1086, https://doi.org/10.1021/nl204423x.

[150] L. Lichtenstein et al., Atomic Arrangement in Two-Dimensional Silica: From Crystalline to Vitreous Structures, The Journal of Physical Chemistry C. 116 (2012) 20426–20432. 10.1021/jp3062866.

[151] A. Takada et al, A molecular dynamics simulation of complex structural changes in amorphous silica at high temperatures. Physics and Chemistry of Glasses - European Journal of Glass Science and Technology Part B. 48. 182-187 (2007).

[152] H. Niu, P.M. Piaggi, M.Invernizzi and M. Parrinello, Molecular dynamics simulations of liquid silica crystallization, Proceedings of the National Academy of Sciences 115(21):201803919 (2018) doi:10.1073/pnas.1803919115.

[153] J. D. Kubicki and A.C. Lasaga, Molecular dynamics simulations of SiO_2 melt and glass: Ionic and covalent models, American Mineralogist 73:941-955 (1988).

[154] L.V. Woodcock, C.A. Angell and P. Cheeseman, Molecular dynamics studies of the vitreous state. Simple ionic systems and silica. J. Chem. Phys., 65:1565-1577.

[155] B. J. Cowen and M. S. El-Genk, On force fields for molecular dynamics simulations of crystalline silica, Computational Materials Science,107 (2015) 88-101,https://doi.org/10.1016/j.commatsci.2015.05.018.

[156] D. Kilymis et al., Vibrational properties of sodosilicate glasses from first-principles calculations. Physical Review B 99.5 (2019): 054209. https://doi.org/10.1103/PhysRevB.99.054209.

[157] P. J. Heaney et al., Silica: Physical behavior, geochemistry and materials applications. Washington, D.C: Mineralogical Society of America (1994).

[158] H. Liu et al., Vibrational spectroscopy analysis of silica and silicate glass networks, Journal of the American Glass Society, 105 (2022), 2355-2384, https://doi.org/10.1111/jace.18206.

[159] R. Bell and P. Dean, Atomic vibrations in vitreous silica. Discuss Faraday Soc. 1970; 50: 55–61.

[160] P.Gaskell, Thermal properties of silica. Part 1.—Effect of temperature on infra-red reflection spectra of quartz, cristobalite and vitreous silica. Trans Faraday Soc. 1966; 62: 1493–504.

[161] F.L. Galeener, Band limits and the vibrational spectra of tetrahedral glasses. Phys Rev B. 1979; 19(8): 4292–7.

[162] P. McMillan, Structural studies of silicate glasses and melts—applications and limitations of Raman spectroscopy. Am Mineral. 1984; 69(7-8): 622–44.

[163] R.M. Almeida and C.G. Pantano, Structural investigation of silica gel films by infrared spectroscopy. J Appl Phys. 1990; 68(8): 4225–32.

[164] A. Agarwal and M. Tomozawa, Correlation of silica glass properties with the infrared spectra. J Non-Cryst Solids. 1997; 209(1-2): 166–74.

[165] D. Sanders, W. Person and L. Hench, Quantitative analysis of glass structure with the use of infrared reflection spectra. Appl Spectrosc. 1974; 28(3): 247–55.

[166] H. Liu, S.H. Hahn, M. Ren, M. Thiruvillamalai, T.M. Gross, J. Du et al., Searching for correlations between vibrational spectral features and structural parameters of silicate glass network. J Am Ceram Soc. 2020; 103(6): 3575–89.

[167] D. Berreman, Infrared absorption at longitudinal optic frequency in cubic crystal films. Phys Rev. 1963; 130(6): 2193.

[168] K. Hübner, L. Schumann, A. Lehmann, H. Vajen and G. Zuther, Detection of LO and TO phonons in amorphous SiO_2 films by oblique incidence of IR light. Phys Status Solidi B. 1981; 104(1): K1–5.

[169] R.M. Almeida, T.A. Guiton, C.G. Pantano, Detection of LO mode in v-SiO_2 by infrared diffuse reflectance spectroscopy. J Non-Cryst Solids. 1990; 119(2): 238–41.

[170] R.M. Almeida, Detection of LO modes in glass by infrared reflection spectroscopy at oblique incidence. Phys Rev B. 1992; 45(1): 161.

[171] P.M.A. Sherwood, Vibrational spectroscopy of solids. Cambridge: Cambridge University Press (1972).

[172] P. Sen and M. Thorpe, Phonons in AX_2 glasses: from molecular to band-like modes. Phys Rev B. 1977; 15(8): 4030.

[173] S. Brawer, Theory of the vibrational spectra of some network and molecular glasses. Phys Rev B. 1975; 11(8): 3173.

[174] S.A. Brawer and W.B. White, Raman spectroscopic investigation of the structure of silicate glasses. I. The binary alkali silicates. J Chem Phys. 1975; 63(6): 2421–32.

[175] R. Laughlin and J. Joannopoulos, Phonons in amorphous silica. Phys Rev B. 1977; 16(6): 2942.

[176] D. De Sousa Meneses, M. Eckes, L. del Campo, C. N. Santos, Y. Vaills and P. Echegut, Investigation of medium range order in silicate glasses by infrared spectroscopy, Vibrational Spectroscopy, 65 (2013) 50-57, https://doi.org/10.1016/j.vibspec.2012.11.015.

[177] B. Bhattarai and D. Drabold, Vibrations in amorphous silica, Journal of Non-Crystalline Solids 439 (2016) 6–14.

[178] J. Sarnthein, A. Pasquarello and R. Car, Origin of the highfrequency doublet in the vibrational spectrum of vitreous SiO_2, Science 275 (1997) 1925–1927.

[179] M. K. Gunde, Vibrational modes in amorphous silicon dioxide, Physica B: Condensed Matter 292 (2000) 286–295.

[180] M. Zhang and J. F. Scott, Raman studies of oxide minerals: a retrospective on cristobalite phases, Journal of Physics: Condensed Matter 19 (2007) 275201.

[181] P. Richet, Y. Bottinga, Glass transitions and thermodynamic properties of amorphous SiO_2, $NaAlSinO_2n+2$ and $KAlSi_3O_8$, Geochimica et Cosmochimica Acta 48 (1984) 453–470.

[182] H. L. Schick, A thermodynamic analysis of the high temperature vaporization properties of silica, Chemical Reviews 60 (1960) 331–362.

[183] D. De Sousa Meneses, M. Eckes, L. del Campo and P Echegut, Phase transformations of crystalline SiO_2 versus dynamic disorder between room temperature and liquid state, Journal of Physics: Condensed Matter 26 (2014) 255402, https://dx.doi.org/10.1088/0953-8984/26/25/255402.

[184] P. Richet, Y. Bottinga, L. Denielou, J. Petitet, C. Tequi, Thermodynamic properties of quartz, cristobalite and amorphous SiO_2: drop calorimetry measurements between 1000 and 1800 K and a review from 0 to 2000 K, Geochimica et Cosmochimica Acta 46 (1982) 2639–2658.

[185] L. B. Skinner et al., Joint diffraction and modeling approach to the structure of liquid alumina, Physical Review B 87, 024201 (2013).

[186] I. Levin and D. Brandon, Metastable Alumina Polymorphs: Crystal Structures and Transition Sequences; J. Am. Ceram. Soc., 81 [8] 1995-2012 (1998).

[187] H. Reiss, I. B.Wilson,The effect of surface on melting point, Journal of Colloid Science 3, 6, 551-561 (1948) ISSN 0095-8522.

[188] S. J. Schneider, Cooperative determination of the melting point of alumina, Pure and Applied Chemistry 21, 1,115-122 (1970).

[189] T. Sata and T. Takahashi, Measurement of the Melting Point of Alumina by means of DTA, Journal of the Ceramic Association, Japan 79, 906, 70-71 (1971) doi:10.2109/jcersj1950.79.90670.

[190] R. F. Geller and P. J. Yavorsky, Melting point of α-alumina, Journal of research of the National Bureau of Standards 34, (1945).

[191] J. Coutures and M. Rand, 'Melting temperatures of refractory oxides - Part II: Lanthanoid sesquioxides', Pure and Applied Chemistry 61, 1461-1482 (1989).

[192] B. Cockayne, M. Chesswas, and D. B. Gasson, Single-crystal growth of sapphire, J Mater Sci 2, 7–11 (1967). https://doi.org/10.1007/BF00550046

[193] H. E. LaBelle, Jr. and A. I. Mlavsky, Growth of controlled profile crystals from the melt: Part I - Sapphire filaments, Materials Research Bulletin 6 (1971): 571-579.

[194] H. E. LaBelle, Jr., Growth of controlled profile crystals from the melt: Part II - Edge-defined, film-fed growth (EFG), Materials Research Bulletin 6, 7 (1971) 581-589, https://doi.org/10.1016/0025-5408(71)90007-9.

[195] M. M. Fejer, J. L. Nightingale, G. A. Magel, and R. L. Byer, Laser-heated miniature pedestal growth apparatus for single-crystal optical fibers, Rev. Sci. Instrum. 55, 1791 (1984).

[196] R. K. Nubling and J. A. Harrington, Optical properties of single-crystal sapphire fibers, Appl. Opt. 36, 5934 (1997).

[197] R. A. Reed and V. S. Calia, Review of aluminum oxide rocket exhaust particles, AIAA Paper No. 93-2819 American Institute of Aeronautics and Astronautics, Washington, DC (1993).

[198] Yu. Plastinin, G. Karabadzhak, B. Khmelinin, G. Baula, and A. Rodionov, Advanced model for soot radiation in the plume, AIAA Paper No. 2001-0660 American Institute of Aeronautics and Astronautics, Reston, VA (2001).

[199] J. M. Burt and I. D. Boyd, High-Altitude Plume Simulations for a Solid Propellant Rocket, AIAA J. 45, 2872 (2007).

[200] Y. Xie, The Effect of Novel Synthetic Methods and Parameters Control on Morphology of Nano-alumina Particles, Nanoscale Research Letters 11 (2016) 10.1186/s11671-016-1472-z.

[201] C.K. Lee et al., Comparative study of electronic structures and dielectric properties of alumina polymorphs by first-principles methods, Phys. Rev. B 76 (2007) 245110.

[202] J.-P. Coutures, D. Massiot,. C. Bessada, P. Echegut, J.-C. Rifflet, and F. Taulelle, Étude par RMN ^{27}Al d'aluminates liquides dans le domaine 1600–2100°C, C. R. Acad. Sci. Paris. 310, 1041 (1990).

[203] D. Massiot, F. Taulelle, and J. P. Coutures, STRUCTURAL DIAGNOSTIC OF HIGH TEMPERATURE LIQUID PHASES BY ^{27}Al NMR, J. Phys. Coll. 51, C5-425(1990).

[204] B. T. Poe, P. F. McMillan, B. Cote, D. Massiot, and J.-P. Coutures, Magnesium and Calcium Aluminate Liquids: In Situ High-Temperature ^{27}Al NMR Spectroscopy, J. Phys. Chem. 96, 8220 (1992).

[205] P. Florian, D. Massiot, B. Poe, I. Farnan, and J.-P. Coutures, A time resolved ^{27}Al NMR study of the cooling process of liquid alumina from 2450 °C to crystallisation, Solid State Nucl. Magn. Reson. 5, 233 (1995).

[206] J. J. Rasmussen, Critical Surface Energies of Al_2O_3 and Graphite, J. Am. Ceram. Soc. 55, 326 (1972).

[207] P. Tyrolerova and W.-K. Lu, Solidification Behavior of Undercooled Liquid Aluminum Oxide, J. Am. Ceram. Soc. 52, 77 (1969).

[208] M. Hemmati, M. Wilson, and P. A. Madden, STRUCTURE OF LIQUID Al_2O_3 FROM A COMPUTER SIMULATION MODEL, J. Phys. Chem. B 103, 4023 (1999).

[209] V. V. Hoang and S. K. Oh, Simulation of pressure-induced phase transition in liquid and amorphous Al_2O_3, Phys. Rev. B 72, 054209 (2005).

[210] A. K. Verma, P. Modak, and B. B. Karki,First-principles simulations of thermodynamical and structural properties of liquid Al_2O_3 under pressure, Phys. Rev. B 84, 174116 (2011).

[211] V. V. Hoang, Thermal hysteresis of a simulated Al_2O_3 system, Phys. Lett. A 335, 439 (2005).

[212] P. K. Hung, L. T. Vinh, D. M. Nghiep, and P. N. Nguyen, Local microstructure of amorphous Al_2O_3, J. Phys.: Condens. Matter 18, 9309 (2006).

[213] S. Ansell et al., Structure of Liquid Aluminum Oxide, Phys. ReV. Lett. (1997) 78, 464.

[214] S. Krishnan et al., Structure of Normal and Supercooled Liquid Aluminum Oxide, Chem. Mater 17, (2005) 2662-2666.

[215] C. Landron, L. Hennet, T. E. Jenkins, G. N. Greaves, J. P. Coutures, and A. K. Soper, Liquid Alumina: Detailed Atomic Coordination Determined from Neutron Diffraction Data Using Empirical Potential Structure Refinement, Phys. Rev. Lett. 86, 4839 (2001).

[216] S. Jahn and P. A. Madden, Structure and dynamics in liquid alumina: Simulations with an ab initio interaction potential, J. Non-Cryst. Solids 353, 3500 (2007).

[217] G. Gutiérrez, A. B. Belonoshko, R. Ahuja, and B. Johansson, Structural properties of liquid Al_2O_3:A molecular dynamics study, Phys. Rev. E 61, 2723 (2000).

[218] M. A. S. Miguel, J. F. Sanz, L. J. Álvarez, and J. A. Odriozola, Molecular-dynamics simulations of liquid aluminum oxide, Phys. Rev. B 58, 2369 (1998).

[219] J.F. Brun et al., Infrared optical properties of α-alumina with the approach to melting: γ-like tetrahedral structure and small polaron conduction. Journal of Applied Physics. 114 (2013) 223501-223501. 10.1063/1.4846077.

[220] S. J. Schneider, Cooperative determination of the melting point of alumina, Pure Appl. Chem. 21, 115 (1970).

[221] V. Petrov and A. Vorobyev, Spectral emissivity and radiance temperature plateau of self-supporting Al_2O_3 melt at rapid solidification. High Temperatures- High Pressures (2007) v. 35/36. pp. 321-329. 10.1068/htjr141.

[222] B.C. Smith, Fundamentals of Fourier Transform Infrared Spectroscopy (2nd ed.). CRC Press (2011). https://doi.org/10.1201/b10777.

[223] I. Levin and D. Brandon, Metastable Alumina Polymorphs: Crystal Structures and Transition Sequences. Journal of the American Ceramic Society, 81 (1998) 1995-2012. https://doi.org/10.1111/j.1151-2916.1998.tb02581.x

[224] C. Pecharromán et al., Thermal Evolution of Transitional Aluminas Followed by NMR and IR Spectroscopies, The Journal of Physical Chemistry B 103 (1999) 6160-6170 doi =10.1021/jp983316q

[225] L. Favaro, A. Boumaza, P. Roy, J. Lédion, G. Sattonnay, J.B. Brubach, A.M. Huntz, R. Tétot, Experimental and ab initio infrared study of χ-, K- and α-aluminas formed from gibbsite, Journal of Solid State Chemistry, 183 (2010) 901-908,https://doi.org/10.1016/j.jssc.2010.02.010.

[226] B.T. Poe et al., Al and Si coordination in $SiO_2 - Al_2O_3$ glasses and liquids: A study by NMR and IR spectroscopy and MD simulations, Chemical Geology, 96 (1992) 333-349

[227] C. I. Merzbacher, W. B. White, The structure of alkaline earth aluminosilicate glasses as determined by vibrational spectroscopy, Journal of Non-Crystalline Solids 130, 1, (1991) 18-34, https://doi.org/10.1016/0022-3093(91)90152-V.

[228] N. Stuart and K. Sohlberg, The Microstructure of γ-Alumina. Energies. 14. 6472 (2021) 10.3390/en14206472.

[229] R.-S. Zhou, R. L. Snyder, Structures and transformation mechanisms of the η, γ and θ transition aluminas, Acta Crystallographica Section B: Structural Science 47 (1991) 617–630.

[230] J.C.M. Garnett, Colours in Metal Glasses and in Metallic Films, Philosophical Transactions of the Royal Society A: Mathematical, Physical and Engineering Sciences. 203 (359–371): (1904) 385–420.

[231] T.C. Choy, Effective Medium Theory. Oxford: Clarendon Press. (1999) ISBN 978-0-19-851892-1.

[232] V.K. Bityukov et al., Two-phase zone at Al_2O_3 meltin by laser radiation and at melt solidification under the conditions of free cooling. Thermophys. Aeromech. 16, 479–489 (2009). https://doi.org/10.1134/S0869864309030160

[233] V.K. Bityukov et al., Influence of the melt thermal conductivity on temperature fields in aluminum oxide upon heating by concentrated laser radiation. High Temp 55, 233–238 (2017). https://doi.org/10.1134/S0018151X17010059

[234] Y. Repelin, E. Husson, Etudes structurales d'alumines de transition. I-Alumines gamma et delta, Materials Research Bulletin 25 (1990) 611–621.

[235] C. Weigel et al., Elastic moduli of $xAlSiO_4$ aluminosilicate glasses: effects of charge-balancing cations. J. Non. Cryst. Solids 447, (2016) 267–272. doi:10.1016/j.jnoncrysol.2016.06.023

[236] L.-G. Hwa, S.-L. Hwang, L.-C. Liu, Infrared and Raman spectra of calcium alumino–silicate glasses, Journal of Non-Crystalline Solids 238, 3 (1998) 193-197, https://doi.org/10.1016/S0022-3093(98)00688-7.

[237] P. Richet, A. Nidaira, D. R. Neuville, T. Atake, Aluminum speciation, vibrational entropy and short-range order in calcium aluminosilicate glasses, Geochimica et Cosmochimica Acta 73, 13,(2009) 3894-3904, https://doi.org/10.1016/j.gca.2009.03.041.

[238] J. F. Stebbins, S. K. Lee, J. V. Oglesby, Al-O-Al oxygen sites in crystalline aluminates and aluminosilicate glasses; high-resolution oxygen-17 NMR results, American Mineralogist (1999) 84 (5-6): 983–986. doi: https://doi.org/10.2138/am-1999-5-635

[239] M.J. Toplis, an D.B. Dingwell, Shear viscosities of $CaO - Al_2O_3 - SiO_2$ and $MgO - Al_2O_3 - SiO_2$ liquids: Implications for the structural role of aluminium and the degree of polymerisation of synthetic and natural aluminosilicate melts. Geochim. Cosmochim. Acta 68, (2004) 5169–5188. doi:10.1016/j.gca.2004.05.041

[240] D.R. Neuville et al., Structure of Mg- and Mg/Ca aluminosilicate glasses: ^{27}Al NMR and Raman spectroscopy investigations. Am. Mineral. 93, (2008) 1721–1731. doi:10.2138/am.2008.2867

[241] R.H. Thomas, Phase Equilibrium in a Portion of the Ternary System $BaO - Al_2O_3 - SiO_2$. J. Am. Ceram. Soc 33, 35–44 (1950).

[242] W.K. Tredway et al., Gel synthesis of glass powders in the $BaO - Al_2O_3 - SiO_2$ system, J. Non. Cryst. Solids 100,(1988) 278–283. doi:10.1016/0022-3093(88)90032-4

[243] C.I. Merzbacher, K.J. McGrath, P.L. Higby, ^{29}Si NMR and infrared reflectance spectroscopy of low-silica calcium aluminosilicate glasses, Journal of Non-Crystalline Solids 136, 3 (1991) 249-259, https://doi.org/10.1016/0022-3093(91)90496-S.

[244] L. Cormier, D. R. Neuville, G. Calas, Structure and properties of low-silica calcium aluminosilicate glasses, Journal of Non-Crystalline Solids, 274,1–3 (2000) 110-114, https://doi.org/10.1016/S0022-3093(00)00209-X.

[245] D. R. Neuville, L. Cormier, A.-M. Flank, V. Briois, D. Massiot, Al speciation and Ca environment in calcium aluminosilicate glasses and crystals by Al and Ca K-edge X-ray absorption spectroscopy, Chemical Geology, 213, 1–3 (2004) 153-163, https://doi.org/10.1016/j.chemgeo.2004.08.039.

[246] D. R. Neuville, L. Cormier, D. Massiot, Al coordination and speciation in calcium aluminosilicate glasses: Effects of composition determined by ^{27}Al MQ-MAS NMR and Raman spectroscopy, Chemical Geology, 229, 1–3, (2006) 173-185, https://doi.org/10.1016/j.chemgeo.2006.01.019.

[247] S. Takahashi, D. R. Neuville, H. Takebe, Thermal properties, density and structure of percalcic and peraluminus $CaO^{\smile}Al_2O_3{}^{\smile}SiO_2$ glasses, Journal of Non-Crystalline Solids 411 (2015) 5-12, https://doi.org/10.1016/j.jnoncrysol.2014.12.019.

[248] M.M. Krzmanc,B.Jančar and D.Suvorov,The influence of tetrahedral ordering on the microwave dielectric properties of $Sr_{0.05}Ba_{0.95}Al_2Si_2O_8$ and (MAl, Ga,MSi, Ge)ceramics,J.Eur.Ceram.Soc.28(2008)3141–3148.

[249] E. El-Meliegy, R. van Noort, Glasses and Glass Ceramics for Medical Applications, Springer, New York (2012).

[250] C.B. Carter, M.G. Norton, Ceramic Materials: Science and Engineering, Springer, New York (2007).

[251] F. Singer,Industrial Ceramics, Springer, The Netherlands (2013).

[252] . A.O. Surendranathan, An Introduction to Ceramics and Refractories,Taylor & Francis, Boca Raton, FL (2014)

[253] L. Barbeeri, A.B. Corradi, C. Leonelli, T. Manfredini, M. Romagnoli, C. Siligardi, The microstructure and mechanical properties of sintered celsian and strontium-celsian glass-ceramics, Mater. Res. Bull., 30 (1995), 27-41

[254] C.E. Semler, W.R. Foster, Studies in the system $BaO - Al_2O_3 - SiO_2$: VI, the system celsian-silica-alumina, J. Am. Ceram. Soc., 53 (1970), 595-598

[255] B. Yoshiki, K. Matsumoto, High-temperature modification of barium feldspar, J. Am. Ceram. Soc., 34 (1951), pp. 283-286

[256] C. Ferone, B. Liguori, A. Marocco, S. Anaclerio, M. Pansini, C. Colella, Monoclinic (Ba, Sr)-celsian by thermal treatment of (Ba, Sr)-exchanged zeolite A, Microporous Mesoporous Mater., 134 (2010), pp. 65-71

[257] Y.M. Sung and S. Kim, Sintering and crystallization of off-stoichiometric $SrO \cdot Al_2O_3 \cdot 2SiO_2$ glasses. Journal of Materials Science 35, 4293–4299 (2000). https://doi.org/10.1023/A:1004880201847

[258] Y.-P. Fu, C.-C. Chang, C.-H. Lin, T.-S. Chin Solid-state synthesis of ceramics in the $BaO - SrO - Al_2O_3 - SiO_2$ system, Ceram. Int., 30 (2004), 41-45

[259] M.J. Hyatt and N.P. Bansal, Crystal growth kinetics in $BaOAl_2O_32SiO_2$ and $SrOAl_2O_32SiO_2$ glasses. JOURNAL OF MATERIALS SCIENCE 31, 172–184 (1996). https://doi.org/10.1007/BF00355142

[260] C. Ferone, B. Liguori, A. Marocco, S. Anaclerio, M. Pansini, C. Colella Monoclinic (Ba, Sr)-celsian by thermal treatment of (Ba, Sr)-exchanged zeolite A Microporous Mesoporous Mater., 134 (2010), 65-71.

[261] Y. Kobayashi, M. Inagaki Preparation of reactive Sr-celsian powders by solid-state reaction and their sintering J. Eur. Ceram. Soc., 24 (2004), 399-404.

[262] A. Marocco, B. Liguori, G. Dell'Agli, M. Pansini Sintering behaviour of celsian based ceramics obtained from the thermal conversion of (Ba, Sr)-exchanged zeolite A J. Eur. Ceram. Soc., 31 (2011), 1965-1973.

[263] N.P. Bansal, J.A. Setlock Fabrication of fiber-reinforced celsian matrix composites Compos. Part A: Appl. Sci. Manuf., 32 (2001), 1021-1029.

[264] W. Lei, R. Ang, X.-C. Wang, W.-Z. Lu Phase evolution and near-zero shrinkage in $BaAl_2Si_2O_8$ low-permittivity microwave dielectric ceramics Mater. Res. Bull., 50 (2014), 235-239.

[265] N. Fréty, A. Taylor, M.H. Lewis Microstructure and crystallisation behaviour of sol–gel derived $1/2SrO - 1/2BaOAl_2O_3 - 2SiO_2$ glass-ceramic J. Non-Cryst. Solids, 195 (1996), 28-37

[266] M.F.M. Zawrah, N.M. Khalil Preparation and characterization of barium containing refractory materials Ceram. Int., 27 (2001), 309-314.

[267] S. V. Krivovichev, Zapiski RMO (2020) 149,16-66.

[268] J. Jones, Order in Alkali Feldspars, Nature 210, 1352–1353 (1966). https://doi.org/10.1038/2101352a0

[269] M.A. Carpenter, Equilibrium thermodynamics of Al/Si ordering in anorthite. Phys Chem Minerals 19, 1–24 (1992). https://doi.org/10.1007/BF00206796

[270] P. Benna, M. Tribaudino, E. Bruno, Al-Si ordering in Sr-feldspar $SrAl_2Si_2O_8$ - IR, TEM and single-crystal XRD evidences. Phys. Chem. Miner 22 (6), (1995) 343-350.

[271] W. Brown, I. Parsons, Alkali feldspars: Ordering rates, phase transformations and behaviour diagrams for igneous rocks. Mineralogical Magazine, 53(369), (1989) 25-42. doi:10.1180/minmag.1989.053.369.03

[272] S. Liu, et al., Degree of Al-Si order in K-feldspar and its effect on K-feldspar's dissolution 90 (2021) 359-369. 10.13133/2239-1002/17479.

[273] W. Lowenstein, The distribution of aluminum in the tetrahedra of silicates and aluminates. Am. Mineral. 39 (1954) 92.

[274] Choi, Wooseung; Choi, Jinhyuk; Hwang, Huijeong; Lee, Yongjae, Physics and Chemistry of Minerals (2022) 49, 15.

[275] K. Al Saghir et al., Transparency through structural disorder: a new concept for innovative transparent ceramics. Chem. Mater. 27:508–514 (2015). http://dx.doi.org/10.1021/cm5037106.

[276] M.A. Carpenter, Equillibrium thermodynamics of Al/Si ordering in anorthite. Phys. Chem. Miner 19 (1), (1992) 1-24.

[277] P. Benna, M. Tribaudino, E. Bruno, Al-Si ordering in Sr-feldspar $SrAl_2Si_2O_8$ - IR, TEM and single-crystal XRD evidences. Phys. Chem. Miner 22 (6), (1995) 343-350.

[278] Griffen, D.A.; Ribbe, P.H, American Mineralogist (1976) 61, p. 414-418

[279] Chiari, G.; Gazzoni, G.; Craig, J.R.; Gibbs, G.V.; Louisnathan, S.J., American Mineralogist (1985) 70, p. 969-974.

[280] NIST Inorganic Crystal Structure Database, NIST Standard Reference Database Number 3, National Institute of Standards and Technology, Gaithersburg MD, 20899, doi: https://doi.org/10.18434/M32147

[281] K. Sharma et al., A new formulation of barium–strontium silicate glasses and glass-ceramics for high-temperature sealant. Int. J. Hydrog. Energy 37:11360–11369 (2012). http://dx.doi.org/10.1016/j.ijhydene.2012.04.142.

[282] M.J. Hyatt and N.P. Bansal, Crystal growth kinetics in $BaOAl_2O_32SiO_2$ and $SrOAl_2O_32SiO_2$ glasses. J. Mater. Sci. 31:172–184 (1996). http://dx.doi.org/10.1007/BF00355142.

[283] N.P. Bansal, Solid state synthesis and properties of monoclinic celsian. J. Mater. Sci. 33:4711–4715 (1998). http://dx.doi.org/10.1023/A:1004484903436.

[284] G.H. Beall, Refractory glass-ceramics based on alkaline earth aluminosilicates. J. Eur.Ceram. Soc. 29:1211–1219 (2009). http://dx.doi.org/10.1016/j.jeurceramsoc.2008.08.010.

[285] A.N. Novikov et al., Al and Sr environment in tectosilicate glasses and melts: Viscosity, Raman and NMR investigation, Chemical Geology 461, (2017) 115-127, https://doi.org/10.1016/j.chemgeo.2016.11.023.

[286] T. Charpentier et al., Structure of Strontium Aluminosilicate Glasses from Molecular Dynamics Simulation, Neutron Diffraction, and Nuclear Magnetic Resonance Studies, J. Phys. Chem. B (2018) 122, 41, 9567–9583

[287] J. Töpel-Schadt et al., Transmission electron microscopy of $SrAl_2Si_2O_8$: Feldspar and hexacelsian polymorphs. J Mater Sci 13, 1809–1816 (1978). https://doi.org/10.1007/BF0054874.

[288] N.P. Bansal, Chemical vapor deposited SiC (SCS-0) fiber-reinforced strontium aluminosilicate glass-ceramic composites. Journal of materials research 12.3 (1997): 745-753.

[289] M.Tribaudino, Thermodynamic behaviour of the high-temperature P1-I1 phase transition along the $CaAl_2Si_2O_8 - SrAl_2Si_2O_8$ join. Physics and Chemistry of Minerals - PHYS CHEM MINER. 32. 314-321. (2005) 10.1007/s00269-005-0469-4.

[290] G. Chiari et al., The structure of partially disordered synthetic strontium feldspar. American Mineralogist. Am. Mineral. (1975) 111-119.

[291] P. Ptáček et al.,The formation of feldspar strontian ($SrAl_2Si_2O_8$) via ceramic route: Reaction mechanism, kinetics and thermodynamics of the process, Ceramics International 42, 7 (2016) 8170-8178, https://doi.org/10.1016/j.ceramint.2016.02.024.

[292] R Le Parc et al.,Anorthite and $CaAl_2Si_2O_8$ glass: low frequency Raman spectroscopy and neutron scattering, Journal of Non-Crystalline Solids 323,1–3, (2003) 155-161, https://doi.org/10.1016/S0022-3093(03)00302-8.

[293] A. Mabrouk et al., Effects of boron on structure of lanthanum and sodium aluminoborosilicate glasses studied by X-ray diffraction, transmission electron microscopy and infrared spectrometry. J. Non-Cryst. Solids, 503–504 (2019) 69-77. doi:10.1016/j.jnoncrysol.2018.09.030

[294] R. J. King, Kaolinite, Geology Today 25, 2, 75-78 (2009) doi: 10.1111/j.1365-2451.2009.00711.x.

[295] I. Bayoumi et al., Rheology of refractory concrete: An article review. Boletín de la Sociedad Española de Cerámica y Vidrio. 61 (2021) 10.1016/j.bsecv.2021.03.003.

[296] K. Yan, Y. Guo, L. Fang, L. Cui, F. Cheng, et T. Li, Decomposition and phase transformation mechanism of kaolinite calcined with sodium carbonate, Applied Clay Science 147, 90-96 (2017) doi: 10.1016/j.clay.2017.07.010.

[297] I. Daou, G. L. Lecomte-Nana, N. Tessier-Doyen, C. Peyratout, M. Gonon, et R. Guinebretiere, Probing the Dehydroxylation of Kaolinite and Halloysite by In Situ High Temperature X-ray Diffraction, Minerals 10, 5, 480, (2020) doi: 10.3390/min10050480.

[298] H. Wang, C. Li, Z. Peng, et S. Zhang, Characterization and thermal behavior of kaolin, Journal of Thermal Analysis and Calorimetry 105 (2011) doi: 10.1007/s10973-011-1385-0.

[299] P. Ptáček, D. Kubátová, J. Havlica, J. Brandštetr, F. Šoukal, et T. Opravil, The non-isothermal kinetic analysis of the thermal decomposition of kaolinite by thermogravimetric analysis, Powder Technology 204, 2, 222-227 (2010) doi: 10.1016/j.powtec.2010.08.004.

[300] H. Cheng, Q. Liu, J. Yang, S. Ma, et R. L. Frost, The thermal behavior of kaolinite intercalation complexes-A review, Thermochimica Acta 545, 1-13, (2012) doi: 10.1016/j.tca.2012.04.005.

[301] E. Gasparini et al., Thermal dehydroxylation of kaolinite under isothermal conditions, Applied Clay Science, 80-81, 417-425, (2013) doi: 10.1016/j.clay.2013.07.017.

[302] P. Ptáček, F. Frajkorová, F. Šoukal, et T. Opravil, Kinetics and mechanism of three stages of thermal transformation of kaolinite to metakaolinite, Powder Technology 264, 439-445, (2014) doi: 10.1016/j.powtec.2014.05.047.

[303] Cheng et al., Dehydroxylation and Structural Distortion of Kaolinite as a High-Temperature Sorbent in the Furnace, Minerals 9, 10, 587 (2019) doi: 10.3390/min9100587.

[304] D. Massiot, P. Dion, J.-F. Alcover, et F. Bergaya, ^{27}Al and ^{29}Si MAS NMR Study of Kaolinite Thermal Decomposition by Controlled Rate Thermal Analysis, Journal of the American Ceramic Society 78, 11, 2940-2944 (1995) doi: 10.1111/j.1151-2916.1995.tb09067.x.

[305] S. Sperinck, P. Raiteri, N. Marks, et K. Wright, Dehydroxylation of kaolinite to metakaolin—a molecular dynamics study , J. Mater. Chem. 21, 7, 2118-2125 (2011) doi: 10.1039/C0JM01748E.

[306] I. Daou, G. Lecomte-Nana, N. Tessier-Doyen, C. Peyratout, M. Gonon, et R. Guinebretiere, Probing the Dehydroxylation of Kaolinite and Halloysite by In Situ High Temperature X-ray Diffraction, Minerals 10, 5, 480 (2020) doi: 10.3390/min10050480.

[307] J. Rocha et J. Klinowski, ^{29}Si and ^{27}Al Magic-angle-spinning NMR Studies of the Thermal Transformation of Kaolinite, p. 8.

[308] A. Ghorbel, M. Fourati and J. Bouaziz, Mater. Chem. Phys., 876–885, 112 (2008).

[309] P. A. Alaba, Y. M. Sani, et W. M. Ashri Wan Daud, Kaolinite properties and advances for solid acid and basic catalyst synthesis, RSC Adv.5, 122, 101127-101147 (2015) doi: 10.1039/C5RA18884A.

[310] https://rruff.info/

[311] W.E. Lee, Characterisation of corrosion mechanisms in refractories by post-mortem microstructural analysis Br. Ceram. Proc. 57 (1997).

[312] A. Hawksworth and W. E. Lee, Microstructural observation of bottom drilling corrosion in electrocast Al2O3-ZrO2-SiO2 refractories, Journal of materials science letters 15.19 (1996): 1702-1704.

[313] D. Hernandez et al., Pyroreflectometry to Determine the True Temperature and Optical Properties of Surfaces, ASME. J. Sol. Energy Eng. (2008) 130(3): 031003. https://doi.org/10.1115/1.2840575.

[314] W. Cao, Synthesis and characterization of highly non-stoichiometric garnet oxides. Chemical engineering. Université d'Orléans (2021).

List of publications and oral presentations in international conferences

Pubblications

- I.M.Ermini, L.Cosson, F.Fayon, D.Zanghi, C.Tardivat, D.De Sousa Meneses; Real time FT-IR observation of materials during their cooling from molten state; Infrared Physics and Technology, 127 (2022) 104424.
- I.M.Ermini, L.Cosson, F.Fayon, I.González de Arrieta, O.Rozenbaum, P.Vespa, D.De Sousa Meneses; Development and application of a Rapid Scan technique for emissivity measurements of cooled down molten materials; Engineering Proceedings (2023) 51(1):8.
- I.M.Ermini, I.González de Arrieta, F.Fayon, P. Vespa, D.De Sousa Meneses; Static and kinetic study of the structure of vitreous silica at high temperatures by infrared emission spectroscopy (submitted to JNCS).
- Paper in progress to be submitted to Infrared Physics and Technology issue VSI: AITA 2023 reserved to selected papers (winner of the Under 35 Best Paper Award).

International conferences

- International Congress on Glass (ICG) 2022 | 3-7 July, Berlin
- DGG-USTV Joint Annual Meeting 2023 | 22-24 May, Orléans
- Glass & Optical Materials Division Annual Meeting (GOMD) 2023 | 4-8 June, New Orleans
- Advanced Infrared Technology and Applications (AITA) 2023 | 10-13 September, Venice; **Winner of the Under 35 Best Paper Award**

Ilse Maria ERMINI

Exploration des systèmes M_xO_y-Al_2O_3-SiO_2 à travers leur dynamique et leur structure, depuis le milieu fondu jusqu'à basse température

Résumé : La science des matériaux vit actuellement des avancées importantes liées notamment à l'originalité et à la diversité accrues des méthodes de synthèse, à la maturité des méthodes de simulation numérique associée à la disponibilité de moyens de calcul de plus en plus performants, mais également et surtout grâce aux perfectionnements des techniques de caractérisation en termes notamment de vitesse et de résolution. Cette convergence des méthodes numériques et des techniques expérimentales ouvre la voie à une étude plus systématique des diagrammes de phase et à l'exploration du comportement des systèmes en dehors de l'équilibre thermodynamique. La possibilité de contrôler l'environnement des milieux fondus et les vitesses de refroidissement constituent des atouts majeurs pour la compréhension de ces systèmes et la possibilité d'élaborer des nouvelles structures à travers le contrôle de leur histoire thermique. On s'intéressera dans cette thèse aux diagrammes d'oxydes M_xO_y−Al_2O_3−SiO_2 (avec M_xO_y = ZrO_2, ZnO, SrO…) à haut point de fusion dont l'analyse nécessite la production de très hautes températures peu atteignables par des dispositifs conventionnels. L'étude de ces systèmes présente un fort intérêt dans différents domaines tels que la production de verres résistants aux alcalins, la conception de réfractaires stables chimiquement ou encore l'élaboration de vitrocéramiques. Le développement d'un nouveau plateau d'essais au laboratoire CEMHTI permettant de confiner les milieux fondus par des techniques hors container et de caractériser à la fois leurs propriétés thermo-physiques et des grandeurs microscopiques intégrant de l'information sur la dynamique et la structure, offre un cadre naturel pour cette étude. L'exploration de la phase liquide et de la zone de surfusion devrait permettre d'identifier les conditions propices à la formation de phases originales qu'elles soient amorphes ou cristallines ainsi que de mieux comprendre les mécanismes microscopiques qui sont les catalyseurs de leur stabilisation. Les compositions sélectionnées constituent des systèmes de choix pour éclairer cette problématique. En effet, le réseau aluminosilicate est très versatile, il favorise l'émergence de propriétés souvent remarquables et son interaction avec les éléments fondants ou intermédiaires doit permettre de comprendre la variabilité des comportements et des structures.

Mots clés : dynamique, hors équilibre, verres, milieux fondus, haute température, microstructure

Exploration of M_xO_y-Al_2O_3-SiO_2 systems through their dynamics and their structure, from the melted medium to the low temperature

Summary : Materials science is currently experiencing major advances linked in particular to the originality and increased diversity of synthesis methods, to the maturity of numerical simulation methods associated with the availability of increasingly efficient means of calculation, but also and especially thanks to improvements in characterization techniques, particularly in terms of speed and resolution. This convergence of numerical methods and experimental techniques opens the way to a more systematic study of phase diagrams and to the exploration of the behavior of systems outside of thermodynamic equilibrium. The possibility of controlling the environment of the molten media and the cooling rates are major assets for understanding these systems and the possibility of developing new structures by controlling their thermal history. In this thesis, we will focus on M_xO_y − Al_2O_3 − SiO_2 oxide diagrams (with M_xO_y = ZrO_2, ZnO, SrO, etc.) with a high melting point, the analysis of which requires the production of very high temperatures which cannot be reached by conventional devices. The study of these systems is of great interest in various fields such as the production of alkali-resistant glasses, the design of chemically stable refractories or even the development of glass-ceramics. The development of a new test platform at the CEMHTI laboratory allowing the confinement of molten media by container-free techniques and characterizing both their thermophysical properties and microscopic quantities integrating information on dynamics and structure, provides a natural setting for this study. Exploration of the liquid phase and the supercooling zone should make it possible to identify the conditions conducive to the formation of original phases, whether they are amorphous or crystalline, as well as to better understand the microscopic mechanisms, which are the catalysts for their stabilization. The selected compositions constitute the systems of choice to shed light on this problem. Indeed, the aluminosilicate network is very versatile, it favors the emergence of often-remarkable properties and its interaction with modifier or intermediate elements must make it possible to understand the variability of behaviors and structures.

Keywords : melts, high temperature, microstructure, out of equilibrium, dynamics, glasses

Conditions Extrêmes et Matériaux :
Haute Température et Irradiation
CEMHTI UPR 3079 CNRS
1D Avenue de la recherche scientifique
45071 Orléans cedex 2, France